Semi-solid Processing of Al-Si7-Mg Alloys

Muhammad Kamran

Chair of Casting Research
University of Leoben, Austria

A thesis submitted for the degree of
Doctor of Philosophy at the University of Leoben
Winter Semester, 2007/2008

Semi-solid Processing of Al-Si7-Mg Alloys

Muhammad Kamran
Chair of Casting Research, University of Leoben
Doctor of Philosophy
Winter Semester 2007/08

Abstract

The cooling slope can be an effective technique for the production of a thixotropic precursor alloy but the control of the microstructure is complex and is dependent upon the processing parameters. This work investigates the semi-solid processing of Al-Si-Mg alloys using the cooling slope technique. A newly determined contact time parameter was used obtaining a correlation with undercooling, inclination angle and flow velocity. For a non-refined non-modified AlSi7Mg alloy, the effect of pouring temperature (680, 660 and 640 °C), contact time (0.04, 0.09 and 0.13 s), inclination angle (20, 40 and 60°), mould material (sand and metal), sample thickness (10 mm to 34 mm in sand mould) and coating on the cooling slope (graphite and boron nitride) were examined with respect to the final microstructure which, for optimal results should be fine and globular. The microstructure and temperature characteristics of the alloy were compared with an as-cast and as-received commercial AlSi7Mg alloy and a commercially produced magnetohydrodynamic stirred (MHD) A356 alloy.

The results indicated that the chemical composition of the alloys have a prominent effect on features such as solidification reaction temperatures, solidification sequence and intermetallic phases. From findings it became clear that methods typically used in semi-solid processing studies to analyse globular grains were erroneous. It was found that the anodizing of samples helped in reducing these errors. The change in alloy characteristics has also a profound effect on the change in fraction solid in the semi-solid range which resulted in the variation in both the temperature and fraction solid limit for thixoforming. The cooling slope has a dual role: the extraction of heat thereby affecting the grain size and morphology both on the slope interface and the bulk melt by creating a thermal undercooling necessary for the columnar to equiaxed transition (CET); and, by influencing the dominant nucleation mechanism. The final observed microstructures were additionally influenced by the heat extraction and thermal gradients imposed by the mould material. This explains the complex and different microstructure observed.

Preface

The work described in this thesis was carried out by the author at the Chair of Casting Research, University of Leoben, Austria from October 2004 to January 2008 under the supervision of Prof. P. Schumacher.

This thesis is submitted for the degree of Doctor of Philosophy at the University of Leoben. The research is original and no part of this thesis has already been accepted or is being submitted for any other degree or qualification in this university or elsewhere. Where the work of others has been used or reported, it is acknowledged in the text.

Muhammad Kamran
University of Leoben, Leoben
Winter Semester, 2007/8

Acknowledgements

The experimentation described in this thesis was carried out in its entirety at the Chair of Casting Research, University of Leoben, Austria. The author would like to express his gratitude to Professor Dr. P. Schumacher, and Dr. B.J. McKay, from the aforementioned chair for their support and excellent supervision.

The author would also like to thank the Higher Education Commission (HEC), Government of Pakistan for their financial support and ÖAD for their managerial help in facilitating my stay in Austria, without whom this research would not have been possible.

Finally I would like to thank my family, friends and work colleagues, especially all those who helped with this study for their support and assistance over the years.

VORLAGE/DECLARATION

Eidesstattliche Erklärung:
Ich erkläre an Eides statt, dass ich diese Arbeit selbständig verfasst, andere als die angegebenen Quellen und Hilfsmittel nicht benutzt und mich auch sonst keiner unerlaubten Hilfsmittel bedient habe.

Affidavit:
I declare in lieu of oath, that I wrote this thesis and performed the associated research myself, using only literature cited in this volume.

Signature: _____

Muhammad Kamran

University of Leoben, Leoben

Winter Semester, 2007/8

Table of Contents

ABSTRACT……...II

PREFACE…...……III

ACKNOWLEDGMENTS……...IV

VORLAGE/DECLARATION……...……V

NOMENCLATURE…..……...…….……X

CHAPTER 1
INTRODUCTION…..…….……...…….....1

CHAPTER 2
LITERATURE REVIEW…….....5

2.1 Introduction……..……..……..5
2.2 Phenomenology…….……7
2.2.1 Rheology and Thixotropy.....……..…..……..7
2.2.1.1 Measurement Techniques……..……...…….…..11
2.2.2 Nucleation and Growth Theories……...……..11
2.3 Semi-solid Processing…...…….……...…..21
2.3.1 Semi-solid Forming Processes…….21
2.3.2 Slurry Feedstock Production……..…….....22
2.4 Cooling Slope/Plate…….....……..23
2.5 Characteristic Parameters……..……26
2.5.1 Material Characteristics……....……....26
2.5.2 Microstructure Characteristics…….29
2.6 Materials Characterisation……..……31
2.6.1 Cooling Curves…....……..…….31
2.6.2 Thermal Analysis……..…..…….32
2.6.2.1 Power Compensated Calorimetry DSC…….……..33
2.7 Fraction Solid and its Measurement…….……..……37
2.7.1 Thermodynamic Methods……...…….....40
2.7.2 Enthalpy...…..……...45
2.7.3 Cooling Curves…...……..……...46
2.7.4 Thermal Analysis..……..……46
2.8 Mechanical Properties…..……..……48
2.9 Commercial Products…...……..49
2.10 Figures...…..……...……..50

CHAPTER 3
EXPERIMENTAL METHODS…..……73

3.1 Introduction……..…..……73
3.2 Materials Selection……..73
3.3 Characterisation of Starting Material……..74
3.3.1 Chemical Analysis……...74
3.3.2 Thermal Analysis…..……...……...…….74
3.3.3 Differential Scanning Calorimetry (DSC)…….....…….....75
3.3.4 Simulation with ThermoCalc®……76
3.4 Melt Handling……..76
3.4.1 Melting……..76
3.4.2 Pouring……77
3.4.3 Temperature Control……...77
3.5 Cooling Slope……..77
3.5.1 Construction……77
3.5.2 Coating……78
3.5.3 Cooling……78
3.5.4 Processing Parameters……..78
3.6 Mould Design and Material……79
3.7 Sample Preparation……..79
3.7.1 Cutting……79
3.7.2 Grinding and Polishing……80
3.7.3 Etching/Anodizing……...80
3.8 Microscopy……81
3.8.1 Optical Microscopy……81
3.8.2 Scanning Electron Microscopy (SEM) ……...81
3.9 Image Analysis……82
3.10 Contact Time Verses Contact Length……...82
3.11 Grain Characteristics……..……...83
3.11.1 Grain Size……...84
3.11.2 Circularity……...84
3.11.3 Elongation……...84
3.12 Figures……...86

CHAPTER 4
RESULTS……..96

4.1 Characterisation of AlSi7Mg Alloys……...96
4.1.1 Introduction……...96
4.1.2 Chemical Analysis……...……96
4.1.3 Cooling Curve Analysis……...97
4.1.4 DSC Analysis……...98
4.1.5 Thermo-Calc® Simulation……....102
4.1.6 Microscopy……102
4.1.7 Summary……105
4.1.8 Tables……107
4.1.9 Figures……112
4.2 Fraction Solid and Fraction Solid Sensitivity……146
4.2.1 Fraction Solid……146
4.2.2 Fraction Solid Sensitivity……...148
4.2.3 Summary……153
4.2.4 Tables……155

4.2.5 Figures……..……..169
4.3. Effect of Processing Parameters…….....174
4.3.1 Introduction……174
4.3.1.1 Microstructure Characteristics and their Measurement……..……174
4.3.1.2 Data Distribution and Analysis……..…174
4.3.2 Effect of Pouring Temperature……...175
4.3.2.1 Constant Contact Time……...175
4.3.2.2 Constant Inclination Angle……....178
4.3.3 Effect of Contact Time……...181
4.3.3.1 Constant Pouring Temperature……...……..181
4.3.3.2 Constant Inclination Angle……...…..……184
4.3.4 Effect of Inclination Angle……....186
4.3.4.1 Constant Contact Time……..187
4.3.4.2 Constant Pouring Temperature……189
4.3.5 Summary……192
4.3.6 Tables……193
4.3.7 Figures……...199
4.4. Effect of Sample Thickness…….……202
4.4.1 Effect of Processing Parameters Combined with the
Effect of Position in 10 mm Thick Sample (Wall to Centre)..……..……...203
4.4.1.1 Effect of Pouring Temperature...……...……203
4.4.1.2 Effect of Contact Time……...…206
4.4.1.3 Effect of Inclination Angle……..…210
4.4.2 Effect of Processing Parameters Combined with
Sample Thickness Variation from 10 mm to 34 mm……214
4.4.2.1 Effect of Pouring Temperature……..215
4.4.2.2 Effect of Contact Time……....219
4.4.2.3 Effect of Inclination Angle……...…..223
4.4.3 Summary……....226
4.4.4 Tables……228
4.4.5 Figures……...……234
4.5. Effect of Mould Material on Final Grain Characteristics…….235
4.5.1 Effect of Pouring Temperature……..235
4.5.1.1 Constant Contact Time……..235
4.5.1.2 Constant Inclination Angle……240
4.5.2 Effect of Contact Time……..244
4.5.2.1 Constant Pouring Temperature……244
4.5.2.2 Constant Inclination Angle……249
4.5.3 Effect of Inclination Angle……253
4.5.3.1 Constant Pouring Temperature……253
4.5.3.3 Constant Contact Time……...258
4.5.4 Summary……262
4.5.5 Tables……264
4.6. Effect of Coating Material……270
4.6.1 Full Coating……....270
4.6.2 Partial Coating……...272
4.6.3 Cooling of slope……273
4.6.4 Summary……....274
4.6.5 Tables……275
4.7. Comparison of Alloys……...276
4.7.1 Comparison of the NGM AlSi7Mg and the COM AlSi7Mg Alloys……276
4.7.1.1 Effect of Inclination Angle and Coatings…….……..276
4.7.1.2 Cooling of slope and Coating……277
4.7.1.3 Effect of Partial Coating……279
4.7.2 Comparison of the NGM AlSi7Mg, COM AlSi7Mg and MHD A356 Alloys…..280
4.7.3 Summary……281

4.7.4.Tables……...……...……283

CHAPTER 5
DISCUSSION……285
5.1 Variations in the Alloys……..……..285
5.1.1 Characteristic Temperature……..……...285
5.1.2 Intermetallic Phases…….....……...290
5.1.3 Solidification Behaviour……...…….292
5.1.4 Fraction Solid and Fraction Sensitivity…….293
5.1.5 Response to Semi-solid Processing using the Cooling Slope Technique….....294
5.1.5.1 Comparison of NGM AlSiMg and COM AlSi7Mg Alloys….....294
5.1.5.2 Comparison of NGM AlSiMg,COM AlSi7Mg and MHD A356 Alloys..295
5.2 Effect of Contact Time……..……296
5.3 Determination of Grain Characteristics…….297
5.4 Evolution of Microstructure……..…...299
5.4.1 Nucleation and Growth on Cooling Slope…….....300
5.4.2 Nucleation, Growth and Coarsening in the Mould ……....303
5.5 Tables…….……...306
5.6 Figures…….……..308

CHAPTER 6
CONCLUSIONS……....323

CHAPTER 7
FUTURE WORK……..326

BIBLIOGRAPHY……328

List of Nomenclature

Symbol	Meaning	Units
K	Constant	-
τ	Shear force	N
τ_y	Yield shear force	N
G	Free energy	J/mol
G_v	Volume free energy	J/mol
γ	Surface free energy	J/mol
ΔG_{cr}	Critical free energy	J/mol
r^*	Critical nucleation radius	m
ΔG^{het}	Free energy for heterogeneous nucleation	J/mol
$\Delta G^{\hom}$	Free energy for homogeneous nucleation	J/mol
G_c	Concentration gradient	at%/m, wt%/m
D	Diffusion coefficient	m^2/s
m	Slope	
Γ	Gibbs Thompson coefficient	Km
k	Partition coefficient	-
V	Interface growth velocity	m/s
C_α	Contiguity	-
$S_{\alpha\alpha}$	$\alpha\alpha$-Grain boundary	-
$S_{\alpha l}$	Boundary between alpha and liquid phase	
f_s	Solid fraction	-
f_s^{Eq}	Solid fraction at equilibrium	-
f_s^{Qd}	Solid fraction quadratic	-
f_s^{Lev}	Solid fraction lever rule	-
f_s^{Sch}	Solid fraction scheil	-
f_s^{Bd}	Solid fraction back diffusion	-
S_v	Solid-liquid interface surface area per unit volume	m^{-1}
N_A	Number of grains per unit area	-

C_p	Specific heat	J/mol.K
T_f	Fusion temperature	^{o}K
$\dot{T}$	Heating rate	^{o}K/s
H	Enthalpy	J/mol
Q	Heat absorbed	Joules

Chapter 1

Introduction

Semi-solid processing as the name suggests is the processing of non-dendritic material between its liquidus and solidus temperatures. In recent years much work has been conducted in exploring this field with respect to understanding the mechanisms involved. The inherent properties of semi-solid materials at the semi-solid processing temperature such as lower heat content, relatively higher viscosity comparable to liquids and low flow stresses, enables the semi-solid process to show distinct advantages over fully liquid and/or fully solid state processes. Some of the important benefits of this technique are: low mould erosion, low energy consumption, improved die filling, less gas entrapment, improved soundness, lower solidification shrinkage, reduced macro-segregation and fine microstructure to name but a few. As a consequence this process is rapidly gaining commercial importance[1,2,3].

Semi-solid processing covers all the shape forming processes which take advantage of the semi-solid range of the alloys for processing. Rheocasting, the first semi-solid process, was discovered in 1971 by Spencer[4] while he was investigating hot tearing during solidification. In his study a liquid like slurry with non-dendritic solid particles was obtained by stirring while cooling a Sn-15%Pb alloy in the semi-solid range[1,2].

In semi-solid processing two basic phenomena, namely Rheology and Thixotropy, play a major role. In Rheology the apparent viscosity of a material in the liquid state varies with change in shear rate. This enables the liquid like slurry to be processed even at sufficiently high solid contents[1,2]. Thixotropy, on the other hand, is the ability of a material to regain the liquid like slurry state from a solid state. In metals with a non-dendritic microstructure a liquid like slurry can be attained on reheating into the semi-solid state[1,2].

A material with a globular shaped microstructure is supposedly the best suitable material for semi-solid processing. For this material it is believed that, when in the semi-solid state, the non-dendritic globular grains easily glide on each on the application of a force[1,2].

A non-dendritic microstructure can be obtained by: stirring[1], either mechanically or electromagnetically[1]; grain refining[2]; low superheat melt processing[3]; solid state mechanical treatment and reheating[1]; reheating a suitable material into semi-solid state[1]; and, by spray forming and densification[1].

To describe the dendritic to non-dendritic transformation, many theories have been proposed. To explain the morphology transformation during stirring: Vogel[5,6] proposed secondary dendrite arm bending and melting due to fluid flow[1,2]: Hellawell[7,8] proposed root melting of the dendrite secondary arm from the stem[1,2]; and, Uhlmann[9,10] suggested a remelting of secondary arm due to ripening as a result of solute pile up in the interdendritic region[1]. Chalmers[11,12] proposed a "Big Bang" nucleation mechanism due to the undercooling of a low superheat melt on the chill mould wall[2], and Ohno[13] proposed a "wall mechanism" due to the undercooling and flow of melt against the mould wall, for a low superheat process[14,15]. The melting of highly stressed grain boundaries on reheating and subsequent ripening of recrystallised grains is believed to be the reason for non-dendritic microstructure development in mechanically strained materials in the semi-solid state[2,16].

Semi-solid processing was divided into different categories by different researchers. Flemings[1] divided semi-solid processing into two subclasses: Rheocasting – which involves the application of a shearing force during solidification to produce a non-dendritic semi-solid slurry that can be then transferred directly into a mould or die to shape a final product[2] in a batch type or continuous manner; Thixoforming – which involves near net shaping of a partially melted non-dendritic alloy slug within a metal die[2], which has two variants Thixocasting and Thixoforging, depending on how the metal is fed into the die.

However, Fan[2] and Atkinson[3] divided the semi-solid processes based on: the preparation method of the feedstock – mechanical stirring, magnetohydrodynamic stirring (MHD), stress-induced melt activation (SIMA), spray forming, ultrasonic

treatment, chemical grain refinement and liquidus casting; and, the shaping processes – Rheocasting, Thixoforming, Thixomolding and Rheomolding.

From the above mentioned feedstock preparation processes liquidus casting has recently gained the attention of researchers in recent years due to its simplicity and adaptability[3]. The most common processes are: New Rheocasting (NRC)[17,18], in which a molten melt near the liquidus temperature is poured into a tilted mould, cooled in a controlled manner and at the required solid fraction, the material is squeeze cast; New MIT semi-solid Rheocasting (SSR™)[3,19], in which a cold rotating graphite rod is immersed for a few seconds in a near liquidus melt and the melt is cooled under controlled conditions; and the cooling slope method[20] in which a liquid melt is poured onto a cooled inclined slope and an undercooled melt is obtained in a mould.

The cooling slope technique, mentioned above, is quite simple but very effective in producing a non-dendritic microstructure. The use of the cooling slope in casting processes in Japan has been reported[21], and evaluated by Haga[20,22], Liu et al.[23], Yano et al[24] and Nomura and co-workers[25,26,27,28,29]. In all the reported data, the cooling slope can produce a final microstructure which is non-dendritic.

Although some work on AlSi7Mg alloys using a cooling slope has been reported[20,22,24,30], the effect of the cooling slope on non-grain refined non-modified AlSi7Mg is not clear, as grain refinement, modification and chemical composition can affect the final microstructure. In addition to these factors, not all the processing variables, affecting the final microstructure, have been studied. As a result in this study, a non-grain refined non-modified AlSi7Mg alloy was processed using the cooling slope technique. The effect of pouring temperature, inclination angle, contact time, mould material, sample thickness and coating material was studied. The results were also compared with a commercial grain refined AlSi7Mg alloy and a commercially produced precursor using a Magnetohydrodynamic stirred (MHD) AlSi7Mg A356 alloy.

In this thesis Chapter 2 reviews the relevant literature thereby giving the reader an insight into the background behind semi-solid processing techniques, the solidification mechanisms involved and the methods for characterising alloys and

determining their suitability. Chapter 3 deals with the experimental methods and procedures used in this study. The results of this research are presented in Chapter 4 and are subsequently discussed in Chapter 5. Conclusions from this work are drawn in Chapter 6 and an outline of future work suggested in Chapter 7, which is followed by a bibliography.

Chapter 2

Literature Review

2.1 Introduction

In normal solidification there are three distinct zones, namely a fine chill, a columnar and an equiaxed zone; the extent of each dependent on the casting process[31] (see Fig. 2.1(a)). Flemings et al.[32,33] in 1971, found that stirring a Sn-15%Pb alloy in the semi-solid state resulted in a globular rather than dendritic morphology (Fig. 2.1(b) & 2.1(c)). They also found that the resulting materials have a low viscosity, when processed in the semi-solid state[32,33]. Since this milestone much research has been conducted with respect to understanding the phenomena and to exploring the different possibilities of utilizing these properties in commercial products.

Processes which deal with a metallic material in the semi-solid range to form a near-net shape product are termed "semi-solid processes" [34]. The material may be a slurry of solid particles in a liquid melt obtained directly from molten metal by stirring, a reheated slug made from stirred slurry in the semi-solid state or a severely deformed material reheated to partial melting, in the semi-solid state[35,36,37].

Similar to die casting, the mould filling temperature, energy extraction, flow in mould filling, and solidification microstructure are critical features which influence the quality of products manufactured by semi-solid forming methods[37]. A reliable feedstock source, robust semi-solid forming technology to minimize the effects of variation in the processing parameters and suitable semi-solid forming alloys are some critical semi-solid forming process requirements[37].

Design for manufacturability takes into account the assurance of proper die filling and the avoidance of micro and macro-shrinkage, cold shuts, etc.

The main advantages of semi-solid processing, mostly relative to die casting[3,19,33,37,38,39,40,41,42] are claimed to be due to,

- Energy efficiency: Metal is not being held in the liquid state over long periods of time[39].
- Higher production rates due to reduced process cycle time compared to pressure die casting.
- Smooth filling of the die with no air entrapment and low shrinkage porosity gives parts of high integrity (including thin-walled sections). It therefore allows application of the process to higher-strength heat-treatable alloys and enables a wide variety of complex geometric forms to be produced[43,44,45], with high dimensional quality[46], improved mechanical properties and close tolerances[47], all as a result of the fine, uniform microstructures.
- Lower processing temperatures reduce the thermal shock on the die, promoting die life and allowing the use of non-traditional die materials. It also enables the processing of high melting point alloys such as tool steels that are difficult to form by other means[32,45], with a reduction in solidification shrinkage[47], reduction in die dwell time, increased die life, and reduced die fatigue due to reduced thermal shock.
- A lower flow stress[41] which requires a lower forging force[41] and a lower impact on the die introduce the possibility of using rapid prototyping dies.
- Reduced solidification shrinkage gives dimensions closer to near net shapes and justifies the removal of machining steps; the near net shape capability (quantified, for example, in[47]) reduces machining costs and material losses.
- Weight reduction relative to other high volume casting processes and a reduced total component cost[42].

The expected disadvantages[1,3,35,46 48] are:

- The cost of raw material as it constitutes about 50% of the cost of the product can be high and the number of suppliers is small.
- Process knowledge and experience has to be continually built-up in order to facilitate the application of the process to new components, which leads to potentially higher die development costs.

- Initially at least, personnel require a higher level of training and skill than with more traditional processes.
- An accurate temperature control is required otherwise liquid segregation due to non-uniform heating can result in a non-homogeneous component.
- No advanced simulation tool exists to facilitate advanced process control.

2.2 PHENOMENOLOGY

Flemings et al.[32,33] observed on the continuous stirring of the metallic alloy in the semi-solid state that not only the microstructure of the alloy changes from dendritic to non-dendritic , but also that the semi-solid slurry showed quite less viscosity compared to that for normal conditions. They also found that on shear, the material behaved as a liquid-like "slurry" and the stress required to deform this slurry was orders of magnitude below the maximum stress required to deform the usual dendritic structure[34]. The apparent viscosity of this slurry rose with an increase in its fraction solid[34,49,50] (Fig. 2.2)[51]. So there are two very important and different phenomena involved in semi-solid processing, which are the rheological behaviour and the transformation of a dendritic to globular structure.

2.2.1 Rheology and Thixotropy

In Newtonian fluids/slurries, measured viscosity is independent of time and shear rate i.e. the shear stress, τ, is proportional to the shear rate, $\dot{\gamma}$ and the constant of proportionality is the viscosity, η. Thixotropic fluids are non-Newtonian, i.e. the shear stress is not proportional to the shear rate. The viscosity is then termed as apparent viscosity and is dependent on shear rate, pressure, temperature, and time[3]. The semi-solid slurries of metallic alloys show thixotropic behaviour[35]. Thixotropy results from the formation of a suitable structure within the slurry, with particle welding possibly occurring in metallic slurries[50,522]. Hysteresis loops are used to confirm the thixotropic nature of metallic slurries[53].

Different models have been suggested to define the trend of the material with shear rate. If the fluid exhibits a yield stress and then gives a linear relationship between shear stress and shear rate, it is termed 'Bingham' material. Then

$$\tau = \tau_y + k\dot{\gamma} \quad \text{Eq. (2.1)}$$

where k is the constant related to viscosity, τ is shear force and $\dot{\gamma}$ is shear rate. The Herschel-Bulkley model is where the behaviour is non-linear after yield i.e.:

$$\tau = \tau_y + k\dot{\gamma}^n \quad \text{Eq. (2.2)}$$

The Ostwald-deWaele relationship:

$$\tau = k\dot{\gamma}^n \quad \text{Eq. (2.3)}$$

where n is a constant, is used to describe the fluids which do not have a yield point and where there is a power law relation between shear stress and shear rate[3].

When the metallic alloy material is step-wise partially solidified by continuous cooling, the melt flows with different shear rates. The fluid within these slurries varies with increasing solid fraction from Newtonian to pseudoplastic and then to Bingham once most of the solid has formed a chain-like structure[52].

It was found that metals also behave like thixotropic slurry in the semi-solid state as cited in[53]. In slurries, on the application of shear force, material deforms elastically and beyond a particular shear stress called the yield stress, material behaves like a fluid. This behaviour is termed as "Rheology".

Understanding of the time-dependent flow behaviour of SSM is essential for the success of semi-solid processing e.g. Rheocasting and Thixocasting[50,53]. Shear-rate dependence on the apparent viscosity was reported in 1974 by P.A. Joly in his Ph.D. thesis entitled "Rheological properties and structure of a semi-solid Sn-Pb alloy" at MIT , as cited in[53].

The transient response of SSM slurry, particularly the abrupt shear rate change in the gate and the cavity within a short period of time, is one of the parameters to be evaluated for better understanding. This is usually achieved by conducting shear rate jump-up and jump-down tests[53,54] (see Fig. 2.3).

A slurry shows the following behaviours with a change in shear rate[53,54]:

- Steady state behaviour
- Transient behaviour

- Thixotropic behaviour

In steady state behaviour for a particular shear rate the apparent viscosity remains the same with constant shear stress, with time. The value of the steady state apparent viscosity only varies with changing shear rate or solid fraction. For a constant shear rate, the apparent viscosity increases with an increase in the solid fraction (see Fig. 2.2). For a constant solid fraction the apparent viscosity decreases with increasing shear rate (see Fig. 2.2) [2,3,53,54].

The apparent viscosity was found to increase with increasing solid fraction in the Sn-15%Pb[34] alloy and decrease with increase in shear rate with time[34].

In transient behaviour the shear stress changes abruptly with sudden change in shear rate. With sudden decrease in shear rate to another shear rate, the shear stress suddenly decreases to a minimum value and then increases to a stable value with time, but never attains the original value at the new shear rate. This phenomenon is termed "shear thinning". However, with a sudden increase in shear rate, the shear stress jumps up to a peak value and then decreases with time to a steady state condition at the given shear rate with time, but this value never decreases to the original value. This phenomenon is termed "shear thickening". These phenomena are explained on the basis of the agglomeration and deagglomeration of the solid particles. At a steady state the solid particles are aggolomerated to a particular size. With change in shear rate, the formation or break-down of these agglomerates occurs with a jump-down or jump-up in shear rate as shown in Fig. 2.4[53,55].

There is a critical shear rate, which is a function of fraction solid, such that only those steady state viscosity values measured above the critical shear rate are meaningful. Similarly the critical solid fraction and characteristic time are also important. Shear thinning occurs at a higher shear rate, and apparent yield at a lower shear rate, under steady state conditions[53].

The size of the primary particles decreases with an increase in stirring rate, which in turn increases the shear rate, resulting in more fragmentation and little sintering between the primary particles[53].

Thixotropy is a time-dependent rheological property of SSM's referring to a reversible suspension structure, an agglomeration or solid particles or a solid skeleton, which develops when the flow is at rest and can be destroyed by the application of shear. On shearing the solid like skeleton breaks down and the slurry behaves in a similar manner to before rest. However, the initial shear force required to break the bonding depends on the rest time. Thixotropy is usually measured with a hyteresis loop developed by a continuous alternative change in shear rate (see Fig. 2.3). The wider the gap between the loop the more thixotropic the slurry[2,3,53,54]. It is important because during the idling phase after filling the shot chamber (casting) and accumulation zone (moulding) the change in structure may alter the rheological behaviour in the subsequent filling of the mould[53].

Resistance of a semi-solid material to flow at a high fraction solid (particularly spray casting) may be caused by; high solid fractions at which the low angle boundaries of adjacent grains are not wetted with the liquid, and solid bonding occurs (about 10-15%). Due to the high co-ordination number of each grain (z~12-14) bonded grains form agglomerates which may span the complete volume of the sample, and the shear force can only be accommodated by breaking of some bonds. Shear force may be accommodated by a combination of translation and rotation of adjacent grains, resulting in shear bands[56]. "Two phase models" for deformation behaviour at higher fraction solid[56] considering the cohesive forces and cohesive limit of solid particles was presented in Fig. 2.5.

Compression experiments on a spray cast alloy in the semi-solid state at high solid fractions, > 0.5, i.e. primary grains remaining equiaxed, showed a non-homogeneous deformation. The non-homogeneous deformation may be due to the localized strain resulting from local softening due to the breaking of the bonds between solid grains and dilatency as a result of the relative motion of solid grains[56].

According to[57] the flow resistance of semi-solid alloys at high fraction solids is due to elasto-plastic deformation at grain contacts, destruction of cohesive bonds between solid particles, resistance to the flow of liquid relative to the solid and resistance to grain rearrangement. The first two phenomena are effective at the initial stage, while the third and fourth factors are effective in the last stage of deformation.

2.2.1.1 Measurement Techniques

Thixotropic behaviour of an alloy can be measured[58,59] by using "Couette Viscometery" [55] to study the viscosity of an alloy with a low to medium volume solid fraction, "Forward and Backward Extrusion" to simulate realistic processing conditions and "Simple Compression"[60] and "Triaxial Compression Experiments"[61] to examine the effect of soaking time, temperature, strain rate and pressure[41,62].

2.2.2 Nucleation and Growth Theories

In this section the nucleation and growth mechanisms involved in semi-solid processing, particularly in the cooling slope technique, are discussed.

The classical homogeneous nucleation theory describes how a sustainable nuclei of the solid phase with critical radius, r^*, in the melt can only form if the volume free energy, ΔG_v, of the cluster is higher than the opposing surface free energy, γ_{LS}, for the given cluster. The critical energy, ΔG_{cr}, and critical radius r* for homogeneous nucleation[14,15,31,63,64] would be:

$$\Delta G = -v_S \Delta G_v + A_{LS} \gamma_{LS} = -\frac{4}{3}\pi r^3 \Delta G_v + 4\pi r^2 \gamma_{LS} \qquad \text{Eq. (2.4)}$$

$$\text{where} \quad r^* = \frac{2\gamma_{LS}}{\Delta G_v} \quad \text{and} \quad \Delta G_{cr} = \frac{16\pi r^3}{3\Delta G_v^2} \qquad \text{Eq. (2.5)}$$

Only a sufficient reduction in the melt temperature gives an embryo a chance to grow above the critical size, as at higher temperatures the embryo remelts before reaching this size. However, heterogeneous nucleation, i.e. nucleation on foreign substances,

facilitates nucleation by reducing the energy barrier (see Fig. 2.6)[15,31,63,64] as given by the following equations:

$$\Delta G^{het} = \Delta G^{\hom} \cdot f(\theta), \quad r^{*het} = r^{*\hom}, \quad \Delta G_{cr}^{het} = \Delta G_{cr}^{\hom} \cdot f(\theta) \qquad \text{Eq. (2.6)}$$

Where,

$$f(\theta) = \frac{1}{4}(2+\cos\theta)(1-\cos\theta)^2 \qquad \text{Eq. (2.7)}$$

In normal casting practice the nuclei form at the mould surface and the primary solid forms quickly in the under-cooled liquid, which is in contact with the mould surface. If the temperature of the melt is near the solidification point, the temperature gradient due to heat-flux, dT_q/dz, is greater than the liquidus temperature gradient, dT_l/dz, so that the interface becomes stable. If an undercooling in front of the planar front appears, it will make the interface unstable and perturbations may appear. Lower undercooling results in a cellular growth morphology while higher undercooling results in a dendritic morphology. In alloys an additional factor arises due to solute segregation ahead of the growing front which reduces the melting point of the alloy and is termed constitutional undercooling (see Fig. 2.7). The criteria for instability of a planar front for a constitutionaly undercooled melt can be described mathematically as[14,15,31,65]:

$$G < mG_c \qquad \text{Eq. (2.8)}$$

$$\frac{G}{V} < -\frac{m\Delta C_0}{D} \qquad \text{Eq. (2.9)}$$

where G is the gradient due to heat flux or temperature gradient, G_c is the concentration gradient, D is the diffusion coefficient of solute in liquid and m is the slope of the liquidus line (see Fig. 2.8).

If the melt becomes highly undercooled, due to the lack of nucleation sites at the mould wall, solidification can start with the nuclei forming in the bulk liquid, away from the interface, growing in an isotropic manner, and are referred to as equiaxed grains. As the latent heat of fusion is evolved at the grain surface, the temperature at the liquid/solid interface will be higher than in the liquid thereby forming a negative

gradient for equiaxed grain growth[15] (see Fig. 2.9)[31]. Growth of the nuclei occurs in three manners (i) globular, (ii) dendritic and (iii) ripened rosette and depends upon the nuclei number and cooling intensity[66]. Equiaxed growth occurs if the dendritic solidification front grows with considerable constitutional undercooling with a positive temperature gradient ahead of the front in the bulk liquid enabling heterogeneous nucleation to occur ahead of the columnar front favouring the equiaxed grain growth[67].

In semi-solid processing a globular/equiaxed microstructure is of primary importance. The globular microstructure in semi-solid processes based on the processing of liquid melt, is achieved by: stirring/agitation, such as mechanical or magnetic etc.; or, static processing, such as New Rheocasting (NRC) or low temperature pouring chemical grain refinement, etc.

In semi-solid processing which involves stirring, it is believed that the equiaxed globular structure is obtained by the growth of the dendrite arms, detached from the main stem of the dendrite either by breaking, bending, root melting or by a combination of these processes. These dendrite fragments then transform to spheroids on subsequent growth in an agitated and shearing, fluid flow[1,6,11].

To explain the globular grain growth, Vogel et al.[6] proposed the bending and growth of secondary arms making a boundary-like misalignment with an angle > 20°, resulting in high angle grain boundaries composed of dislocations with a sufficient high stress to be wetted by the liquid (the solid-solid stress higher than the solid-liquid stress). This results in the detachment of the secondary arm from the main stem and this detached arm acts as a free floating grain[14,68,69] (see Fig. 2.10). Liquid can wet the grain boundaries which have a high energy. The condition for wetting to occur is that $\gamma_{sl} \leq 2\gamma_{gb}$, where γ_{sl} is the energy of solid/liquid interface and γ_{gb} energy of grain boundary which, leads to the detachment of the deformed dendrite arm into the liquid[16]. This nuclei multiplication phenomenon was supported by Doherty et al.[69], while Hellawell[7,8] suggested that instead of shearing off the secondary arm from the stem, local melting of the secondary arm at the root is more favourable due to temperature fluctuations[70,71] (see Fig. 2.11). Flemings[1] mentioned that dendrite fragments fractured from the primary dendrite, gradually become dendritic, then

rosette and finally spherical as a result of ripening, shearing and abrasion, with liquid and/or other grains during solidification (see Fig. 2.12).

Instead of dendrite fragmentation, Mao et al.[72] found that a low temperature gradient and, reduced constitutional and temperature undercooling due to a homogeneous temperature and solute field, can reduce the growth rate of primary arms to that of secondary arms or even less, resulting in a rosette structure. Furthermore Martorano et al.[73] reported that a decrease in the columnar front velocity caused dendritic arm remelting and fragmentation and a near-zero thermal gradient in the liquid will prevent the fragments from remelting. However, Esaka et al.[74] have mentioned that only a tangential flow effectively allows melt to penetrate into the interdendritic regions to cause remelting of the secondary arms due to temperature and/or concentration fluctuations, enabling a mechanical breakdown to occur. These broken dendrite fragments are moved into the bulk with the flowing melt and can grow into an equiaxed manner if the condition in the bulk is suitable for growth.

However, Wu et al.[71] reported that globular crystals can form through direct nucleation from the liquid phase rather than the fragmentation dendrites. They also presented a model showing that the nuclei can transform to globules on growth with an increase in stirring or fluid velocity. But at lower stirring velocities a rosette like structure is prominent due to the higher growth rate.

Another investigation has suggested that an agitation or turbulence destabilizes the diffusion boundary layer and prevents the solute build up ahead of the solid-liquid interface in addition to establishing a uniform temperature distribution, thus suppressing the dendritic growth by decreasing the constitutional and thermal undercooling. This develops a condition suitable for copious nucleation throughout the melt[75,76] and resulting in the stability of the planar front producing a globular morphology[77,78]. Stirring not only reduces the boundary layer to stabilise the planar growth but also homogenizes the solute concentration ahead of the growing front. In addition it also favours continuous nucleation during solidification due to the lower and homogeneous temperature in the melt as a result of efficient latent heat removal resulting in the absence of recalescence[79].

The above phenomena is supported by Mao et al.[72,80] who showed that the melt flow motion induced by electromagnetic stirring for a short time, transformed the rosette primary phase grains into spherical ones in a low temperature poured melt. It was observed that the forced multiple nucleation of primary grains can continue to grow in a globular shape under controlled cooling conditions[17,18].

For the semi-solid processes, in which metals and their alloys are processed statically, a 'Big Bang' or copious nucleation mechanism has been suggested by Chalmers[11]. This assumes that the grains can grow from the pre-dendritic nuclei formed during pouring by the initial chilling action of the mould. These grains are then carried into the bulk by fluid flow and if the centre of the mould is sufficiently undercooled, these grains will grow in an equiaxed manner[15]. Daves[81] and Ohno[13] have experimentally proved the existence of this mechanism during solidification using a gauze immersion method for an Al-2%Cu alloy[15]. The phenomenon of the "Big Bang" nucleation mechanism, suggested by Chalmers[11] has successfully been utilized to produce thixocast billets[82,83] with a globular rheocast microstructure[65,83,84].

Similarly, direct observations of the solidification of transparent organic liquids with metal-like solidification characteristics and numerical modelling showed that globular crystals form through direct nucleation in the liquid rather than by the growth of broken dendrite fragments[75,85,86]. This phenomenon more suitably explains the globular grain structure developed by controlled nucleation and growth in the early stages of solidification[75,87] and the low temperature pouring processes in general, such as the NRC process.

Biloni and Chalmers[12] have also reported that nucleation occurs only at the time of pouring. When a melt at a low temperature is poured into a mould, a part of the melt is undercooled when entering the mould, and this is sufficient to facilitate nucleation. The amount of undercooled liquid depends on the amount of superheat and the rate of heat extraction, and in the case of chill casting nucleation occurs throughout the melt and a completely equiaxed microstructure can be obtained. As the pouring temperature increases, the amount of undercooled melt decreases and similarly the number of nuclei also decrease. Furthermore the convection of hot melt in the bulk remelts most of the existing free floating nuclei. On the growth of the free floating

nuclei a diffusion layer is formed with a lower temperature than the surrounding liquid until the growing neighbouring nuclei or dendritic columnar dendrites impinge on each other. However, different types of mechanical action or forced fluid motion enhance the columnar to equiaxed transition probably through a remelting multiplication mechanism, depending on the superheat.

Ohno[13] pointed out that normally grains grow from the nucleation site on the mould wall. The grains grow from narrow stems that make a grain vulnerable to plastic deformation and detachment. Thus as melt washes over the mould surface, thousands of dendritic fragments are washed into the melt, which may continue to attach to the mould wall and most probably will act as the seeds for new grains. There is an element of runaway catastrophe in this process as one dendrite falls, it will lean on its neighbours and encourage their fall. The survival of these detached fragments depends on the interior temperature. With very low casting temperatures the whole casting may solidify with an equiaxed structure[14,15].

To confirm the wall nucleation mechanism, Hutt et al.[88] used a gauze and found that in the case of the survival of the nuclei formed by the wall crystal mechanism, no grain transition occurred, while for a case where the constitutional undercooling mechanism dominates, the grain size and morphology is determined by the nucleant potency, the solute concentration and the temperature gradient in the liquid. A similar study made by Wang et al.[89] showed that up to ~ 50 ℃ superheat the wall crystals can survive depending on their size. To avoid the reduction in the nucleation events on the cup wall and the destruction of existing nuclei a 10-20 ℃ superheat was recommended[17,18].

Zhang et al.[90] proposed a mechanism of particle-drift and blending compressing, and considered that the dendrites are difficult to be mechanically broken, therefore dendrite fracture was not the main reason for the formation of a non-dendritic structure. The transferring of heat and mass during solidification is greatly changed by vigorous convection. Particle-drift greatly increases the heterogeneous nucleation and blending-compression changes the growth morphology of primary grains and makes the grain growth relatively uniform in all directions resulting in a near globular shape[71]. Molenaar et al.[91] experimentally showed that globular crystals form

through the direct solidification from the liquid phase instead of fragments of broken dendrites by using transparent succinonitrile-5%water solution, as cited in[71].

The size of primary particles increases with an increase in holding time, decrease in the solidifying temperature and increase in stirring time. In these conditions, due to the increased chance for collision among primary particles, the Ostwald ripening and coalescence of primary particles may occur[59]. Primary particle size decreases at the first stage of stirring due to fragmentation and then increases when isothermal stirring continued after 5 min[59]. Casting temperature and holding time has little effect on the form and size of secondary particles, however the amount decreases with lower casting temperature[92]. However, Gauge experiments showed that "wall crystals" are the dominant source of nuclei at low pouring temperatures (675 °C in Al-Si alloys)[89], while the detachment of eutectic Si crystals and the free growth of the detached crystal in the liquid has been reported[93]. Its change from a faceted to near spherical morphology was suggested to be due to the coalescence and fracture of brittle Si particles[94].

In addition to the wall mechanism, lowering the pouring temperature also promotes the formation of equiaxed solidification[11,75] and it was found that the lower the pouring temperature, the higher the undercooling and the longer the time for recalescence to start to occur which favours higher number densities of nuclei[95]. Lashkari et al.[96] explained that a highly undercooled melt near a wall at lower pouring temperature results in copious or "big bang" nucleation. This results in a rise in the melt temperature at the mould wall due to the release of the excessive latent heat of fusion. However, this rise in temperature is not enough to increase the melt temperature sufficiently to remelt the nucleated particles. Fluid flow during pouring and natural convection from the wall region establish a uniform cooling rate, and results in uniform and multi-directional cooling, associated with the geometry of the mould. This facilitates the formation of a fine equiaxed as-cast structure, which leads to the complete elimination of the columnar zone in the casting and promotes the formation of fine equiaxed grains throughout the entire zone[9,10,12,75,87,97,98]. As the superheat is decreased, the amount of thermal undercooling increases which facilitates the nucleation and increases the survival rate of nuclei[83]. Spaepen and Fransaer[99] used the droplet technique and confirmed that nuclei formation ceases due to recalescence[99].

As the pouring temperature increases, the mechanism of copious nucleation reduces and requires a longer time to establish a uniform cooling rate which results in a higher tendency for the nuclei to remelt, which results in the development of the primary phase into a dendritic morphology[100,101,102,103].

In the liquidus casting process, the melt before pouring has no superheat and it is undercooled on pouring. Therefore, nucleation may take place in the entire melt due to undercooling and even during pouring. The growth of the nuclei will be equiaxed in nature. A non dendritic growth will occur if the temperature gradient in the melt is positive and greater than a critical value determined by the constitutional undercooling. An equiaxed dendritic growth will occur if the temperature gradient is negative in the melt ahead of the growing front and constitutional undercooling has occurred[31].

It is also found that an increase in the pouring height results in a homogeneous temperature field in the flow of melt, which restricts the rosette type growth and the melt flow in the mould promotes a ripening effect with the primary grains transforming from a rosette to spherical[100,102].

The Mullins-Sekerka stability criteria[97,104] for a planar front with a small undercooling accompanied by a high saturation of nucleation sites can be used to explain the formation of non-dendritic structures[75,87,97,104] as mentioned above. The Mullins-Sekerka stability criteria[104] for a planar surface, simplified by Kurz and Fisher[31], is given as:

$$G \geq \frac{V \Delta T_0}{D} - \frac{\Gamma k V^2}{D^2} \qquad \text{Eq. (2.10)}$$

where G is the temperature gradient; V is the interface growth velocity; ΔT_0, is the temperature difference between the solidus and liquidus temperature at its initial concentration; D is the diffusion coefficient; k is the partition coefficient and Γ is the Gibbs-Thompson coefficient ($\sigma/\Delta S_f$), where σ is the solid-liquid interface energy and ΔS_f is the fusion entropy. In equation (Eq. 2.10) the first term on the right hand side indicates the constitutional undercooling favouring the formation of a perturbation on the planar interface, whilst the second term on the right hand side is the energy associated to the new perturbation, which it is necessary to overcome for the

perturbation to become stable. From this equation (Eq. 2.10) it can be seen that constitutional undercooling, growth velocity and temperature gradient are the controlling parameters. Decreasing the interface growth velocity by increasing the number of nuclei and lowering the constitutional undercooling by fluid flow, will result in a reduction in temperature gradient necessary for an interface to become stable, which will result in a uniform temperature throughout the melt suitable for fine and equiaxed grain growth[66].

Uggowitzer and Kaufmann[105] considered the Gibbs-Thomson contribution in terms of curvature undercooling as a key parameter in addition to the thermal and constitutional undercooling which counter the effect of these undercoolings. The formation of a perturbation or the transformation from a planar morphology to dendritic morphology depends on the relative degree of different undercoolings. They suggested, to obtain a spherical growth and avoid dendritic growth in the semi-solid range, one has to (i) provide a high number of nuclei in the melt, (ii) restrict the spacing between the nuclei by homogeneous distribution in the melt and (iii) cool the melt slowly. It has been reported that due to multiplication or copious nucleation the mean free path between the nuclei decreases and grain growth becomes restricted and the heat flow becomes multidirectional, which results in spherical primary particles[95].

The above mentioned criteria has been simulated[105,106,107] and in practice it was observed that at a constant cooling rate, the grain morphology changed from globular to dendritic with an increase in pouring temperature while at a constant temperature, the morphology transformed from globular to dendritic with an increase in cooling rate. However, the effect of pouring temperature can be depressed if the number of nucleation events can be increased, e.g. by the wall nucleation mechanism[105].

However, Dong et al. [66] reported that in liquidus semi-continuous casting, nucleation may occur: (i) due to isothermal holding near the liquidus, the temperature field may become uniform through convection and diffusion and many clusters of atoms form (an undercooling of 1-5 °C is sufficient to develop clusters into free nuclei throughout the melt); (ii) some of the grains formed on the wall are broken off and are transported in the bulk melt where they become free nuclei; and, (iii) heterogeneous nucleation

takes place on foreign particles. However, it was the first criterion which was found to be the major contributor in the nucleation phenomena.

Similarly Fan[108] has also suggested that for a 100% survival rate of the nuclei the following condition should be met: (1) uniform temperature and chemical composition throughout the melt; (2) well dispersed heterogeneous nucleation agents; and, (3) effective removal of latent heat to avoid recalescence.

While Dong et al. [66] found that only the initial reduction of melt temperature into the semi-solid range is responsible for the grain shape by controlling the nucleation density, while subsequent cooling rate change the size of the grains, by ripening and coarsening. It should be noted that equiaxed grain growth occurs dendritically if the melt is constitutionally undercooled as the solid grows at a higher temperature than the surrounding liquid due to an imposed negative gradient[15,31]. However, coarsening and spheroidisation will occur if the melt is held in the semi-solid range[1,2,83,105,109,110].

Depending upon the above mentioned theories but particularly those for static copious nucleation with wall mechanism, different semi-solid processes have been developed with a combination of these aforementioned nucleation mechanisms.

According to Easton[83] in the New Rheocasting (NRC) process, the melt is poured onto the chilled wall of the cup, which rapidly cools the melt, providing the thermal undercooling required for the formation of nuclei on heterogeneous nucleation sites that are available in the melt whilst the final grain size depends on growth kinetics, ripening and spheroidisation mechanisms and the number of nucleation events[17,83,105,111].

In the MIT Rheocasting process, a cold graphite rod is immersed into the melt with a low superheat and stirred for 5 – 20 s. This induces an undercooling due to high thermal conductivity and produces wall crystals in he melt which are easily detached from the rod due to its non wetting nature[19].

While, in the Swirled Enthalpy Equilibrium Device (SEED) the low temperature melt is poured into a tilted metallic mould and swirled[79,95,112].

Wang et al.[101] has also reported that a suitable structure for thixoforming, can be obtained by pouring the melt at 625 to 650 °C in a steel mould with a cylindrical cavity.

Similarly with the other low temperature pouring processes such as cooling slope, the melt, when poured onto the ramp surface, is immediately cooled down and nuclei form on the slope surface. The nucleated particles are sheared due to the force of the flowing melt and are thus transported into the bulk and consequently the mould[113]. Simulations have shown that the number of nuclei are higher for melts with a lower superheat with the size and solid fraction increasing with increase in the contact length of the cooling slope[113]. Ideal conditions would be where nucleation can easily take place on the melt/plate contact surface and at the same time the melt can easily flow and can separate off the solidified phase from the slope wall[27,28]. A coating on the cooling slope facilitates the precipitating crystals to be easily separated from the cooling plate wall[25].

2.3 SEMI-SOLID PROCESSING

Semi-solid processes have been categorized into two classes according to their objectives: semi-solid forming processes- which are used to produce a final product; and slurry/feedstock producing processes- which are used to prepare a slurry or a precursor for subsequent processing[2,3].

2.3.1 Semi-solid Forming Processes

Semi-solid processes can be divided into the following categories[1,34] (see Fig. 2.13)[114]:

- Rheocasting[1,3,33,34,49,115,116].
- Thixoprocesses[1,2,3,33,34,35,49,50,107,117,118]
- Compocasting[1,2,34,49,119-125]
- Rheorefining[1,34,49]

- Thixomolding® [2,3,126,127,128,129]
- Rheoforming[76,77,130,131,132]

Young and Eisen[133], however, categorised these processes into semi-liquid, semi-solid and slurry on demand processes. In the "Semi-liquid" (SL) processing solid slugs are heated in convection ovens and the material is processed at a lower solid fraction. Whereas in "Semi-solid" (SS) processing solid slugs are heated with inductive heating and the material is processed at a maximum solid fraction. In "Slurry on demand" process the liquid is cooled to semi-solid processing temperatures by stirring mechanically or electromagnetically and the resulting slurry is poured into the shot sleeve of the die.

2.3.2 Slurry/Feedstock Production

Many processes have been developed over the years to produce a slurry or feed material for further processing. All processes involving liquid metal can both provide slurry for the immediate production of the finished product or may produce a material for subsequent semi-solid processing (see Fig. 2.14)[134]. These processes are categorized[35] as:

- Stirring Processes[1,3,33,134,135]
- Near Liquidus Processes [2,22,35,136,137]
- Solid State Deformation[3,57,117,118,138]
- Liquid Treatment Processes[3,39,89,139]
- Other Processes[2,3,82,140]

Stirring and near liquidus process are of more importance with respect to this study. In the stirring processes, the apparatus consists of a ladle, surrounded by a furnace for controlled cooling, a stirring device, discharge or slurry transfer equipment and other controlling equipment (see Fig. 2.15).

In Electromagnetic Stirring[109,141,142], the melt is stirred vigorously by a magnetic field[143,144] instead of a mechanical stirrer (see Fig. 2.16). A Magnetohydrodynamic (MHD) stirring process is the most common process used in industry and is described

in detail in the patent by Winter et al., as cited in[37]. The process involves cooling a molten melt while it is mixed by moving the applied magnetic field across the full cross-section of the mould, over the entire solidification range[23,37,39,57,70,109,145]. Alloys ranging from Al alloys to steels have been successfully processed[40,141,142,146,147] using this technique.

In Liquidus Casting, the molten metal is cooled in a graphite crucible to a temperature just above that of the liquidus. Then just before casting the melt is allowed to flow through a bottom pouring mechanism into a mould thereby directly resulting in an equiaxed, non-dendritic microstructure, consisting of fine globular primary particles surrounded by a eutectic[2,22,35,136,137].

Commercial processes which lie within this category include the "New Rheocasting (NRC®) Process" developed by UBE[3,17,18,83] (see Fig. 2.17(a)), the "New Direct Thermal Method" (DTM)[84] (see Fig. 2.1(b)), the "Rapid Slug Cooling Technology" (RSCT)[137,148] (see Fig. 2.17(c)), the "Cooling Plate Process" [3,25,28,149,150,156] (see Fig. 2.18(a)), which includes either a combination of cooling plate and roll casters[151] or a combination of cooling plate with twin roll casters[151,152,153], and the "Semi-solid Rheocasting" SSR™[3,19,106,154,155] (see Fig. 2.18(b)) developed at MIT using a combination of low temperature and stirring for short period of time.

2.4 COOLING SLOPE/PLATE

The cooling plate is a liquidus casting process which exploits the "Big bang" mechanism for dendrite transformation. In the cooling plate process, a low superheat melt is poured onto an inclined plate which is continuously cooled. This plate is coated with a suitable material to avoid adhesion of the melt and enables the easy detachment of crystals nucleated upon it. The cooled liquid slurry is then collected in a mould at its lower end[2,3,148,150,156,157].

Cooling slopes can be manufactured using different materials such as mild steel[20,22,24,150,151,152,153,158] for aluminium alloys, and copper[25,26,28,29], ceramic[153] and tool steel[148,157] for the processing of aluminium alloys, magnesium alloys, cast irons and steel. Cooling plates can be cooled or heated with water and oil[148,157]. Many

studies[25,26,27,148] used a boron nitride (BN) coating to facilitate the detachment of the nucleating primary crystals at the slope interface. The contact length may vary from 100 to 500 mm and the inclination angle from 5° to 60° depending upon the alloy, contact length and superheat. The cooling plate was generally used independently but Haga[151,152,153,158,159] incorporated it with different types of twin roll casters. The cooling slope materials, processing conditions and alloys processed by different researchers are tabulated in Table 2.1.

It has been reported[148] that the temperature of the cooling plate has no prominent effect on microstructure, nevertheless a slurry with approximately 10% fraction solid can easily be obtained at the end of the plate.

The mechanism involved in the cooling slope/plate has been explained by Muumbo et al.[25,26]. In their theory, under the condition of a BN coating, which facilitates nuclei wash out with flow and a cooling rate of up to 67 K/s, nucleation will initiate along the melt/plate contact surface and the melt flow action will draw nucleated crystals into the melt stream before they come into contact with adjacent crystals to form a solid shell. Nucleation and growth of the primary phase taking place in the semi-solid state is influenced by the degree of undercooling, amount of nucleating agents, flow field and the rate of fragmentation of primary particle dendritic arms. The temperature of the molten metal is normally lower near the plate wall and along the free surface due to conduction and radiation effects respectively. Convection arising from the flow provides a mechanism for the dissipation of superheat and thus the detachment of nuclei from the plate wall.

Nomura et al. [25,28] also observed that low flow velocities encountered at low inclination angles cause early solidification of the melt along the cooling plate, while excessive turbulence at high inclination angles increases the likelihood of gas entrapment within the mould cavity.

Table 2.1: Cooling plate specifications data

Material	coating	Contact length	Inclination (°)	Plate cooling	Mould	Pouring Temp. (℃)	Alloy	Combination
Mild Steel[20]	BN	(100), 300	60	-	Metal , (Insulator)	(640), 680, 720	Al6Si	No
Mild Steel[22]	BN	250 (300 x 50)	60	Water Cooling	Copper	620, 650	A356	No
Mild Steel[150]	-	-	-	Water Cooling	Steel mould	10-20° superheat	Al-alloys	No
Mild Steel[30]	BN	150, 250 (300 x 50)	60	Water Cooling	Copper, Insulator	630, 650 670	A356 A390	No
-[24]	-	(200)50, 100, 150	(60), 40, 80	-	Preheated mould	(9), 19, 29, 39℃ superheat,	A91D	No
Copper [28]	BN	500	10	Water Cooling	Metal	1300	High Cr Cast Iron	No
Copper[29]	BN	500	10	Water Cooling	Metal	1300	High Cr Cast Iron	No
Copper[25]	BN	-	(10), 5- 15	Water cooling	Sand, Graphite, Steel	-	Gray Cast Iron	No.
Copper[27]	BN	-	10	Water cooling	Metallic Mould	-	Gray Cast Iron	No
Copper[26]	BN	-	(10) 5-15	-	-	-	Gray Cast iron	
Mg_2O[156]	BN	200	24	-	Steel with BN	1550	X210CrW12 100Cr6	No
Tool Steel[148,157]	BN	470	(5), 10, 30	17 – 230	Ceramic		AlSi7Mg0.3	No
Mild Steel[158]	BN	100,300 400 x 40	30,60	-	-	640-720	A1050	CS + melt drag twin roll caster
Mild Steel[152]	BN	300 x 100	60	Water cooling	-	630, 650	A356	CS + melt drag twin roll caster
Mild Steel[151]	BN	200 x 100	30	-	-	595-640	AZ31B, AZ91D, AM50A, AM60B	CS + melt drag twin roll caster
Mild Steel[153,159]	BN	300 x 100	60	Water cooling	-	15K superheat	A1050, A3004, A5083, A5182, A6063, A356	CS + melt vertical type twin roll caster

2.5 CHARACTERISTIC PARAMETERS

The characteristic parameters to qualify the materials and quantify the microstructures for their suitability for semi-solid processing can be grouped into material characteristics and microstructure characteristics.

2.5.1 Material Characteristics

Characteristic parameters to be evaluated before selecting an alloy and during processing, as proposed by some researchers are enlisted herein.

Tzimas et al.[160] proposed the following criteria:

- *Fraction solid*: The behaviour of a semi-solid material is very sensitive to the value of fraction solid[1,161]. An increase in fraction solid results in an increased apparent viscosity and significant internal damage as a result of localized strain[1], which in turn causes difficulties in die-filling and defects in the final product. Generally the accepted fraction solid volume during processing should be no more than 0.6.
- *Morphology of solid grains*: An equiaxed rosette-like solid grain exhibits more resistance to deformation and results in an increased apparent viscosity than a spheroidal grain[109].
- *Spatial distribution of liquid phase*: Occasionally some liquid resides inside the solid grains, due to the grain growth process[1]. This type of liquid adversely affects the ability of a material to deform as it decreases the effective liquid available for deformation, resulting in the requirement of a higher temperature for processing. This entrapment of liquid is quite prominent on reheating of the MHD stirred samples[1].
- *Viscosity of the liquid phase and connectivity of solid phase*: These parameters also affect the processing.
- *Grain boundary cohesion*: The resistance to deformation depends upon the degree of grain boundary cohesion, which reduces with the degree of segregation along the grain boundary, resulting in more liquid.

Liu et al.[23] suggested thixoformability criteria depending on thermodynamic predictions as follows:

- The highest "knee" on the fraction liquid vs. temperature curve should occur between 30% and 50% liquid (see Fig. 2.19). This point is the temperature at which the eutectic phase has been melted and primary phase starts melting. Above the knee, liquid formation is controllable with time because, kinetically, the rate of melting of primary phase above the knee tends to be slower than below.
- Fraction liquid sensitivity at 0.4 fraction liquid, $\left(\frac{df_l}{dT}\right)_{f_l = 0.4}$ should be as small as possible. Experience in thixoforming suggests that the minimum "working window" between the temperature at fraction liquid 0.3, $T_{0.3}$, and temperature at fraction solid 0.5, $T_{0.5}$, is about 6 K, with the fraction liquid sensitivity at 0.4 fraction solid being 0.03 K^{-1}. This "working window" is necessary as the outer skin of the slug always heats up first with the inner material requiring some additional time during which the skin temperature increases further. A value higher than 0.5 fraction solid in the outer skin may result in the start of liquid dripping from the skin area. This figure is representative of a slug size which is necessary for processing automotive components approximately 0.5 Kg in weight. For alloy systems other than aluminium alloys, this figure would be different depending upon the thermal conductivity. Other workers[23,162] have proposed a general figure of 0.015 K^{-1}, based on temperature control to within ±3 f_s during processing (see Fig. 2.20)[163].

Kaufmann et al.[17,18,164,165] suggested criteria depending on solid fraction and microstructure for thixoformability.

- Thermodynamic criteria i.e. the solidification range, ΔT_{sl}, width of processing temperature range (particularly between 40 to 60%, $\Delta T_{40/60}$), fraction solid sensitivity with respect to temperature fluctuations, S^*_{50} (k^{-1}), at 50% in this case, and the sensitivity of enthalpy with temperature, L^*_{50} (kJ $mole^{-1}K^{-1}$), also at 50% in this case.
- Contiguity, C_α, of a solid phase is a measure of solid-solid contact in a semi-solid structure and is defined as given in equation 2.11 as the average fraction

of the surface area shared by one grain with all neighbouring grains of the same phase.

$C_\alpha = 2S_{\alpha\alpha}/(2S_{\alpha\alpha} + S_{\alpha l})$ Eq. (2.11)

where Sαα is the αα grain boundaries and $S_{\alpha l}$ is the boundary between the α-phase and the liquid phase. Contiguity helps to describe the distribution of phases in coarse two phase alloys quantitatively. To standardize the parameter, contiguity is multiplied with volume fraction resulting in volume contiguity. In fully solid state volume contiguity, the volume contiguity is equal to 1 when the material undergoes normal deformation on the application of force. In the semi-solid state the solid skeleton consists of solid phase connected by solid-solid bridges. At a volume contiguity value of more than 0.3, on deformation, the liquid phase is expelled and a densification of solid phase occurs. The bonds between the solidly bounded particles are not broken resulting in no thixotropic behaviour. However, at a contiguity volume lower than 0.1 the solid skeleton is so weakly bound that the billet becomes unstable and loses its shape stability.

- Kopp et al., as cited in[17], suggested an additional parameter, latent heat per phase fraction variation, L^*/S^*, or sensitivity of fraction solid per energy input or output. Larger ratios show less sensitivity and are thus more favourable.

Quality of slug i.e. grain size of the primary phase, D_α, shape factor, f_s, and contiguity volume, f_sC_α, for which the upper limits are 150 μm, 2.0 and 0.3 respectively .

Fan[166,167,168,169] suggested a selection criteria based on thermodynamic data particularly for Al and Mg alloys. The criteria are as given below:

- Temperature sensitivity of solid fraction. For good processability, temperature sensitivity of fraction solid, df_s/dT, should be ≤ 0.015 at the processing temperature.
- The solidification temperature range, ΔT_{s_ss}, between solidification temperature, T_s, and semi-solid processing temperature, T_{ss}, should be $10°C \leq \Delta T_{s\text{-}ss} \leq 150°C$.
- The alloy should have the potential to age harden, i.e. to precipitate Mg_2Si with a ratio of Mg to Si content of Mg:Si = 0.634:0.366 in weight percent.
- The proportion of primary phase, $f_{\alpha p}$, should be ≥ 0.6.

- The limitation of secondary phases is also important, e.g. $f_{Mg2Sip} \leq 0.05$.
- Influence of composition tolerance on SSM processability. An alloy with a minor change in composition having a large effect on processing temperature and fraction solid is not suitable.

Fan[2] and Liu et al.[169] have also suggested some other factors, which are:

- Solidification range, $T_{S\text{-}L}$, pure metals and eutectic alloys are not suitable due to a narrow solidification range and too wide a range, respectively, which may lead to hot tearing.
- Rheological properties in the semi-solid state, which include processing conditions and the proportion, morphology, size and distribution of solid phase in the liquid matrix.
- The castability of the alloy is also critical as the alloy has to be cast in a die cavity, similar to conventional casting.

- An additional criterion was suggested by Tzimass and Zavalianglos[170] as:

$$\Delta f_S = 0.01 \cdot \left| \frac{df_S}{dT} \right| \cdot T_{SS} \leq 0.06 \qquad \text{Eq. (2.12)}$$

to find a suitable processing temperature range[171], where T_{SS} is the semi-solid processing temperature.

2.5.2 Microstructure Characteristics

The most common microstructure characteristics for a semi-solid processed microstructure are as given below.

Equivalent Diameter

Equivalent diameter[82,146,172,173,174] is the diameter of a circle having the same area as that of the particle (see Fig. 2.21(a)). It can be calculated as:

$$Equivalent\,Diameter = \left(\frac{4 \times Area}{\pi} \right)^{0.5} \qquad \text{Eq. (2.13)}$$

Circularity / Roundness

Circularity[38,146,175,176] or roundness[82] can be calculated as:

$$Sphericity / Roundness = \frac{(Perimeter)^2}{4\pi \times Area} \quad \text{Eq. (2.14)}$$

Another variant of circularity is called Shape Factor [172,173,177], which is basically the reciprocal of circularity or roundness as:

$$ShapeFactor = \frac{4\pi \times Area}{(Perimeter)^2} \quad \text{Eq. (2.15)}$$

Elongation Aspect Ratio

Another shape related characteristic is the elongation or aspect ratio (AR)[174] defined as:

$$AR = \frac{Minimum\ Feret\ diameter}{Maximum\ Feret\ diameter} \quad \text{Eq. (2.16)}$$

where, maximum and minimum Feret diameters are the maximum and minimum length of the feature (see Fig. 2.21(b)). However, an inverse is also used e.g. by the image analysis software "NIS Elements Br 2.30 SP4 Build 387 Basic Research" from Nikon and given by:

$$AR = \frac{Maximum\ Feret\ diameter}{Minimum\ Feret\ diameter} \quad \text{Eq. (2.17)}$$

It is claimed that the AR defined by Eq. (2.16) is preferable as the values are bound in the range of 0 to 1, and can easily be compared. In contrast to circularity, AR is more sensitive to the elongation of the grain[174]. However, Basner[115] used circular shape factor with respect to a maximum Feret diameter ($CSFc_{max}$) as a circularity indicator as given by:

$$CSF_{C\max} = \frac{4 \times Area}{\pi \cdot (Maximum\ Feret\ diameter)^2} \quad \text{Eq. (2.18)}$$

which is more sensitive to elongation than contour roughness, and he observed similar values for the processed conditions.

Loué and Suéry[178] have suggested another shape factor, CSF_{mod} as :

$$CSF_{\text{mod}} = \frac{1}{6\pi f_\alpha} \cdot \frac{S_v^2}{N_A} \quad \text{Eq. (2.19)}$$

where, f_α is the fraction solid of α-particles, S_v is the surface area of solid-liquid interface per unit volume and N_A is the number of grains per unit area of section of the specimen under observation.

2.6 MATERIALS CHARACTERISATION

The characteristics of material/alloy are important as they help to determine attributes necessary for semi-solid processing. An alloy can be characterised for phases, microstructure, morphologies, and temperatures using various techniques which include cooling curves, Thermal analysis i.e. DSC and modelling i.e. thermodynamic simulations etc.

2.6.1 Cooling Curves

Cooling curves are used to determine the critical solidification characteristics of alloys like the liquidus, solidus and formation temperatures of various phases during solidification. Computer-aided cooling curve analysis (CA-CCA) readily incorporates procedures to calculate parameters such as total latent heat, fractions solid etc. for multi-component alloys from a cooling curve[179]. These temperatures are readily obtained from the first derivative of the cooling curve, i.e. $\delta T/\delta t$[179]. A sudden change in the derivative indicates a phase change as the slope of the cooling curve changes with a change in heat evolution as a result of a phase transformation.

In addition to the first derivative, the determination of a zero line or base line, which is calculated on the basis of first derivative of the cooling curve in a single phase region i.e. above the liquidus or below the solidus (assuming no transformation occurs in this range), is important for calculations such as latent heat, etc. Traditional Cooling Curve Analysis (CCA) uses a croning sand cup with single central thermocouple. The curve is analyzed by a Newtonian Thermal Analysis method

(NTA) to generate the zero curve[180], which is based on the assumption of the absence of thermal gradients inside the sample during the cooling process[181,182]. The Fourier Thermal Analysis (FTA) method assumes that the macroscopic heat flow present in the melt during its cooling and solidification is governed by conductive heat transfer and latent heat generation due to solidification[183]. It is based on the numerical processing of the temperature data obtained from two thermocouples situated at different radial positions, within a cylindrical mould, which contains the melt to be studied during its solidification[183,184] and produces a zero curve on these bases[179,185].The difference between the NTA and FTA is shown in Fig 2.22. The relative accuracy of both the methods can be estimated using DSC[179].

Solidification characteristic temperatures can be obtained with the help of the first derivative of temperature with time, as shown in Fig. 2.23. The initial downward concave region *'1'* shows the cooling of the liquid. The end point *'a'* corresponds to the start of solidification when the release of latent heat starts which causes a sharp increase in the derivative value, in region *'2'* until point *'b'*. The intersection of region *'3'* and *'4'* corresponds to the dendritic coherency point, DCP or liquidus arrest temperature[180]. However, Bäckerud et al.[186] used the two thermocouple technique to estimate the DCP as a point where the difference between the two thermocouples, ΔT, is minimum as shown in Fig. 2.24. It can also be obtained from the first derivative of the cooling curve as a temperature corresponding to the intersection point of extrapolated lines of the back end of the first peak and the straight part of the derivative curve, just after the start of solidification of primary phase, (point D), as can be seen in Fig. 2.24[179]. Point *'c'* gives the start of eutectic solidification, which ends at point 'd' through region *'5'*. The point *'a'* can be calculated as the deviation point of the curve from region *'1'* to region *'2'* and points *'c'* and *'d'* can be calculated as the lowest points on the first derivative curve[181].

2.6.2 Thermal Analysis

According to Woodruff[187] thermal analysis provides useful information about the characteristic temperatures (liquidus, solidus and eutectic temperatures etc.), helps identify non-equilibrium species in an alloy and can also be used to study the kinetics

of melting during heating and kinetics of solidification on cooling. For studying the thixoforming characteristics heating up a sample closely simulates the practical conditions.

The two most common techniques used in thermal analysis are Differential Thermal Analysis, DTA (Fig. 2.25), and Differential Scanning Calorimetry, DSC, (Fig. 2.26)[188].

Differential Scanning Calorimetry, DSC, is a well established technique and is used to solve a wide range of materials problems such as studying precipitation or phase changes in alloy systems, and the kinetics of these phase transformations. The energy change that is detected is often the latent heat for melting or a phase change. Methods of quantifying the measurement lead to the improved knowledge of chemical and microstructural changes occurring in the material. The DSC results must be calibrated against a calibrant material for the scale under consideration and the calibrant must be stable in that temperature range. The material must also be available in high purity form, be easy to handle, of low toxicity, and be well defined thermodynamically. A single crystal or particle of calibrant is better to get a single characteristic peak[188].

Determining the melting point and latent heats are typical applications of DSC technique, which is more accurate than cooling curve analysis and is applicable for many materials including metals and alloys. DSC measures the energy (heat) evolved or absorbed by a sample as it is cooled or heated or held at a temperature. However, DSC is limited to very small samples, in the milligram range, and by cooling and heating rates[179].

2.6.2.1 Power Compensated Calorimetry DSC

In this type of DSC, the heat to be measured is (almost totally) compensated with electric energy, i.e. by increasing or decreasing the heat in Joules. The measuring system, (Figs. 2.27) consists of two identical micro-furnaces, made of a Platinum-Iridium alloy, each of which contains a temperature sensor (Platinum resistance thermometer) and a heating resistor (Platinum wire). The micro-furnace is about 9 mm in diameter, approximately 6 mm in height and has a mass of approximately

2 g. The time constant is smaller than 2 seconds and the thermal noise is about 2 μW. The maximum heating power is approximately 14 W and maximum heating rate ~ 500 K/min. Both furnaces are separated from each other (thermally decoupled) and are positioned in an aluminium block of constant temperature[188].

DSC Data Analysis

During heating up, the same heating power is supplied to both furnaces via a control circuit, (Fig. 2.28) in order to change their mean temperature in accordance with the preset heating rate. When an asymmetry occurs in the samples, a temperature difference occurs between the micro-furnace containing the sample and the micro-furnace containing the reference sample. The control circuit tries to compensate the reaction heat flow rate by proportional control by increasing or decreasing an additional heating power. Short heat conduction, relatively small mass of micro-furnaces, compensation of the reaction heat flow rate by electric heating power and electric control of heating are the distinguishing features of the power compensation DSC method[188].

The characteristic terms of the DSC curve to describe the measured curve are (see Fig. 2.29)[188]:

- *Zero line*, the curve measured when the DSC is empty, showing the thermal behaviour of the system.
- *Base line*, the line constructed in the peak range to measure characteristic temperatures.
- *Peak*, the maximum or minimum point in the disturbed region of the otherwise linear DSC curve.

and the characteristic temperatures in the peak area of the DSC curve are[188]:

- T_i, *initial peak temperature*, at this point the measured values deviate from the base line and the peak begins,
- T_e, *extrapolated peak onset temperature*, here the tangent on the ascending peak intersects the base line or extrapolated line,

- T_p, *peak maximum temperature*, the maximum value between the measured values and the base line,
- T_c, *extrapolated peak completion temperature/off-set temperature*, here the tangent on the descending peak intersects the base line or extrapolated line,
- T_f, *final peak temperature*, the point where the peak again reaches the baseline and peak is complete.

Specific Heat Measurement

Specific heat of a material is the amount of heat required to heat up one gram of sample to one degree Celsius. Specific heat is the basic parameter to measure the amount of heat a material contains in general and is used to measured the amount of heat evolve during solidification of an alloy if the change in fraction solid over the solidification temperature is known.

DSC data can also be used to measure the change in specific heat value with temperature for a phase. The specific heat for different phases and at different temperatures can be measured by a ratio method[189] using the data from the DSC run as:

$$C_{ps} = \left(\frac{S_s - S_e}{S_c - S_e} \right) \cdot \frac{m_c}{m_s} \cdot C_{pc} \qquad \text{Eq. (2.20)}$$

where, C_{ps} and C_{pc} are specific heats for sample and empty crucible, S_s, S_c and S_e are DSC data values for sample, calibrant and empty crucible, while m_s and m_c are mass of the sample and the calibrant. The ratio method relies on specific heat and mass of calibrant to compare with an unknown sample. So the calibrant material should be well calibrated and its specific heat must be known to within ± 0.5%, and measured by two different adiabatic calorimeters, as cited in[189].

Enthalpy measurement

Enthalpy can be useful in determining the solid fraction and is thus an important parameter in understanding semi-solid processing.

From specific heat data, the enthalpy change over a range of temperature or a phase change can be easily measured. The ideal way to measure the enthalpy is to hold the

sample at a tiny temperature step and determine when the largest intake of heat occurs to maintain the temperature. As this is not a practical method, DSC can be used despite its shortcomings. Enthalpy, ΔH can be measured from specific heat, C_p as[189]:

$$\Delta H = \int_{T1}^{T2} C_p \, dT \qquad \text{Eq. (2.21)}$$

Procedure

The 'Absolute' Dual Step Method[188] can be used to measure DSC curves for all the samples. The description of this method is as follows:

1. The heat flow rate of the zero line must first be determined using empty crucibles (of equal weight) in both the sample and the reference positions. The scanning region and the heating rate should be identical to that planned for the samples.
2. The sample should then be placed in the sample crucible, while the reference crucible is left empty, and heated or cooled in the range and at the rate for which zero line has been calculated.
3. The zero line is subtracted from the sample DSC curve to obtain the actual DSC curve for further calculations.

The sample is heated or cooled at a prescribed heating or cooling rate. It should be noted that any calibration is only valid for that particular heating rate at which it was carried out, largely because the sensors in any DSC are relatively remote from the sample and thus a thermal gradient may exist between the sample and the sensor[189]. When different ramps are used, different transition temperatures may be observed, which can be corrected by testing several heating rates and then extrapolating back to a zero heating rate[188].

It is possible that different cooling rates may change the microstructure of the sample. Normally 10 °C/min is the optimum heating rate which gives minimum noise in the data and any difference with lower rates is not considerable[150,189]. During slow heating rates equilibrium may be establish and peaks may not be observable. For large

samples a slow heating rate is best to avoid the internal gradient, which must be minimized to ensure a simultaneous transition throughout the sample, as cited in[189].

However, true values may be influenced by instrumental lag. Normally the heating runs are used to obtain the solidus and the cooling runs to obtain the liquidus, but the liquidus value may be affected by undercooling so an offset from the heating curve must be considered as the liquidus[189].

The atmosphere in which the DSC furnace is contained is generally controlled to avoid oxidation or other reactions between the material and its environment, which may impair results[189].

It should be noted that smaller transitions such as eutectic reactions may not be detected by DSC if the cumulative effect does not exceed the detection limit of the instrument. These transitions are separated from the main transition on cooling, but will be subjected to undercooling[189].

2.7 FRACTION SOLID AND ITS MEASUREMENT

For making a semi-solid process favourable for industry, fluctuations in processing temperature, heat dissipation from the surface to the centre, the temperature difference between the surface and centre and precision in process control are necessary parameters to be controlled[163].The processing force required to form a product in semi-solid processing depends on the fraction solid at the working temperature. At very low fraction solids, this force coincides with high pressure die casting and at very high fraction solids it resembles that required for hot forging (see Fig 2.30)[190,191,192].

For best forming conditions it is supposed that a sufficient inter-granular liquid should be available to wet the grain surface so that intergranular bonds if not broken, become sufficiently weak that a very small shear force can break them and material can start flowing like a viscous fluid showing non-Newtonian fluid flow behaviour[52]. Therfore, a wide temperature range with minimum change in fraction solid is usually

chosen for processing and is referred to as the processing window. The fraction solid sensitivity is the parameter which helps to determine the relative change in fraction solid during this given temperature range. Materials with a eutectic or materials which can exhibit a eutectic due to segregation are usually the preferred candidates for semi-solid processing, provided they have a sufficiently large solidification range[160]. The solid fraction just above the eutectic point is supposed to be ideal as sufficient liquid due to the melting of the eutectic phase is available and temperature changes do not affect the fraction solid too much. This is because the rate of melting of the primary solid is low and the molten eutectic is available to wet the grain boundaries. A small fluctuation in temperature does not affect the amount of eutectic too much as the eutectic solidifies at a constant temperature and requires sufficient time to completely solidify. The primary solid provides necessary strength to prevent the solid skeleton from deforming during reheating and handling with the eutectic melt acting as a lubricant which when sufficient facilitates the deformation.

The fraction solid in the material plays a key role in all types of semi-solid processing. In rheocasting the material should not be cooled to a fraction solid that can prevent it from flowing during pouring/processing. While, in thixoforming processes, the material should not have too low a solid fraction that it becomes difficult to retain its shape or too high a fraction solid that it cannot flow on processing[1,2].

The deformation behaviour of any partially melted alloy depends on the fraction of solid[191,192]. If the fraction solid of a material is too low it will behave sluggish during die filling, whilst at too high a fraction solid the material requires approximately the same force to deform as for the fully solid material. Therefore, the rate of change of fraction solid with temperature is important. A temperature range where the rate is small is an ideal range for processing. However, as variation in processing temperature is common in industrial processing, the sensitivity of the solid fraction to temperature should be a minimum for the practical application of the process[193].

According to Liu et al.[23] for the optimum conditions during thixoforming processes a solid fraction between 50-70% for the feedstock is critical (Fig. 2.19). Heating must be conducted without too much melting of the primary α-phase. A higher solid fraction above 70% may resist the flow in the forming process, while a solid fraction below 50% results in difficulties in controlling the heating temperature and the

material is subject to slumping or tilting known as 'Elephant Footing' due to the tendency of the liquid to migrate to lower billet extremes, as cited in[23]. A solid fraction which is too high, ~ 90%, has a significant effect on hot tearing and porosity during solidification[162]. So, for better control of the process the fraction solid sensitivity, at 0.6 fraction solid, should be as small as possible, i.e. $\left(\frac{df_s}{dT}\right)_{f_s = 0.6} \approx 0$.

Cremer et al. [163] have considered a maximum change in fraction solid or liquid at the process temperature which they determined should not be more than 6% for process control. Therefore, the prediction of solid fraction with respect to temperature is extremely important in assessing the stability of an alloy for thixoforming/semi-solid processing.

The thermal and mechanical behaviour of an alloy in the mushy zone also depends on the solid fraction besides the morphology of the solid phase[194,195,196]. The deformation of the semi-solid alloy is a result of liquid flow and deformation and re-arrangement of solid grains. As solid fraction helps to estimate the materials' strength during solidification, so it helps in understanding the rheological behaviour of solidifying alloys[197,198,199]. The effective rheology of the solid-liquid mixture is a function of the rheology of each component. The contribution from each component of the semi-solid system is a function of solid fraction[194]. The fraction of solid not only controls the rheological behaviour but also the evolution of the structure in the semi-solid state, as has been cited in[193].

In literature different criteria and fraction solid ranges have been reported for various materials such as: a fraction solid range from 45 to 55% for an Al-7%Si (UNI 3599) alloy[200]; from 54 to 60% fraction solid for Al alloys[163]; less than 60% fraction solid[201]; 30 to 70% fraction solid with a temperature range of 10 - 45 °C for Al alloys[148]; 40 to 60% fraction solid for thixocastng and 75 to 90% fraction solid for thixoforging of steels, with a temperature difference > 10 °C[202]; fraction solid from 60 to 80% for thixoforging and 40 to 60% for thixocasting for steels and aluminium alloys[203]; 40 to 80% fraction solid for steels[217]; 40 to 60% fraction solid but with a temperature variation < ±2.5 °C[17,18,164]; etc.

In terms of solid fraction and respective strength values, three stages can be identified[194] as:

i) below the coherency point f_s^{ch}, the material behaves like a suspension and no significant strength is developed, so no significant stress can be measured,

ii) between the coherency point f_s^{ch}, and maximum packing solid fraction, f_s^{pk}, the shear stress stays at a relatively low level as solid grains are able to rearrange themselves even if some packing occurs, and

iii) above the maximum packing solid fraction, f_s^{pk}, a solid network forms and required shear stress increases more significantly with solid fraction.

For controlling a casting process, we need a relationship between the latent heat evolved in terms of solid fraction, f_s, and temperature, T[205]. The fraction solid and temperature relationship, f_s - T, can be evaluated directly or through its effects on the physical properties of a material. The more commonly used methods[193] are:

- Thermodynamic data (equilibrium phase diagrams)
- Thermal analysis techniques (DTA, DSC, ...)
- Quantitative metallography (samples quenched from semi-solid state)
- Ultrasonic monitoring (propagation speed of ultrasonic waves)
- Measurement of electric resistance / magnetic permeability
- Mechanical response (compression test, indentation test, back extrusion test, etc.)

2.7.1 Thermodynamic Methods

Measurement of a relation between solid fraction (f_s) and temperature (T) sing thermodynamic data is the easiest and most commonly used method. Different variations in the methods using the thermodynamic data have been introduced, to describe the f_s - T relationship, by Kurz and Fischer[31], Chen and Tsai[206] and also reported by other authors[193,194,205,207,208]. These relationships depend on the solute distribution in the material which in turn is related to dendritic micro-segregation. The

theoretical analysis of solidification is based on equilibrium solidification, as cited in[205]. In equilibrium solidification, it is assumed that complete diffusion of the solute occurs between the solid and liquid phase during solidification, so that the solid fraction, f_s^{Eq} at a given temperature T is given by:

$$f_s^{Eq} = \frac{T_l - T}{T_l - T_s} \qquad \textit{where} \qquad T_s < T < T_l \qquad \text{Eq. (2.22)}$$

and T_l, T_s are the liquidus and solidus temperatures respectively. The quadratic relationship between f_s and T is given by [194]:

$$f_s^{Qd} = 1 - \left(\frac{T - T_s}{T_l - T_s} \right)^2 \qquad \textit{where} \qquad T_s < T < T_l \qquad \text{Eq. (2.23)}$$

In non-equilibrium solidification, complete diffusion is assumed in the liquid, while in the solid phase, the diffusion of solute is limited or negligible. The well known Lever Rule assumes that the solidification process permits sufficient diffusion and a complete equilibrium between the liquidus and solidus is established[31,193,194,205,207,208]. The lever rule allows the determination of solid fraction of solid, f_s^{Eq}, for a binary phase diagram at a given temperature, T, in the semi-solid state. It uses a tie line intersection from the liquidus and solidus lines at solute compositions, C_s, and C_l, respectively, assuming that these lines are linear, using the following relationship:

$$f_s^{Lev} = \left(\frac{C_l - C_0}{C_l - C_s} \right) = \frac{C_l - C_0}{(1-k)\, C_l} \qquad \text{Eq. (2.24)}$$

$$f_s^{Lev} = \frac{(T_f - T) - m_l\, C_0}{(T_f - T)(1-k)} \qquad \text{Eq. (2.25)}$$

$$f_s^{Lev} = \frac{1}{1-k} \left(\frac{T - T_l}{T - T_f} \right) \qquad \textit{where} \qquad T_s < T < T_l \qquad \text{Eq. (2.26)}$$

where, T_f is the fusion temperature of pure metal, T_l is the melting point of the pure solvent, m_l is the slope of the liquidus line, C_o is the alloy composition, C_s and C_l are the solute composition in the solid and liquid, respectively. The constant k is the equilibrium partition coefficient which is expressed as:

$$k = \left(\frac{C_s}{C_l} \right) = \frac{T_f - T_l}{T_f - T_s} \qquad \text{Eq. (2.27)}$$

A complementary, limiting case, approach to analyse equilibrium solidification is to assume, that solute diffusion in the solid phase is small enough to be considered negligible and, that diffusion in the liquid is extremely fast, fast enough that when

diffusion is complete it results in the segregation of solute in the solid phase. Gulliver in 1922, Scheil in 1942 and Pfann in 1952 as cited in[15], tried to incorporate these segregation phenomena during solidification into the normal lever rule using the equilibrium partition coefficient, *k*, (Gulliver-Scheil equation). In this case the solid fraction, f_s^{Sch} would be[31,193,194,205,206,208]:

$$f_s^{Sch} = 1 - \left(\frac{C_l}{C_0}\right)^{\frac{1}{k-1}} \qquad \text{Eq. (2.28)}$$

$$f_s^{Sch} = 1 - \left(\frac{T - T_f}{T_l - T_f}\right)^{\frac{1}{k-1}} \qquad \textit{where} \qquad T_e < T < T_l \qquad \text{Eq. (2.29)}$$

and T_e is the eutectic temperature. Although the Scheil equation is the most commonly used, an inconsistency was observed[209,210] when applied under different solidification conditions showing a weakness in the assumption of negligible diffusion in the solid phase.

The above derivation of the Scheil equation (Eqs. 2.28, 2.29) has quite severe limitations when applied to multi-component alloys. It is not possible to derive this equation using the same mathematical method as above, if the partition coefficient *k* is dependent on temperature and/or composition. The Scheil equation is applicable only to dendritic solidification and can not, therefore, be applied to eutectic alloys. Furthermore, it can also not be used to predict the formation of intermetallics (e.g. the Laves phases) during solidification. Using thermodynamic modelling like CALPHAD and thermodynamic databases like Thermo-Calc®[211], all the above disadvantages can be overcome, as they use a step-wise approach[207] as shown in Fig. 2.31, and can utilize the phase diagrams and Scheil equation to predict the weight fraction of solid in complex multi-component alloy systems [207].

Although non-equilibrium conditions prevail during commercial processing, during and after solidification and particularly on partial remelting, back diffusion of the solute results in a shift from a fully segregated condition towards near equilibrium conditions[31,63,193]. As a result the fraction solid increases with time on holding in the semi-solid state and will thus reach its equilibrium fraction and achieve a steady state. Similarly at the initial stage, due to non-equilibrium cooling, the values for solid fraction are approximately that obtained using the Scheil equation. However, on

holding, equilibrium is achieved due to the high diffusion rate of solute in the solid as well as other processes like coarsening, ripening and coalescence and the values predicted are more similar to the Lever rule (Fig. 2.32) [194].

The Scheil equation can be modified to allow some back diffusion into the solid during a small isothermal increment in solidification. However, the flux balance needs to be maintained during this isothermal step in the solid and liquid phases[207]. This improvement of the Scheil equation was reported by Brody and Flemings[110] and later modified by Clyne and Kurz[212] by incorporating the Back-Diffusion parameter[205] (see Fig. 2.33). With a constant *k*, the relationship between composition and solid fraction would be[205,207]:

$$C_s = k C_0 \left[1 - (1 - 2\alpha k)\ f_s\ \right]^{\frac{1-k}{1-2\alpha k}} \qquad \text{Eq. (2.30)}$$

$$\frac{C_l}{C_0} = \left[1 -\ f_s\ (1 - 2\alpha k)\right]^{\frac{1-k}{1-2\alpha k}} \qquad \text{Eq. (2.31)}$$

and thus fraction solid can be defined as:

$$f_s^{Bd} = \left(\frac{1}{1-2\alpha k}\right)\left[1 - \left(\frac{T_f - T}{T_f - T_l}\right)^{\frac{1-2\alpha k}{k-1}}\right] \qquad \text{Eq. (2.32)}$$

where α is a function (Fourier number), which takes account of solute back diffusion as given by:

$$\alpha = \frac{D_s\, t_{sl}}{x^2} \qquad \text{Eq. (2.33)}$$

where t_{sl} is the time the alloy spends in the semi-solid state during solidification and partial melting, D_s is the diffusion coefficient of the solute in the solid state and x is the characteristic distance for back diffusion (half of the grain size in equiaxed grains and half of the secondary arm spacing, λ in a dendritic structure).

A number of different expressions have been developed for α , notably by Clyne and Kurz[212] and others as cited in[207]. The modified Fourier number, α´ by Clyne and Kurz[212], is the thermal history of the alloy as described below[31,193]:

$$\alpha' = \alpha\left[1 - \exp\left(-\frac{1}{\alpha}\right)\right] - 0.5\exp\left(-\frac{1}{2\alpha}\right) \qquad \text{Eq. (2.34)}$$

and the fraction solid calculated by incorporating the modified Fourier number, α´, in Eq. 2.34] as incorporated by many solidification models for semi-solid processing[31,63,193], as cited in[193,205]:

$$f_s^{Bd} = \left(\frac{1}{1-2\alpha' k}\right)\left[1-\left(\frac{T_f - T}{T_f - T_l}\right)^{\frac{1-2\alpha' k}{k-1}}\right] \quad \text{Eq. (2.35)}$$

$$f_s^{Bd} = \left(\frac{1}{1-2\alpha' k}\right)\left[1-\left(\frac{T_f - T}{m_l C_0}\right)^{\frac{1-2\alpha' k}{k-1}}\right] \quad \text{Eq. (2.36)}$$

The Fourier number, α, may vary from 0 (Scheil condition i.e. no diffusion in solid) to ∞ (Equilibrium condition), whilst the modified Fourier number, α´, varies from 0 to 0.5 under the same conditions[31,193]. The value for the fraction solid calculated by the expression incorporating back diffusion lies in between the values calculated by the Lever rule and Gulliver-Scheil expression, as shown in Fig. 2.33[207].

The Fourier number, α, decreases with increasing cooling rate[31,63,193] as indicated by the following relation:

$$\alpha \propto \dot{T}^{-1/3} \quad \text{Eq. (2.37)}$$

It can be explained that for a given alloy, a high cooling rate during solidification reduces the local solidification time, increases the amount of residual non-equilibrium eutectic and reduces the degree of homogenization. On the other hand this reduces the grain size which in turn reduces the diffusion distance and time for homogenization[193].

It should be noted that the thermodynamic parameters, like latent heat of the solidification, remain constant for all these approaches. A comparison of all the above mentioned f_s -T relationships for a low carbon steel are shown in Fig. 2.34. It can be noted that at the initial stage all f_s values remain the same for all fraction solid calculation models[205].

During partial melting, the heating rate is so high (~ 170 K/min for an A356 alloy from room temperature to processing temperature i.e. it takes 200 s to heat to above the eutectic temperature) [193], that there is no homogenization and dissolution of the

non-equilibrium eutectic in the solid state is negligible (as 24 min are required for a 10 % non-equilibrium eutectic around a 40 μm grain in an Al-Cu alloy to homogenize) [58]. The soaking period at the processing temperature is to promote spheroidization of the microstructure and uniform distribution of the liquid phase in the sample. Homogenization occurs depending upon the alloy system and grain size, resulting in a decrease in eutectic content, with the homogenization time for different alloys reported in[58,193].

Yim et al. [38] assumed complete mixing of the liquid by stirring and local equilibrium at the solid/liquid interface to consider the diffusion through the solid, and presented a relationship between the fractions solid and stirring temperature as[213]:

$$f_s = \frac{1}{1-\beta k}\left[1-\left(\frac{T_M - T_S}{T_M - T_L}\right)^{\frac{1}{\eta}}\right] \qquad \textit{where} \qquad \text{Eq. (2.38)}$$

$$\beta = \frac{3\gamma}{1+3\gamma}\ , \qquad \gamma = \frac{2D_S}{k^2} \qquad \textit{and} \qquad \eta = \frac{k-1}{1+\beta k} \qquad \text{Eq. (2.39)}$$

where k is equilibrium partition co-efficient, T_S is the processing temperature, T_L and T_M are the liquidus temperatures of the alloy with initial concentration C_o and melting point of the pure solvent, respectively, while D_S is the diffusion coefficient of solute in the solid phase. This expression fits quite well with the experimental data (Fig. 2.35).

2.7.2 Enthalpy

A more practical approach is thought to be the enthalpy method[214,215]. The basis of this approach is widely used in the modelling of solidification processes, based on the assumption that the enthalpy of a material is an algebraic sum of the enthalpies of constituent phases in the material according to their volume fraction. So that the enthalpy[162] for an alloy is given by:

$$H = \left(C_{p,s}\, f_s + C_{P,l}\, f_l\right)T + f_l\, L \qquad \textit{or} \qquad \text{Eq. (2.40)}$$

$$H = \left(H_s\, f_s + H_l\, f_l\right) \qquad \textit{so} \qquad \text{Eq. (2.41)}$$

$$f_s = \frac{H - H_s}{H_l - H_s} \qquad \textit{as}\ f_s + f_l = 1 \qquad \text{Eq. (2.42)}$$

where $C_{P,\,s}$ and $C_{P,\,l}$ are the heat capacities and H_s and H_l are the enthalpies of solid and liquid phases respectively, and L is the latent heat of fusion. An enthalpy-temperature graph[162] is used for the calculation of solid fraction as shown in Fig 2.36. The enthalpy lines of the fully solid and the fully liquid material are extrapolated to a given temperature, T, to give corresponding H_s and H_l values which enable the solid fraction to be calculated, as shown in Fig. 2.36[162].

It should be noted that an accurate fraction solid cannot be determined directly using enthalpy measurements in alloys because enthalpy changes with composition of the states considered and segregation changes in the compositions of the phases[162].

2.7.3 Cooling Curves

The solid fraction, at different stages and temperatures can be calculated from a cooling curve by analysing the cumulative area between the first derivative and zero curves, drawn by either the Newtonian or Fourier methods and by taking the fraction of area between these curves. The calculation of the solid fraction using the Newtonian method is simpler as it does not require any thermo-physical properties like specific heat etc. [179].

2.7.4 Thermal Analysis

Thermal analysis techniques such as Differential Thermal Analysis (DTA) and Differential Scanning Calorimetry (DSC) are the most frequently used for the evaluation of the solid fraction, as cited in[185,193]. In thermal analysis methodology, the heat of melting or cooling is measured and the area or partial area under the heat flow curve gives the solid fraction for a given temperature. DSC has an advantage over DTA, in that it directly measures the heat of melting or heat of solidification during the solid-liquid phase transformation. The sample ~ 5mg in mass, is heated from the solid state to the 100 % fully liquid state with the differential heat flow rate, *dQ/dt*, required by the specimen in order to be kept at an identical temperature with the reference sample, measured as a function of temperature, when heated at a

constant rate. The energy absorbed during heating contributes to the overall change in heat content of the solid and liquid phases, as cited in[193]:

$$\frac{dQ}{dt} = m\left(f_s C_{p,s} + (1 - f_s) C_{P,l} + \Delta \frac{df_s}{dT} \right) \frac{dT}{dt} \qquad \text{Eq. (2.43)}$$

where m is the mass of the sample, $C_{P,s}$ and $C_{P,l}$ are the heat capacities of the solid and liquid respectively, and ΔH is the heat of melting. The baseline is defined as to isolate the heat of formation of liquid or df_s/dT, for simplicity in calculation. This base line may be a straight line if the heat capacities of the solid and liquid do not change too much; otherwise a sinusoidal base line (extrapolation of the initial and final base lines with the thermodynamic transformation temperature) is used to determine the lower boundary of the area under the DSC curve as shown in Fig. 2.29. More accurate methods require knowledge of the exact values of heat capacities of the solid and liquid phases[216].

Since the measurements are performed at a fixed heating rate, $\dot{T}$, the decrease in the solid fraction with increasing temperature can be calculated from the increase in absorbed heat and from Eq. 2.43, we can get[193]:

$$df = \frac{1}{\dot{T} m \Delta H}\left(\frac{dQ}{dt}\right) dT = \frac{1}{\dot{T} m} \int_{T_s}^{T} \frac{1}{\Delta H}\left(\frac{dQ}{dt}\right) dT \Leftrightarrow \Delta f_s = 1 - f_s(T) \qquad \text{Eq. (2.44)}$$

and assuming that the heat of melting is independent of the temperature, so the composition of the solid phase, is linearly proportional to the amount of the melted alloy, then Eq. 2.44 becomes:

$$f_s(T) = 1 - \frac{1}{m \Delta \mathrm{H}} Q(T) \qquad \text{Eq. (2.45)}$$

where $Q(T)$ is the heat absorbed from the start of melting up to the temperature T of the alloy, or area under the DSC curve[193].

Quantitative metallography of the quenched samples[162,193,194] and ultrasonic monitoring and electric resistance and magnetic permeability methods can also be used for fraction solid calculations but some practical constraints have been observed[193].

2.8 MECHANICAL PROPERTIES

The mechanical properties of semi-solid AlSi7Mg alloys reported by different researchers compared to other common processes are tabulated as follows.

Table 2.2: Properties of SAG Thixalloy[145].

Alloy	Ultimate Tensile Strength (N/mm^2)	Tensile strength (Nmm^2)	Elongation (%)	Heat treatment
AlSi7Mg0.3	210	110	12	as cast
AlSi7Mg0.6	220	120	9	as cast
AlSi7Mg0.3	300	230	12	T6
AlSi7Mg0.6	330	280	8	T6

Table 2.3: Mechanical properties achieved by SSM and SL and competing casting processes [133].

Alloy and Heat Treatment	Process	Ultimate Tensile Strength (MPa)	Yield Strength (MPa)	Elongation (%)	BHN
A356.0-T6 (a)	SSM-cast	300	225	12	90
A356.0-T5 (c)	SSM-cast	260	170	15	80
A356.0-T5 (b)	SSL-cast	260		5.4	
A356.0-T6 (a)	Squeeze cast	300	225	12	90
A356.0-T6 (a)	Permanent mould cast	280	205	10	90

(a) SSM, Squeze cast and permanent mold comparison data from NADCA standards for SSM and Squeeze cast processes, 1999,

(b) SSL data from Magneti-Marelli S.p.A., 1998

(c) SSM cast data from Aluminum-Pechiney, 1999

Table 2.4: Properties of New Process Al-Si alloys alloy[217].

Alloy	Processs	Yield Strength (MPa)	Ultimate Tensile Strngth (MPa)	Elongation (%)
AlSi7Mg0.7	Semi-liquid die casting	282	348	11.2
	Squeeze casting	268	328	5.6
AlSi7Mg0.3	Semi-liquid die casting	198	282	17.1
	Squeeze casting	195	286	12.4
AlSi7Mg0.3 with grain refinement	Semi-liquid die casting	298	198	15

2.9 COMMERCIAL PRODUCTS

Parts produced from semi-solid processing have a wide range of applications.

Automotive parts

- Suspension parts[1,133,145]: engine brackets[218], lateral suspension support[218], rear suspension[218], front suspension[218], suspension control arm[219], multilink suspension (rear suspension assembly)[42], automotive suspension arms[42].
- Automotive brake system[1]: disk and drum[218], hub[218].
- Steering parts[1,218]: steering Knuckle[218], steering arm[218].
- Engine parts: drive train[219], oil pressure part[220], engine/transmission brackets[237], rocker arm pedestal[37], timing belt brackets[37], fuel rails[133,221], automotive pulley[133], engine oil pump cover[133].
- Safety components[145]: air bag container[43].
- Air cooler housing part[145].
- Wheels for passenger car[220].
- Bicycle parts[42,220].
- Cylinder case for gas valve[220].

Other parts

- Casing of mobile phone set[222], camera case[2], personal computer case[220].
- Parts for transmission of electricity[220], electrical connectors[1], computer actuator[43].
- Golf putter[4], golf club sole plate[4].
- Ergonomic pen[4].

2.10 FIGURES

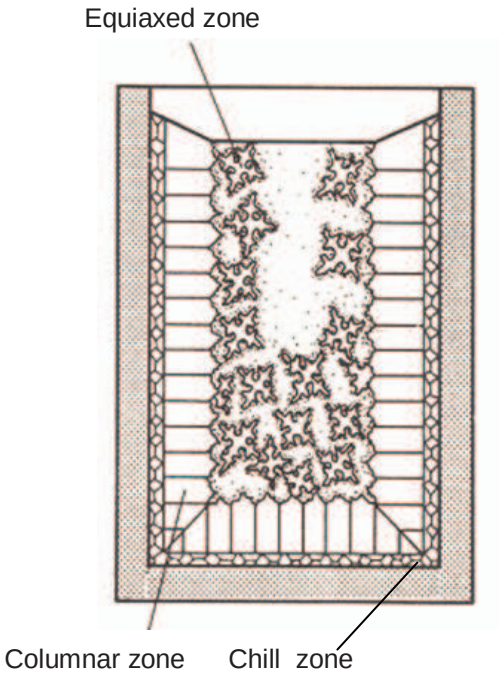

(a)

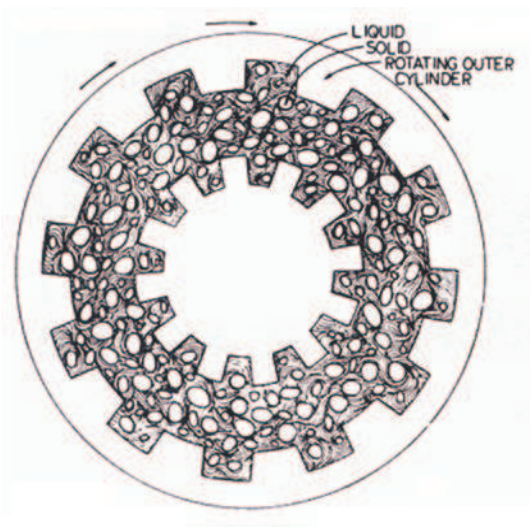

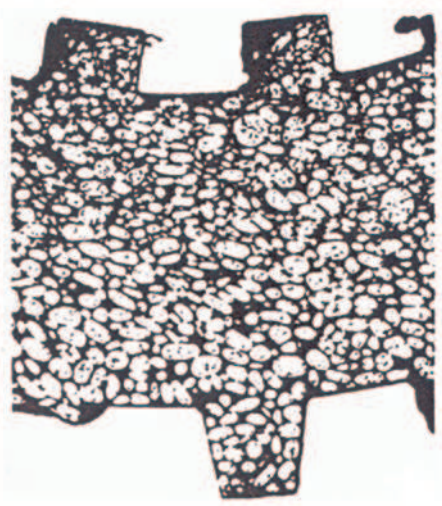

(b) (c)

Fig 2.1: Comparison of schematic structure formed: (a) characteristic structure in sand casting [31]; (b) schematic structure formed between the concentric cylinders[34], (c) microstructure of the Sn-15%Pb sample sheared at 500 rpm, during cooling to a fraction solid 0.6 and water quenched[34]

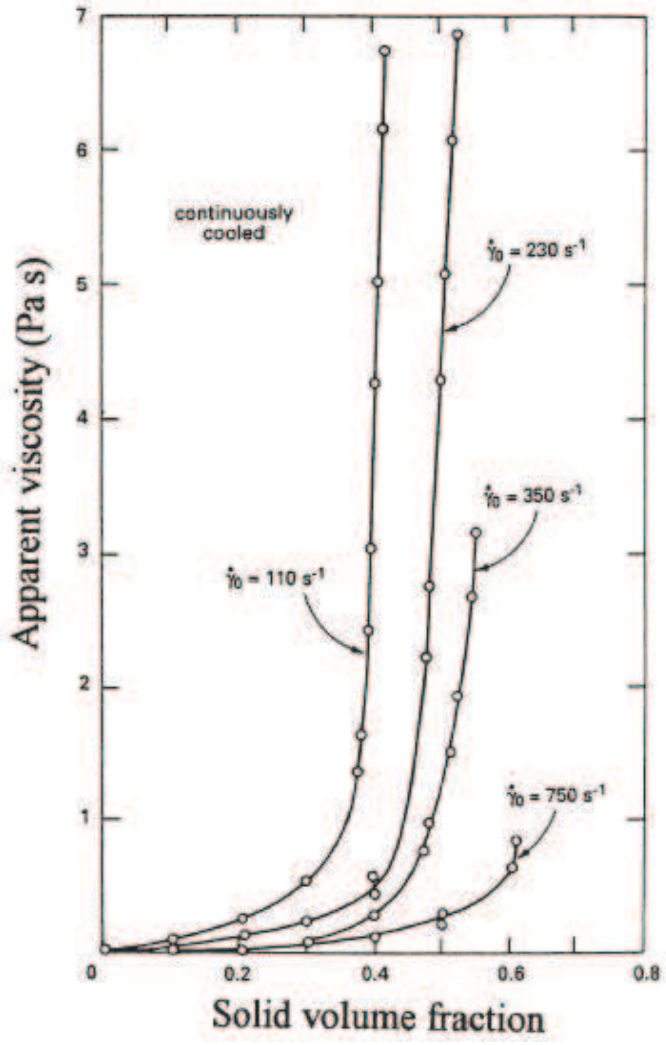

Fig. 2.2: Apparent viscosity versus solid fraction f_s for a Sn-15Pb alloy sheared continuously and cooled at 0.33 K/min. at different shear rates[51].

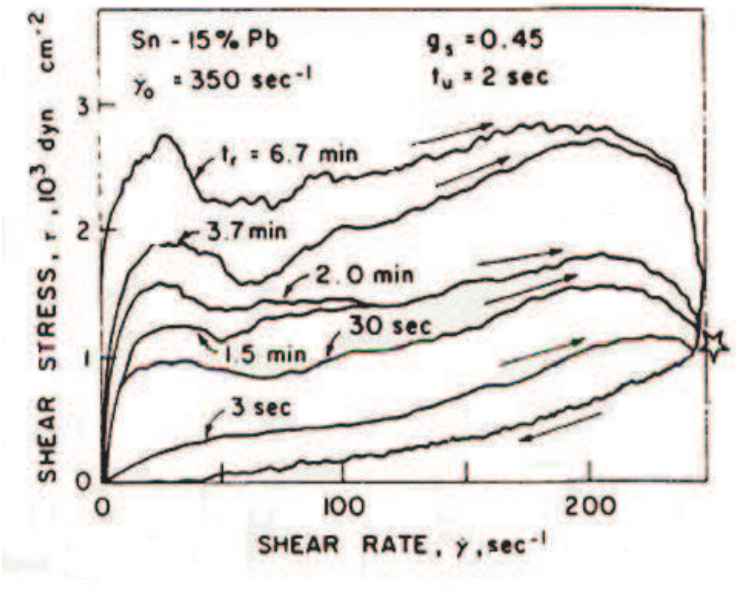

Fig. 2.3: Hysteresis loops showing the thixotropic behaviour of a Sn-15Pb alloy and the effect of the rest time on the degree of thixotropy. The star indicates the starting point of the loop[54].

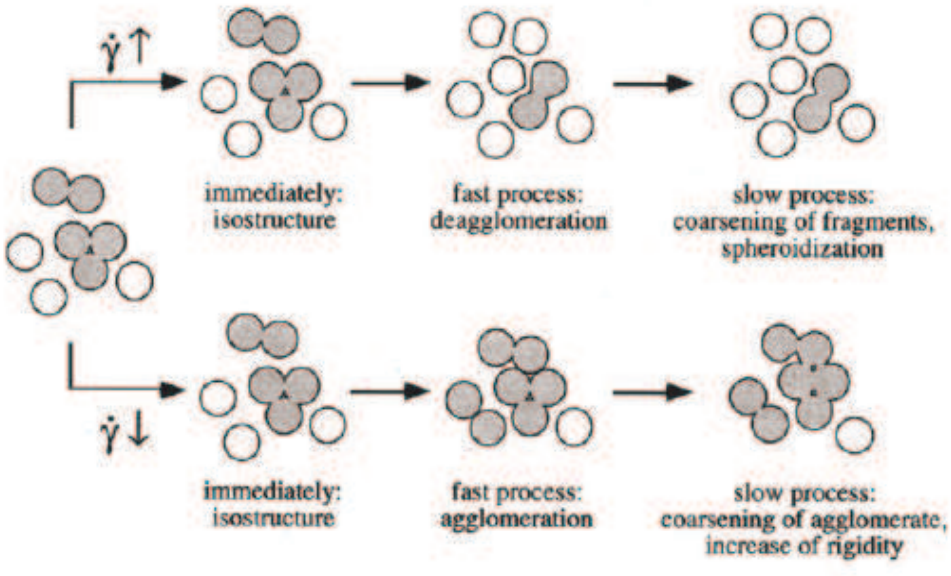

Fig. 2.4: Schematic model describing the fast and slow processes in a semi-solid material's structure after shear rate up and down jumps[55].

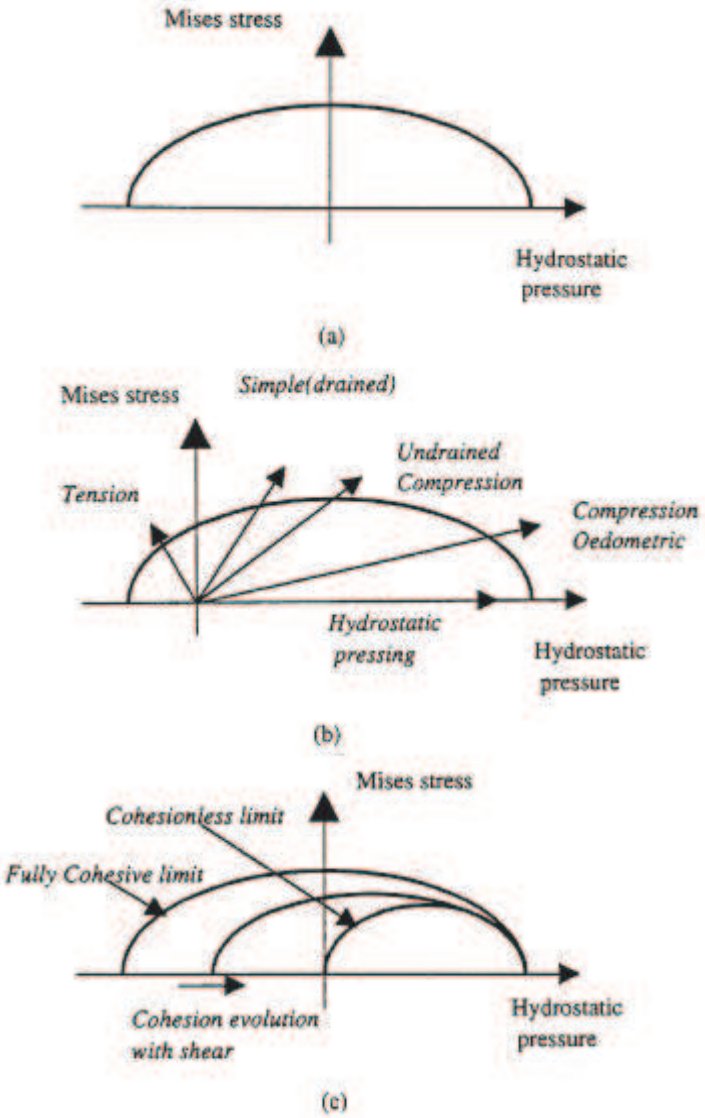

Fig. 2.5: “Two Phase” models for deformation behaviour at high solid fractions [2].

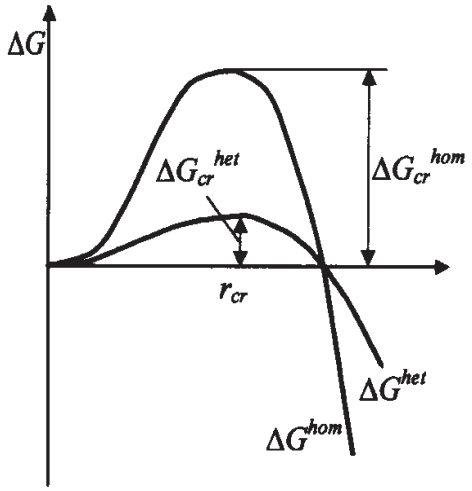

Fig. 2.6: Comparison of homogeneous and heterogeneous nucleation [15].

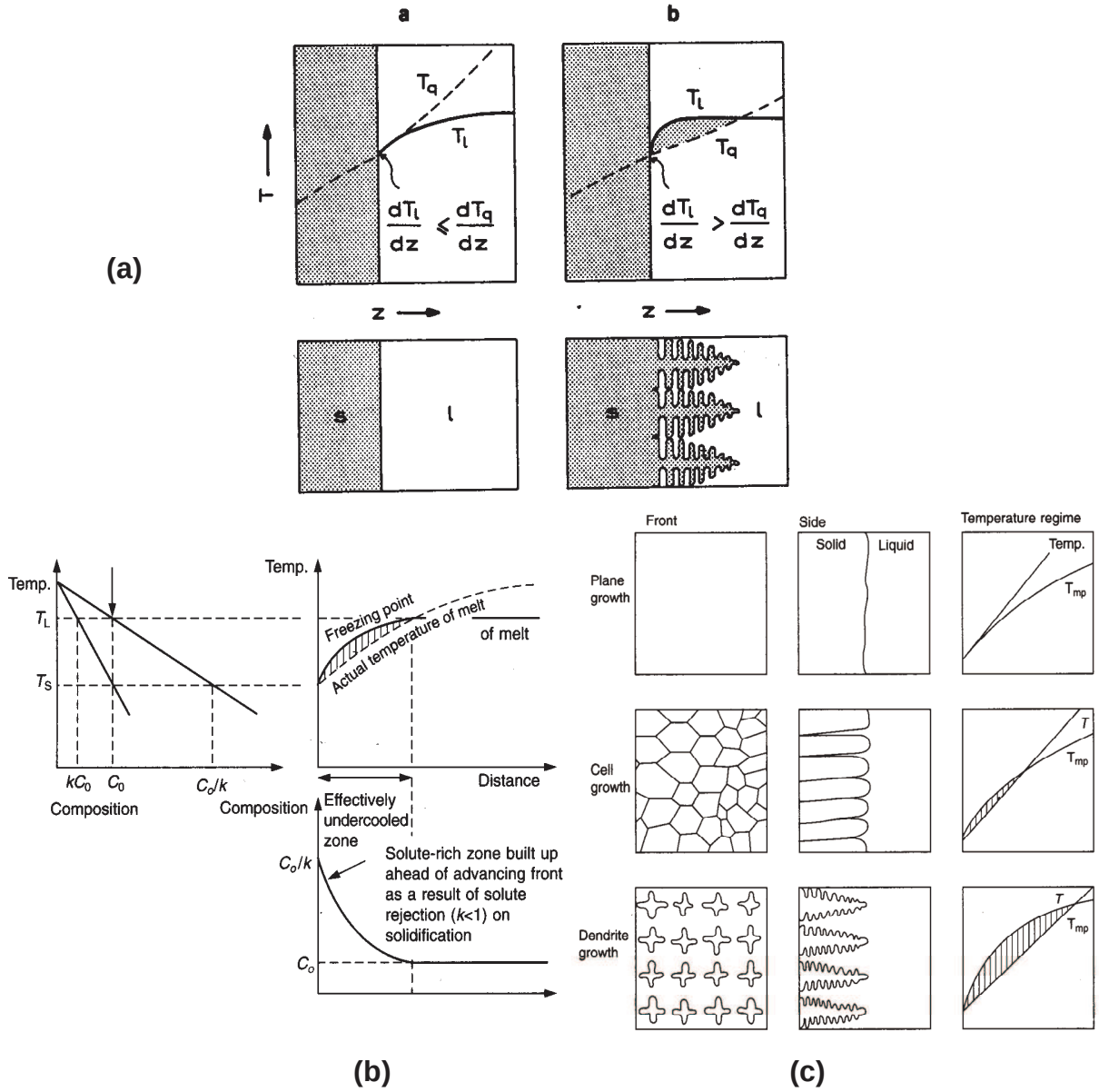

Fig. 2.7: Comparison of temperature undercooling and constitutional undercooling and resultant morphology: (a) temperature undercooling due to heat flux and liquidus temperature gradient and growth morphology [31]; (b) constitutional undercooling [14]; and, (c) change in morphology with different degree of undercooling[14].

(a)

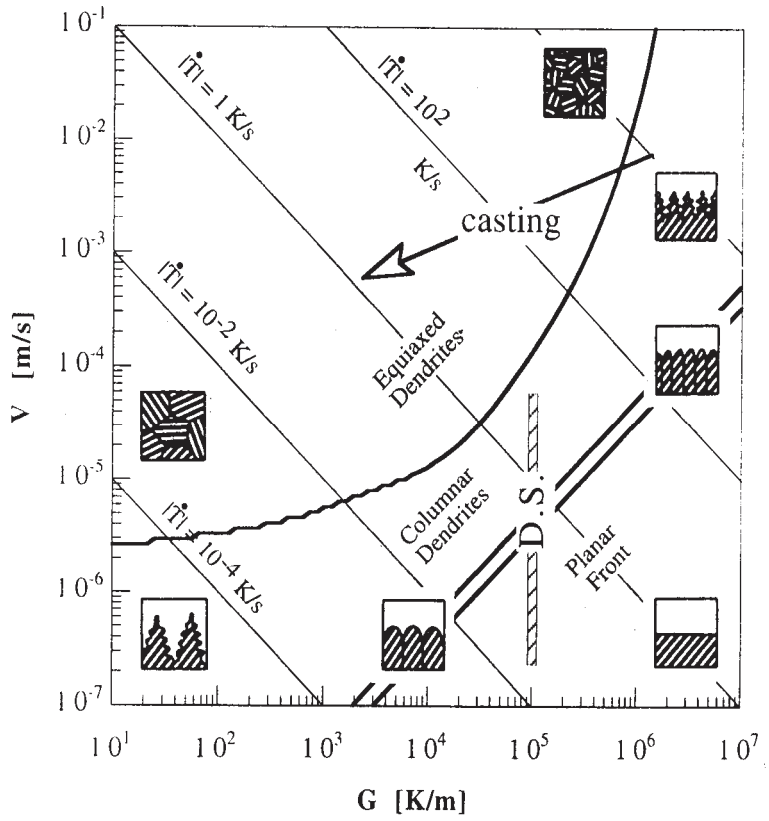

(b)

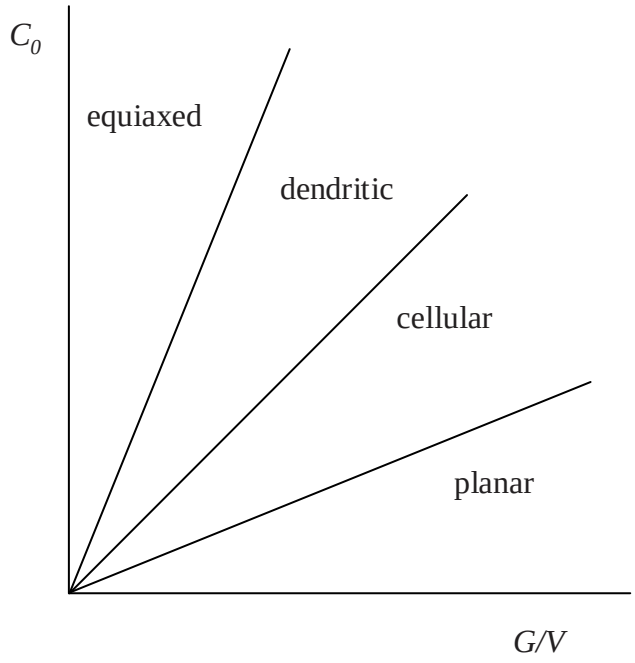

Fig. 2.8: Transformation in grain morphology: (a) with respect to thermal gradient and growth velocity[31]; and, (b) thermal gradient, growth velocity and composition[15].

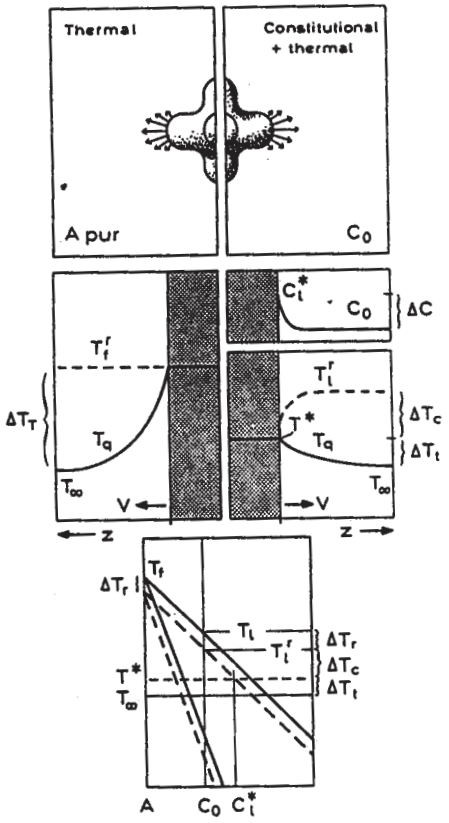

Fig. 2.9: Comparison of type of undercooling and its nature for an equiaxed grain to grow: (left side) pure melt and (right side) an alloy [31].

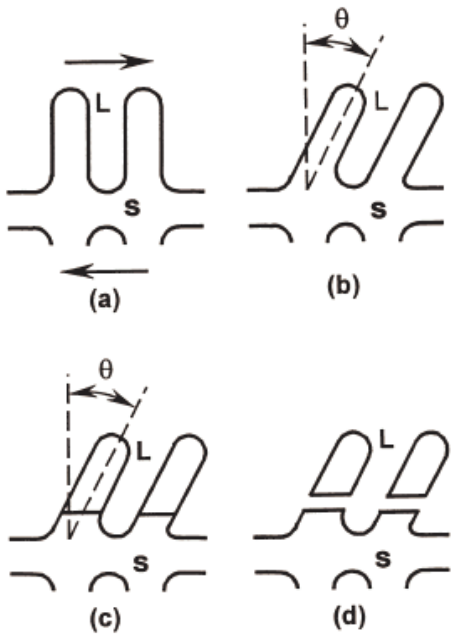

Fig. 2.10: Schematic illustration of dendrite arm fragmentation by the mechanical fracture mechanism [69].

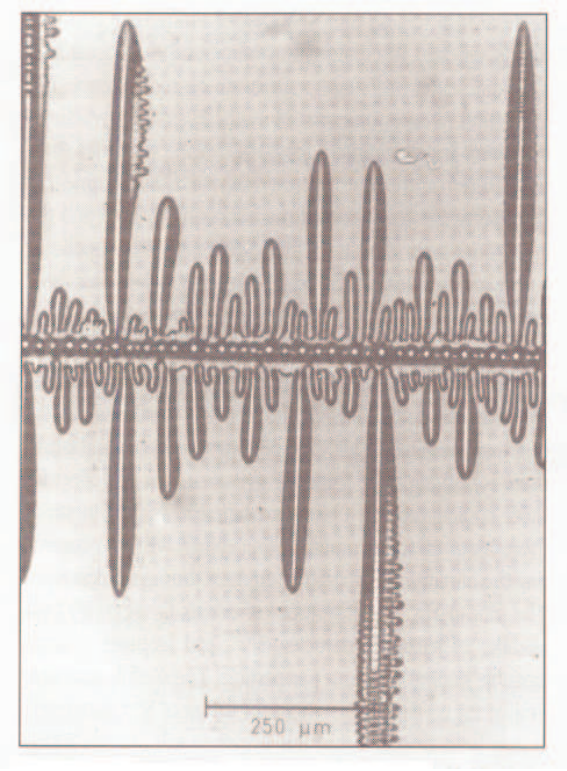

Fig. 2.11: A ripened dendrite of NH_4Cl, grown from an aqueous solution at steady state conditions, showing how secondary arms are necked at the roots where they join the primary spine[8].

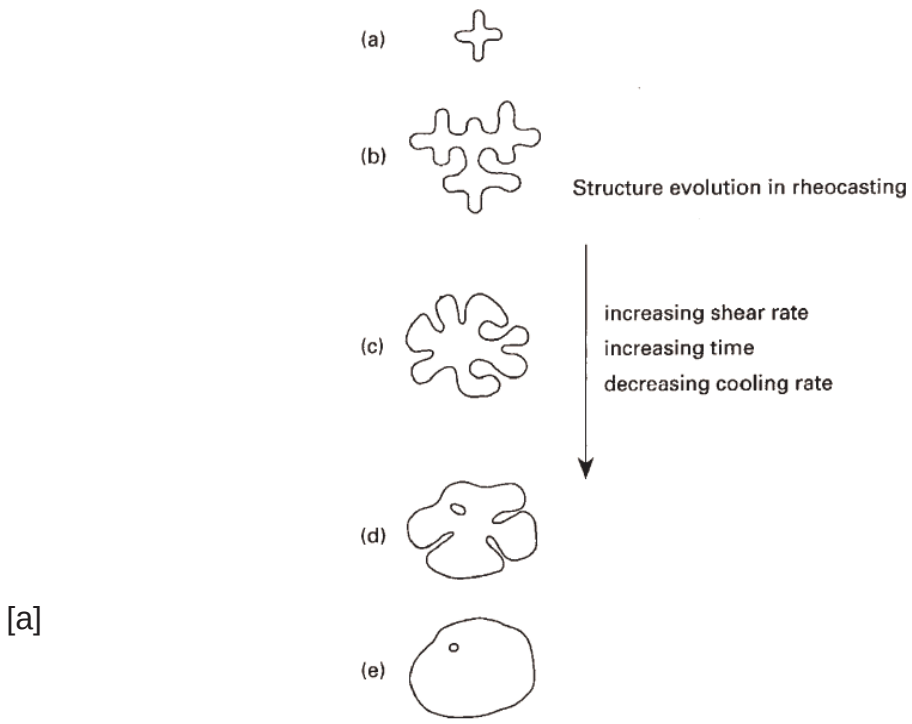

[a]

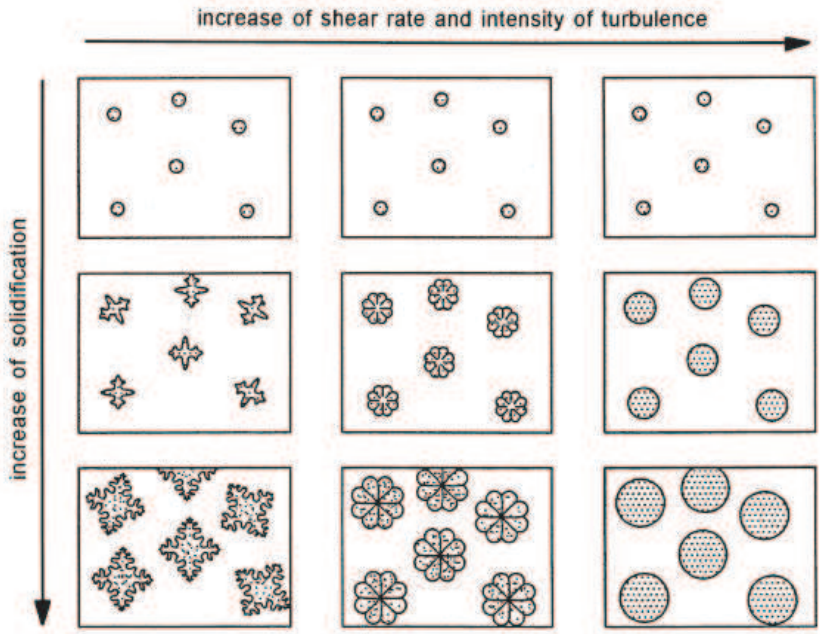

[b]

Fig. 2.12: Schematic section of evolution of structure during solidification with vigorous agitation: [a] different stages in transformation from dendrite to globular morphology: (a) initial dendritic fragment; (b) dendritic growth; (c) rosette; (d) ripened rosette; (e) spheroid [3]; and, [b] schematic illustration of morphological transition from dendritic to spherical via rosette with increase in shear rate and intensity of turbulence [2].

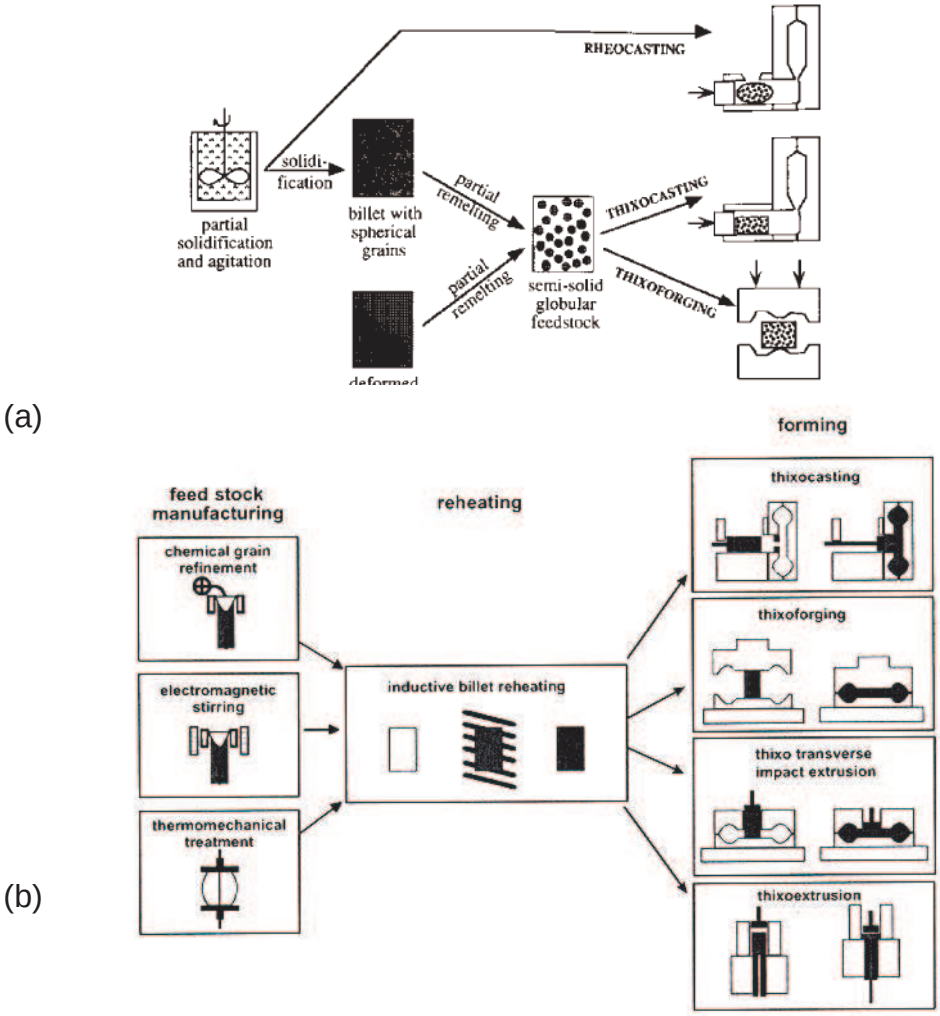

Fig. 2.13: Schematic comparison of thixoprocesses: (a) [2]; (b) [114]

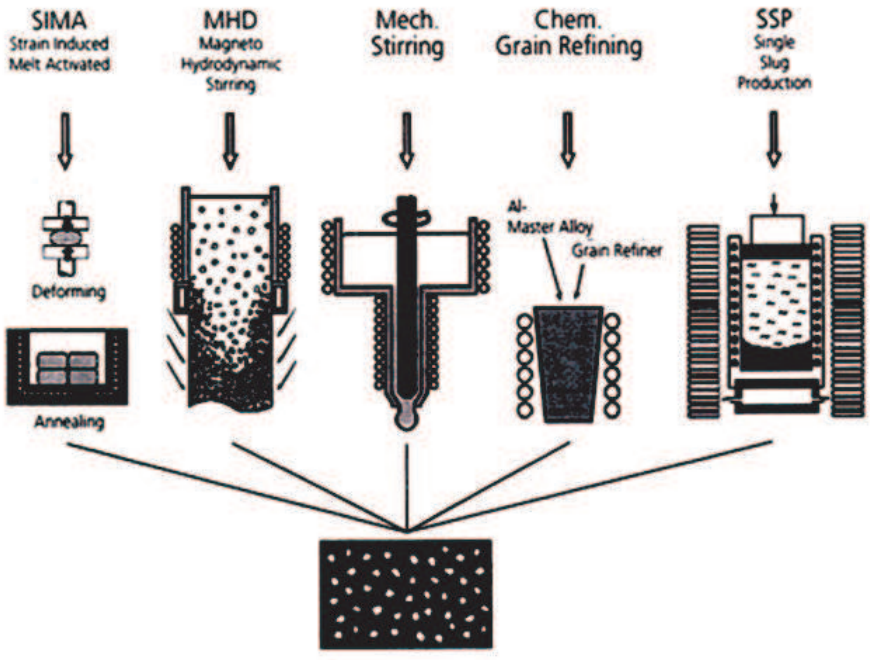

Fig. 2.14: Comparison of feedstock production routes [134].

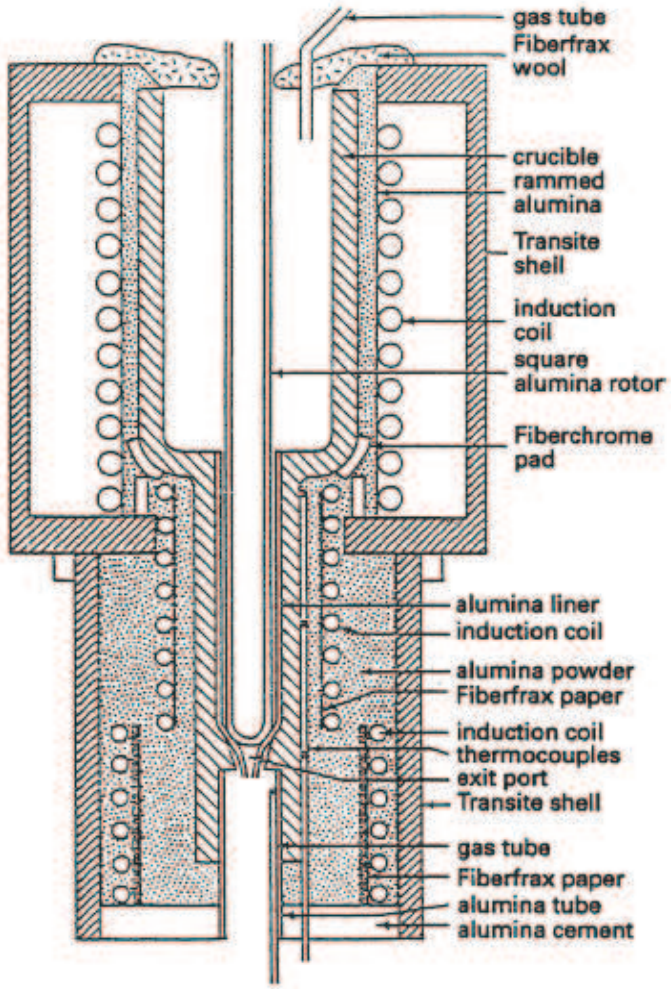

Fig.2.15: Schematic diagram of high temperature continuous Rheocaster [49].

(a)

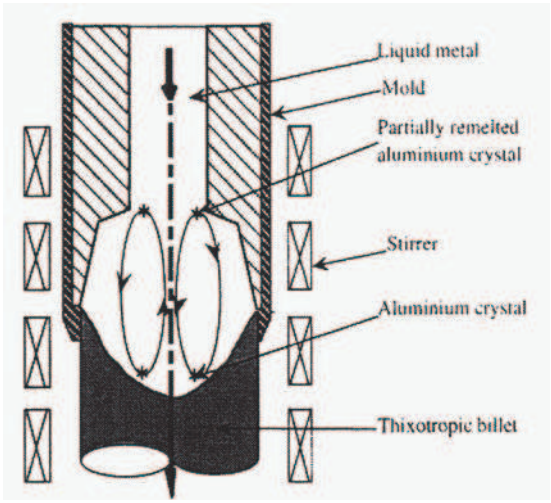

(b

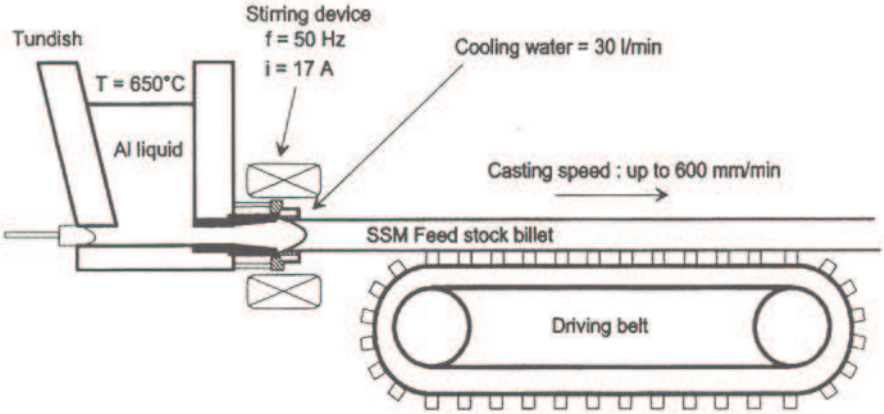

(c)

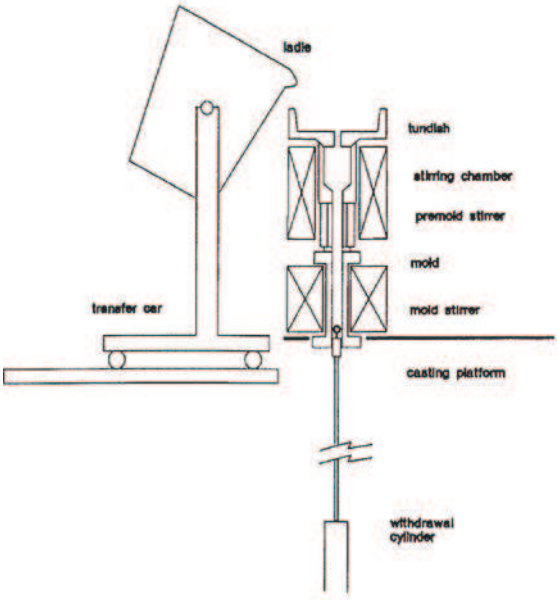

Fig. 2.16: Schematic diagrams of: (a) Vertical Electromagnetic stirrer[109]; (b) Horizontal Electromagnetic stirrer[143]; and ISC Continuous stirrer[144].

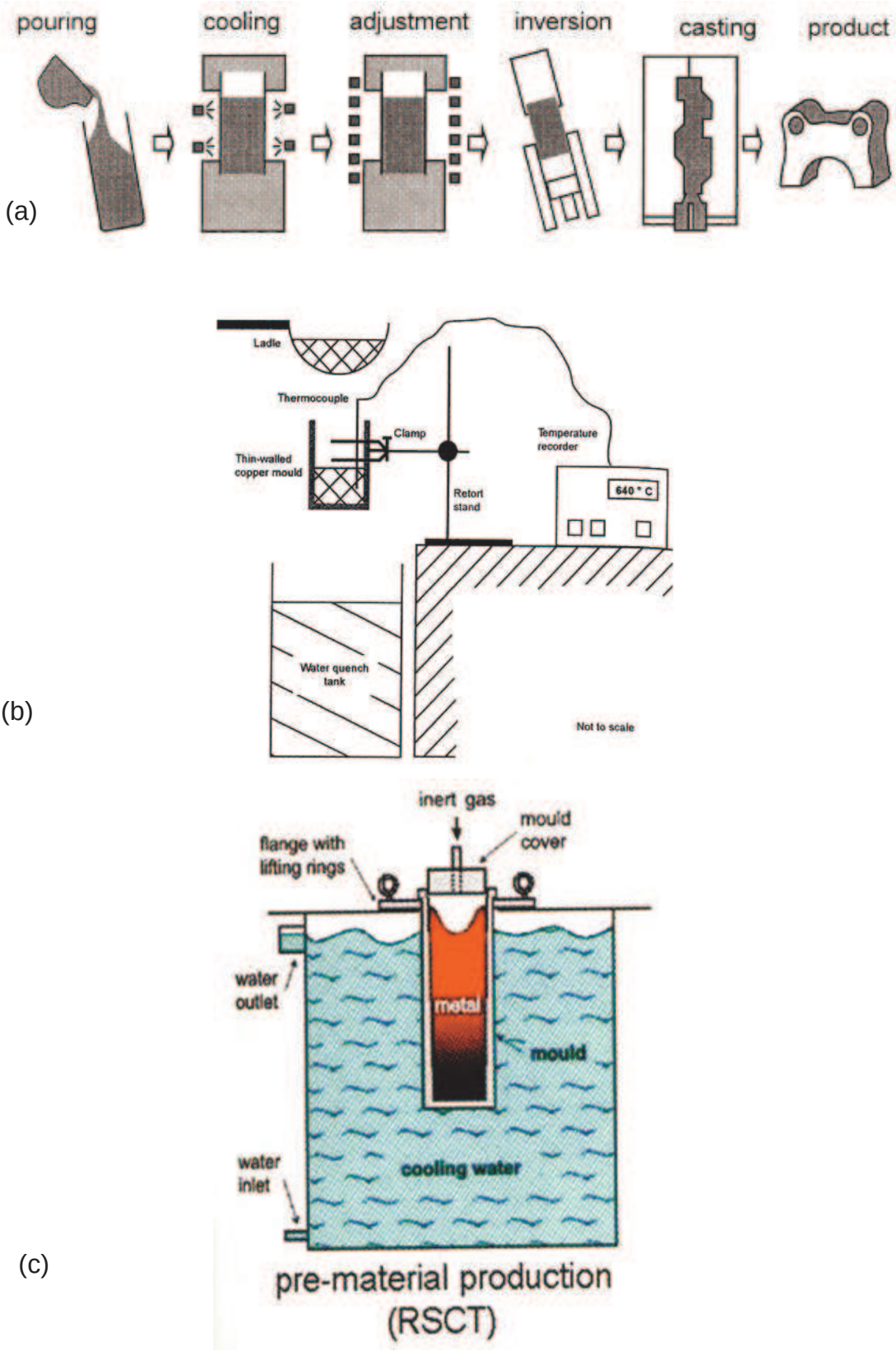

Fig. 2.17: Schematic illustration of: (a) NRC® process[2]; (b) Direct Thermal Method, DTM process[84]; and, (c) Rapid-Slug-Cooling-Technology, RSCT, process[137,148].

(a)

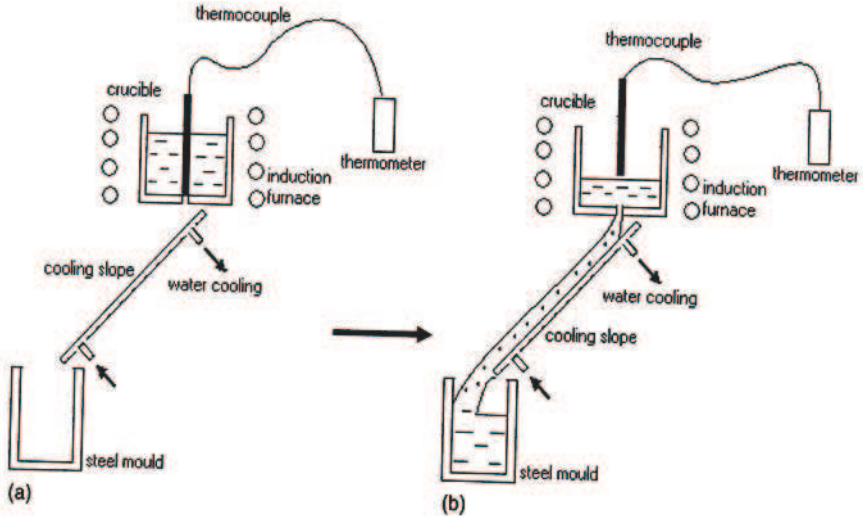

(b)

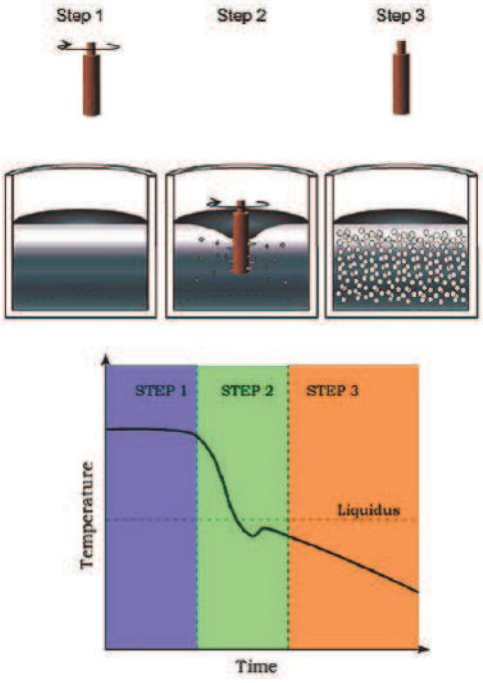

Fig 2.18: Schematic illustration of: (a) Cooling slope[150]; and, (b) Semi-solid Rheocasting SSR™ process[19].

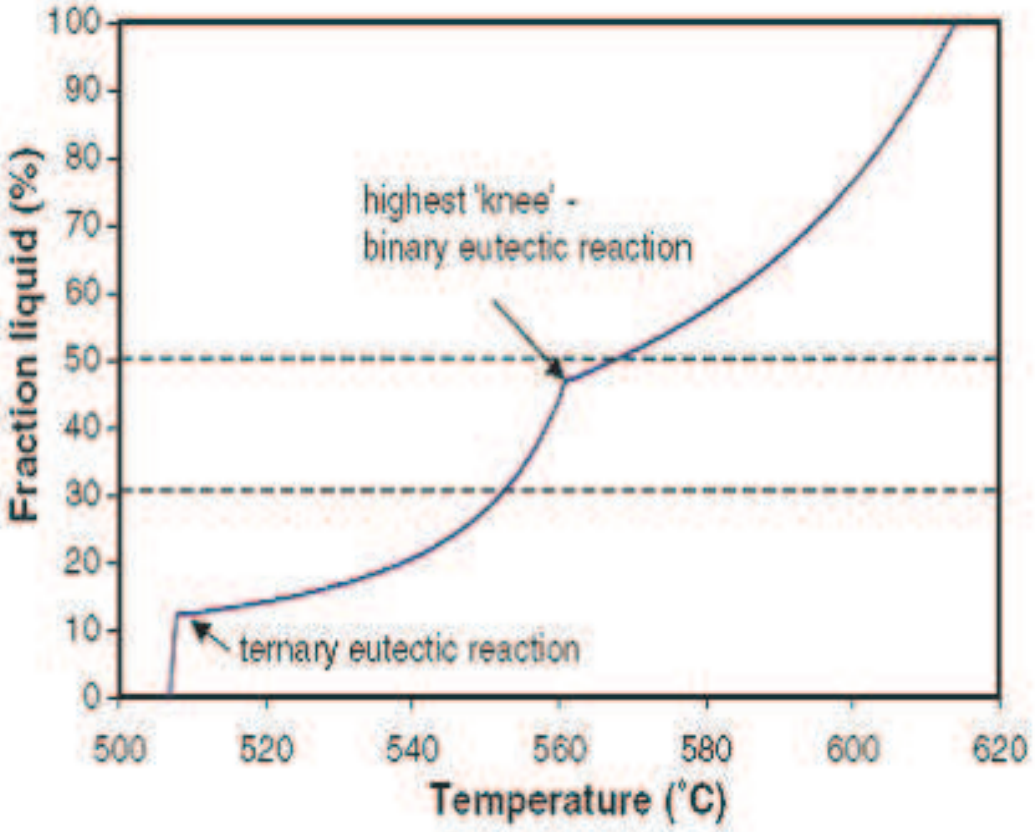

Fig. 2.19: Schematic of a typical fraction liquid vs. temperature curve from MTDTA prediction[23].

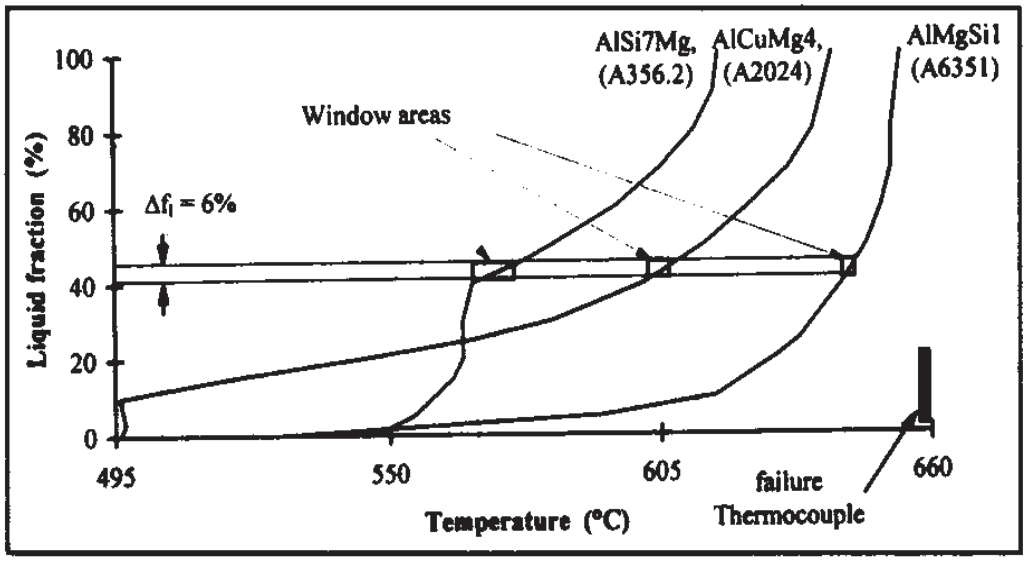

Fig. 2.20: Temperature window corresponding to a ±3% change in liquid[163].

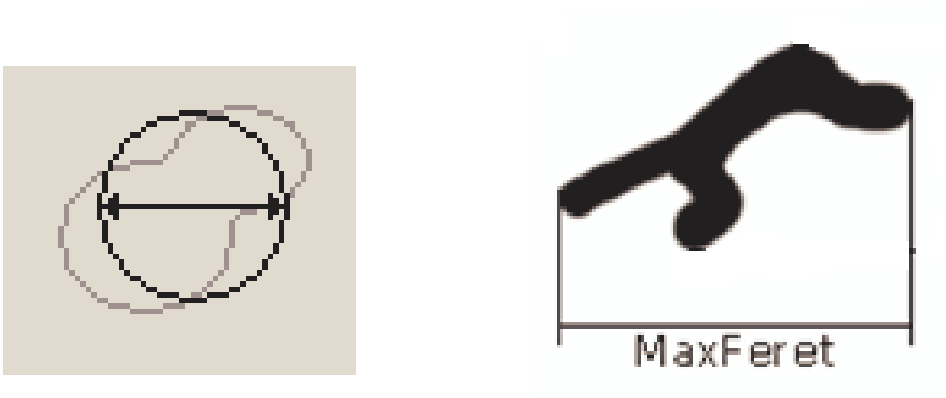

(a) (b)

Fig. 2.21: Schematic to show the grain characteristics: (a) equivalent diameter; and , (b) MaxFeret diameter.

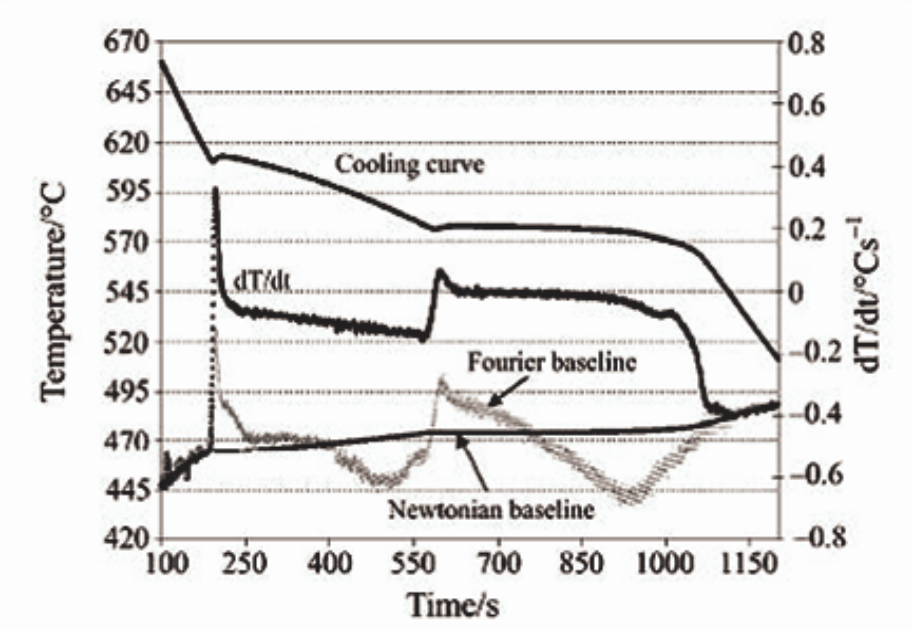

Fig. 2.22: Comparison of Newton and Fourier Cooling Curve analysis for an A356 alloy [185].

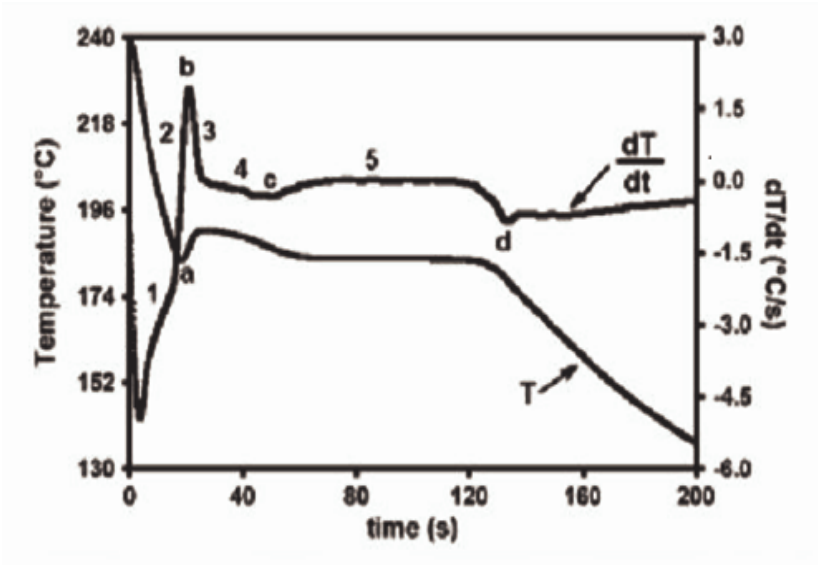

Fig. 2.23: First derivative of a cooling curve showing relevant features considered for t determination [181].

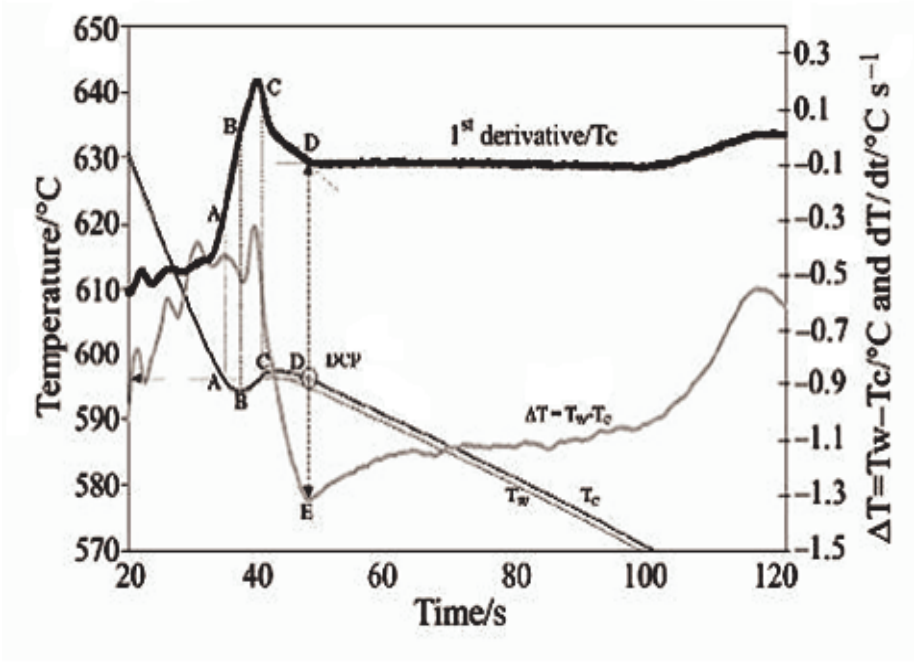

Fig. 2.24: Cooling, first derivative and ΔT curves for a 319-aluminium alloy[179].

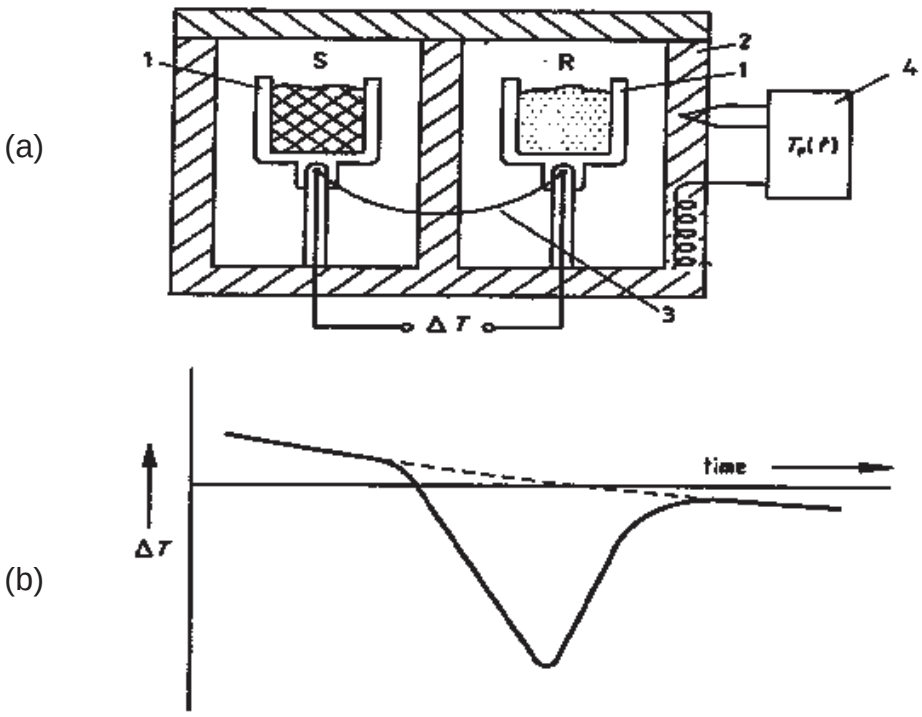

Fig. 2.25: Differential Thermal analysis (DTA): (a) Schematic diagram of apparatus; 1 crucible, 2 furnace, 3 differential thermocouple, 4 controller, S sample, R reference sample; and (b) Schematic measured curve (endothermic transition)[188].

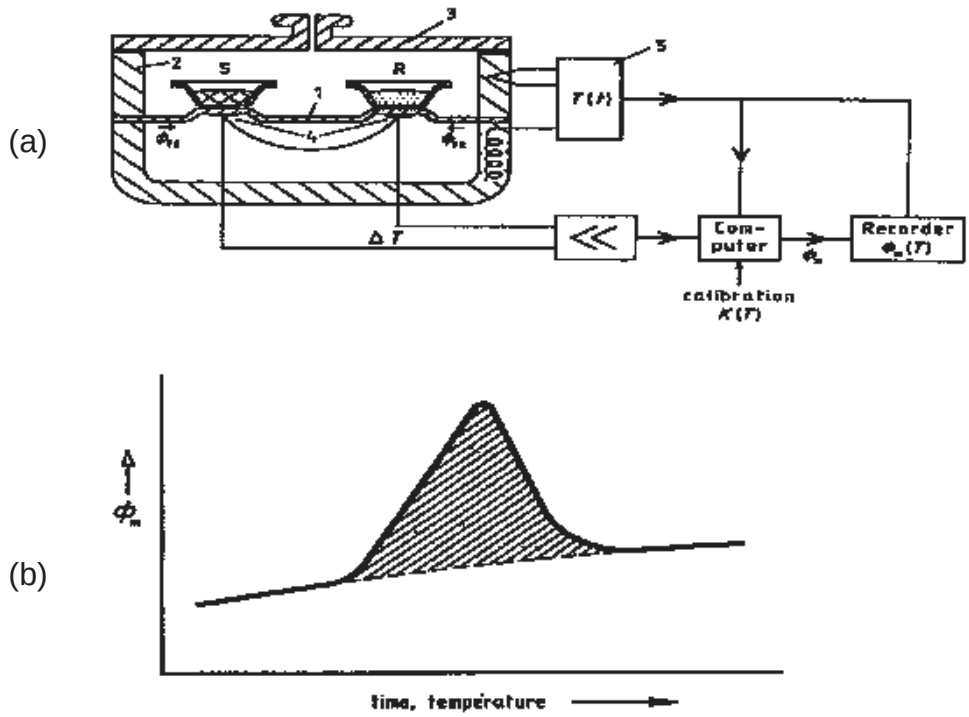

Fig. 2.26: Differential Scanning Calorimetry (DSC): (a) Schematic diagram of apparatus; disk, 2 furnace, 3 lid, 4 differential thermocouple, 5 controller, S sample, R reference sample; and (b) Schematic measured heat flow rate curve[188].

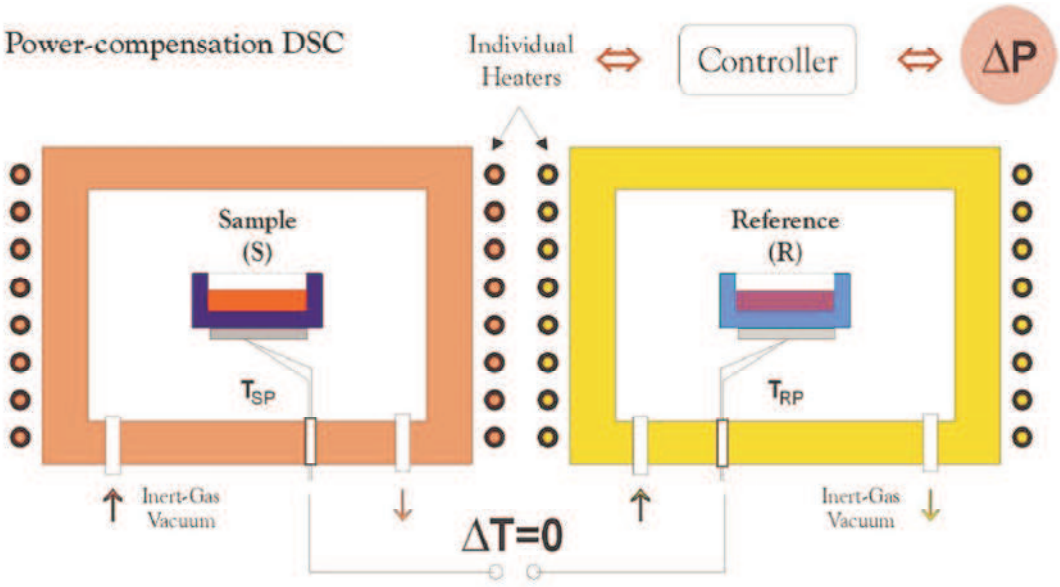

Fig. 2.27: Schematic diagram for Power Compensation DSC apparatus[188].

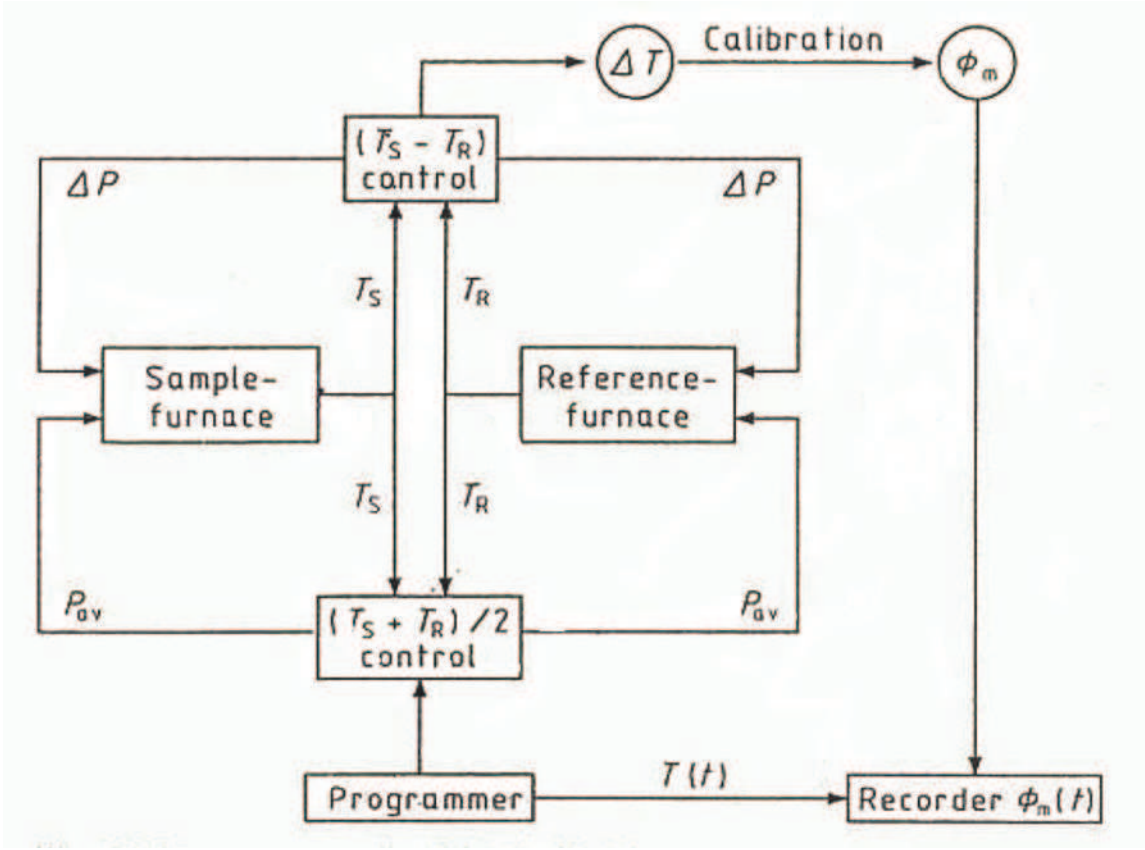

Fig. 2.28: Block diagram showing the function principle . *TS* , *TR* are the temperatures of sample and reference furnaces, *ΔT = TS - TR*, *Pav* average heating power, ΔP compensation heating power and *Φm* measured heat flow rate or measuring signal[188].

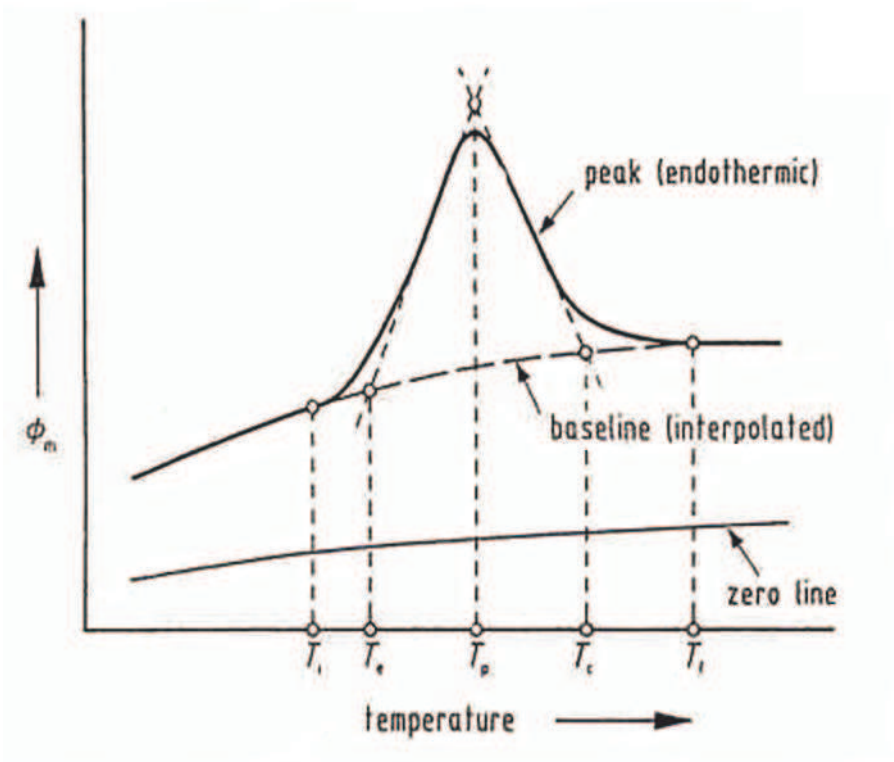

Fig. 2.29: Definition of zero line, baseline, peak and characteristic temperature[188].

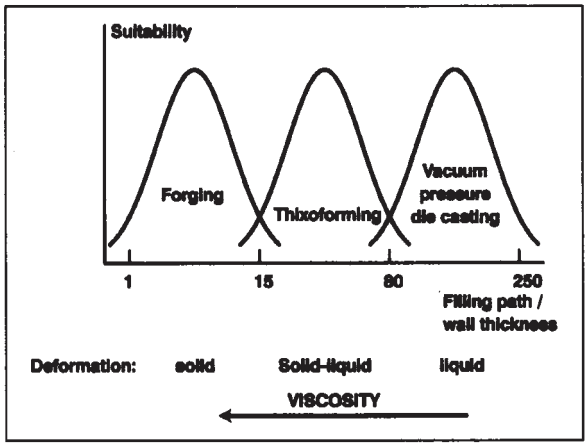

Fig. 2.30: Geometric differentiation of the forging, thixoforming and vacuum pressure die casting based on viscosity, which depends on the fraction solid in the material[190].

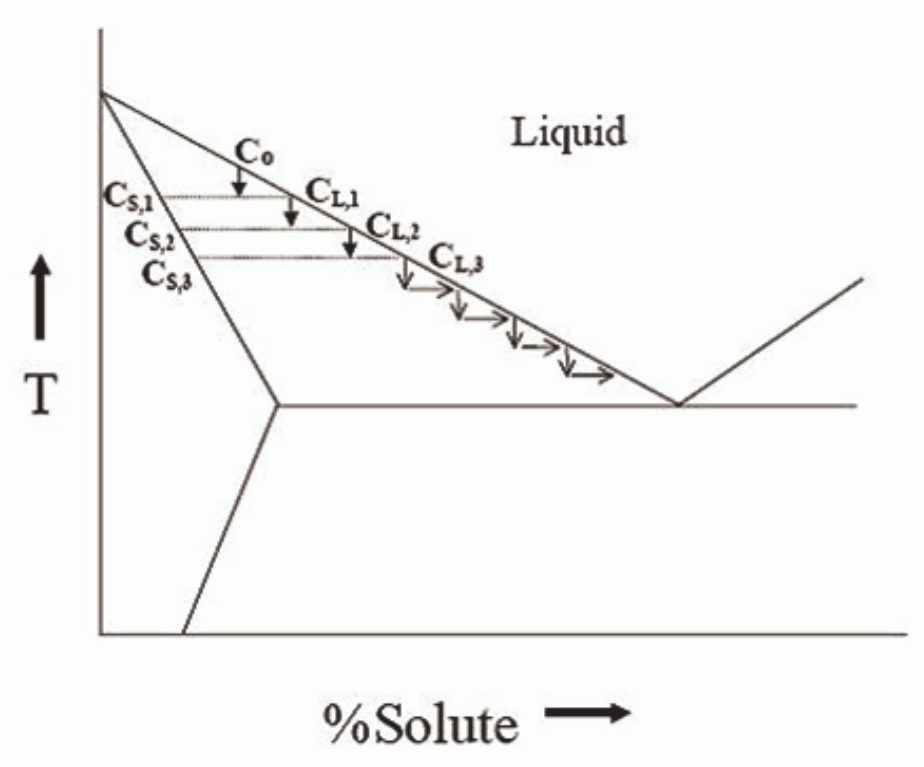

Fig. 2.31: Schematic representation of step-wise technique used in Gulliver-Schiel expression[207] to measure fraction solid in the solidification range.

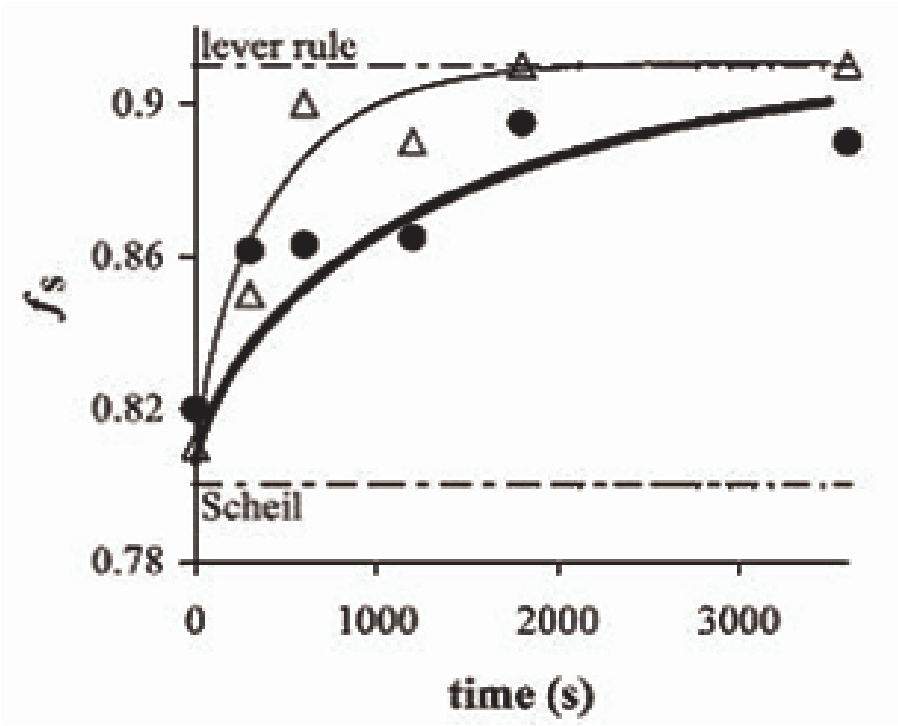

Fig. 2.32: Solid fraction evolution during partial remelting of two Al-8 wt.% Cu alloys at 550 °C. The full lines represent the results of the numerical calculation based on the solute diffusion in the solid phase (•, refined alloy; Δ, unrefined alloy)[194]. The figure also shows that the equilibrium conditions can be achieved with longer holding time.

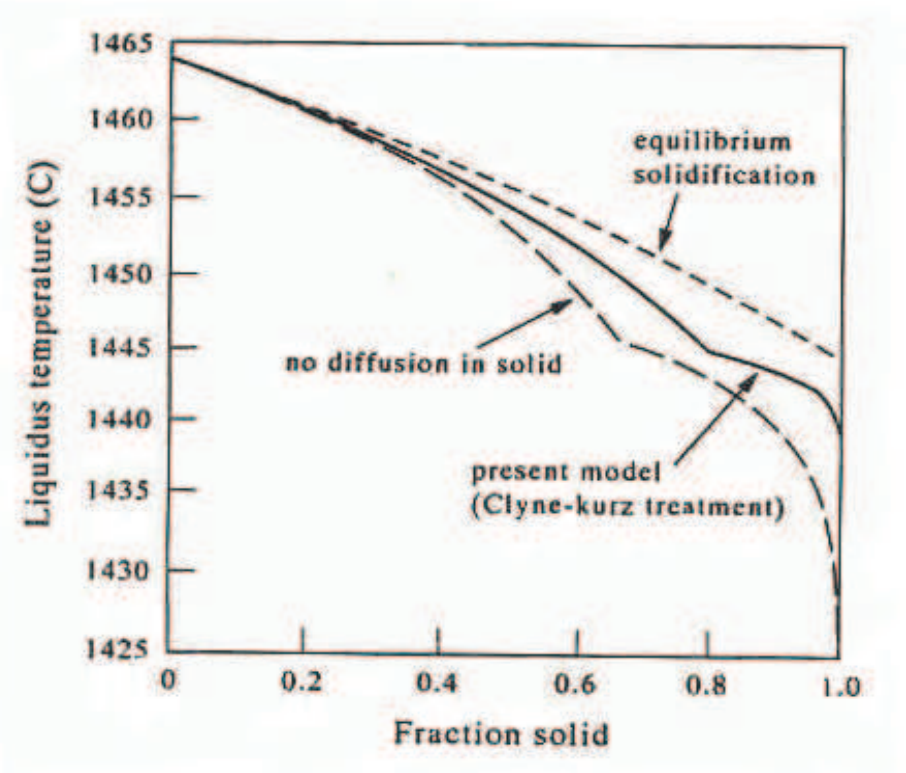

Fig. 2.33: Comparison between various calculation modes of solidification in an austenitic stainless steel from Yamada and Matsumiya as cited in[207], showing the values obtained using Clyne-Kurz back-diffusion expression lie in between those for Lever rule and Scheil expression.

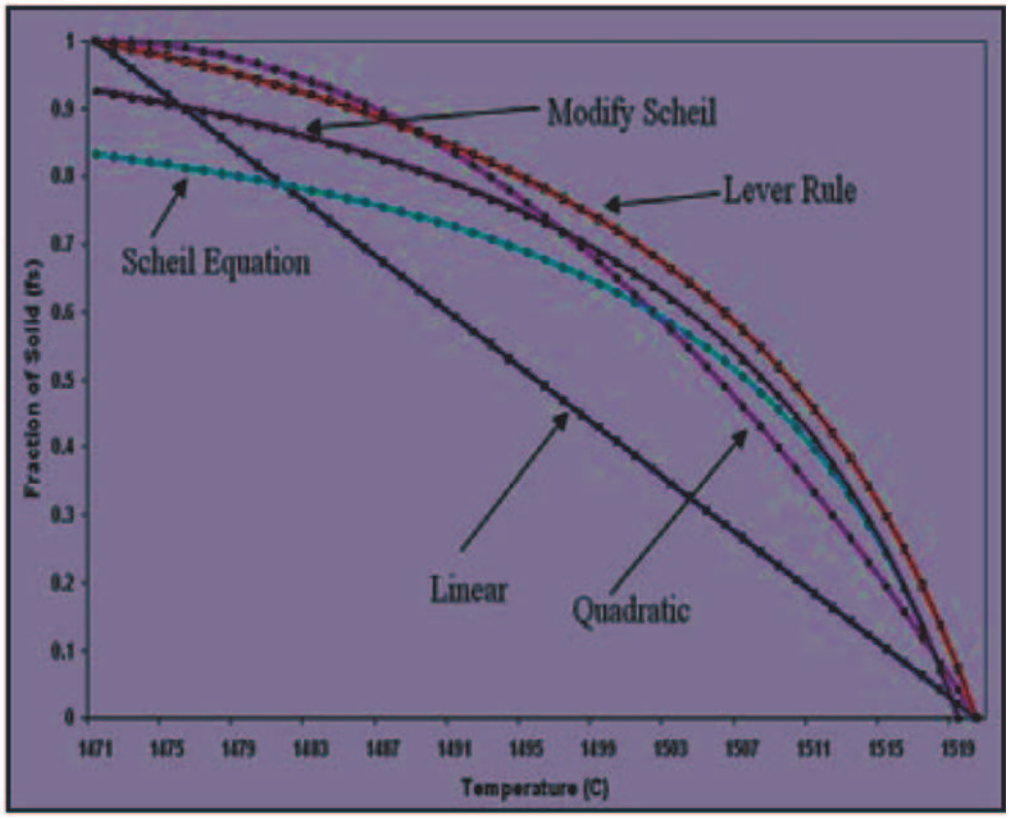

Fig. 2.34: Fraction solid and temperature relationship of low carbon steel in various modes[205].

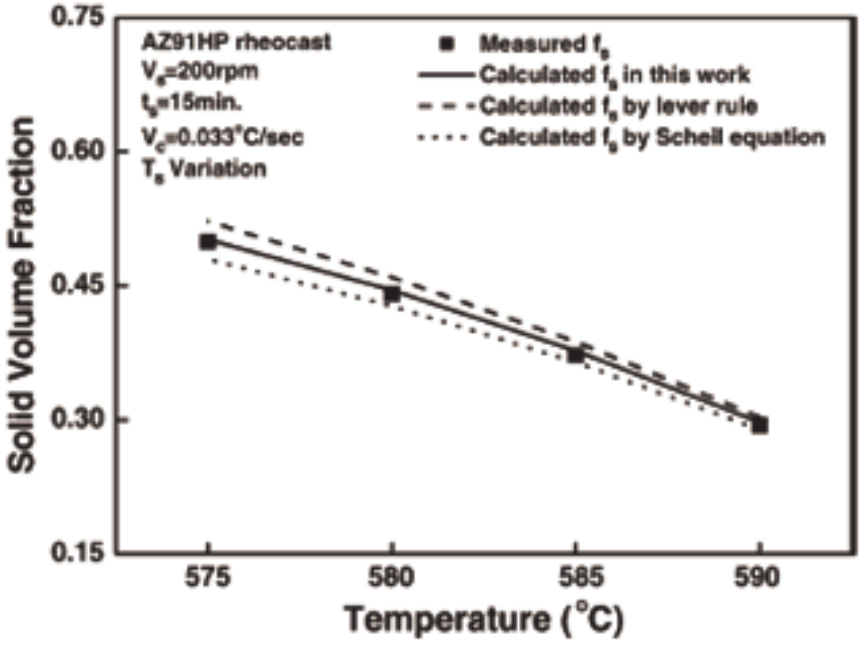

Fig: 2.35: Fraction solid calculated at different processing temperatures[38].

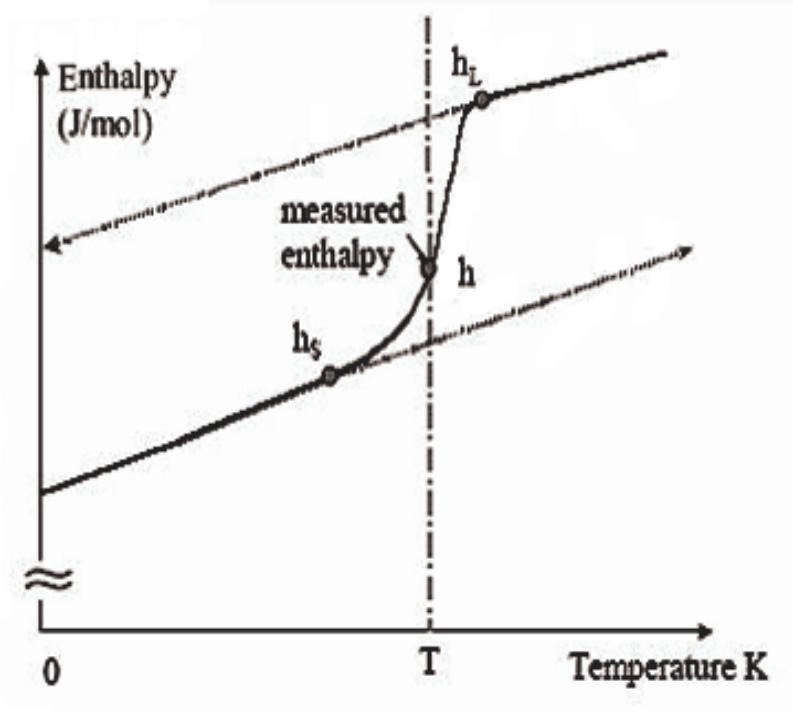

Fig. 2.36: A schematic plot of enthalpy vs. temperature for an alloy[162].

Chapter 3

Experimental Methods

3.1 INTRODUCTION

In this research work, a cooling slope apparatus[150] was used to examine the effect of slope length, slope cooling, slope angle, pouring temperature, mould material and coating on the microstructure. The aim of this work was to examine the microstructure obtained, evaluate its resultant as-cast characteristics, and determine if it could be beneficial for subsequent thixoforming processes. The experimental procedures adopted are described in detail in this chapter. These include the selection of the alloy material, its characterisation, its processing using the cooling slope, mould design choice and analysis of the final microstructure using optical microscopy which was used in combination with image analysis techniques.

3.2 MATERIALS SELECTION

For this current study a non-grain-refined un-modified hypoeutectic AlSi7Mg0.12 alloy, hereinafter referred to as NGM AlSi7Mg, was selected. This alloy composition was chosen because of its importance in industrial casting practice. For a comparative study a commercial AlSi7Mg alloy, hereinafter referred to as COM AlSiMg, was processed using the aforementioned cooling slope method[150]. To examine the tendency and efficiency of the process in producing a material with a characteristic

microstructure suitable for subsequent thixoforming, the cast samples were compared with a Magnetohydrodynamic (MHD) (see Section 2.3) produced A356 alloy material, hereinafter referred to as MHD A356. The NGM AlSi7Mg and MHD A356 alloy materials were received as continuous cast billets, 77 mm in diameter and processed by SAG GmbH, Austria. The COM AlSi7Mg alloy was received in the form of ingots, ~ 74 x 74 mm in cross-section as shown in Fig. 3.1.

3.3 CHARACTERISATION OF STARTING MATERIAL

All three alloy materials were characterised for their exact chemical composition, cooling behaviour, liquidus and solidus temperatures, and compared – with respect to the effect of their inherent diversity due to composition variation along the cross-section during casting process.

3.3.1 Chemical Analysis

The chemical analysis was conducted using at least three samples from each alloy material at differing positions thereby limiting the effect of segregation, if any, with the average composition measured. The analysis was made using a spectrum analysis with the ICP-OES (Inductive Coupled Plasma – Optical Emission Spectroscopy) method at the Austrian Foundry Research Institute. The Si content was measured by gravimetric analysis as the Si content of the alloys was greater than the detection limit of the instrument.

3.3.2 Thermal Analysis

For cooling curve analysis a croning sand cup as shown in Fig. 3.2(a), was employed to facilitate the thermal response of each alloy during solidification and thus enable an accurate determination of the liquidus temperature. The sand cup has an internal

diameter of 71 mm and a height of 72 mm and had a single K-type tellurium coated Chromel-Alumel thermocouple positioned at its centre. The metal alloy was superheated to above 700°C before pouring. The croning sand cup was placed and connected to a measuring instrument using a stand from the company Pylet, as shown in Fig. 3.2(b). The molten metal was poured into the cup at room temperature (see Fig. 3.2(c)).

The croning sand cup containing the Chromel-Alumel thermocouple was connected via a balancing circuit and "Log100" software installed on a laptop computer (Fig. 3.2(d)) was utilized for logging the data acquired. In this study a Tectip cup produced by L&N Metallurgical Products Co. was used. This croning sand cup is now only available under the trade name of Quik-cup and is supplied by Heraeus Electro-Nite GmbH.

3.3.3 Differential Scanning Calorimetry (DSC)

For the measurement of the liquidus and solidus temperature for the NGM AlSi7Mg, COM AlSi7Mg and MHD A356 alloys and to determine the phase transformations and their associated temperature ranges, a Perkin-Elmer® Diamond DSC operated using Pyris7 software was used, as shown in Fig. 3.3. Each sample, a disk 1 mm high and 5 mm in diameter with a mass of ~ 15 mg, was prepared from each alloy, placed in a graphite crucible and covered with a graphite lid (Fig. 3.4). Before performing any experiments, the furnaces were cleaned by heating to 600 °C under an argon atmosphere to remove any volatiles present from previous experiments. The apparatus was calibrated with Indium + Zinc using a heating rate of 10 °C/min in an argon atmosphere.

The sample crucible and an empty reference crucible were placed in the furnaces of the Diamond DSC apparatus. The samples were heated from 400 °C (where they were held for 1 min for equilibration) to 640 °C at a heating rate of 10 °C/min. They were then held at 640 °C for 1 min before cooling at the same rate of 10 °C/min to 400 °C. Argon gas was purged throughout these heating and cooling runs.

The data was saved and exported in ASCII code for further processing in Origin@ 7GSR2 software from OriginLab Corporation. The Perkin-Elmer Pyris7 software was used to subtract the base line obtained from the heating and cooling run from that of the empty graphite crucibles for an identical temperature range. The peak temperature, onset, offset, area/partial area under the curve, specific heat and enthalpy were all measured from the data.

3.3.4 Simulation with Thermo-Calc®

The alloy liquidus and solidus temperature, fraction solid, expected phases, their temperature range and their approximate percentage in the alloy were simulated using Scheil module from the TCC™ version of the Thermo-Calc® Software[211]. This enabled the validation of the data obtained from experimental techniques (cooling curve, DSC, microscopy). The TTAL5 version 5.0 database, originally called Al-DATA, was used and is a comprehensive database for all the major commercial Al-alloys.

3.4 MELT HANDLING

The NGM AlSi7Mg, COM AlSi7Mg and MHD A356 alloys were melted, held and poured on to a cooling slope. Temperatures were strictly controlled to assure the repeatability of the experiments.

3.4.1 Melting

An electric resistance furnace from Naber systems was used to melt the alloys, as shown in Fig. 3.5. The furnace has a maximum melting capacity of 50 Kg for Al and can heat to 1100 °C with a power of 13.5 KW using a 400 V electric supply. An A6 clay bonded crucible having an upper diameter (TOD) of 130 mm, height (HT) of 165 mm and outer bottom diameter (BOD) of 95 mm, as shown in Fig. 3.6, with a

maximum capacity of 2.7 Kg for Al, was used to contain the alloy melt when heating up to 720 °C for processing.

3.4.2 Pouring

The dross (oxide surface layer) was removed to avoid any oxide entrapment. The crucible containing the molten metal was handled manually for pouring. The pouring was made at different temperatures of 640, 660 and 680 °C, according to the requirements.

3.4.3 Temperature Control

The furnace temperature was controlled by an automatic temperature controller. The temperature of the melt in the crucible was controlled manually by a portable Chromel-Alumel thermocouple, connected to a Roline digital meter which could measure temperatures up to 1260 °C.

3.5 COOLING SLOPE

The cooling slope was constructed of copper. The angle of the cooling slope, the pouring length, coating and cooling could all be varied.

3.5.1 Construction

A rectangular copper plate with a groove to allow melt flow and internal holes to enable water cooling was used in this study. The copper plate was 500 mm long, 50 mm wide and 25 mm in height, as shown in the schematic (see Fig. 3.7). The groove for the liquid metal flow was 9 mm deep, 24 mm wide at the bottom and

27 mm at the top. Two holes 10 mm in diameter were drilled through the plate on the bottom side, as indicated on the schematic, to allow water circulation and thus enable cooling of the plate. To measure the temperature of the plate and water four holes 0.6 mm in diameter were drilled (two on each end) for thermocouples. A picture of the apparatus is shown in Fig. 3.8.

3.5.2 Coating

To avoid the adhesion of alloy melt to the cooling slope, coatings were applied. Either graphite or boron nitride (BN) was sprayed on to the cooling slope, as shown in Fig. 3.9, and dried, prior to the pouring of the melt. The effect of both the graphite and BN coating was evaluated.

3.5.3 Cooling

The alloys were processed with and without cooling of the slope. The slope was cooled with flowing water. The incoming water was at room temperature and its flow rate was ~ 3.50 l/min. The temperature of the water, slope and melt at the bottom of the cooling slope was assessed with the help of temperature acquisition software "Log100" using the computer set-up shown in Fig. 3.2(d).

3.5.4 Processing Parameters

The molten alloys were poured on to the cooling slope at temperatures of 640, 660 and 680 °C. The slope was coated with graphite and/or BN, had contact lengths of 80 – 480 mm and was inclined at angles of 20, 40 and 60°. The effect of these parameters on the final microstructure was then evaluated.

3.6 MOULD DESIGN AND MATERIAL

The molten metal was poured on to the cooling slope at temperatures of 640, 660 and 680 °C and collected in either a sand or metal mould at the bottom of the slope. The sand mould was prepared by curing a mixture of quartz sand and sodium silicate with CO_2 gas. The sand mould was used to create a stepped sample, 76 mm in height and 100 mm in length, as shown in Figs. 3.10(a), 3.11(a) and 3.12(a). The width of the sample was 10, 22 and 34 mm having a step height of 25 mm. The dimensions are as shown in the schematic in Fig. 3.10(a). The cast samples are shown in Fig. 3.12(a).

The metallic mould was a conical cylinder having a bottom diameter of 51 mm, a top diameter of 70 mm and a height of 51 mm (see Figs. 3.10(b), 3.11(b)) and 3.12(b). It was water cooled at a rate of 6.7 l/min.

3.7 SAMPLE PREPARATION

For the examination and evaluation of the microstructures, samples were prepared using the following steps.

3.7.1 Cutting

Samples were sectioned using a cut-off saw as indicated in the schematic shown in Fig. 3.13. All the sand cast samples were cut from the center. The sample from the thin section was cut from the lower side of one half of the sand cast sample, to examine the microstructure at the far end of the sand mould. Samples from the middle and top section were cut in a way to include the edge and center of the sample i.e. from the side to the center. The schematic indicating the cutting planes is shown in Fig. 3.13(a). In the metallic mould samples, the sample was initially cut from the center. The sample from the bottom was taken from the bottom center. The other

samples were taken from the side to bottom to observe the change in morphology from the skin to center of the sample as shown schematically in Fig. 3.13(b).

3.7.2 Grinding and Polishing

A Stuers Knuth Rotor grinding machine was used to grind the samples manually on 80, 200 and 400 grit papers, while an ATM automatic Saphir 350E rotating disk, combined with Rubin 520 sample handling rotating head was used for fine grinding on 600 and 1200 grit papers, polishing on 3 μm and 1 μm diamond pasted cloths and OP-S polishing (equipment is shown in Fig. 3.14). Samples were cleaned thoroughly before moving to a finer grit by submerging them in ethanol and placing them in a Bransonic 92 ultrasonic bath for 2-3 mins, to remove any unbound coarse particles. This was particularly important for samples containing rough surfaces and pores, etc..

During grinding, water was used as a coolant and lubricant, whilst during the polishing clothes were impregnated with 3 μm or 1 μm diamond paste and sprayed respectively with 3 μm or 1 μm water based diamond suspension. Polishing cloths were continuously lubricated by drop wise pouring of a mixture of ethanol and 12 % glycol. Samples were cleansed with soap, washed with water and sprayed with Ethanol and dried. The final polishing was made with OP-S suspension containing fine silica. The samples were then washed using water on the OP-S cloth before rinsing in ethanol. The samples were ground on 600 and 1200 grit paper and polished on 3 μm and 1 μm clothes for 3 minutes each. For the OP-S polishing step, samples were polished with OP-S suspension for 3 minutes and subsequently washed with water for one minute on the same cloth whilst still being rotated. They were then cleaned with ethanol and dried. During the polishing steps the samples were also cleaned ultrasonically before proceeding to a finer one, to avoid contamination.

3.7.3 Etching/Anodizing

To observe the microstructure of the NGM AlSi7Mg, COM AlSi7Mg and MHD A356 alloys (for the samples which had been processed under different casting

conditions using the cooling slope technique), polished samples were etched with 0.15% HF solution in water for 20 s. Samples were also anodized with Barker's etch to clearly distinguish the grains when using an optical microscope with cross-polarized light and Lambda (λ) filter. The composition of this etchant was 1 ml of HBF_4, 1 ml of HF, 24 ml of C_2H_5OH and 74 ml of water. Samples were anodized using this solution by making the sample the anode and a Ti plate the cathode. A voltage of 20 V and anodizing time of 1 minute was used. The anodized samples were produced at the Austria Foundry Research Institute on an automatic "ATM Kistall 620" anodizing machine thereby enabling reproducible results for each sample to be obtained.

3.8 MICROSCOPY

The as-polished and anodized samples were studied using both optical and scanning electron microscopy, whilst etched samples were examined using just optical microscopy.

3.8.1 Optical Microscopy

The microstructures of the samples were studied at magnifications of 25, 50 100 and 500X using an inverted stage "Leica Reichert-Jung MeF3A" microscope (see Fig. 3.15). For examination of the anodized samples, cross-polarized light with a λ filter was required. The digital image was captured using a Nikon Digital Sight DS-Fi1 camera and the image was saved in a JPEG format for image analysis.

3.8.2 Scanning Electron Microscopy (SEM)

Scanning Electron Microscopy (SEM) was used to study the intermetallic phases present in the samples. A FEI QUANTA 200 3D Dual beam ESEM equipped with an

Oxford Instruments INCA x-sight EDX system (see Fig. 3.16) was used for this study. The SEM was operated at 10 - 20 KV at a working distance of 15 mm and spot size of 5 to 7. The images were obtained using the Solid State Backscatter Electron Detector (SSBSED) with Z-contrast imaging and with the Secondary Electron Detector (SED) which produced Secondary Electron Images (SEI's). INCA microanalysis Suite issue 17 + SP1 version 4.07 software was used to obtain energy dispersive x-ray (EDX) spectrums and elemental maps from spots and areas respectively.

3.9 IMAGE ANALYSIS

The images obtained from the optical microscope using the Nikon Digital Sight DS-Fi1 camera were analyzed quantitatively using the accompanying NIS Elements Br 2.30 SP4 Build 387 Basic Research software from Nikon. Quantitative parameters such as grain size, area, perimeter, circularity and sphericity of the primary particles were measured.

3.10 CONTACT TIME VERSES CONTACT LENGTH

In this study contact time rather than contact length, was used. Contact length can be converted to its respective contact time. Contact time was measured using Manning's Equation[223] (Eq. 3.1), used to measures the velocity of the fluid flowing in a channel. The Manning equation for flow in a rectangular open channel (see Fig. 3.17) is given as:

$$V = \frac{k}{n} R^{2/3} S^{1/2} \qquad \text{(Eq. 3.1)}$$

where,

$$R = \frac{A}{P}, \qquad A = yb \qquad \text{and} \qquad P = 2y + b \qquad \text{(Eq. 3.2)}$$

where, A is flow cross-sectional area, b is channel bottom width, k is unit conversion factor (1.49 for Imperial units, 1.0 for metric units), n is the Manning coefficient, P is

wetted perimeter, R is Hydraulic radius of the flow cross-section, S is slope of channel bottom or water surface, V is average velocity of the water and y is water depth. To measure the time the following equation was used.

$$t = \frac{D}{V} \qquad \text{(Eq. 3.3)}$$

where, D is the distance traveled and time is in seconds.

Using the dimensions of the cooling slope, given in Fig. 3.7 the measured contact time with corresponding contact length for different inclination angles is given in Table 3.1. It can be observed that for the same length a contact time of 0.04 s at an inclination angle of 60° is similar to a contact time of 0.09 s at an inclination angle of 20° and so on.

Table 3.1: Relationship of melt-plate contact time with cooling plate length (cm) with corresponding inclination angles.

Contact Time (s)	Cooling plate length (cm)		
	20°	40°	60°
0.04	7	11	16
0.09	15	23	33
0.13	23	34	49

For the calculation the following data was used:

Height (*y*)	:	0.01 m
Width of channel (*b*)	:	0.025 m
Slope (*S*)	:	Tan (inclination angle)
k	:	1
n	:	0.011 (brass)

3.11 GRAIN CHARACTERISTICS

In this study grain size, circularity or circular shape factor (CSF) and elongation or aspect ratio (AR) were calculated to compare the relative grain sizes, couture and equiaxed nature of the semi-solid microstructures obtained using the cooling slope.

3.11.1 Grain Size

In this study the equivalent diameter i.e. the diameter of a circle with the same area as the feature (see Fig. 3.18(a))[224], was used to estimate its size. Mathematically it is given by:

$$Equivalent\ diameter = \left(\frac{4 \times Area}{\pi}\right)^{1/2} \qquad \text{(Eq. 3.4)}$$

3.11.2 Circularity

The circularity, sphericity or circular shape factor (CSF)[174] is most commonly used to compare the grains with respect of their roundness[225]. It is basically a ratio between area and perimeter and has been described differently by different researchers. However, in this study it was as given by[174] and mathematically presented as:

$$CSF = \frac{4\pi \times Area}{(Perimeter)^2} \qquad \text{Eq. (3.5)}$$

where, the perimeter was calculated automatically using image analysis software from four projections in the directions 0, 45, 90 and 135 degrees using Crofton's formula:

$$Perimeter = \frac{\pi \times (Pr_0 + Pr_{45} + Pr_{90} + Pr_{135})}{4} \qquad \text{(Eq. 3.6)}$$

According to this expression a perfect circle shows a circularity or circular shape factor equal to 1. As this shape characteristic of the grain is dependent on the perimeter, so it is very sensitive to contour irregularities that increase the perimeter. It is therefore also a measure of the contour smoothness of the grain[174].

3.11.3 Elongation

The elongation or aspect ratio (AR), as mentioned above defines the relative equiaxed nature of the grains[174,226], as a ratio of the dimensions of the features. In this study

the expression incorporated in the image analysis software "NIS Elements Br 2.30 SP4 Build 387 Basic Research" from Nikon was used and is given by:

$$AR = \frac{Maximum\ Feret\ diameter}{Minimum\ Feret\ diameter} \qquad \text{Eq. (3.7)}$$

where, the maximum Feret is the maximal value of the set of Feret's diameters (see Fig. 3.18(b)). Generally (for convex objects), Feret's diameter at angle α equals the projected length of object at angle α, $\alpha \in (0,180)$; NIS-Elements calculates Feret's diameter for α=0, 10, 20, 30, ... , 180. While the minimum Feret value is the minimal value of the set of Feret's diameters. Generally (for convex objects), Feret's diameter at angle α equals the projected length of object at angle α, $\alpha \in (0,180)$; NIS-Elements calculates Feret's diameter for α=0,10,20, 30, ... , 180.

3.12 FIGURES

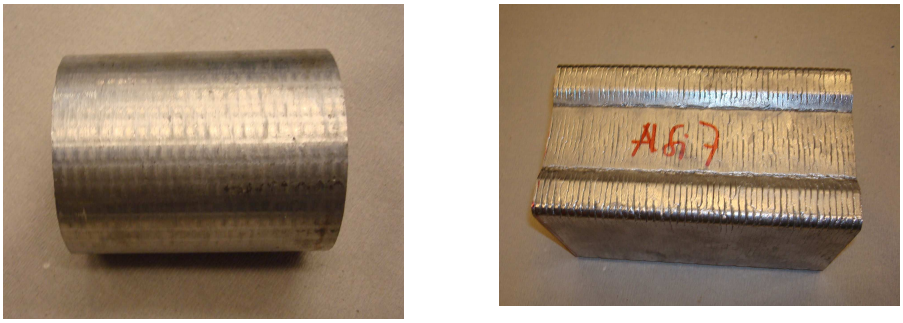

(a) (b)

Fig. 3.1: Form of as-received material: (a) billet for both the NGM AlSi7Mg and MHD A356 alloys; and, (b) ingot for the COM AlSi7Mg alloy.

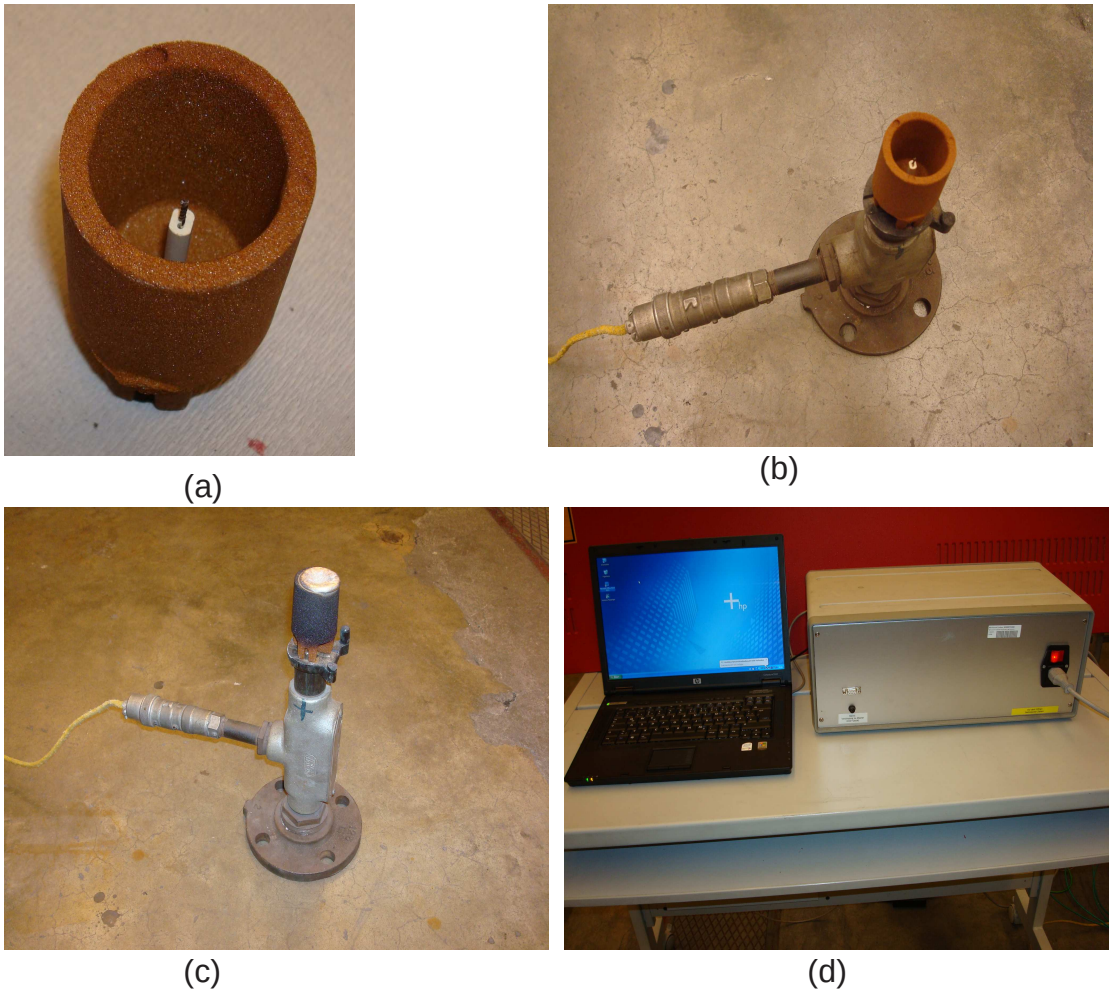

(a) (b)

(c) (d)

Fig. 3.2: Cooling curve experiment: (a) croning sand cup; (b) croning sand cup assembly; (c) after pouring; and, (d) data acquisition system.

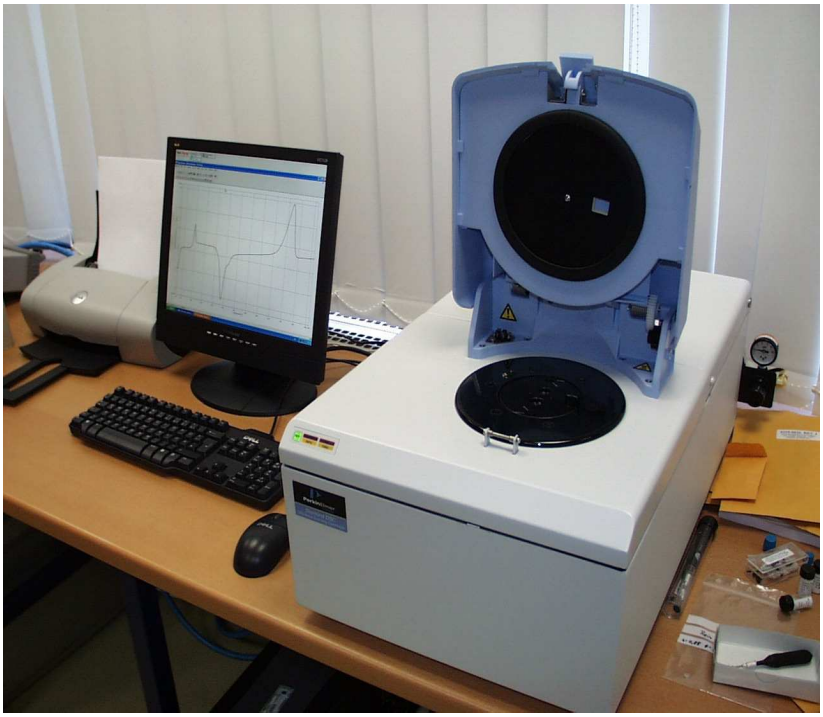

(a)

(b)

(c)

Fig. 3.3: PerkinElmer® Diamond DSC: (a) main DSC apparatus; (b) comparison of Platinum-Iridium Diamond DSC furnace (small) with conventional one (bigger); and, (c) furnace cover in open (left) and closed position (right).

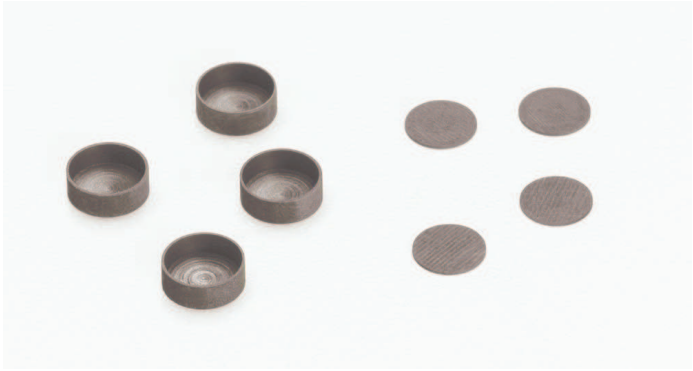

Fig. 3.4: Graphite sample pans and covers (from PerkinElmer®).

Fig. 3.5: Electric resistance melting/holding furnace.

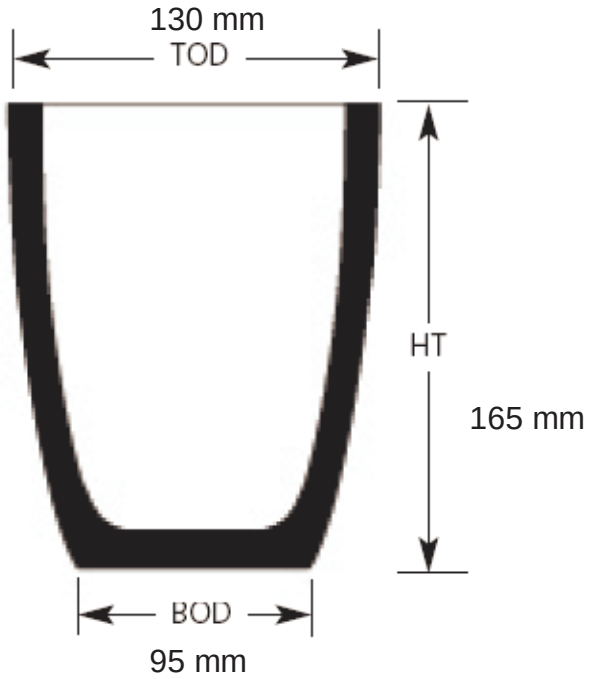

Fig. 3.6: Schematic of clay bonded graphite crucible with dimensions.

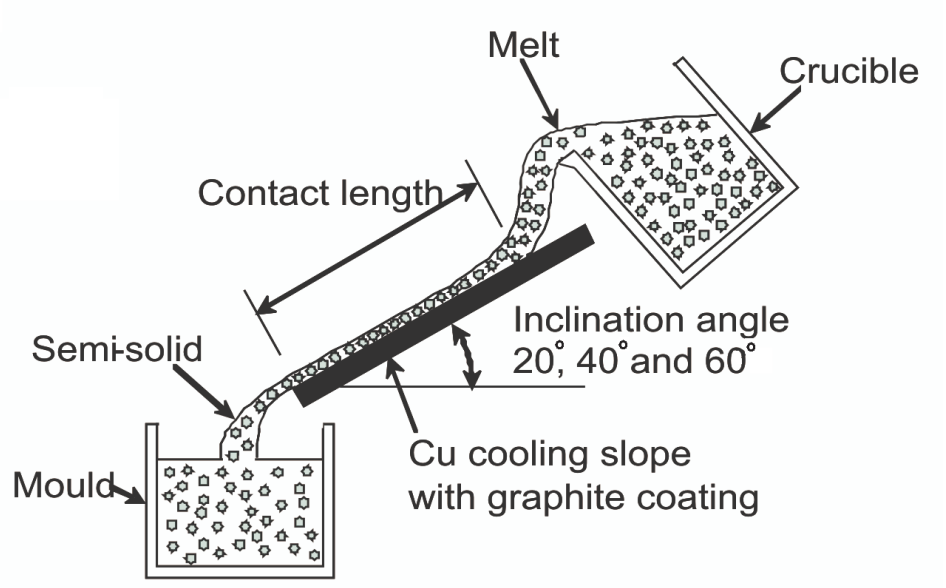

(a)

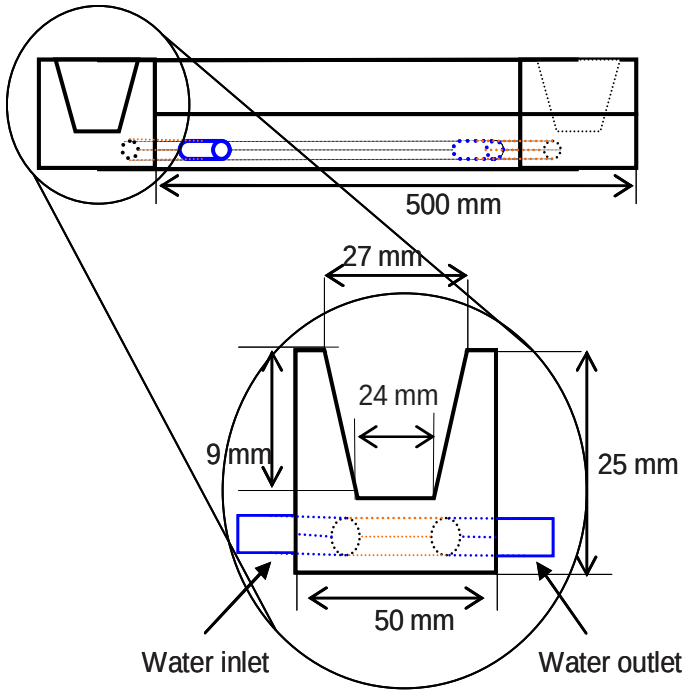

(b)

Fig. 3.7: Schematic illustration of cooling slope: (a) general view; and, (b) dimensions.

Fig. 3.8: Cooling slope assembly as used in this study.

Fig. 3.9 Coating materials - graphite and boron nitride.

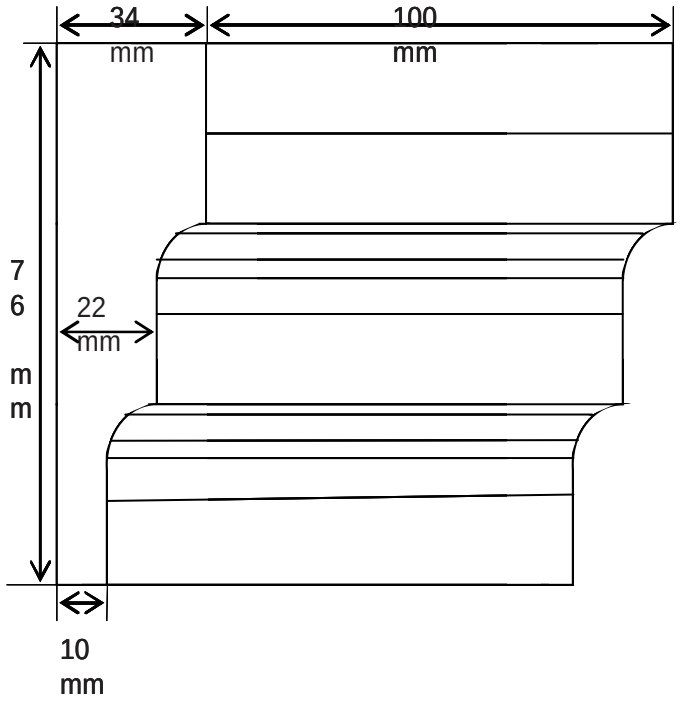

(a)

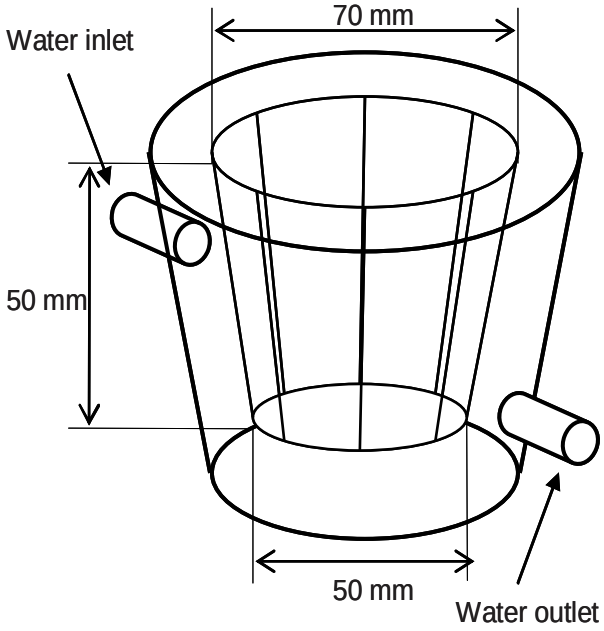

(b)

Fig. 3.10: Schematics of: (a) sand mould; and, (b) metallic mould.

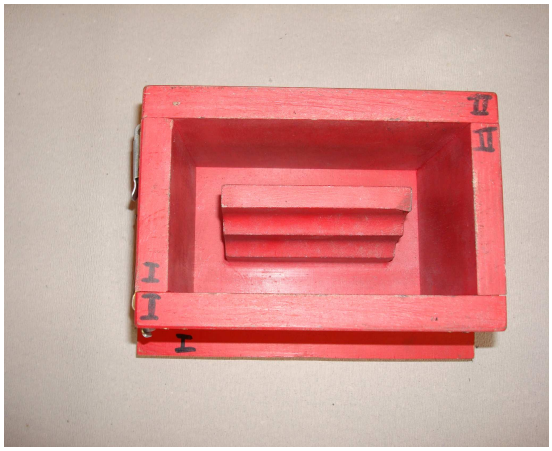

(a)

(b)

Fig. 3.11: Moulding accessories: (a) pattern and mould box for sand mould preparation; and, (b) metallic mould.

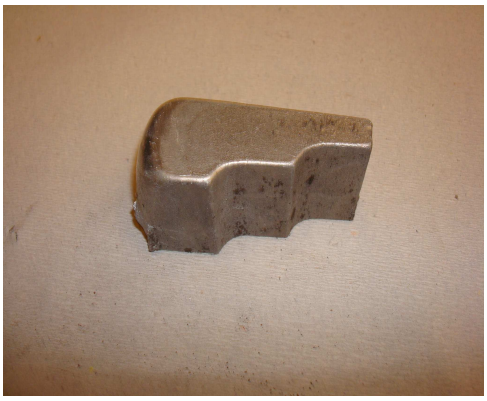

(a)

(a)

Fig. 3.12: Cast samples: (a) sand casting; and, (b) metallic mould casting.

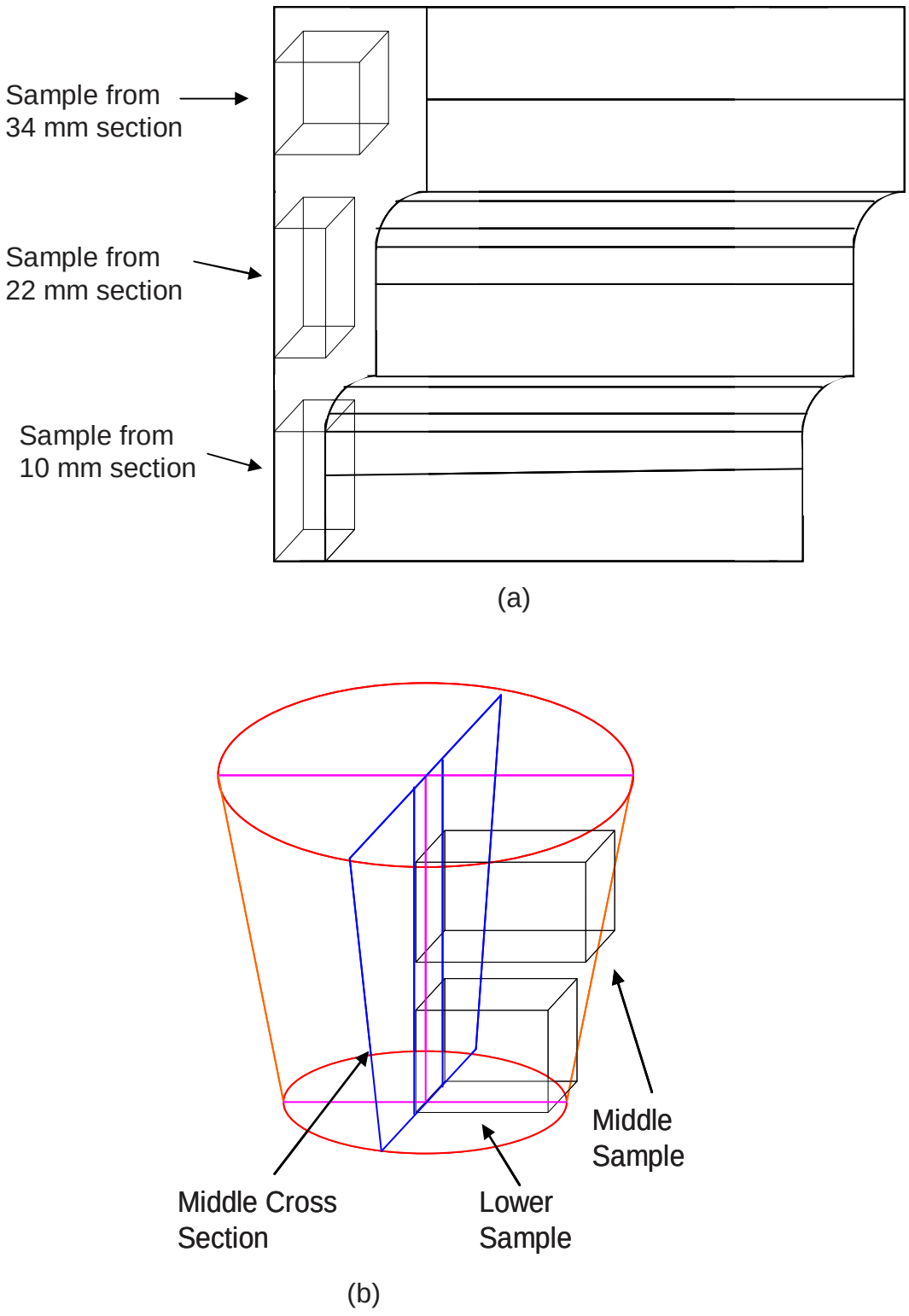

Fig. 3.13: Schematic showing positions from which samples were taken for: (a) sand casting; and, (b) metal mould casting.

Fig. 3.14: Grinding and polishing facility used in this research work.

Fig. 3.15: Optical Microscope used for optical microscopy.

Fig.3.16: SEM facility used for SEM microscopy.

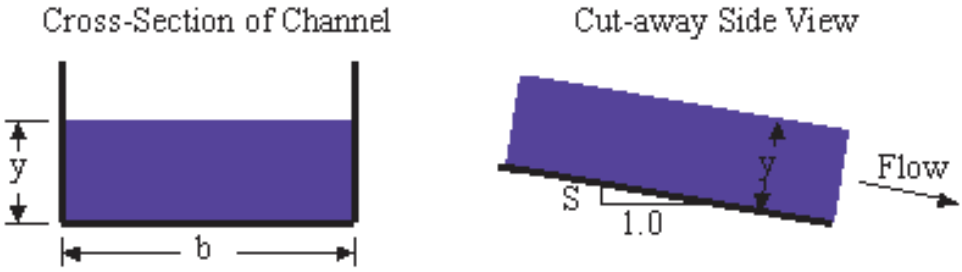

Fig. 3.17: Schematic to show the parameters involved in calculating the flow velocity in the Manning Equation.

(a) (b)

Fig. 3.18: Schematic to show the grain characteristics: (a) equivalent diameter; and , (b) MaxFeret diameter.

Chapter 4

Results

In this section the results obtained from the characterisation of the three AlSi7Mg alloys (non-grain refined non-modified AlSi7Mg (NGM AlSi7Mg), commercial grain refined AlSi7Mg (COM AlSi7Mg) and magnetohydrodynamic stirred commercial semi-solid precursor A356 (MHD A356)) in the as-received and as-cast states are presented. Results include those for the fraction solid sensitivity and effect of processing parameters, sample thickness, mould material and coating. A comparison study has been made and the findings are discussed in Chapter 5.

4. 1 CHARACTERISATION OF AlSi7Mg ALLOYS

4.1.1 Introduction

In this chapter the as-received and as-cast materials in the form of non-grain refined non-modified AlSi7Mg (NGM AlSi7Mg), commercial AlSi7Mg (COM AlSi7Mg) and Magenetohydrodynamic stirred A356 (MHD A356) alloys are characterised using chemical analysis, cooling curve, DSC, Thermo-Calc™ simulations and SEM studies.

4.1.2 Chemical Analysis

The Induction Coupled Plasma Optical Emission Spectrometry (ICP-OES) test and gravimetric measurement results for the NGM AlSi7Mg, COM AlSi7Mg and MHD A356 alloys are given in Table 4.1.1. The Si content of the three alloys varies from 7.02 wt% for the NGM AlSi7Mg and 7.06 wt% for the COM AlSi7Mg to

7.40 wt% for the MHD A356 alloy. The Fe content was slightly lower in the NGM AlSi7Mg i.e. 0.09 wt%, as compared with 0.11 wt% for both the COM AlSi7Mg and MHD A356 alloys. The NGM AlSi7Mg alloy had a Mg content of 0.16 wt% whilst the COM AlSi7Mg and the MHD A356 alloys had values of 0.39 and 0.33 wt% respectively. A very small amount of copper was also found to be present in all three alloys (0.005, 0.01 and 0.004 wt% in the NGM AlSi7Mg, COM AlSi7Mg and MHD A356 alloys respectively). Furthermore Ti was found to be 0.006 wt% in the NGM AlSi7Mg, 0.13 wt% in the COM AlSi7Mg and 0.11 wt% in the MHD A356 alloy. Other elements present like Mn, Cr, Ni and Zn had contents less than 0.005 wt%, while Pb and Sn were found to be less than 0.01 wt% each.

4.1.3 Cooling Curve Analysis

Cooling curve analysis was carried out for the NGM AlSi7Mg, COM AlSi7Mg and MHD A356 alloys to observe the solidification behaviour and sequence of phase formation at pouring temperatures of 820 °C. The cooling curves obtained from the molten NGM AlSi7Mg, COM AlSi7Mg and MHD A356 alloys showed three distinct regions, as shown in Fig. 4.1.1(a)., corresponding to the primary (region 1), eutectic (region 2) and co-eutectic (region 3) phase formation. These three regions are shown in Fig. 4.1.1(b) to Fig. 4.1.1(d).

The characteristic temperatures of these different phases for the three alloys were calculated from the cooling curves by analyzing the change in slope in the curve of the 1st derivative (see Section 2.7.3) which is shown in Fig. 4.1.2.

The nucleation temperature for the primary phase, T_N, was found to be 615.4, 611.4 and 614.2°C for the NGM AlSi7Mg, COM AlSi7Mg and MHD A356 alloys respectively. The minimum temperature, T_{min}, during undercooling was 613.0, 614.9 and 608.4 °C, and the peak temperature, T_{peak}, was found to be 614.1, 615.3 and 609.0 °C for the NGM AlSi7Mg, COM AlSi7Mg and MHD A356 alloys respectively. The growth of the primary phase, T_{growth}, started at 615.6 °C for the NGM AlSi7Mg alloy, 616.2 °C for the COM AlSi7Mg alloy and at 611.3 °C for the MHD A356 alloy. The dendritic network coherency point, *TDCP*, where the growing dendrites impinge each other and the thickening of secondary arms begins, was established at temperatures of

615.6, 616.2 and 611.0 °C for the NGM AlSi7Mg, COM AlSi7Mg and MHD A356 alloys with time (see Table 4.1.2).

The eutectic phase nucleated (T_N) at 577.7, 562.6 and 567.3 °C for the NGM AlSi7Mg, COM AlSi7Mg and MHD A356 alloys respectively. The minimum temperature, T_{min}, was found to be 577.1, 561.6, and 564.5 °C and the peak temperature, T_{peak}, was 577.2, 561.7 and 564.5 °C for the NGM AlSi7Mg, COM AlSi7Mg and MHD A356 alloys respectively. The growth of the eutectic phase (T_{growth}) started at 577.8, 563.7 and 564.9 °C and eutectic growth finished (T_{finish}) at 541.5, 555.3 and 554.7 °C for the NGM AlSi7Mg, COM AlSi7Mg and MHD A356 alloys respectively (see Table 4.1.2).

The co-eutectic phase was observed over a temperature range of 555.3 to 541.1 °C for the COM AlSi7Mg alloy and 554.7 to 536.7 °C for the MHD A356 alloy. However, this phase was not observed in the NGM AlSi7Mg alloy (see Fig. 4.1.1(d) and Table 4.1.2).

4.1.4 DSC Analysis

Heat flow curves obtained for the NGM AlSi7Mg, COM AlSi7Mg and MHD A356 alloy samples were assessed with respect to solidification characteristics using a power compensation DSC apparatus. These DSC traces were processed by subtracting the zero line obtained for the heating and cooling of empty graphite pans with lids, over the whole processing temperature range under the same experimental conditions, as described in Section 3.3.3 (see Fig. 4.1.3(a)). At least three runs were processed for each sample to check the reproducibility and it was found that DSC traces were reproducible, as is illustrated in Fig. 4.1.3(b) for the NGM AlSi7Mg alloy samples on heating.

The endothermic and exothermic peaks observed in the DSC heating and cooling traces respectively, are shown for the NGM AlSi7Mg alloy in Fig. 4.1.4(a), for the COM AlSi7Mg alloy in Fig. 4.1.4(b) and for the MHD A356 alloy in Fig. 4.1.4(c).

The reproducibility and the temperature lag due to the applied heating and cooling rate can be observed in these DSC graphs.

In all cases, during heating, peak 1 is long, gradually rising and on reaching its maximum drops suddenly, while peak 2 is short and sharp. Peak 3 is visible only in the COM AlSi7Mg alloy and peak 4 is evident in all three alloys but only when the trace is analysed using the 1st derivative for the heat flow data with respect to temperature.

In the cooling curve both peak 1 and peak 2 are sharp for all three alloys. Peak 3 is relatively prominent both in the COM AlSi7Mg and MHD A356 alloys. Peak 4 can be seen in all alloys with the aid of the first derivative of the corresponding heat flow curves.

On heating the peak temperature was calculated as the intersection point of the extrapolated ascending and descending part of the peak with the local base line (see Section 2.6.2). For the measurement of the onset and offset of the peak, the following procedure was adopted. A tangent is drawn at the point on the DSC trace corresponding to the peak on the first derivative. A straight line is drawn locally between the start and end point of the peak as a base line. The intercept of the tangent with this line gives the onset or offset depending on the direction considered as discussed in Section 2.7.3 (see Fig. 4.1.3(c)). A similar procedure was applied for the DSC heat flow traces for cooling runs.

The onset, offset, peak temperatures and temperature range for each peak for both the heating and cooling runs of the DSC traces were calculated for all the samples for all three alloys and are given in Tables 4.1.3 - 4.1.9. In the following section average values (shown in Tables 4.1.10 - 4.1.13) were used for data analysis, discussion and comparison.

The calculated average values for peak 1 shown in the DSC heat flow traces in Fig. 4.1.4 for the heating and cooling runs, are given in Table 4.1.10. For the NGM AlSi7Mg alloy, on heating, peak 1 occurred in the temperature range 586.0 to 620.4 °C with 615.9 ± 0.5 °C the maximum peak temperature, 587.4 ± 0.9 °C the onset temperature and 618.4 ± 0.4 °C the offset temperature. For the COM AlSi7Mg

alloy this peak occurred in the temperature range 581.0 to 623.0 ℃ with 615.7 ± 0.5 ℃ the maximum peak temperature, 582.3 ± 1.1 ℃ the onset temperature and 620.6 ± 0.5 ℃ the offset temperature. While for the MHD A356 alloy peak 1 occurred in the temperature range 582.5 to 621.5 ℃ with 616.4 ± 2.0 ℃ the maximum peak temperature, 582.9 ± 0.5 ℃ the onset temperature and 619.8 ± 0.7 ℃ the offset temperature, during the heating run.

However, on cooling peak 1 is quite sharp in its shape. For the NGM AlSi7Mg alloy it occurred in the range of 564.8 to 610.1 ℃ with 605.7 ± 1.6 ℃ the maximum peak temperature, 603.3 ± 1.3 ℃ the onset temperature and 607.5 ± 2.3 ℃ the offset temperature. For the COM AlSi7Mg alloy this peak occurred in the temperature range from 567.9 to 615.2 ℃ with 611.4 ± 0.2 ℃ the maximum peak temperature, 606.4 ± 0.5 ℃ the onset temperature and 613.8 ± 0.4 ℃ the offset temperature. For the MHD A356 alloy this peak occurred in the temperature range 568.7 to 616.2 ℃ with 608.9 ± 2.1 ℃ the maximum peak temperature, 605.7 ± 1.5 ℃ the onset temperature and 611.2 ± 2.8 ℃ the offset temperature, in the cooling trace, as given in Table 4.1.10.

The calculated average temperature values for peak 2 for heating and cooling runs in the DSC heat flow shown in Fig 4.1.4 are given in Table 4.1.11. For the NGM AlSi7Mg alloy on heating, peak 2 occurred in the temperature range 569.6 to 588.4 ℃ with 582.4 ± 0.5 ℃ the maximum peak temperature, 577.0 ± 0.6 ℃ the onset temperature and 583.1 ± 0.4 ℃ the offset temperature. For the COM AlSi7Mg alloy this peak occurred in the temperature range 562.9 to 583.6 ℃ with 578.4 ± 0.7 ℃ the maximum peak temperature, 573.3 ± 1.1 ℃ the onset temperature and 579.5 ± 0.9 ℃ the offset temperature. While for the MHD A356 alloy, peak 2 occurred in the temperature range 562.6 to 564.2 ℃ with 579.0 ± 0.5 ℃ the maximum peak temperature, 574.6 ± 0.7 ℃ the onset temperature and 580.1 ± 0.8 ℃ the offset temperature, in the heating trace.

With respect to the cooling trace, for the NGM AlSi7Mg alloy peak 2 occurred in the temperature range 552.8 to 575.3℃ with 569.8± 0.5℃ the maximum peak temperature, 564.6 ± 0.7 ℃ the onset temperature and 574.0 ± 0.3 ℃ the offset temperature. For the COM AlSi7Mg alloy, this peak occurred in the temperature range 551.6 to 569.8℃ with 563.9 ± 0.7 ℃ the maximum peak temperature,

559.3 ± 1.2 °C the onset temperature and 567.1 ± 0.5 °C the offset temperature. For the MHD A356 alloy this peak occurred in the temperature range 552.4 to 569.6 °C with 562.9 ± 0.8 °C the maximum peak temperature, 559.7 ± 0.9 °C the onset temperature and 567.6 ± 0.7 °C the offset temperature, as given in Table 4.1.11.

The calculated average values for peak 3 for the DSC heat flow traces for heating and cooling runs are given in Table 4.1.12. On heating, peak 3 was only observed in the COM AlSi7Mg alloy. This peak occurred in the temperature range 559.4 to 563.3 °C with 562.2 ± 0.3 °C the maximum peak temperature, 561.2 ± 0.6 °C the onset temperature and 562.9 ± 0.1 °C the offset temperature, as given in Table 4.1.12.

However, in the cooling traces peak 3 was observed in the COM AlSi7Mg and MHD A356 alloys. For the COM AlSi7Mg alloy this peak occurred in the temperature range 541.2 to 552.0 °C with 548.2 ± 0.7 °C the maximum peak temperature, 544.2 ± 0.4 °C the onset temperature and 551.4 ± 0.4 °C the offset temperature in the cooling trace. For the MHD A356 alloy this peak occurred in the temperature range 540.9 to 552.8 °C with 549.2 ± 0.3 °C the maximum peak temperature, 545.3 ± 0.3 °C the onset temperature and 552.2 ± 0.3 °C the offset temperature, as given in Table 4.1.12.

The calculated average temperature values for peak 4 for the DSC heat flow traces for heating and cooling are given in Table 4.1.13. On heating, peak 4 can only be identified with the help of the 1st derivative. The small step on the 1st derivative curve corresponds to a slight kink in the actual curve. This peak is not clearly visible on the actual curve as it has been overlapped by peak 2. For the NGM AlSi7Mg alloy this peak occurred in the temperature range 573.4 to 577.4 °C. For the COM AlSi7Mg and the MHD A356 alloy this peak occurred in the temperature range 573.2 to 575.2 °C and from 573.9 to 575.7 °C, respectively as given in Table 4.1.13.

On cooling, peak 4 occurred in the temperature range 564.0 to 565.6 °C, 556.0 to 560.0 °C and 558.2 to 559.9 °C, for the NGM AlSi7Mg alloy, COM AlSi7Mg and MHD A356 alloys, respectively as given in Table 4.1.13.

4.1.5 Thermo-Calc® Simulation

Thermo-Calc® simulation software [211] using the TTAL5 database, which was specially developed for commercial Al-alloys, was used to predict and verify the formation of possible phases based on the Scheil equation. According to this Scheil simulation, for the NGM AlSi7Mg alloy the primary aluminium phase formation starts at 616.0 °C and the eutectic phase formation starts at 575.8 °C as shown in Fig. 4.1.5(a). The co-eutectic phase, *β-AlFeSi* phase, is supposed to form at 571.3 °C. The transformation of the *β-AlFeSi* to $AlFeMg_3Si_6$ and Mg_2Si phases may begin to occur at 560.5 and 556.2 °C respectively, although the amount of these phases may be negligible in practice and may not be observed experimentally (see Fig. 4.1.6(a)). The solidification process is completed at 555.5 °C, as given in Table 4.1.14.

For the COM AlSi7Mg alloy (see Fig. 4.1.5(b)), the primary aluminium phase starts to solidify at 616.5 °C and the eutectic phase will start to form at 573.8 °C. The prominent co-eutectic phase *β-AlFeSi* should form at 567.5 °C. The transformation of the *β-AlFeSi* to $AlFeMg_3Si_6$ alloy and formation of Mg_2Si should occur at 561.2 °C and 556.8 °C respectively. These phases can readily be observed in this alloy compared to the NGM AlSi7Mg alloy (see Fig. 4.1.6(b)). The solidification is completed at 556.2 °C, as given in Table 4.1.14.

For the MHD A356 alloy (see Fig. 4.1.5(c)), the primary aluminium phase starts to solidify at 614.0 °C and the eutectic phase will start to form at 574.8 °C. The prominent co-eutectic phase *β-AlFeSi* may form at 568.6 °C. However, transformation of the *β-AlFeSi* to $AlFeMg_3Si_6$ in the alloy and formation of Mg_2Si may occur at 561.0 °C and 557.0 °C respectively. These phases are more prominent in this alloy as compared to the NGM AlSi7Mg alloy (see Fig. 4.1.6(c)). The solidification is completed at 556.2 °C, as given in Table 4.1.14.

4.1.6 Microscopy

The NGM AlSi7Mg, COM AlSi7Mg and MHD A356 alloys, both in the as-received and as-cast state, were examined using optical and electron microscopy techniques to analyse their characteristic microstructures. As-polished optical micrographs of the

three alloys, in the as-received state (see Fig. 4.1.7) revealed α–Al grains surrounded by a small fine eutectic. The *α*–Al grains displayed a dendritic morphology and the eutectic was observed in the interdendritic regions. The micrographs of the COM AlSi7Mg (see Fig 4.1.7(b)) and MHD A356 (see Fig 4.1.7(c)) alloys appear to very similar with the α–Al grains having DAS ~ 20 – 30 μm. However, the NGM AlSi7Mg alloy shows a smaller α-Al (DAS ~ 5 – 10 μm) grain size and marginally coarser eutectic. In all the as-received samples no intermetallic phases could be readily observed.

Examining the three alloys in the as-cast state, (see Fig 4.1.8) a dramatic effect on the eutectic is apparent. This eutectic displays a more needle-like acicular structure. The eutectic is so coarse that it is difficult to discern the dendritic nature of the α-Al grains especially within the NGM AlSi7Mg alloy (see Fig. 4.1.8(a)).

A closer inspection of the interdendritic regions in the as-cast samples revealed the presence of intermetallic phases. In the NGM AlSi7Mg alloy two different phases were observed. These phases were similar in size, shape and appearance to phases described in the literature [297, 307]. They include a *β-AlFeSi* plate-like phase (see Fig. 4.1.9(a), 4.1.9(c)) and a *π-AlFeMgSi* phase (see Fig. 4.1.9(b), 4.1.9(c)).

These two phases were also observed in the COM AlSi7Mg alloy exhibiting a similar size and morphology (see Fig. 4.1.10(a), 4.1.10(b)). In addition a chineses-script-like Mg_2Si phase was also evident (see Fig. 4.1.10(c)). These three phases were also evident in the as-cast MHD A356 alloy (see Fig. 4.1.11) again displaying a similar size and morphology to those in the NGM AlSi7Mg and COM AlSi7Mg alloys.

To confirm the compositions of the phases observed, SEM equipped with EDX was employed. Using BSD with Z-contrast intermetallic phases were observed in the as-received alloys (see Fig 4.1.12). In general for all the three alloys, the intermetallic phases were < 10 μm and randomly distributed in interdendritic regions.

Intermetallic phases in the as-received NGM AlSi7Mg alloy displayed a long plate-like morphology. EDX analyses from these particles showed the presence of Al, Si, Mg and Fe (see Fig. 4.1.13). These elements were proven to be related by elemental mapping (see Fig. 4.1.14). Typical compositions from the EDX spot results indicate

Al 78.95 at%, Si 12.92 at%, Mg 5.63 at%, and Fe 2.49 at% suggesting a *π-AlFeMgSi* phase. No other co-eutectic phases were observed.

EDX spot analyses also showed that this Al-Si-Mg-Fe phase was also present in the COM AlSi7Mg alloy and was of a similar size and shape (see Fig. 4.1.15). In addition Ti rich particles were also observed indicative of heterogeneous particles added for grain refinement (see Fig. 4.1.16). Elemental mapping revealed that the Ti had no association with Fe, Si and Mg as shown in Fig. 4.1.17.

The as-received MHD A356 alloy again showed the presence of the Al-Fe-Si-Mg phase (see Fig. 4.1.18) displaying a similar size and morphology to that observed in the NGM AlSi7Mg and COM AlSi7Mg alloys. In addition spherical and star-like particles, approximately 5 μm in size, were found. EDX spot analyses from these, revealed Sr, Al, Si and Mg as shown in Figs. 4.1.19 and 4.1.20. The presence of Sr containing particles showed that the alloy was modified.

SEM analyses were also conducted on the as-cast alloys. Results for the NGM AlSi7Mg alloy revealed: a needle/lath-like phase approximately 2 – 5 μm (see Fig. 4.1.21(a)) in width and 100 μm in length with EDX spot analyses indicating an Al-Fe-Si-Mn phase (see Fig 4.1.22); and a non-faceted phase ~ 1 – 40 μm in size (see Fig. 4.1.21(a)) with EDX spot analyses indicating Sn-Al-Mg phase as shown in Fig. 4.1.23. Elemental mapping confirmed both these phases (see Fig. 4.1.24). Results for the as-cast COM AlSi7Mg alloy revealed two phases; a needle-like phase ~ < 50 μm long and < 5 μm wide (see Fig. 4.1.21(b)), with EDX spot analyses indicating an Al-Si-Fe-Mg phase (see Fig. 4.1.25); and a deformed non-faceted phase ~ < 50 μm in size (see Fig. 4.1.21(b)) with EDX spot analyses indicating an Al-Fe-Si phase (see Fig. 4.1.26). The elemental composition was confirmed for both phases by elemental mapping (see Fig. 4.1.27).

In the as-cast MHD A356 alloy four phases were evident: a needle/lath–like phase ~ < 200 μm in length and ~ < 5 μm in width (see Fig. 4.1.21(c)) which EDX spot analyses indicated was an Al-Fe-Si phase (see Fig. 4.1.28); a phase with Chinese script-like morphology, < 20 μm in size (see Fig. 4.1.21(c)) which elemental mapping showed to be a Mg-Si phase (see Fig. 4.1.29); a network-like phase < 30 μm in size (see Fig. 4.1.21(c)) which EDX spot analyses indicated was Al-Fe-Si-Mg (see

Fig. 4. 1.30) and spherical shaped particles ~ 5 μm in diameter (see Fig. 4.1.21(c)) which EDX spot analyses indicated were Sr and Pb phases (see Fig. 4.1.31 and 4.1.32). Elemental mapping was again used to confirm elements within the phases (see Figs. 4.1.21(c), 4.1.33, and 4.1.34).

4.1.7 Summary

From the chemical composition, cooling curve, DSC and Thermo-Calc® data the results can be summarised as follows:

1. The NGM AlSi7Mg alloy showed a lower solidification temperature (615.5 °C for cooling curve and 607.5 °C for the DSC traces) compared (616.2 °C for cooling curve and 613.8 °C for DSC traces) for the COM AlSi7Mg alloy. This is in spite of having a lower Si and Mg content (7.02 wt% Si and 0.16 wt% Mg compared to 7.06 wt% Si and 0.39 wt% Mg), although in theory it should be higher as predicted by Thermo-Calc® (616.0 °C as compared to 615.5 °C) and by the use of empirical formula (615.6 °C compared to 614.3 °C). This anomaly may be due to the absence of grain refinement.
2. The solidification temperature for the MHD A356 alloy was lower than the NGM AlSi7Mg for all measurements due to the higher Si and Mg content (7.40 wt% Si and 0.33 wt% Mg).
3. The eutectic temperature for the NGM AlSi7Mg alloy was considerably higher than the COM AlSi7Mg alloy for the cooling curves (577.8 °C compared to 563.7 °C) compared to the DSC traces (577.0 °C compared to 573.3 °C on heating) and Thermo-Calc® simulations (575.8 °C compared to 573.8 °C).
4. In the NGM AlSi7Mg alloy only one co-eutectic reaction was observed as compared to two co-eutectic reactions each for the COM AlSi7Mg and MHD A356 alloys due to the very low Mg content.

From the optical and SEM investigations of the as-received and as-cast samples the phases formed could be investigated resulting in the following:

1. In the as-received samples the NGM AlSi7Mg alloy contained a *π-AlMgFeSi* co-eutectic intermetallic phase similar to the other two as-received alloys. In

addition, the COM AlSi7Mg alloy also contained Ti particles and the MHD A356 alloy contained Sr particles indicating refinement and modification, respectively

2. In the as-cast samples, the NGM AlSi7Mg alloy indicated the presence of a β-AlFeSi phase and Sn particles, whilst the COM AlSi7Mg alloy showed *π-AlMgFeSi*, *β-AlFeSi* and Mg_2Si phases and the MHD A356 alloy showed Sr and Pb particles in addition to the phases found in the COM AlSi7Mg alloy.
3. DSC heat flow data for the cooling cycle and their corresponding Thermo-Calc® simulations indicated that a very small amount of *π-AlMgFeSi* phase may also form in the NGM AlSi7Mg alloy, however it was not observed in the as-cast samples.

4. 1.8 Tables

Table 4.1.1: Chemical Composition of Alloys (wt%).

Alloy	%Si	%Mg	%Fe	%Cu	%Mn	%Cr	%Ni	%Zn	%Pb	%Sn	%Ti
NGM AlSi7Mg	7.02	0.16	0.09	0.005	<0.005	<0.005	<0.005	<0.005	<0.01	<0.01	0.006
COM AlSi7Mg	7.06	0.39	0.11	0.010	0.007	<0.005	<0.005	<0.005	<0.01	<0.01	0.130
MHD A356	7.40	0.33	0.11	0.004	<0.005	<0.005	<0.005	<0.005	<0.01	<0.01	0.110

Table 4.1.2: Temperatures obtained from cooling curve data obtained at a pouring temperature ~ 820 ℃.

	Primary Phase				*TDCP*
	T_N (℃)	T_{min} (℃)	T_{peak} (℃)	T_{growth} (℃)	(℃)
NGM AlSi7Mg	629.8	613.0	614.1	615.6	615.6
COM AlSi7Mg	624.0	614.9	615.3	616.2	616.2
MHD A356	622.8	608.4	609.0	611.3	611.0

	Eutectic Phase					Co-eutectic Phase
	T_N (℃)	T_{min} (℃)	T_{peak} (℃)	T_{growth} (℃)	T_{finish} (℃)	(℃)
NGM AlSi7Mg	577.7	577.1	577.2	577.8	541.5	-
COM AlSi7Mg	562.6	561.6	561.7	563.7	555.3	555.3 - 541.1
MHD A356	567.3	564.5	564.5	564.9	554.7	554.7 - 536.7

Table 4.1.3: Calculated temperature values for peak 1 during heating from the DSC Heat Flow traces (shown in Fig. 4.1.4).

Alloy	Sample	Range (℃)	Onset (℃)	Peak (℃)	Offset (℃)
NGM AlSi7Mg	1	588.4 - 620.4	588.4	616.5	618.7
	2	587.0 - 618.9	587.0	615.5	617.9
	3	586.8 - 619.5	586.8	615.9	618.5
COM AlSi7Mg	1	582.3 - 621.7	582.3	615.2	621.1
	2	583.6 - 621.3	583.6	616.2	620.3
	3	582.3 - 623.0	582.3	615.4	620.7
	4	581.0 - 621.5	581.0	616.2	620.1
MHD A356	1	583.6 - 620.1	583.6	615.5	619.0
	2	582.8 - 620.9	582.8	614.0	619.5
	3	582.6 - 621.4	582.6	617.9	620.4
	4	582.5 - 621.5	582.5	618.1	620.3

Table 4.1.4: Calculated temperature values for peak 1 during cooling from the DSC Heat Flow traces (shown in Fig 4.1.4).

Alloy	Sample	Range (℃)	Onset (℃)	Peak (℃)	Offset (℃)
NGM AlSi7Mg	1	575.3 - 605.8	601.9	603.9	604.9
	2	564.8 - 609.9	603.9	606.8	608.8
	3	574.8 - 610.1	604.2	606.3	608.8
COM AlSi7Mg	1	568.0 - 615.2	604.9	611.6 (610.5, 611.6)*	614.3
	2	567.9 - 614.8	602.6	611.4	613.8
	3	569.8 - 615.0	606.1	611.6	613.6
	4	568.9 - 614.8	606.7	611.1	613.5
MHD A356	1	569.6 - 613.3	604.6	607.7 (608.6)*	610.7
	2	569.4 - 608.7	604.3	606.7	607.5
	3	568.7 - 615.7	606.9	610.1	613.2
	4	568.8 - 616.2	607.2	611.2	613.5

* shows the value of overlapping peak

Table 4.1.5: Calculated temperature values for peak 2 during heating from the DSC Heat Flow traces (shown in Fig 4.1.4).

Alloy	Sample	Range (℃)	Onset (℃)	Peak (℃)	Offset (℃)
NGM AlSi7Mg	1	570.0 - 588.4	577.6	583.0	582.6
	2	569.6 - 587.0	577.0	582.2	583.4
	3	569.9 - 586.8	576.5	582.1	583.2
COM AlSi7Mg	1	562.9 - 582.3	573.0	578.6	579.8
	2	563.1 - 583.6	574.8	579.3	580.4
	3	563.3 - 582.3	572.8	578.0	579.5
	4	563.3 - 581.0	572.4	577.8	578.3
MHD A356	1	564.2 - 583.6	575.3	579.7	581.3
	2	562.6 - 582.8	575.0	578.8	579.7
	3	562.7 - 582.6	574.4	578.8	579.6
	4	562.8 - 582.5	573.8	578.7	579.8

Table 4.1.6: Calculated temperature values for peak 2 during cooling from the DSC Heat Flow traces (shown in Fig 4.1.4).

Alloy	Sample	Range (℃)	Onset (℃)	Peak (℃)	Offset (℃)
NGM AlSi7Mg	1	554.3 - 575.3	565.1	570.1 (571.7)*	574.4
	2	5532 - 574.8	563.8	569.2 (568.3, 571.0)*	573.9
	3	552.8 - 574.8	564.8	569.9 (569.1, 571.)*	573.9
COM AlSi7Mg	1	552.0 – 568.0	558.2	563.2	566.8
	2	551.8 - 567.9	558.5	563.4	566.7
	3	551.6 - 569.8	560.7	564.7	567.7
	4	551.7 - 568.9	559.9	564.3	567.2
MHD A356	1	552.4 - 569.6	560.0	564.1 (565.4)*	568.7
	2	552.8 - 569.6	560.5	562.6	567.4
	3	552.6 - 568.7	558.4	562.3	567.2
	4	552.6 - 568.8	559.9	562.7	567.2

* shows the value of overlapping peak

Table 4.1.7: Calculated temperature values for peak 3 during heating from the DSC Heat Flow traces (shown in Fig 4.1.4).

Alloy	Sample	Range (℃)	Onset (℃)	Peak (℃)	Offset (℃)
NGM AlSi7Mg	1				
	2				
	3				
COM AlSi7Mg	1	559.4 - 562.3	561.5	562.3	562.8
	2	559.7 - 563.2	561.8	562.5	563.1
	3	560.0 - 563.3	560.8	562.0	562.9
	4	560.1 - 563.3	560.6	562.0	562.8
MHD A356	1				
	2				
	3				
	4				

Table 4.1.8: Calculated temperature values for peak 3 during cooling from the DSC Heat Flow traces (shown in Fig 4.1.4).

Alloy	Sample	Range (℃)	Onset (℃)	Peak (℃)	Offset (℃)
NGM AlSi7Mg	1				
	2				
	3				
COM AlSi7Mg	1	541.9 – 552.0	544.5	548.8	551.8
	2	542.0 - 551.8	544.6	548.8	551.7
	3	541.9 - 551.6	543.9	547.4	551.1
	4	541.2 - 551.7	544.0	547.9	551.3
MHD A356	1	540.9 - 552.4	545.7	548.9	552.1
	2	541.3 - 552.8	545.4	549.6	552.5
	3	542.7 - 552.6	545.2	549.2	552.4
	4	541.9 - 552.6	544.9	549.2	551.8

Table 4.1.9: Calculated temperature values for peak 4 from the DSC Heat Flow traces.

Alloy	Sample	Heating	Cooling
		Range (℃)	Range (℃)
NGM AlSi7Mg	1	574.6 - 577.4	565.1 - 565.6
	2	573.4 - 576.5	564.0 - 564.6
	3	574.0 - 576.4	564.5 - 565.5
COM AlSi7Mg	1	573.5 - 574.5	556.8 - 557.6
	2	574.2 - 575.2	556.0 - 556.7
	3	573.6 - 574.4	558.7 – 560.0
	4	573.2 - 574.1	558.4 - 559.3
MHD A356	1	574.7 - 575.7	559.3 - 559.9
	2	573.9 - 574.6	558.6 - 559.2
	3	574.2 - 574.9	558.2 - 558.9
	4	574.0 - 575.0	558.5 - 559.2

Table 4.1.10: Average temperature values obtained from data in tables 4.1.3 and 4.1.4 for peak 1 calculated from the DSC Heat Flow traces (shown in Fig 4.1.4).

		Temperature ℃			
	Alloy	Range	Onset	Peak	Offset
Heating	NGM AlSi7Mg	586.0 - 620.4	587.4 ± 0.9	615.9 ± 0.5	618.4 ± 0.4
	COM AlSi7Mg	581.0 - 623.0	582.3 ± 1.1	615.7 ± 0.5	620.6 ± 0.5
	MHD A356	582.5 - 621.5	582.9 ± 0.5	616.4 ± 2.0	619.8 ± 0.7
Cooling	NGM AlSi7Mg	564.8 - 610.1	603.3 ± 1.3	605.7 ± 1.6	607.5 ± 2.3
	COM AlSi7Mg	567.9 - 615.2	606.4 ± 0.5	611.4 ± 0.2	613.8 ± 0.4
	MHD A356	568.7 - 616.2	605.7 ± 1.5	608.9 ± 2.1	611.2 ± 2.8

Table 4.1.11: Average temperature values obtained from data in tables 4.1.5 and 4.1.6 for peak 2 calculated from the DSC Heat Flow traces (shown in Fig 4.1.4).

		Temperature ℃			
	Alloy	Range	Onset	Peak	Offset
Heating	NGM AlSi7Mg	569.6 - 588.4	577.0 ± 0.6	582.4 ± 0.5	583.1 ± 0.4
	COM AlSi7Mg	562.9 - 583.6	573.3 ± 1.1	578.4 ± 0.7	579.5 ± 0.9
	MHD A356	562.6 - 564.2	574.6 ± 0.7	579.0 ± 0.5	580.1 ± 0.8
Cooling	NGM AlSi7Mg	552.8 - 575.3	564.6 ± 0.7	569.8 ± 0.5	574.0 ± 0.3
	COM AlSi7Mg	551.6 - 569.8	559.3 ± 1.2	563.9 ± 0.7	567.1 ± 0.5
	MHD A356	552.4 - 569.6	559.7 ± 0.9	562.9 ±0.8	567.6 ± 0.7

Table 4.1.12: Average temperature values obtained from data in tables 4.1.7 and 4.1.8 for peak 3 calculated from the DSC Heat Flow traces (shown in Fig 4.1.4).

		Temperature ℃			
	Alloy	Range	Onset	Peak	Offset
Heating	NGM AlSi7Mg	-	-	-	-
	COM AlSi7Mg	559.4 - 563.3	561.2 ± 0.6	562.2 ± 0.3	562.9 ± 0.1
	MHD A356	-	-	-	-
Cooling	NGM AlSi7Mg	-	-	-	-
	COM AlSi7Mg	541.2 - 552.0	544.2 ± 0.4	548.2 ± 0.7	551.4 ± 0.4
	MHD A356	540.9 - 552.9	545.3 ± 0.3	549.2 ± 0.3	552.2 ± 0.3

Table 4.1.13: Average temperature values obtained from data in table 4.1.9 for peak 4 calculated from the DSC Heat Flow traces (shown in Fig 4.1.4).

Alloy	Temperature ℃	
	Heating Range	Cooling Range
NGM AlSi7Mg	573.4 - 577.4	564.0 - 565.6
COM AlSi7Mg	573.2 - 575.2	556.0 - 560.0
MHD A356	573.9 - 575.7	558.2 - 559.9

Table 4.1.14: Phase formation temperature (℃) as obtained from Thermo-Calc® Simulation.

Alloy	Primary Phase	Binary eutectic	Ternary eutectic with *β-Al_5FeSi*	Ternary eutectic with *π-$Al_8Mg_3FeSi_6$*	Quaternary eutectic with *π-$Al_8Mg_3FeSi_6$* and *Mg_2Si*	End of solidification
NGM AlSi7Mg	616	575.8	571.3	560.5	556.2	555.5
COM AlSi7Mg	616.5	573.8	567.5	561.2	556.8	556.2
MHD A356	614.0	574.8	568.6	561.0	557.0	556.2

4.1.9 Figures

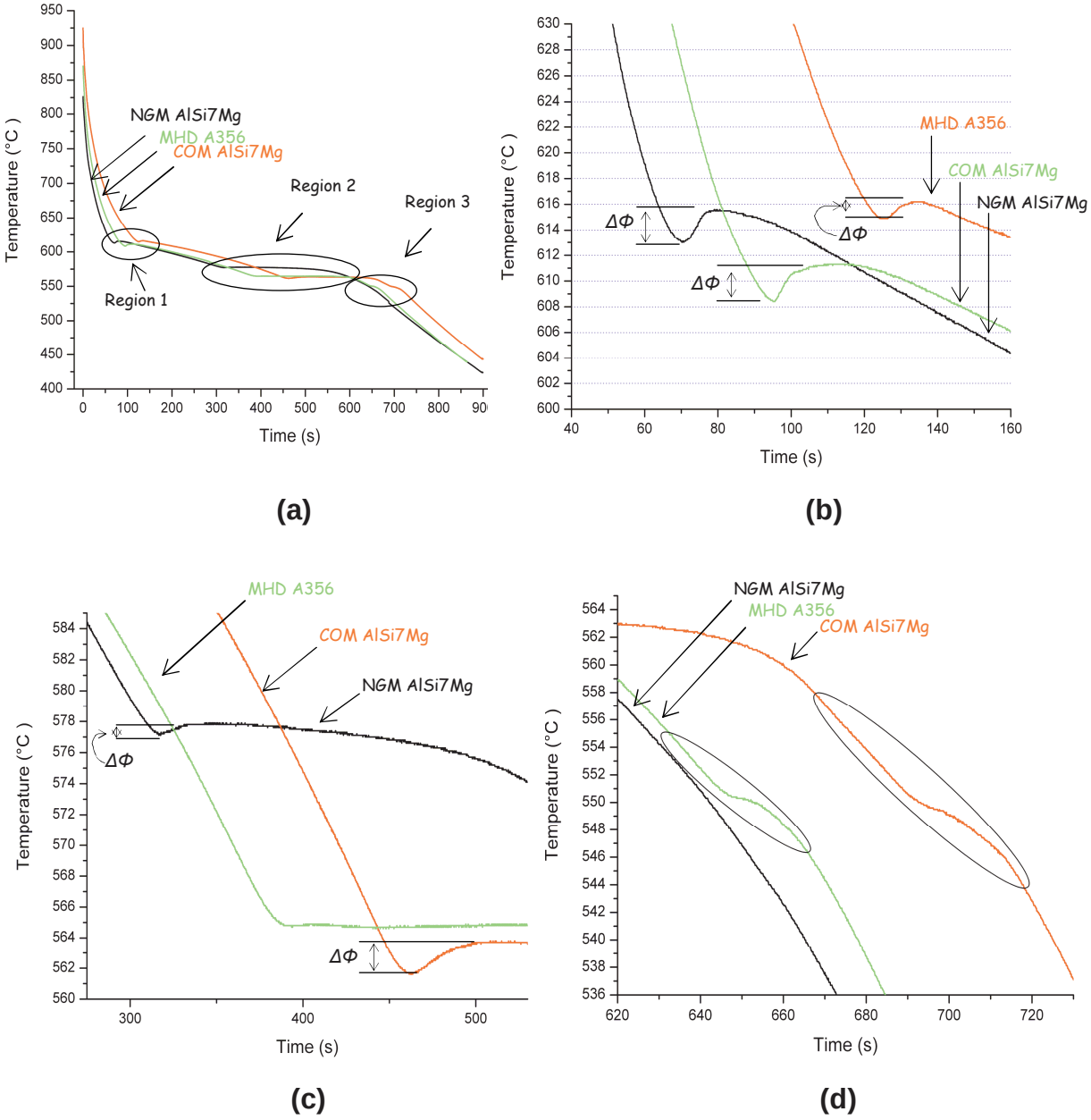

Fig. 4.1.1: The cooling curves for the alloys poured at 820 °C: (a) cooling curves showing three distinct regions; (b) elaborated region 1 showing recalescence ($\Delta\Phi$) for primary phase; (c) elaborated region 2, showing recalescence for binary eutectic phase; and, (d) elaborated region 3 showing co-eutectic phase transformation.

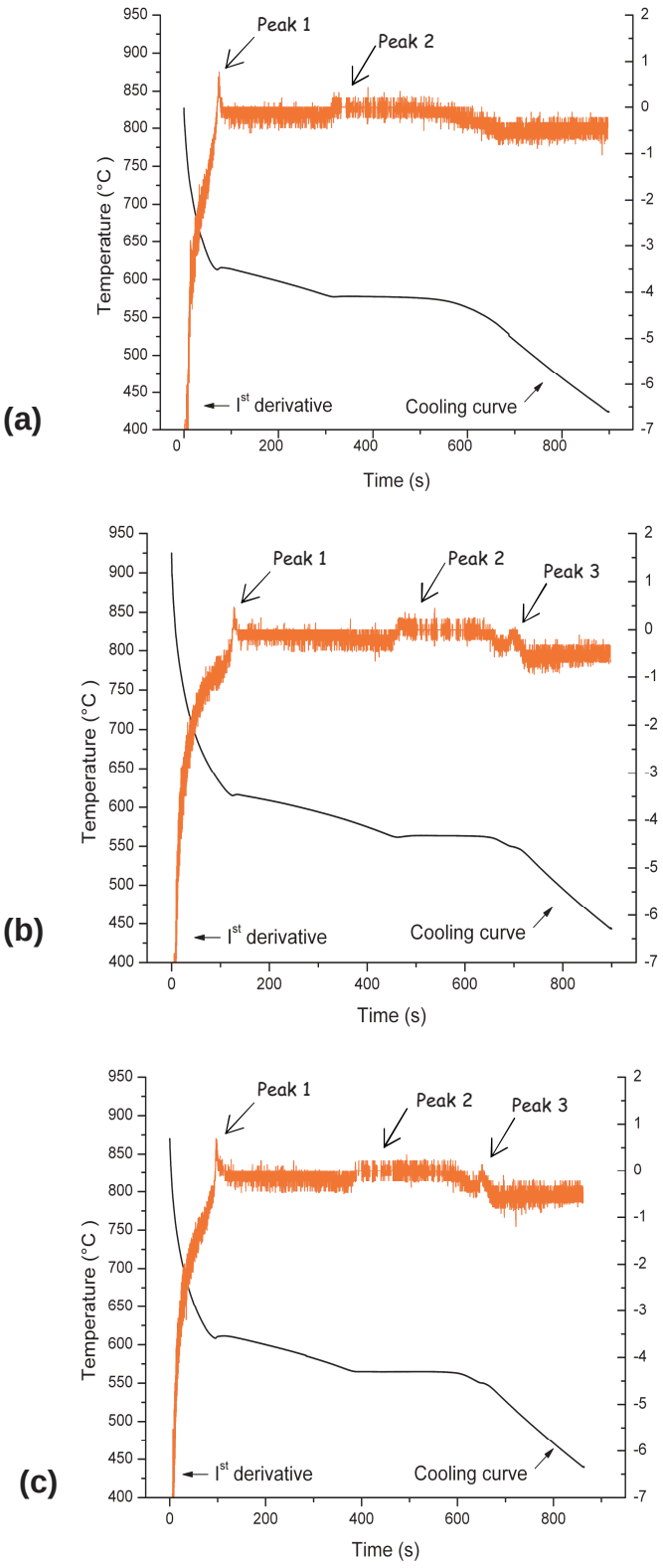

Fig. 4.1.2: The cooling curve and its first derivative for: (a) the NGM AlSiMg alloy; (b) the COM AlSi7Mg alloy; and, (c) the MHD A356 alloy, poured at 820 °C. Figures also show the chracteristic peaks on the 1st derivative curve.

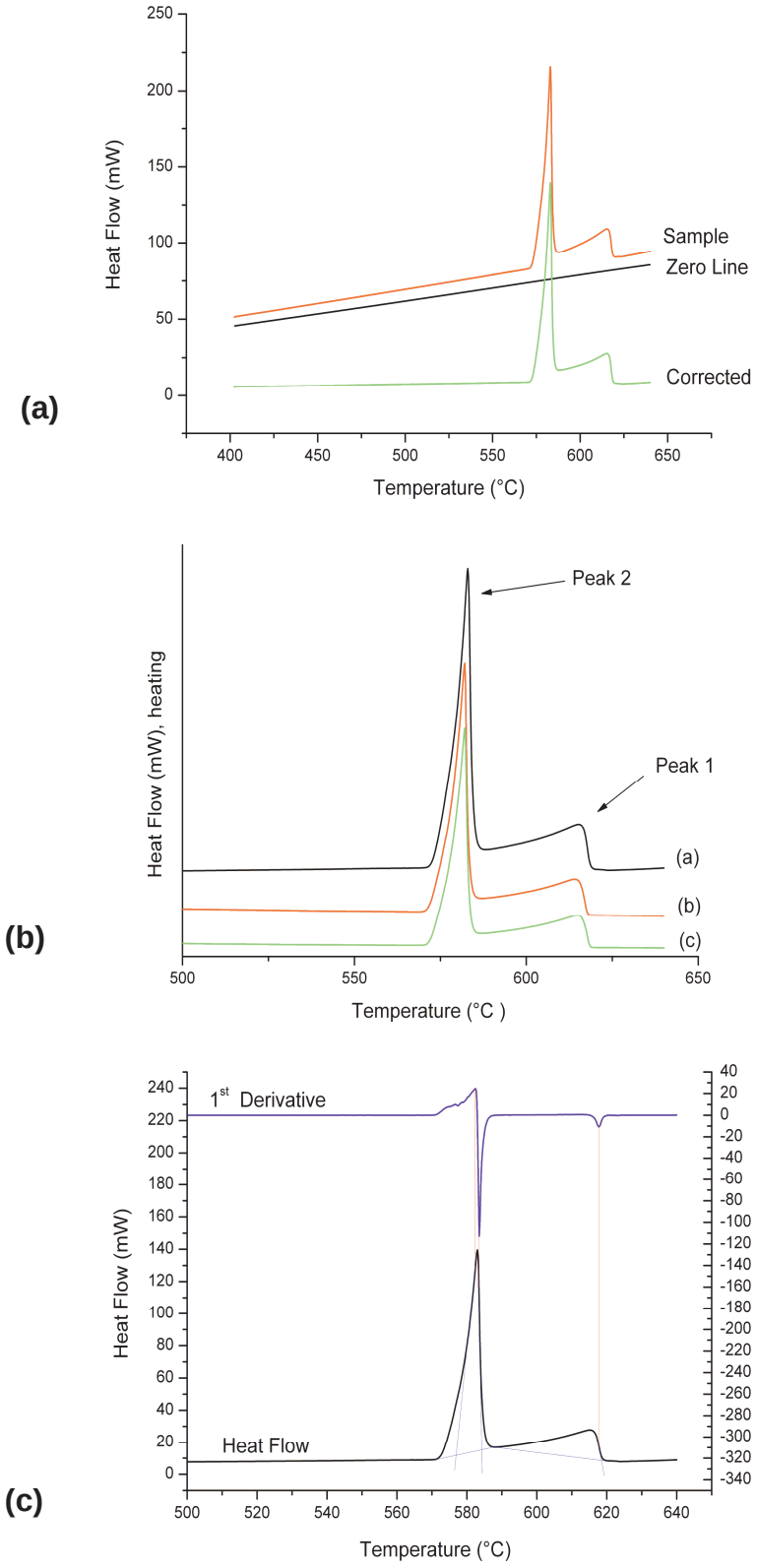

Fig. 4.1.3: DSC heat flow data: (a) DSC heat flow curve as measured and corrected; (b) reproducibility of DSC heat flow data for different samples of the NGM AlSi7Mg alloy; and, (c) estimation of characteristic data for a phase transformation from the DSC heat flow data.

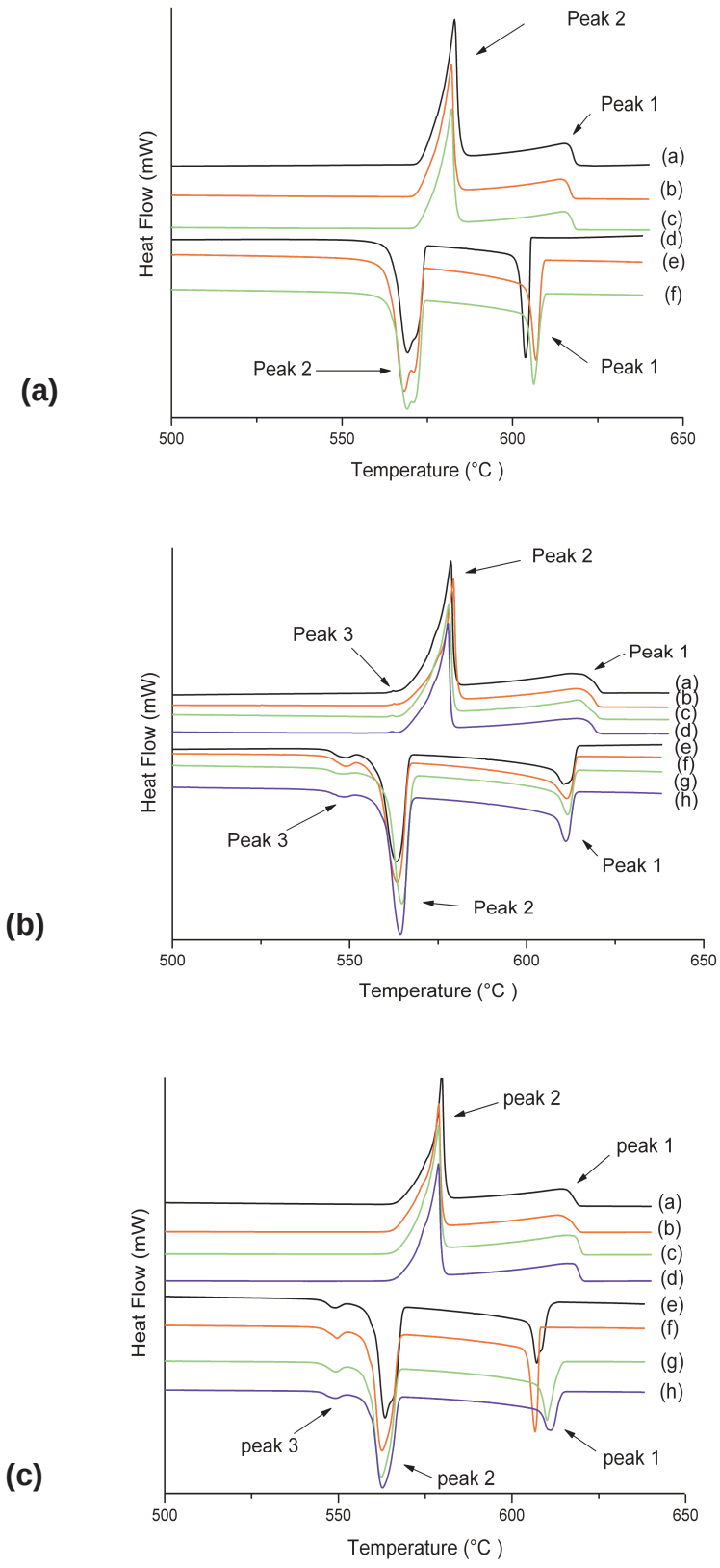

Fig. 4.1.4: Comparison and reproducibility of DSC heat flow data for heating and cooling runs in: (a) the NGM AlSi7Mg alloy; (b) the COM AlSi7Mg alloy: and, (c) the MHD A356 alloy.

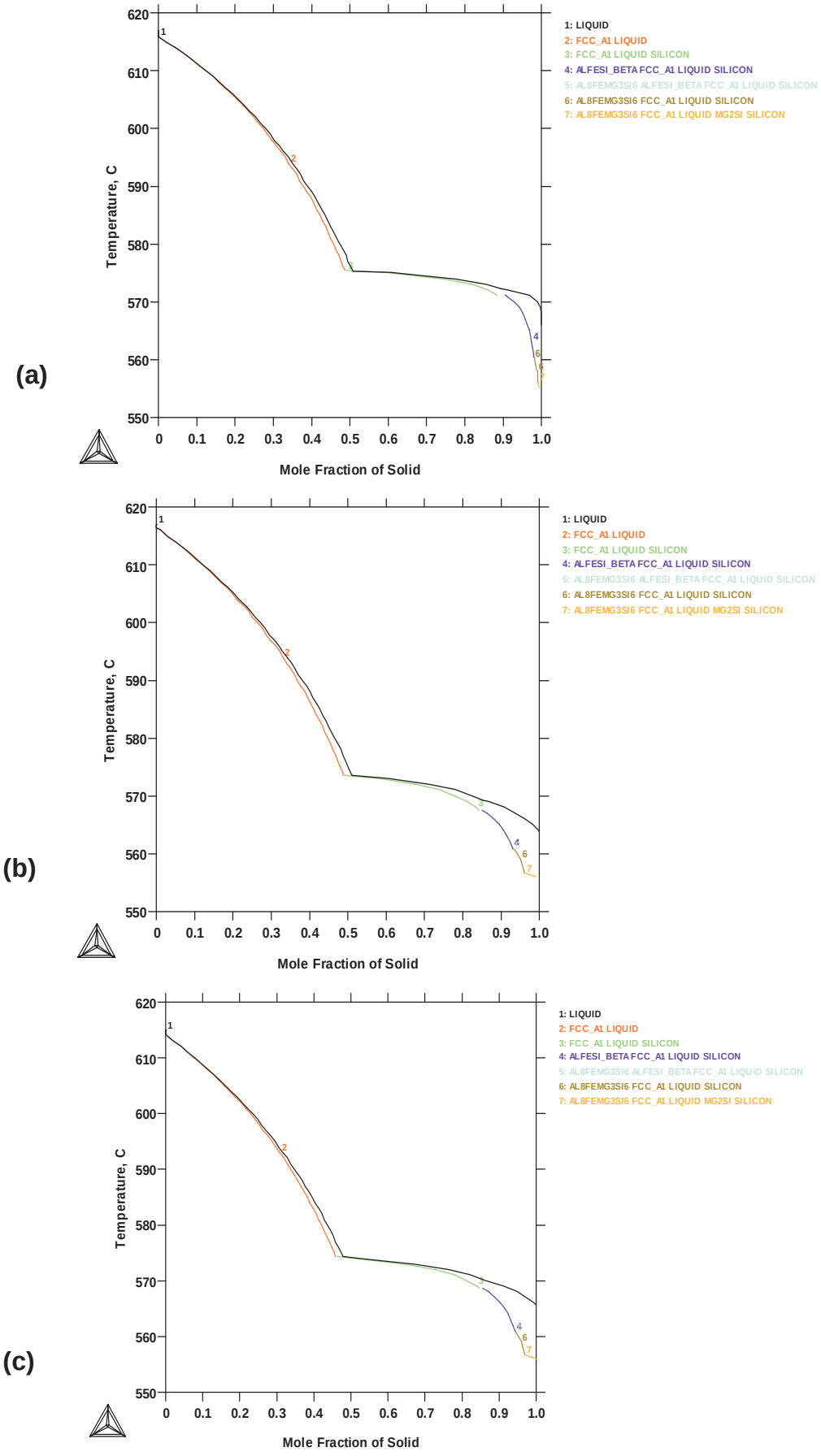

Fig. 4.1.5: The mole fraction solid and sequence of solidification reactions with respect to a decrease in temperature for: (a) the NGM AlSi7Mg alloy; (b) the COM AlSi7Mg alloy; and, (c) the MHD A356 alloy, simulated by the Scheil simulation module using Thermo-Calc ® software.

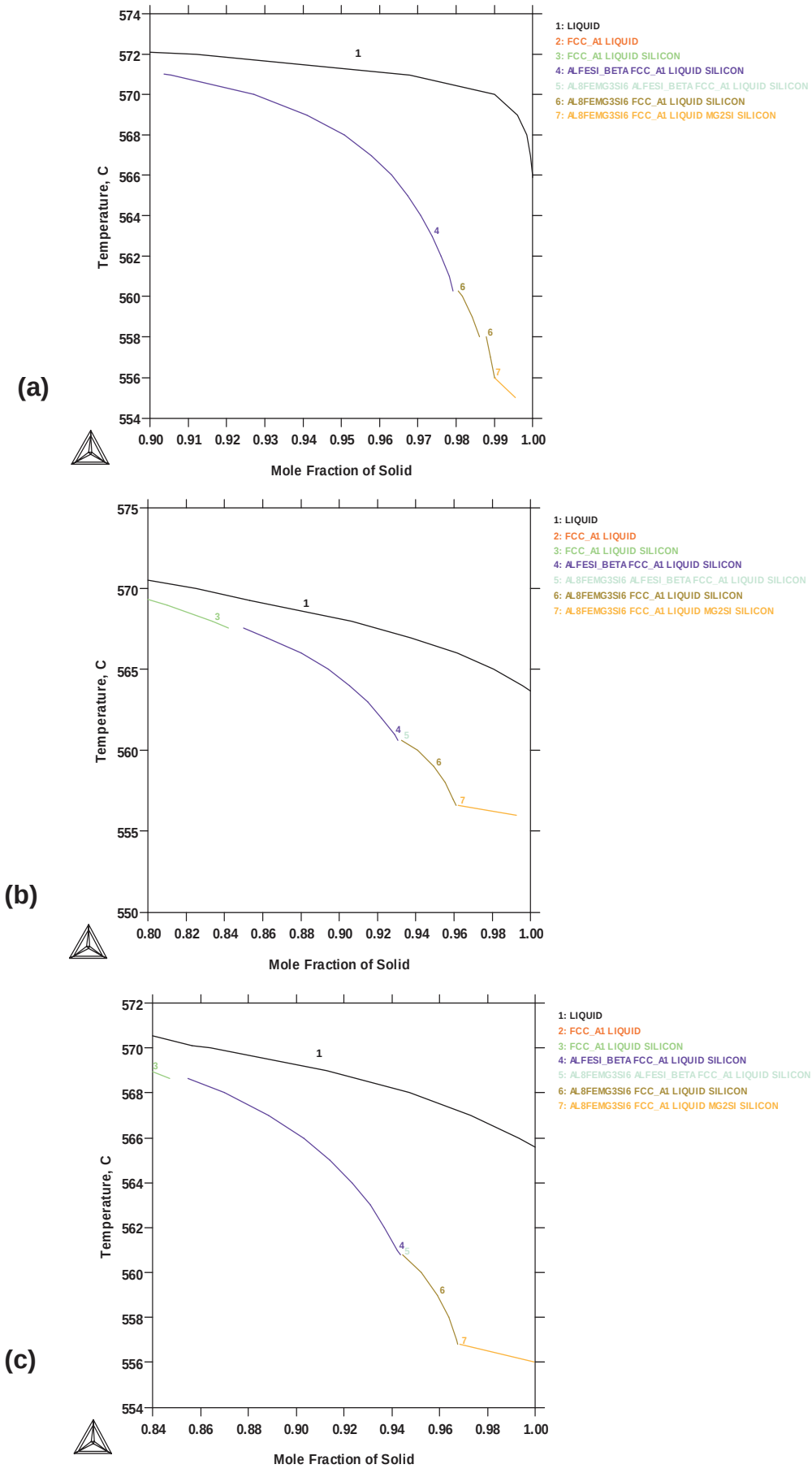

Fig. 4.1.6: Enlarged view of right hand side of the corresponding Figs. shown in Fig. 4.5 enabling a comparison of the co-eutectic phases for: (a) the NGM AlSi7Mg alloy; (b) the COM AlSi7Mg alloy; and, (c) the MHD A356 alloy.

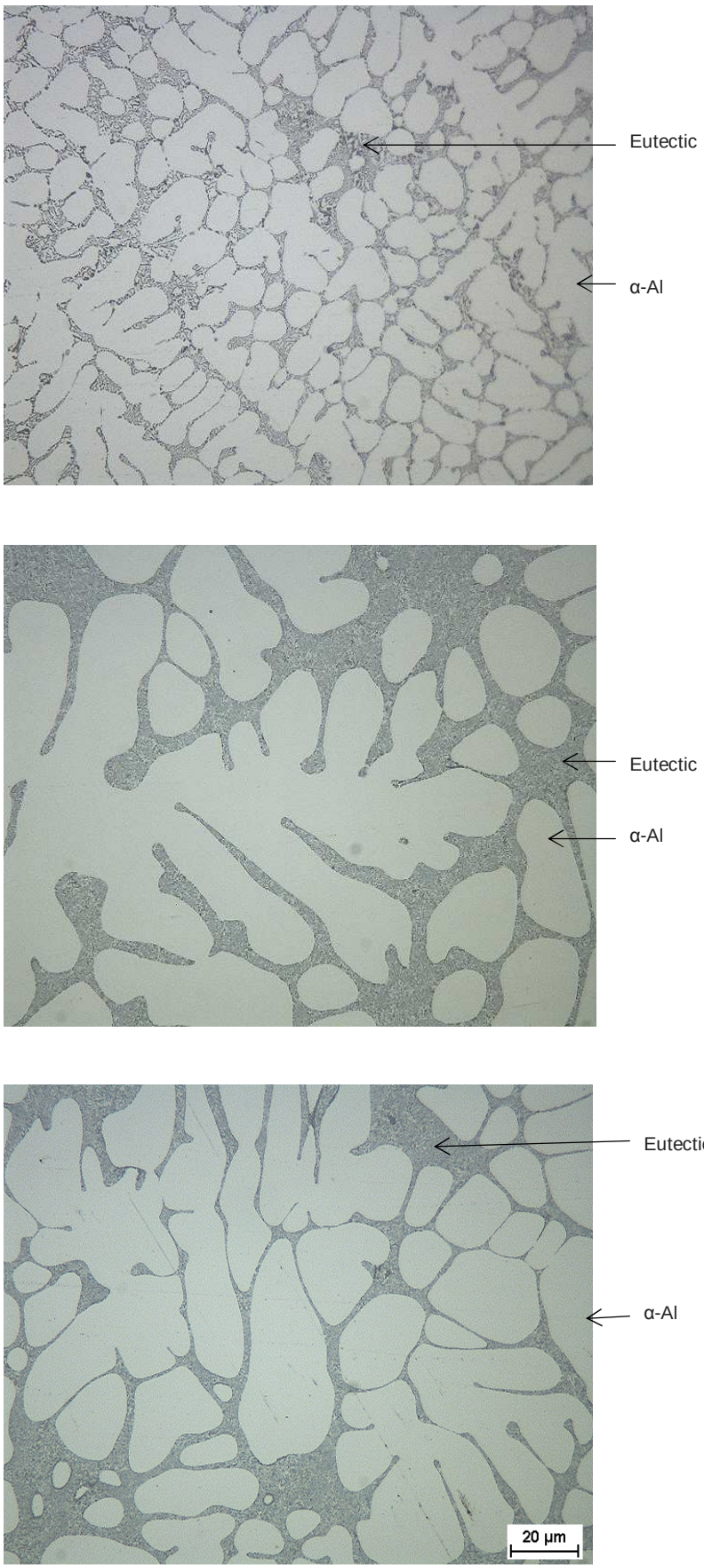

Fig. 4.1.7: Bright field optical micrographs of the as-received alloys showing different phases; bright area shows the primary phase and gray area shows the eutectic phase in: (a) the NGM AlSi7Mg alloy; (b) the COM AlSi7Mg; and, (c) the MHD A356 alloy.

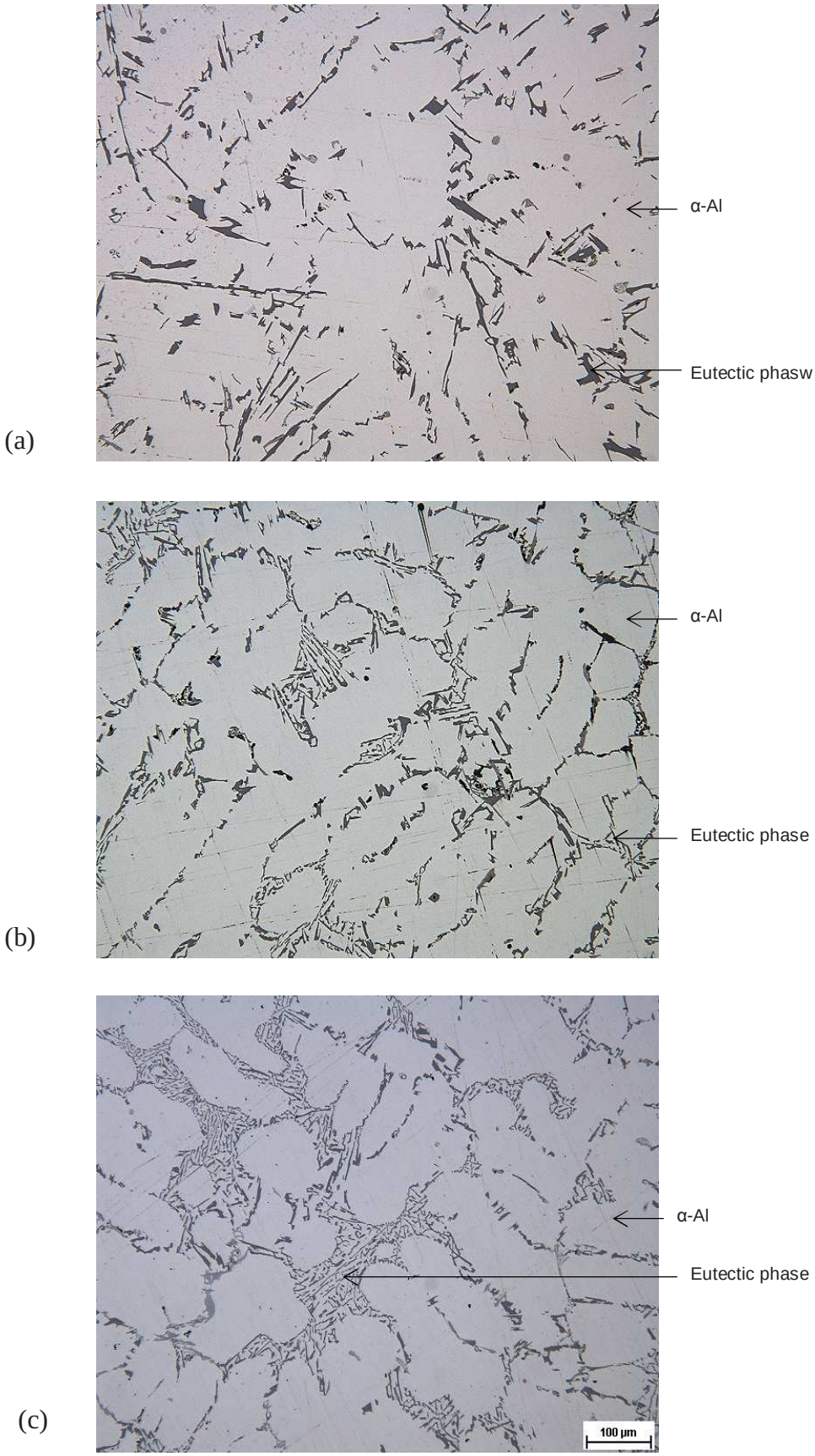

Fig. 4.1.8: Bright field optical micrographs of the as-cast alloys showing different phases; bright area shows the primary phase and gray area shows the eutectic phase in: (a) the NGM AlSi7Mg alloy; (b) the COM AlSi7Mg; and, (c) the MHD A356 alloy.

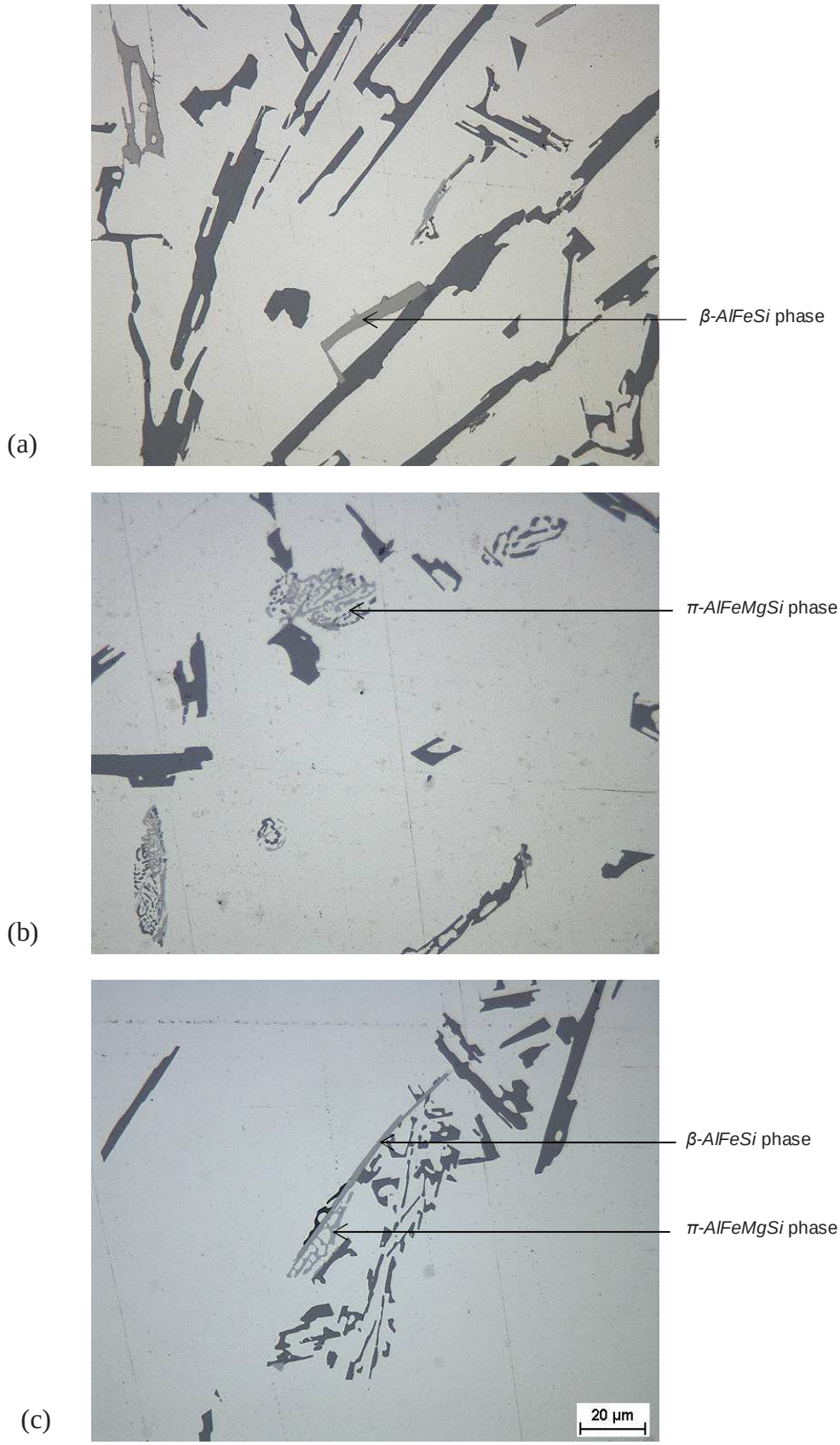

Fig. 4.1.9: Bright field optical micrographs of the as-cast NGM AlSi7Mg alloy showing different intermetallic phases: (a) the light gray plate-like *β-AlFeSi*; (b) nest-like *π – AlFeMgSi* phase; and, (c) co-existing *β-AlFeSi* and *π –AlFeMgSi* phases.

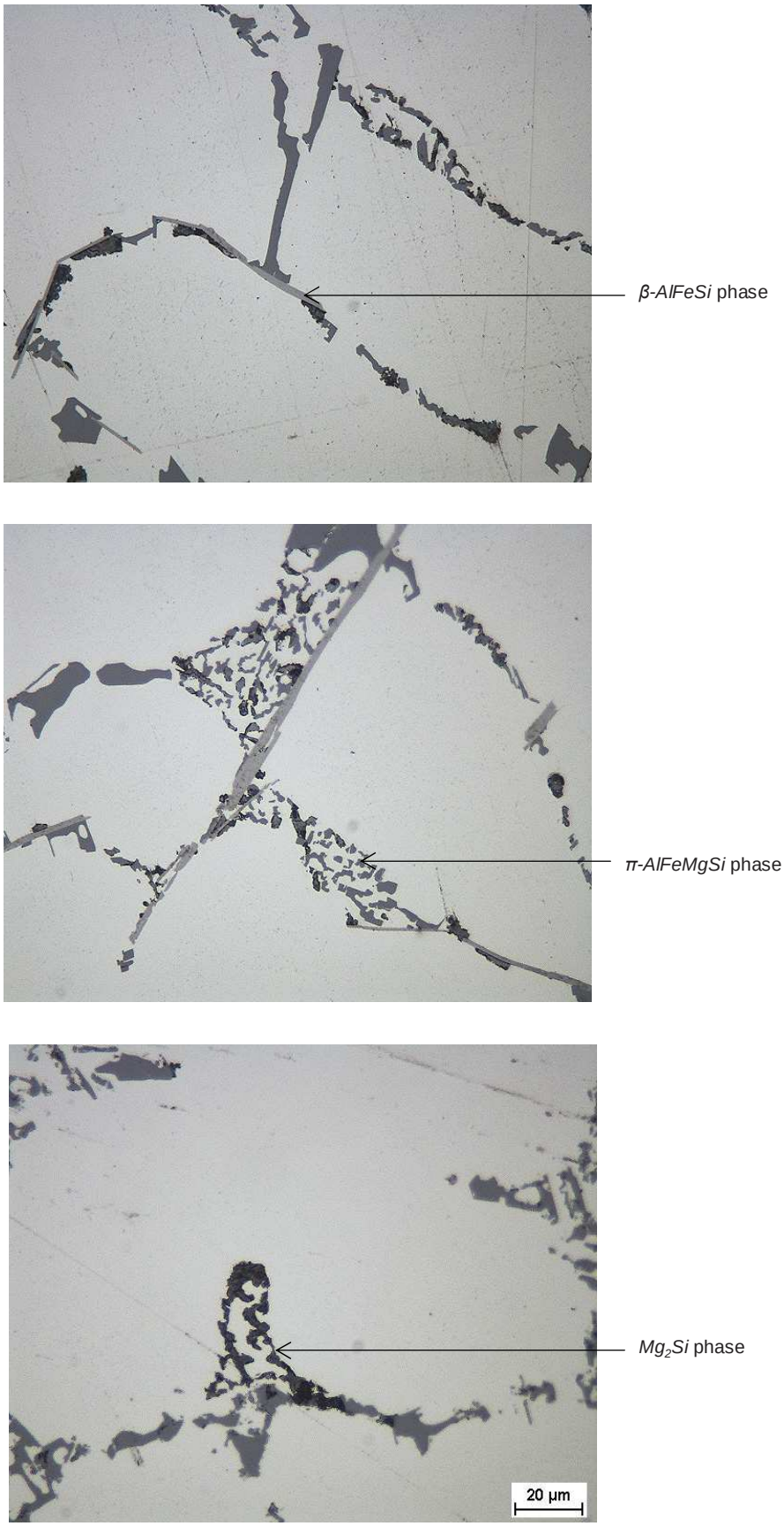

Fig. 4.1.10: Bright field optical micrographs of the as-cast COM AlSi7Mg alloy showing different intermetallic phases: (a) the light gray plate-like *β-AlFeSi*; (b) the nest-like *π – AlFeMgSi* phase; and, (c) co-existing dark Chinese script-like Mg_2Si phase.

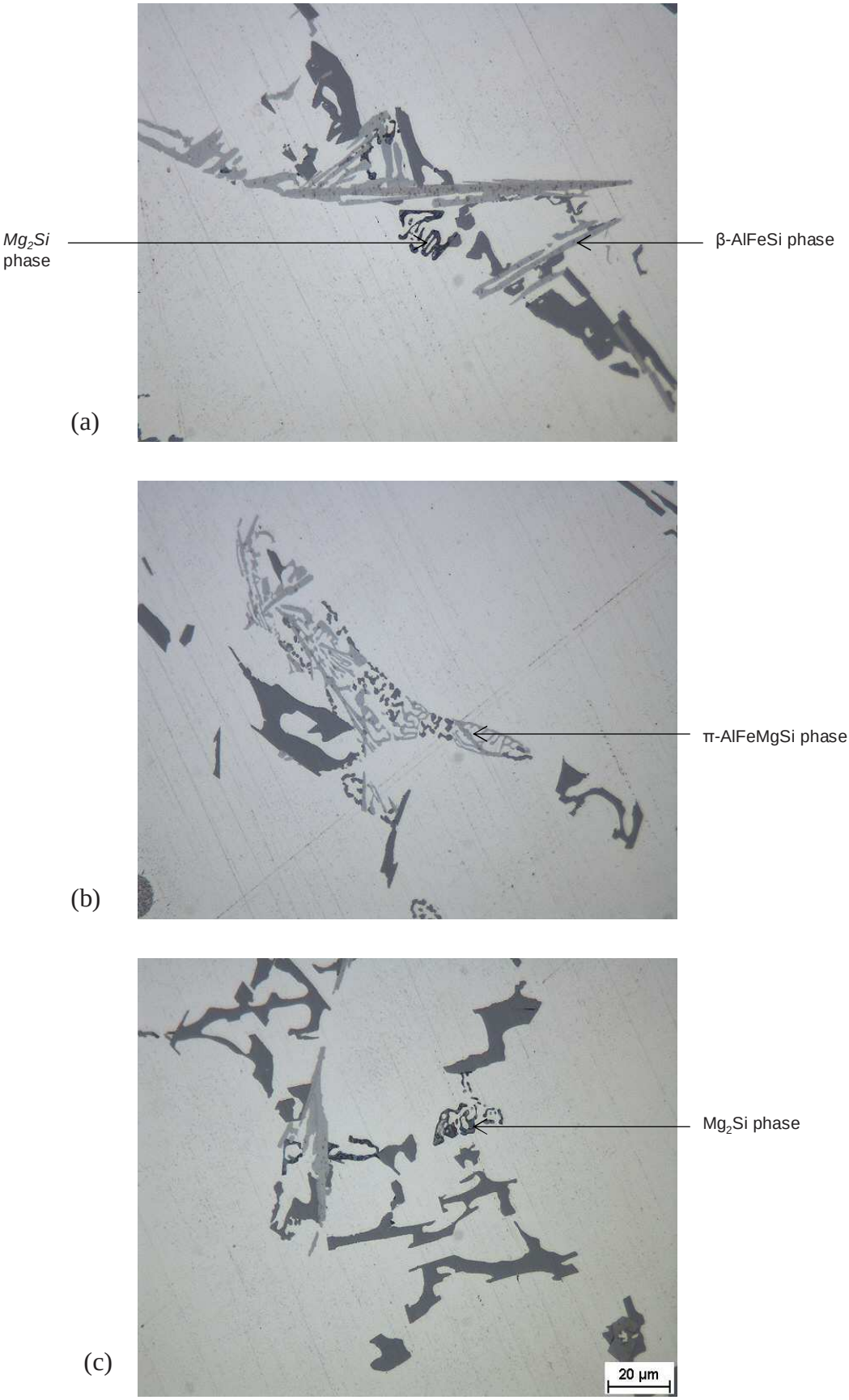

Fig. 4.1.11: Optical micrographs of as-cast MHD A356 alloy showing different intermetallic phases: (a) the light gray plate-like *β-AlFeSi*; (b) the nest like *π – AlFeMgSi* phase; and, (c) dark Chinese script-like Mg_2Si phase.

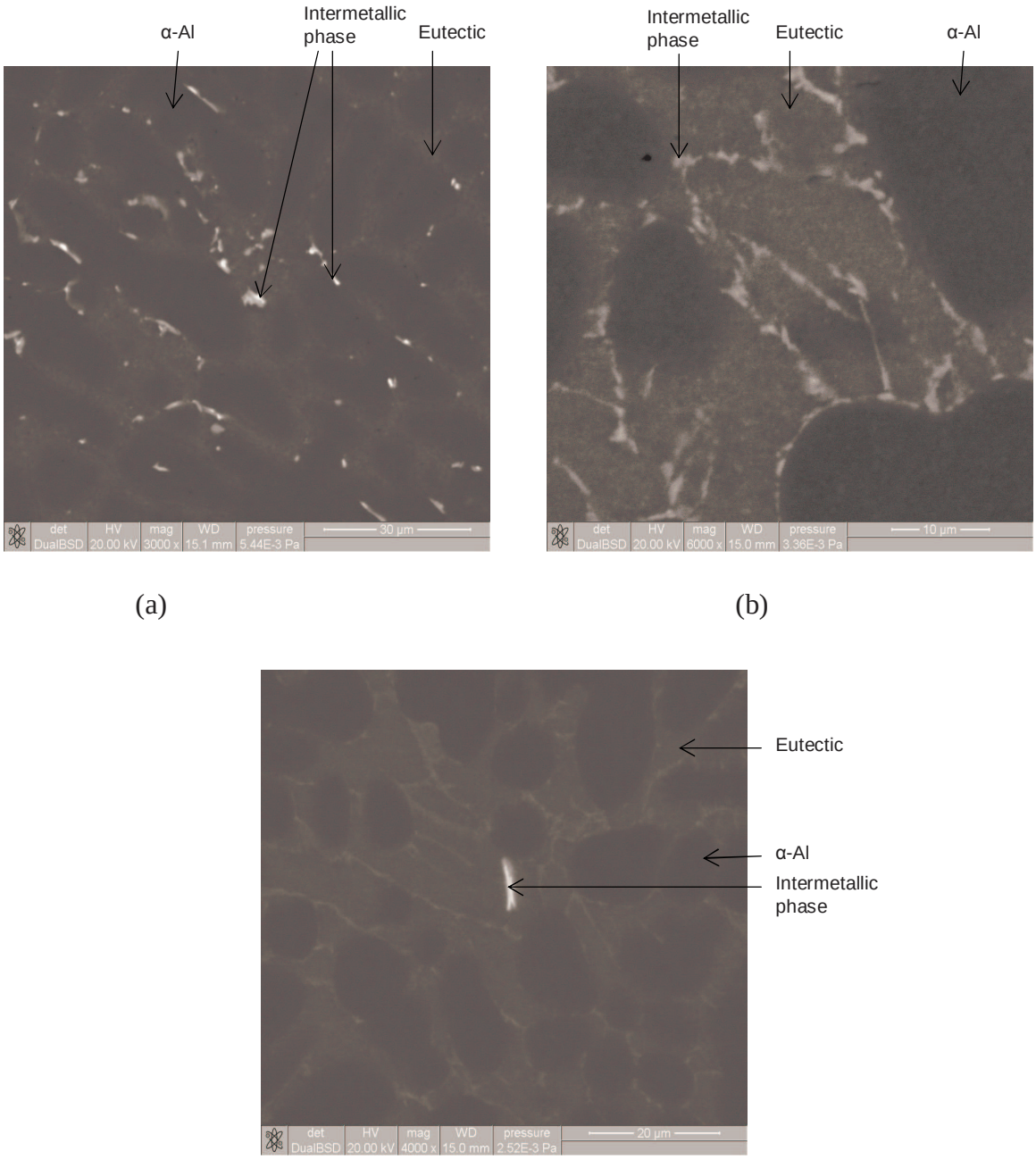

Fig. 4.1.12: SEM BSE Z-contrast images of as-received alloys showing different intermetallic phases: (a) the NGM AlSi7Mg alloy; (b) the COM AlSi7Mg; and, (c) the MHD A356 alloy.

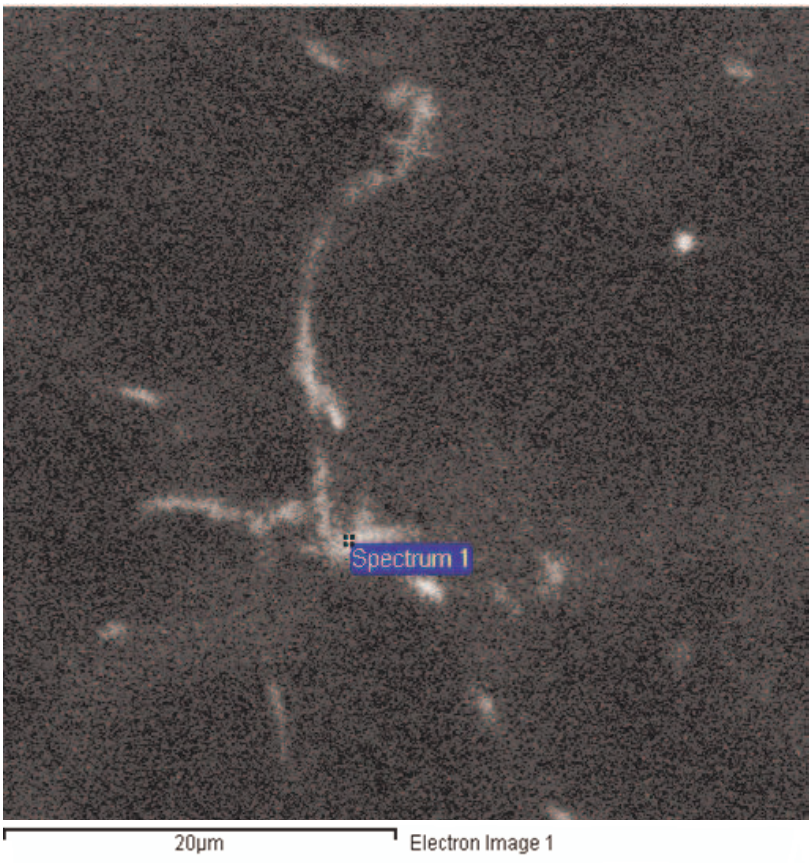

Spectrum processing :
Peaks possibly omitted : 2.972, 7.478 keV
Processing option : All elements analyzed (Normalised)
Number of iterations = 5
Standard :
Mg MgO 1-Jun-1999 12:00 AM
Al Al2O3 1-Jun-1999 12:00 AM
Si SiO2 1-Jun-1999 12:00 AM
Fe Fe 1-Jun-1999 12:00 AM

Element	Weight%	Atomic%
Mg K	4.94	5.63
Al K	76.92	78.95
Si K	13.11	12.92
Fe K	5.03	2.49
Totals	100.00	

Fig. 4.1.13: SEM BSE image and corresponding spectrum of elements at the selected point for the as-received NGM AlSi7Mg alloy.

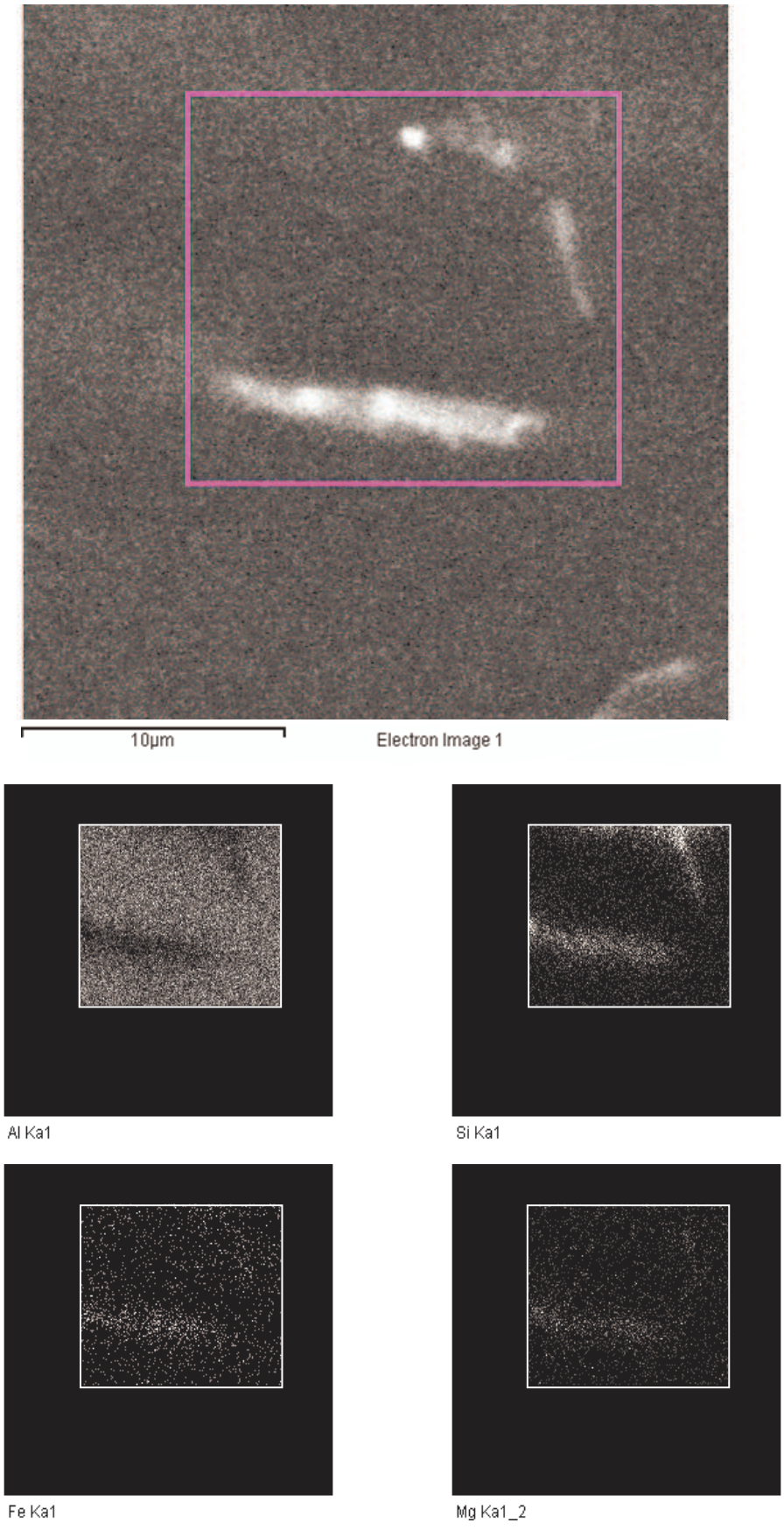

Fig. 4.1.14: SEM BSE image and corresponding elemental maps for the selected area for the as-received NGM AlSi7Mg alloy.

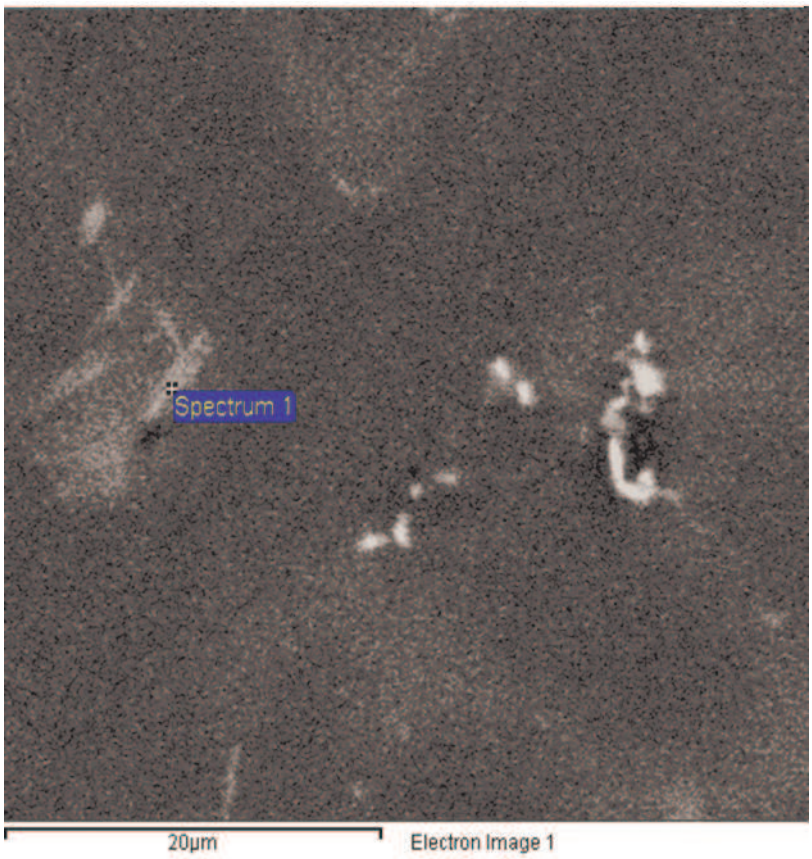

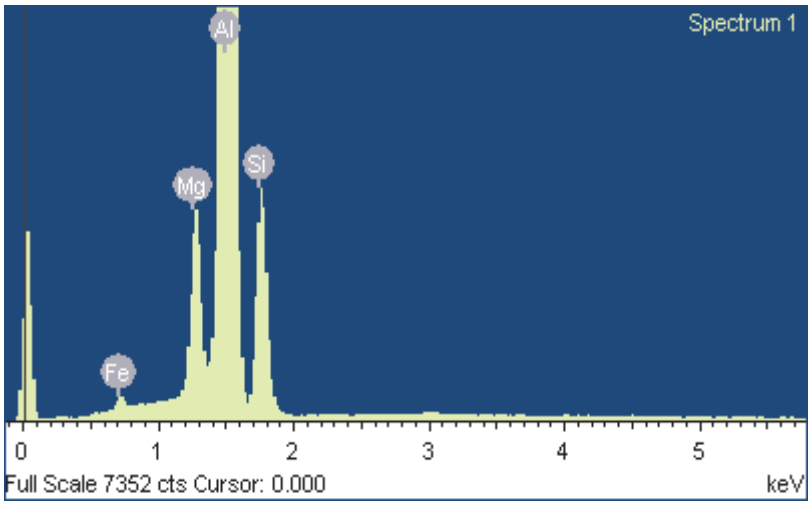

Spectrum processing :
Peak possibly omitted : 2.980 keV
Processing option : All elements analyzed (Normalised)
Number of iterations = 5
Standard :
Mg MgO 1-Jun-1999 12:00 AM
Al Al2O3 1-Jun-1999 12:00 AM
Si SiO2 1-Jun-1999 12:00 AM
Fe Fe 1-Jun-1999 12:00 AM

Element	Weight%	Atomic%
Mg K	4.76	5.37
Al K	75.57	76.70
Si K	17.10	16.68
Fe K	2.56	1.26
Totals	100.00	

Fig. 4.1.15: SEM BSE image and corresponding spectrum of elements at the selected point for the as-received COM AlSi7Mg alloy.

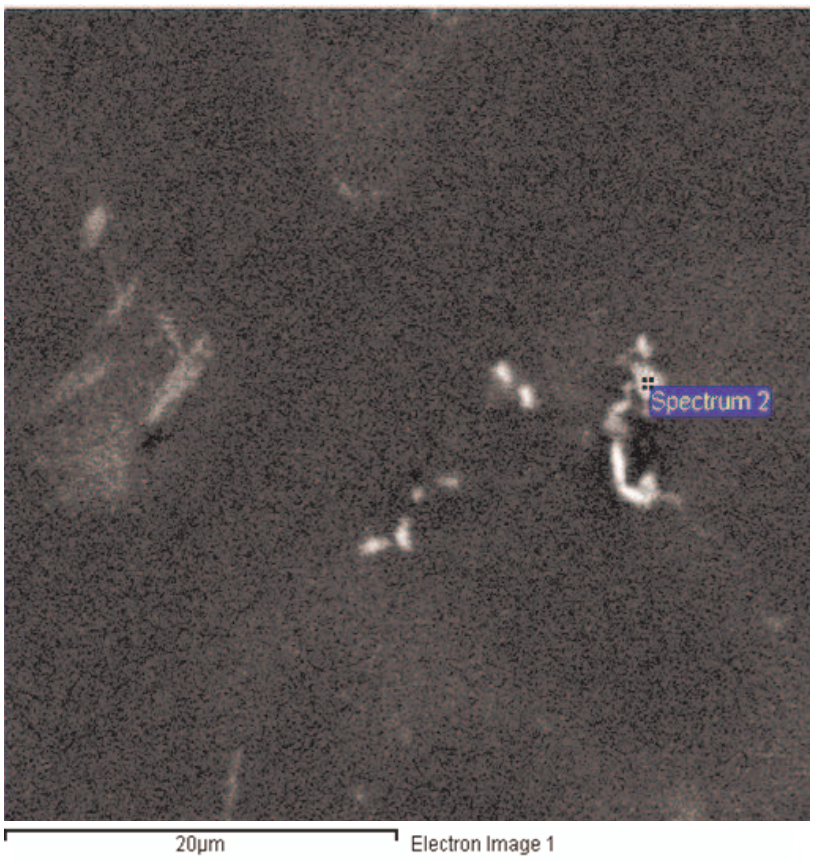

Spectrum processing :
Peak possibly omitted : 2.981 keV
Processing option : All elements analyzed (Normalised)
Number of iterations = 5
Standard :
Mg MgO 1-Jun-1999 12:00 AM
Al Al2O3 1-Jun-1999 12:00 AM
Si SiO2 1-Jun-1999 12:00 AM
Ti Ti 1-Jun-1999 12:00 AM

Element	Weight%	Atomic%
Mg K	0.26	0.31
Al K	68.29	74.25
Si K	14.30	14.93
Ti K	17.15	10.51
Totals	100.00	

Fig. 4.1.16: SEM BSE image and corresponding spectrum of elements at the selected point for the as-received COM AlSi7Mg alloy.

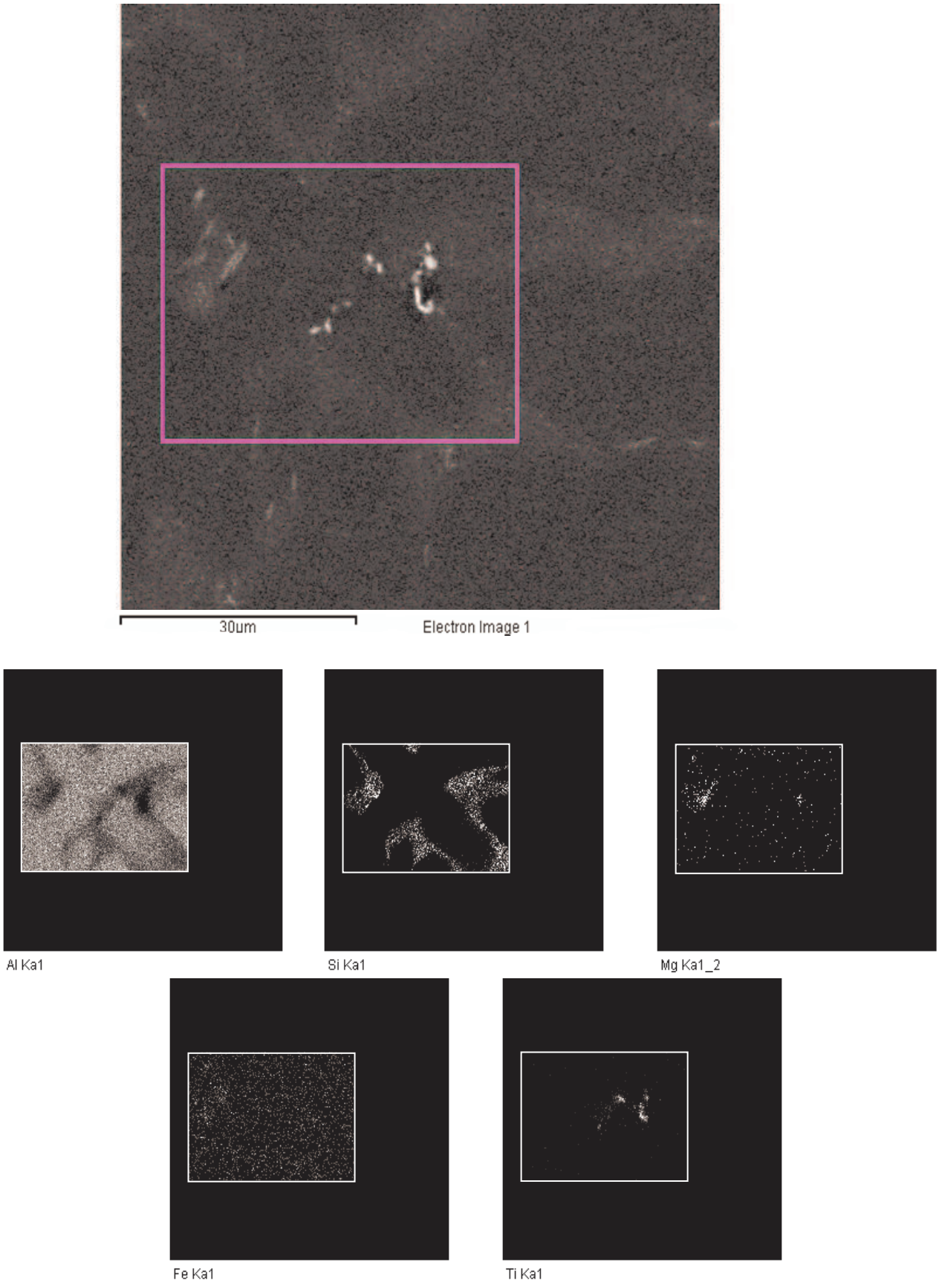

Fig. 4.1.17: SEM BSE image and corresponding elemental maps for the selected area for the as-received COM AlSi7Mg alloy.

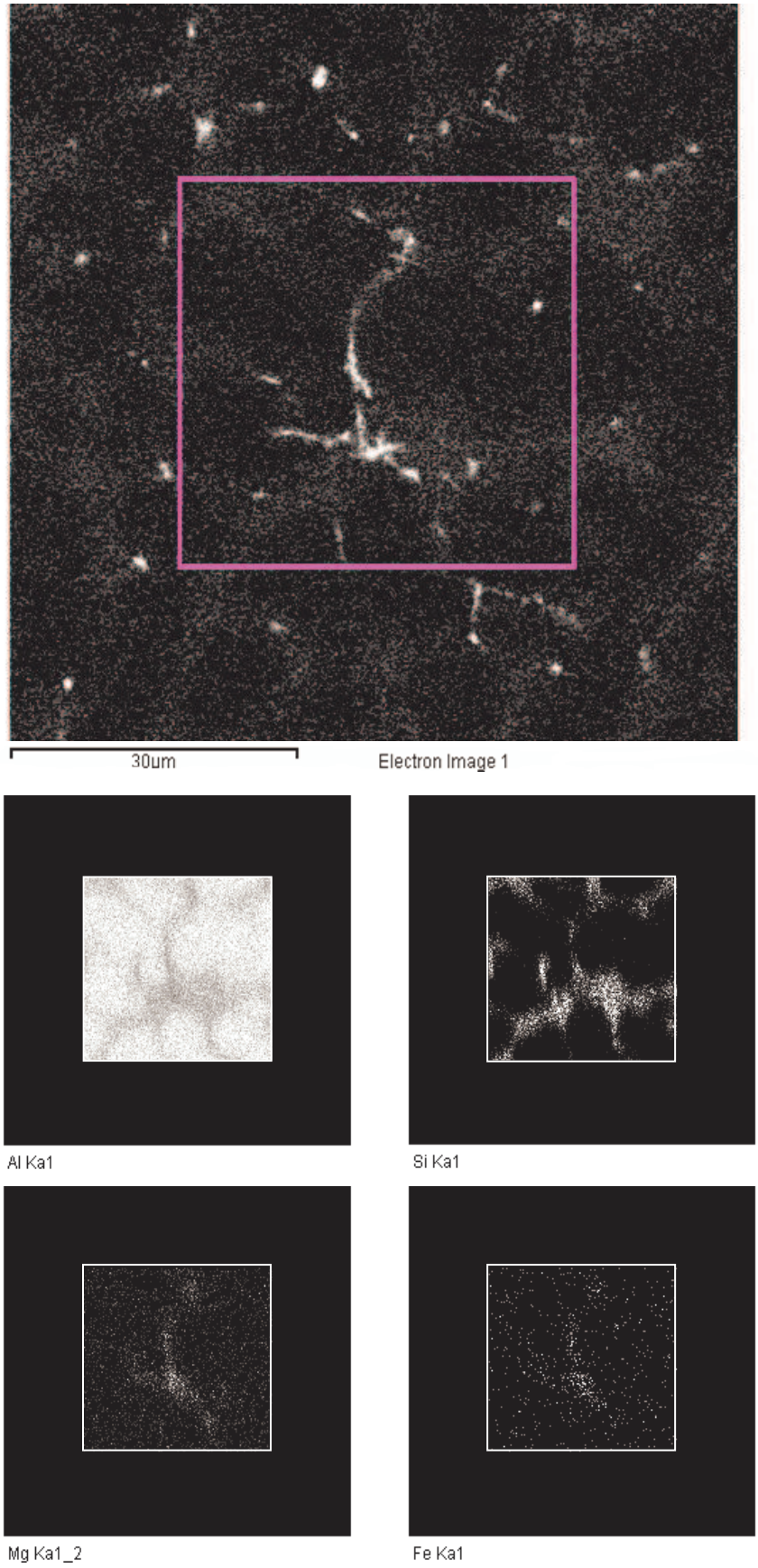

Fig. 4.1.18: SEM BSE image and corresponding elemental maps for the selected area for the as-received MHD A356 alloy.

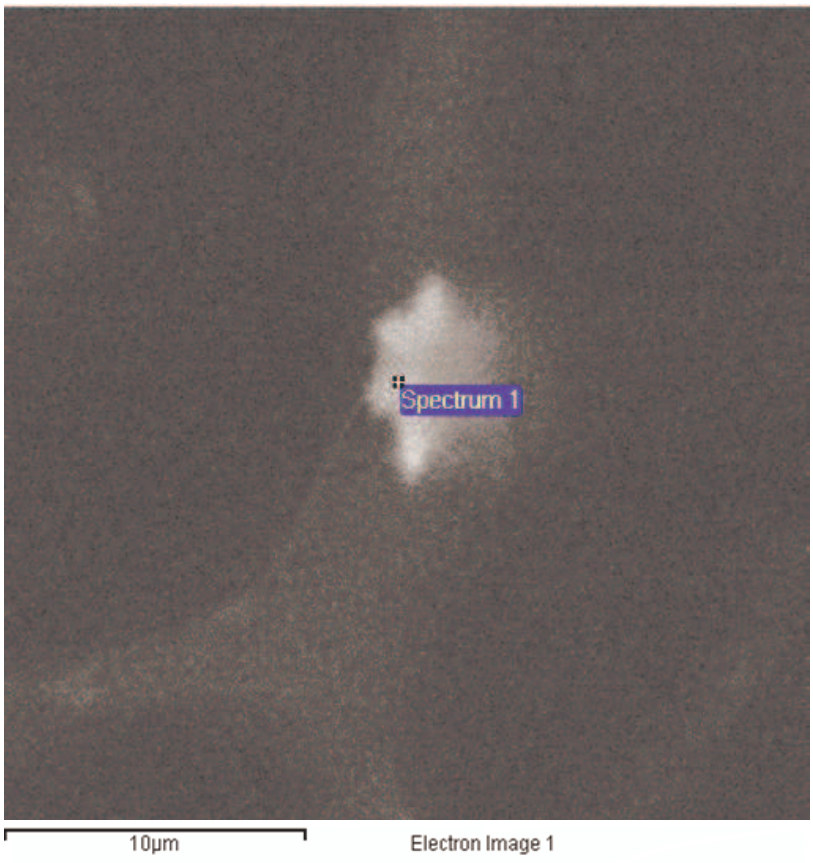

Spectrum processing :
Peaks possibly omitted : 0.261, 2.979, 3.698 keV
Processing option : All elements analyzed (Normalised)
Number of iterations = 5
Standard :
Mg MgO 1-Jun-1999 12:00 AM
Al Al2O3 1-Jun-1999 12:00 AM
Si SiO2 1-Jun-1999 12:00 AM
Sr SrF2 1-Jun-1999 12:00 AM

Element	Weight%	Atomic%
Mg K	0.80	0.95
Al K	68.66	73.45
Si K	22.24	22.86
Sr L	8.30	2.74
Totals	100.00	

Fig. 4.1.19: SEM BSE image and corresponding spectrum of elements at the selected point for the as-received MHD A356 alloy.

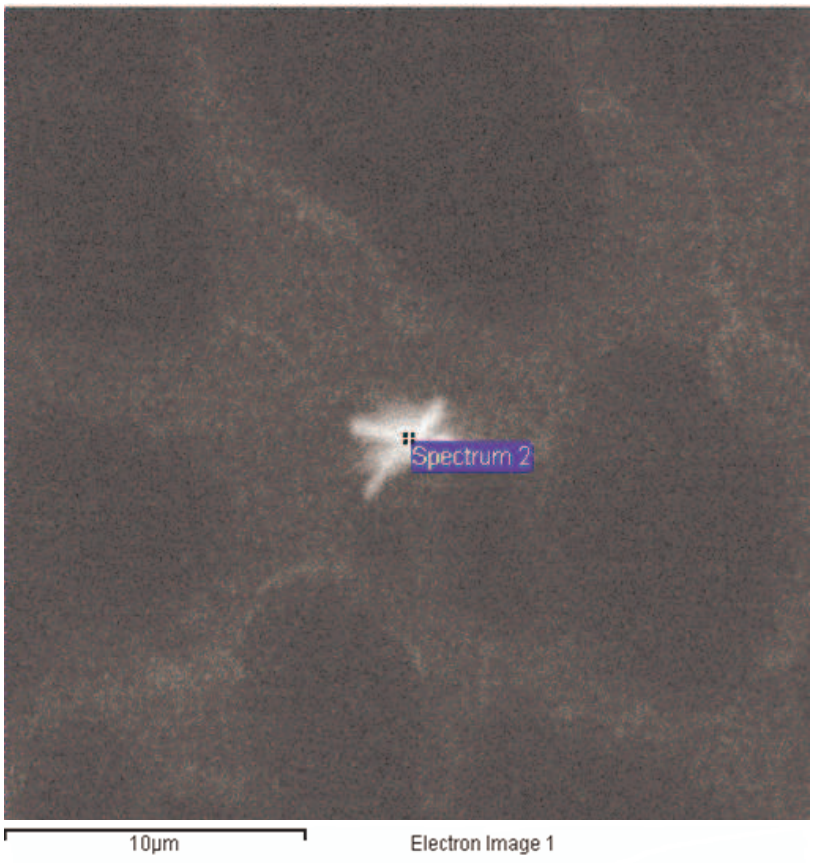

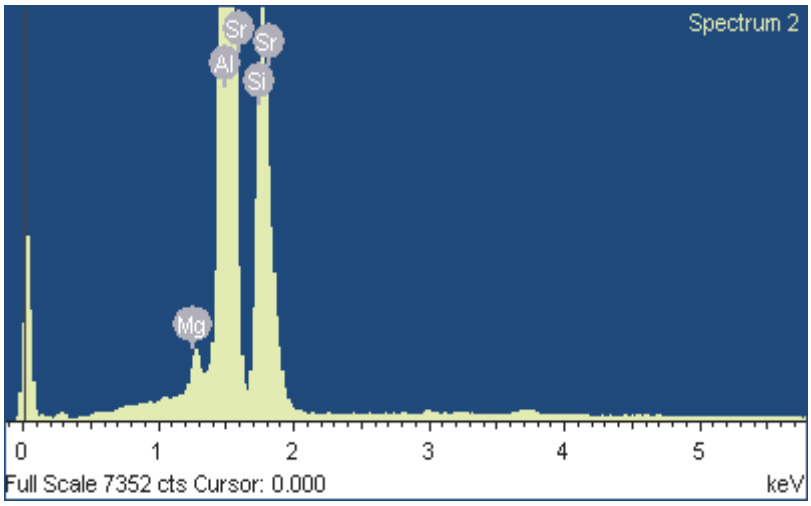

Spectrum processing :
Peaks possibly omitted : 0.265, 2.988, 3.695 keV
Processing option : All elements analyzed (Normalised)
Number of iterations = 5
Standard :
Mg MgO 1-Jun-1999 12:00 AM
Al Al2O3 1-Jun-1999 12:00 AM
Si SiO2 1-Jun-1999 12:00 AM
Sr SrF2 1-Jun-1999 12:00 AM

Element	Weight%	Atomic%
Mg K	0.99	1.23
Al K	60.04	67.43
Si K	24.36	26.28
Sr L	14.61	5.05
Totals	100.00	

Fig. 4.1.20: SEM BSE image and corresponding spectrum of elements at the selected point for the as-received MHD A356 alloy.

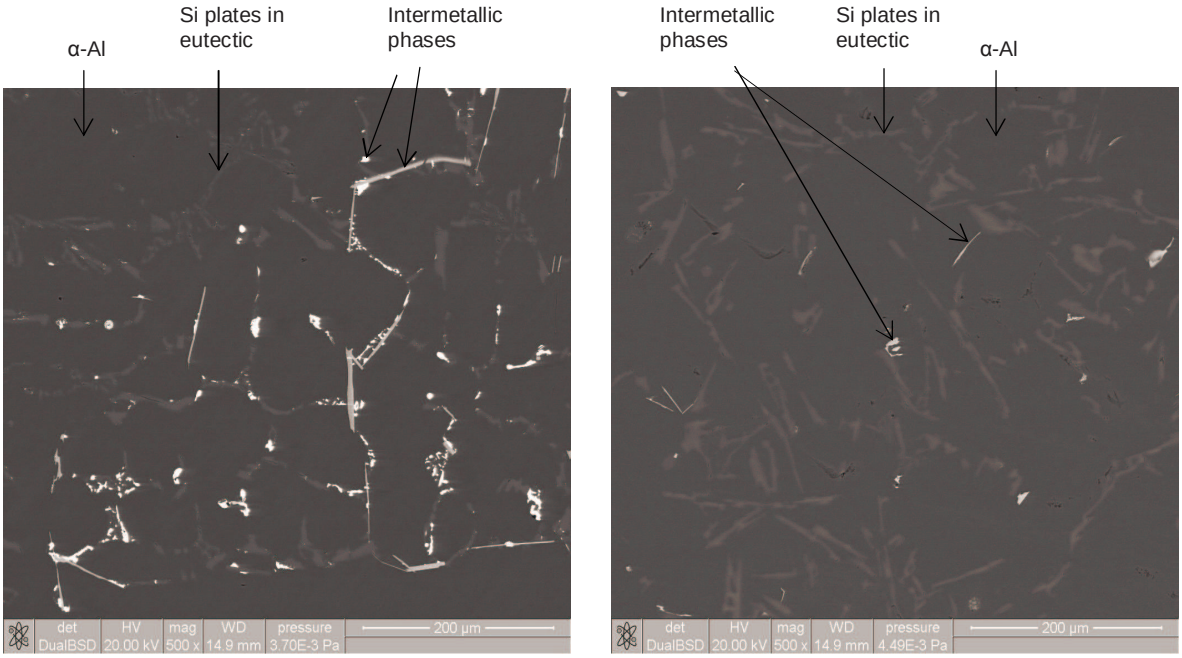

(a) (b)

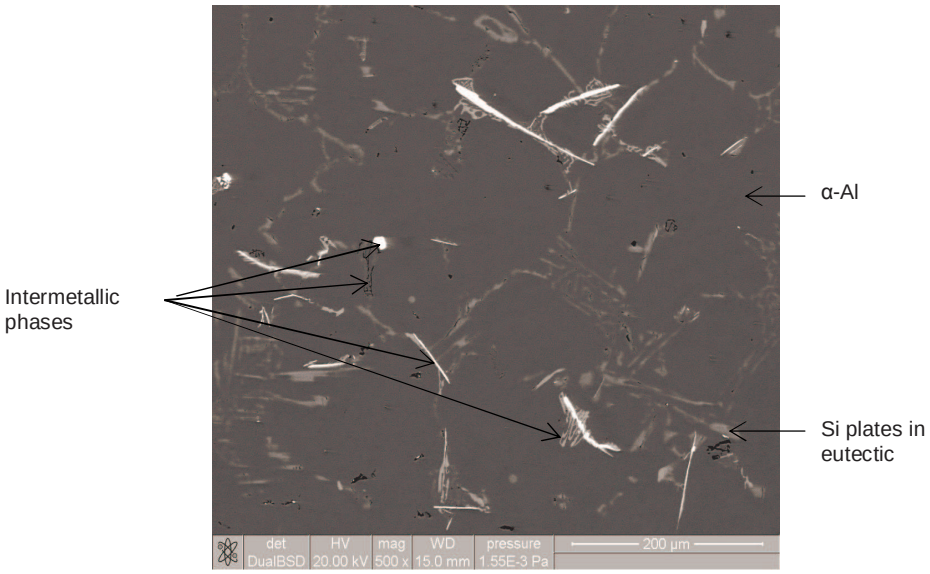

(c)

Fig. 4.1.21: SEM BSE Z-contrast images of as-cast alloys showing different phases; black area shows the primary phase, gray area shows the eutectic phase and bright and dark phases are intermetallic phases in: (a) the NGM AlSi7Mg alloy; (b) the COM AlSi7Mg; and, (c) the MHD A356 alloy.

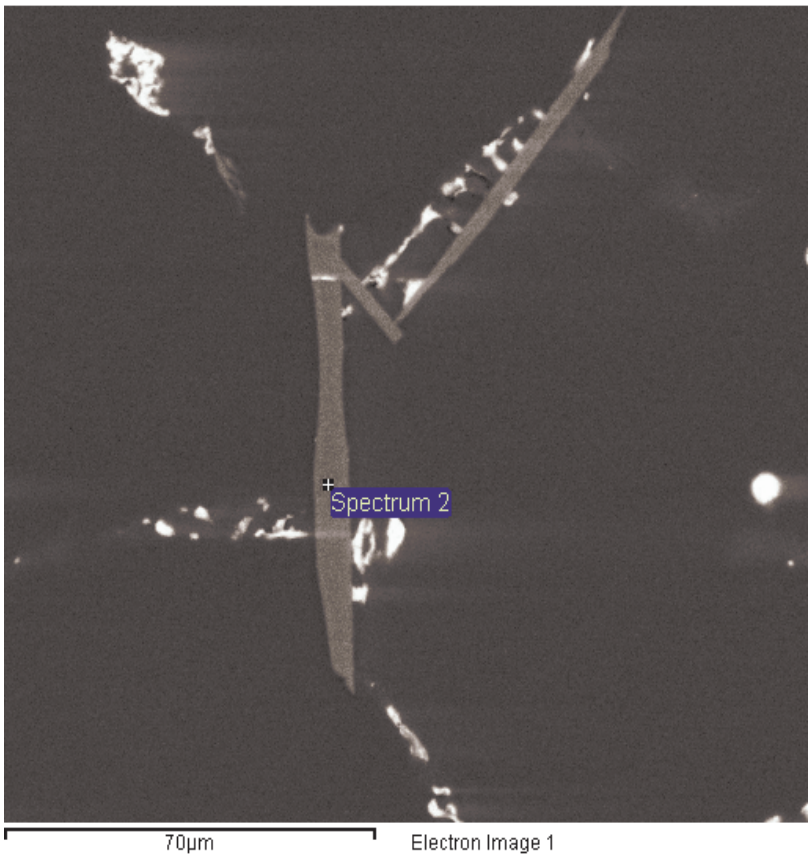

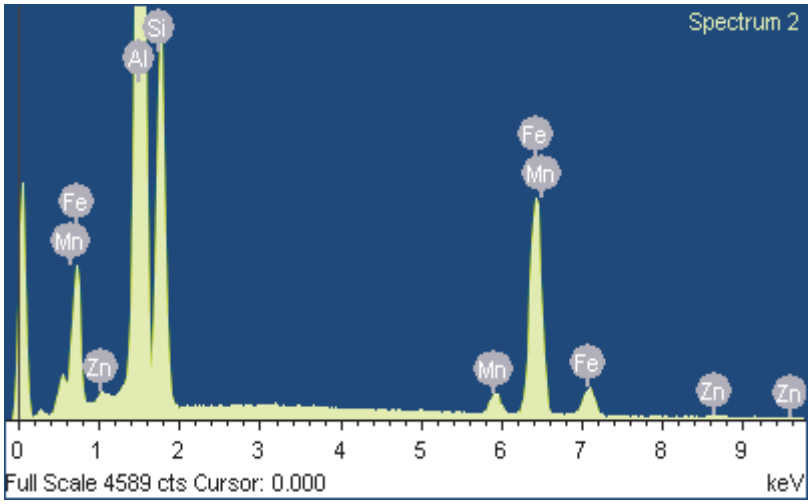

Spectrum processing :
Peak possibly omitted : 0.265 keV
Processing option : All elements analyzed (Normalised)
Number of iterations = 5
Standard :
Al Al2O3 1-Jun-1999 12:00 AM
Si SiO2 1-Jun-1999 12:00 AM
Mn Mn 1-Jun-1999 12:00 AM
Fe Fe 1-Jun-1999 12:00 AM
Zn Zn 1-Jun-1999 12:00 AM

Element	Weight%	Atomic%
Al K	54.13	63.59
Si K	18.54	20.92
Mn K	1.92	1.11
Fe K	24.99	14.18
Zn K	0.42	0.20
Totals	100.00	

Fig. 4.1.22: SEM BSE image and corresponding spectrum of elements at the selected point for the as-cast NGM AlSi7Mg alloy.

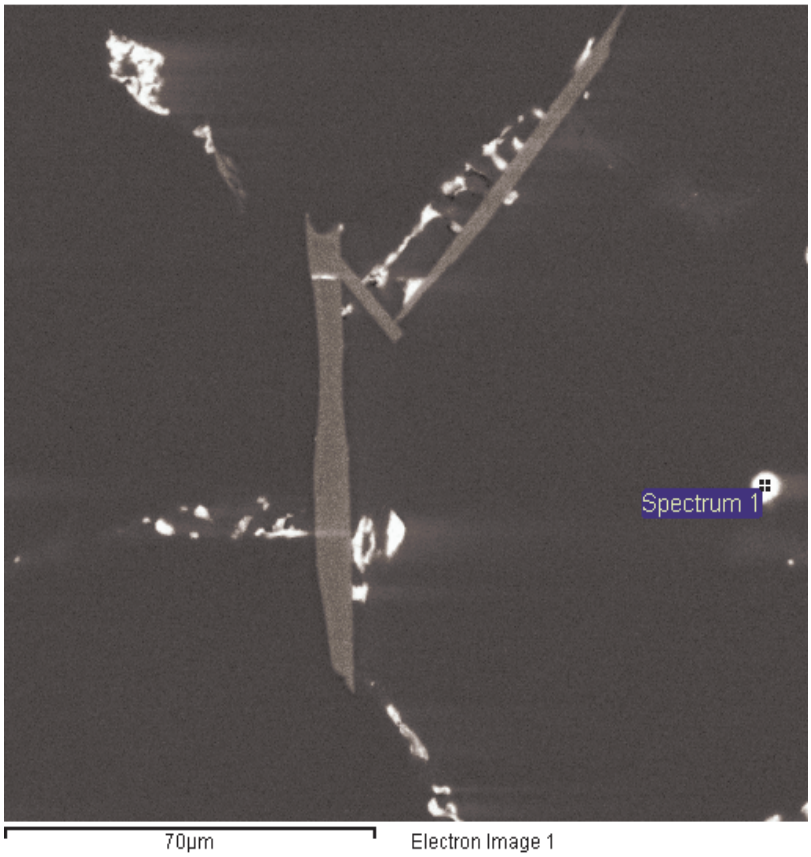

Processing option : All elements analyzed (Normalised)
Number of iterations = 3
Standard :
Mg MgO 1-Jun-1999 12:00 AM
Al Al2O3 1-Jun-1999 12:00 AM
Sn Sn 1-Jun-1999 12:00 AM

Element	Weight%	Atomic%
Mg K	0.53	2.39
Al K	1.48	6.08
Sn L	98.00	91.53
Totals	100.00	

Fig. 4.1.23: SEM BSE image and corresponding spectrum of elements at the selected point for the as-cast NGM AlSi7Mg alloy.

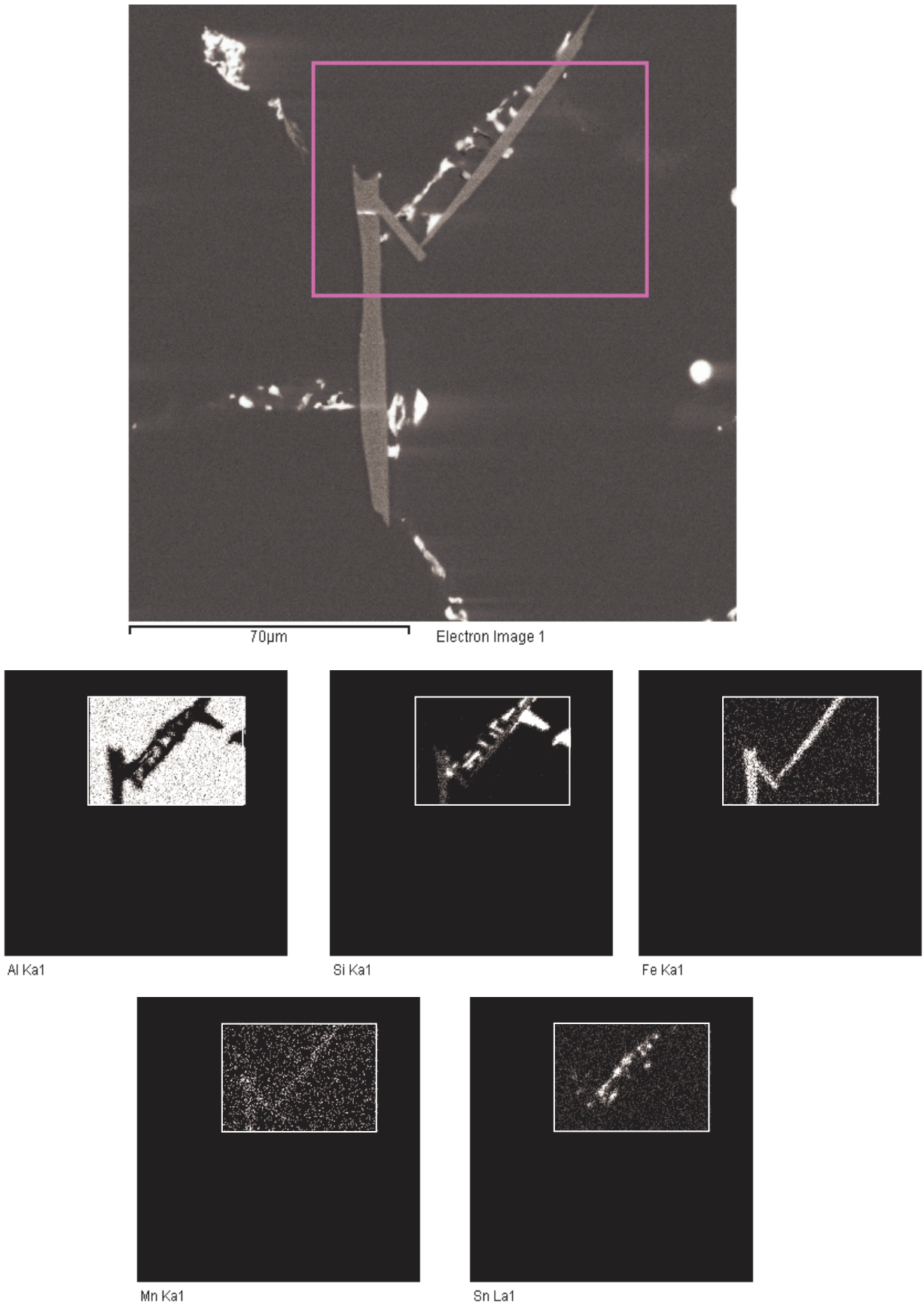

Fig. 4.1.24: SEM BSE image and corresponding elemental maps for the selected area for the as-cast NGM AlSi7Mg alloy.

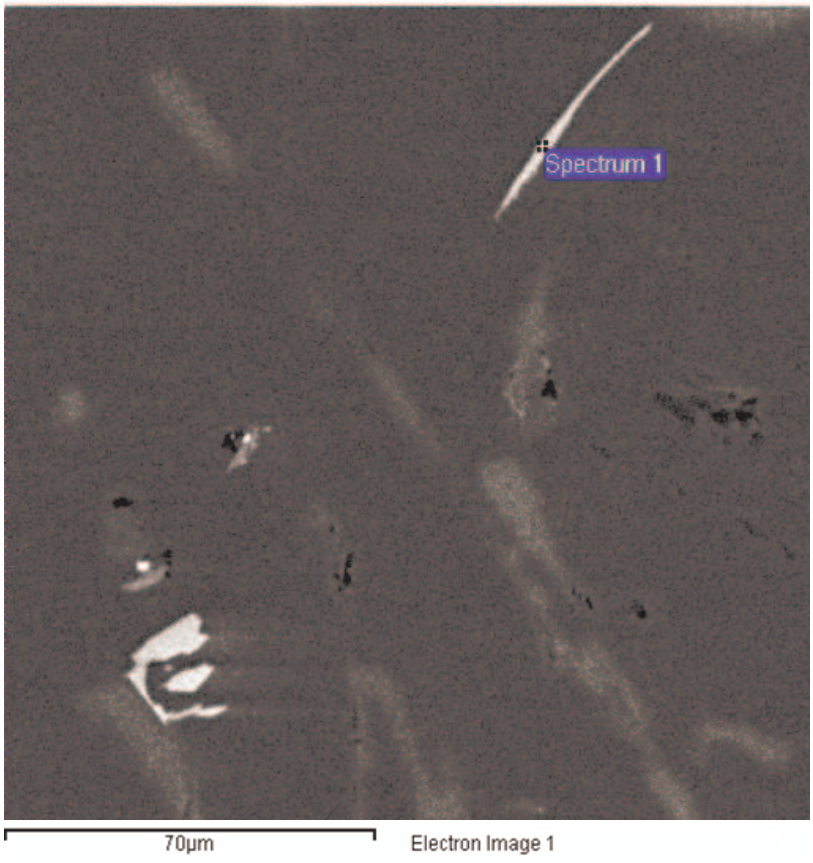

Processing option : All elements analyzed (Normalised)
Number of iterations = 5
Standard :
Mg MgO 1-Jun-1999 12:00 AM
Al Al2O3 1-Jun-1999 12:00 AM
Si SiO2 1-Jun-1999 12:00 AM
Fe Fe 1-Jun-1999 12:00 AM

Element	Weight%	Atomic%
Mg K	1.37	1.62
Al K	77.11	82.23
Si K	9.96	10.20
Fe K	11.56	5.96
Totals	100.00	

Fig. 4.1.25: SEM BSE image and corresponding spectrum of elements at the selected point for the as-cast COM AlSi7Mg alloy.

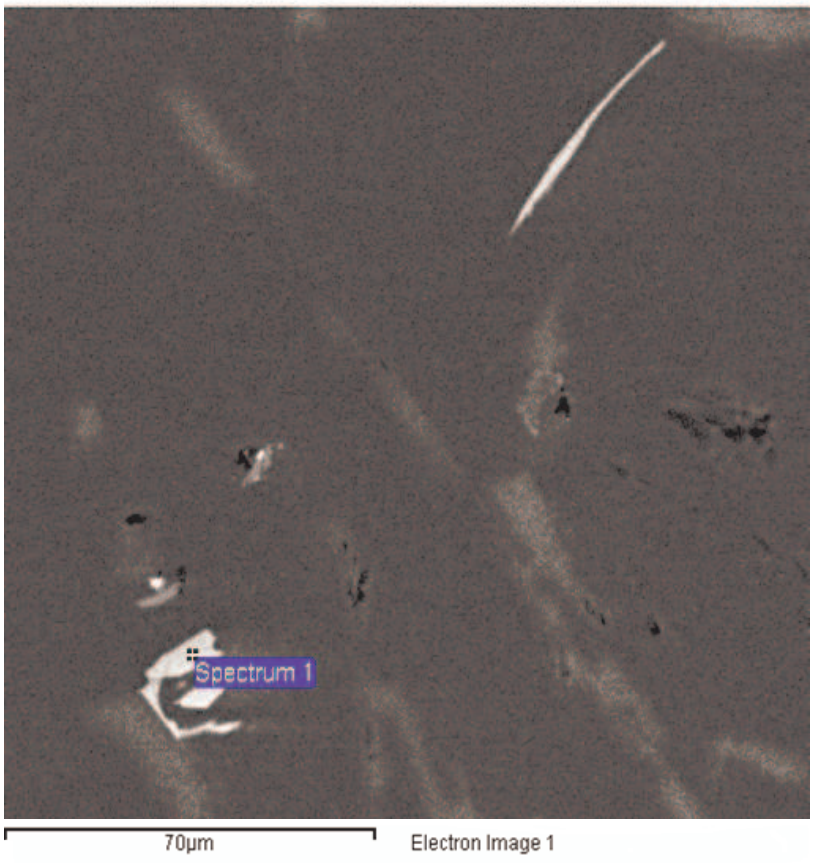

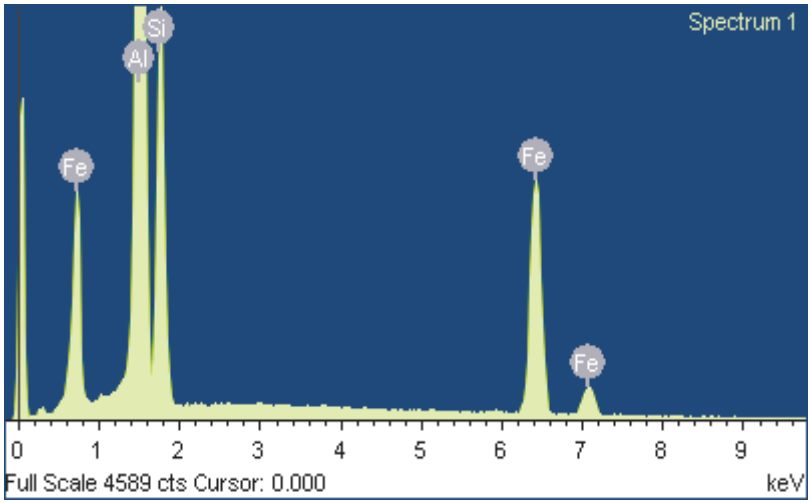

Processing option : All elements analyzed (Normalised)
Number of iterations = 5
Standard :
Al Al2O3 1-Jun-1999 12:00 AM
Si SiO2 1-Jun-1999 12:00 AM
Fe Fe 1-Jun-1999 12:00 AM

Element	Weight%	Atomic%
Al K	59.69	68.52
Si K	16.63	18.34
Fe K	23.69	13.14
Totals	100.00	

Fig. 4.1.26: SEM BSE image and corresponding spectrum of elements at the selected point for the as-cast COM AlSi7Mg alloy.

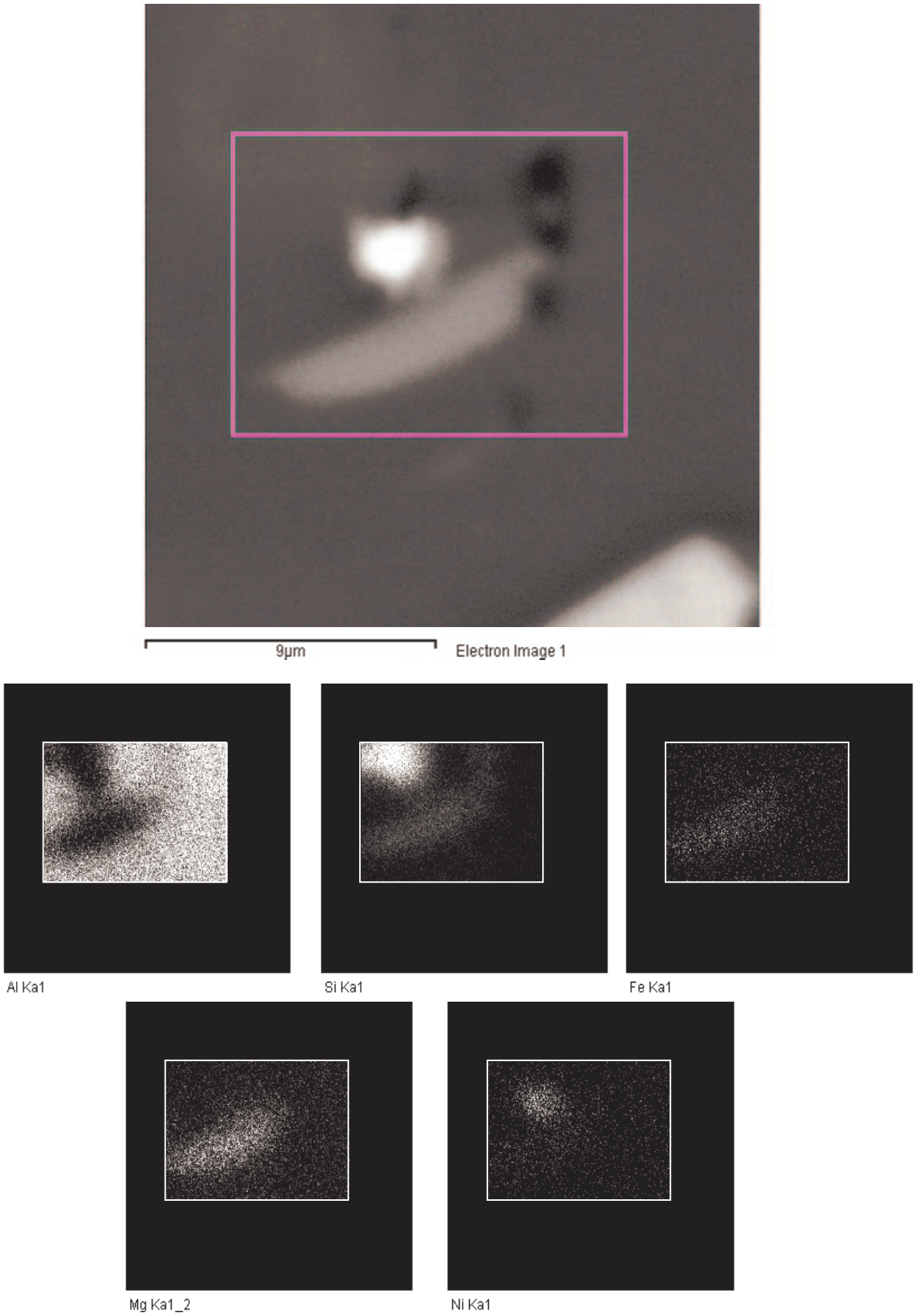

Fig. 4.1.27: SEM BSE image and corresponding elemental maps for the selected area for the as-cast COM AlSi7Mg alloy.

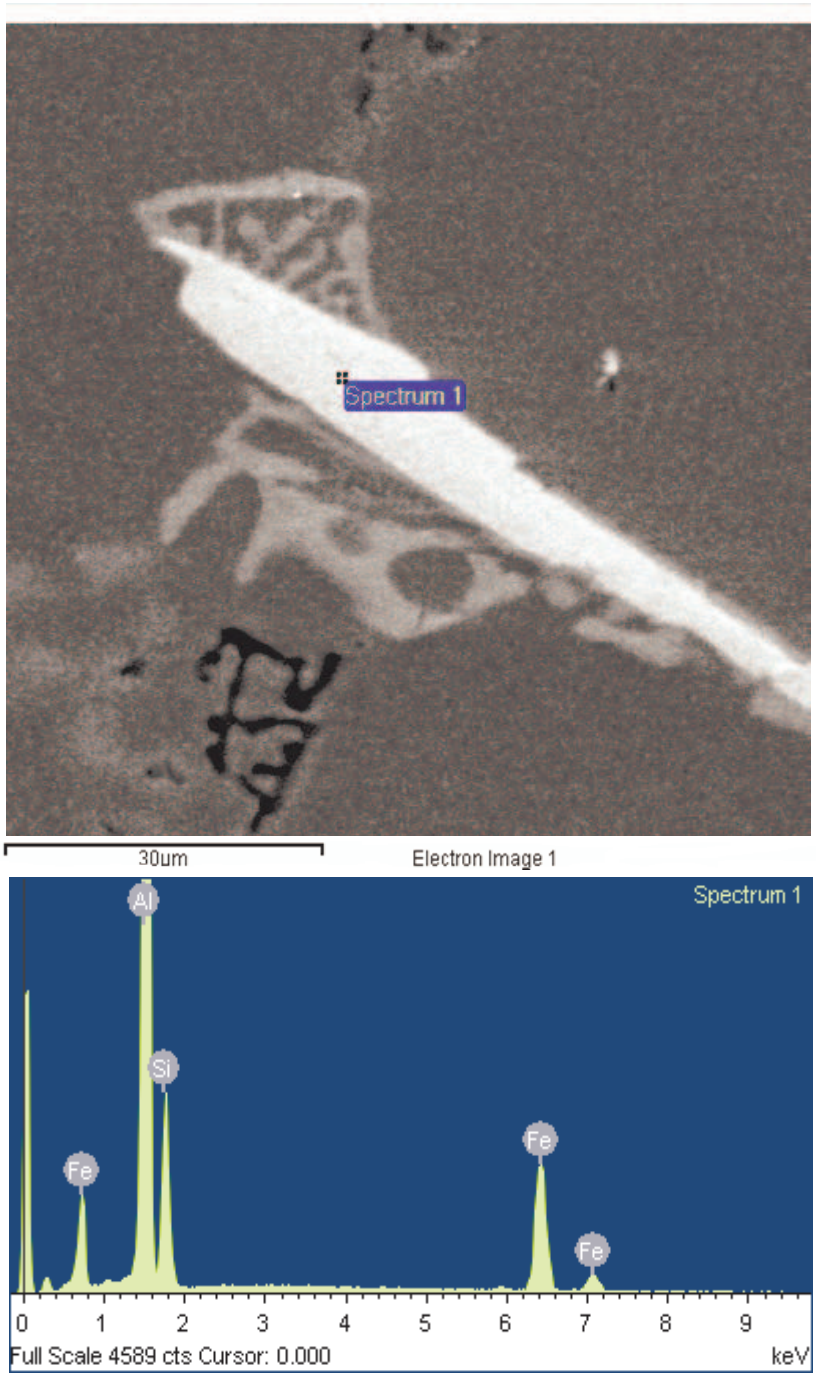

Spectrum processing :
Peaks possibly omitted : 0.267, 1.020, 5.887 keV
Processing option : All elements analyzed (Normalised)
Number of iterations = 5
Standard :
Al Al2O3 1-Jun-1999 12:00 AM
Si SiO2 1-Jun-1999 12:00 AM
Fe Fe 1-Jun-1999 12:00 AM

Element	Weight%	Atomic%
Al K	55.57	65.42
Si K	16.55	18.72
Fe K	27.88	15.86
Totals	100.00	

Fig. 4.1.28: SEM BSE image and corresponding spectrum of elements at the selected point for the as-cast MHD A356 alloy.

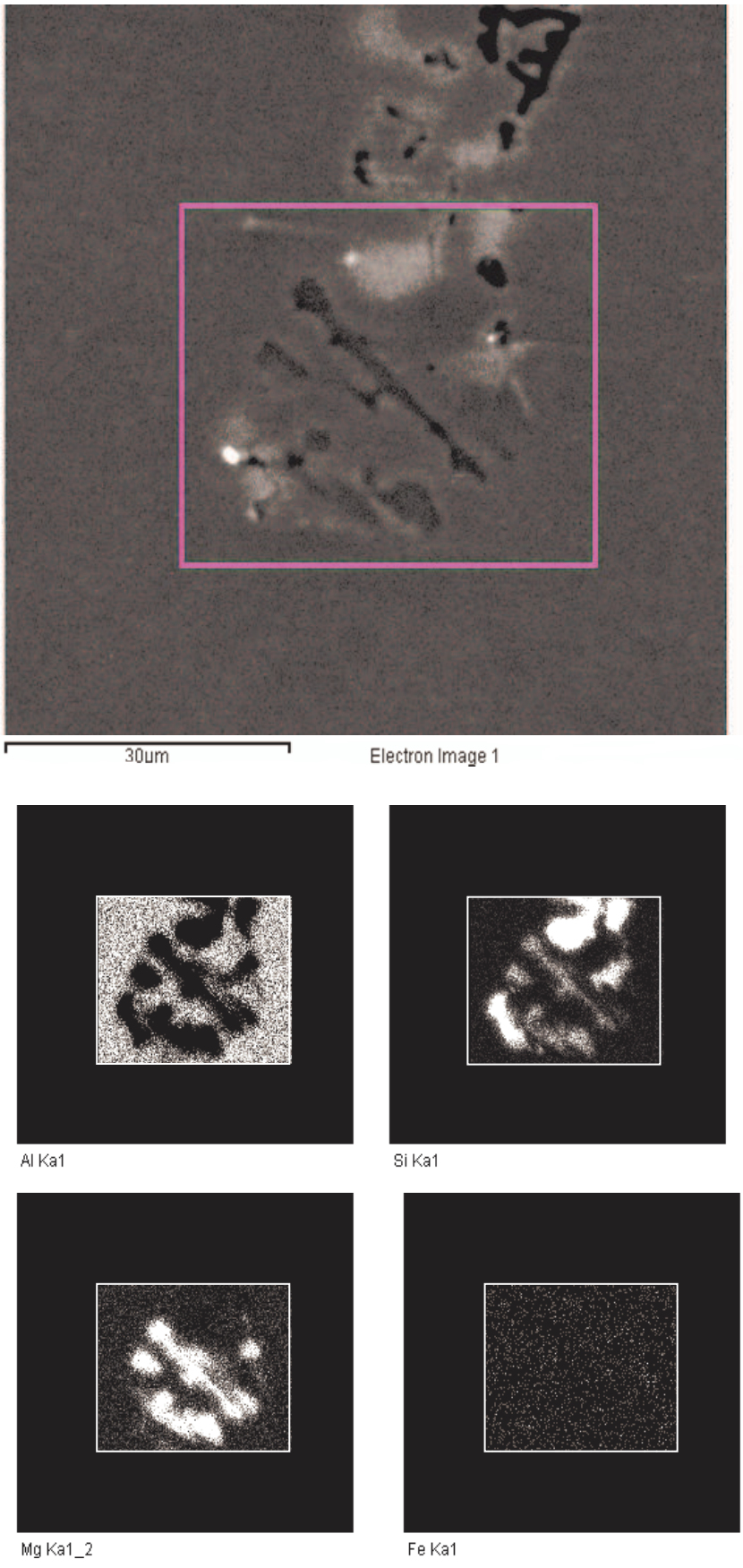

Fig. 4.1.29: SEM BSE image and corresponding element map for the selected area for the as-cast MHD A356 alloy.

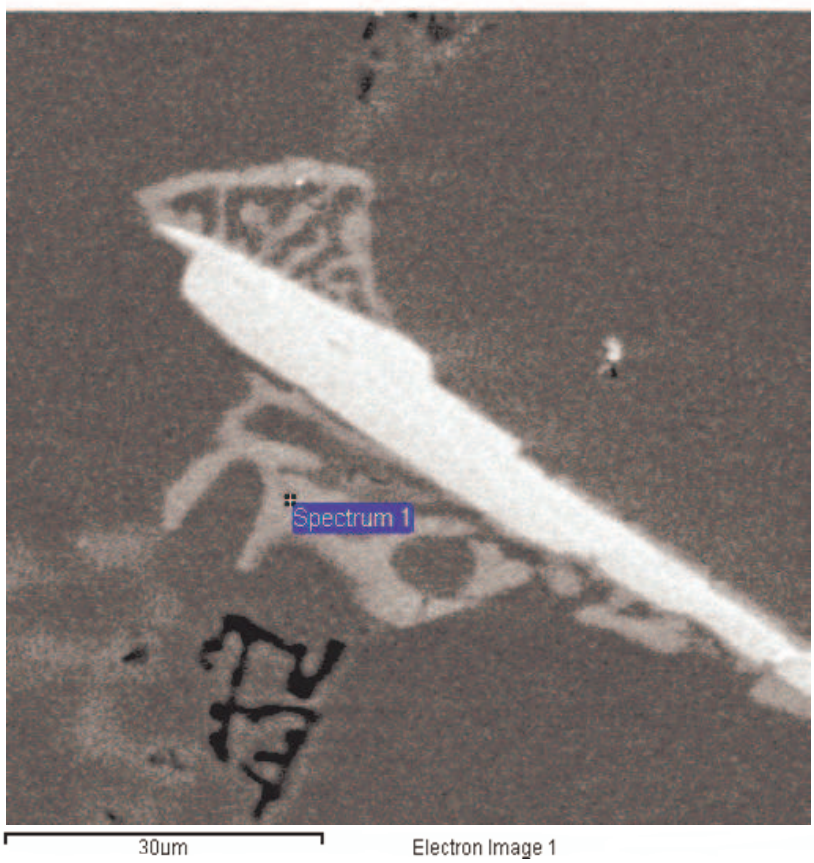

Processing option : All elements analyzed (Normalised)
Number of iterations = 5
Standard :
Mg MgO 1-Jun-1999 12:00 AM
Al Al2O3 1-Jun-1999 12:00 AM
Si SiO2 1-Jun-1999 12:00 AM
Fe Fe 1-Jun-1999 12:00 AM

Element	Weight%	Atomic%
Mg K	14.31	16.65
Al K	50.68	53.13
Si K	24.94	25.12
Fe K	10.07	5.10
Totals	100.00	

Fig. 4.1.30: SEM BSE image and corresponding spectrum of elements at the selected point for the as-cast MHD A356 alloy.

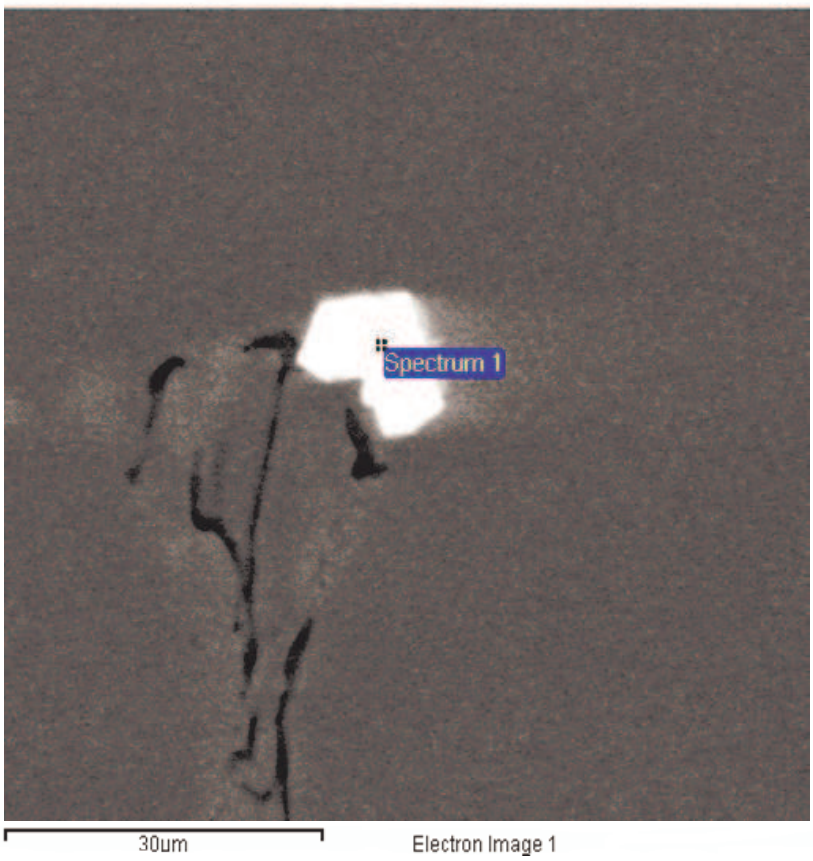

Processing option : All elements analyzed (Normalised)
Number of iterations = 5
Standard :
Mg MgO 1-Jun-1999 12:00 AM
Al Al2O3 1-Jun-1999 12:00 AM
Si SiO2 1-Jun-1999 12:00 AM
Sr SrF2 1-Jun-1999 12:00 AM
W W 1-Jun-1999 12:00 AM

Element	Weight%	Atomic%
Mg K	0.30	0.52
Al K	28.03	43.95
Si K	24.59	37.05
Sr L	30.22	14.59
W M	16.87	3.88
Totals	100.00	

Fig. 4.1.31: SEM BSE image and corresponding spectrum of elements at the selected point for the as-cast MHD A356 alloy.

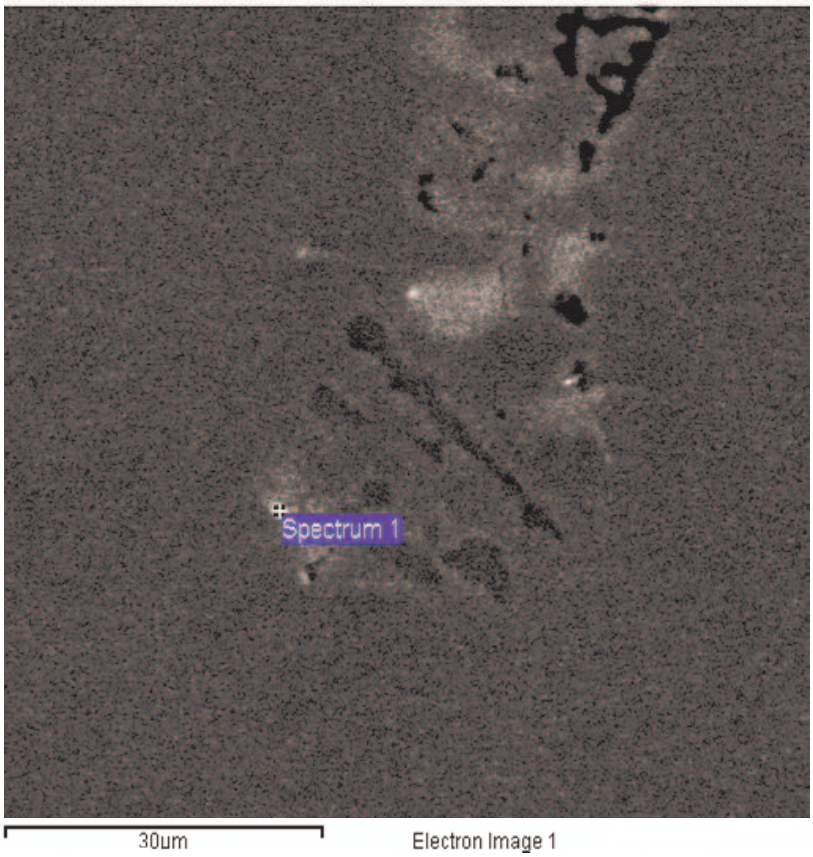

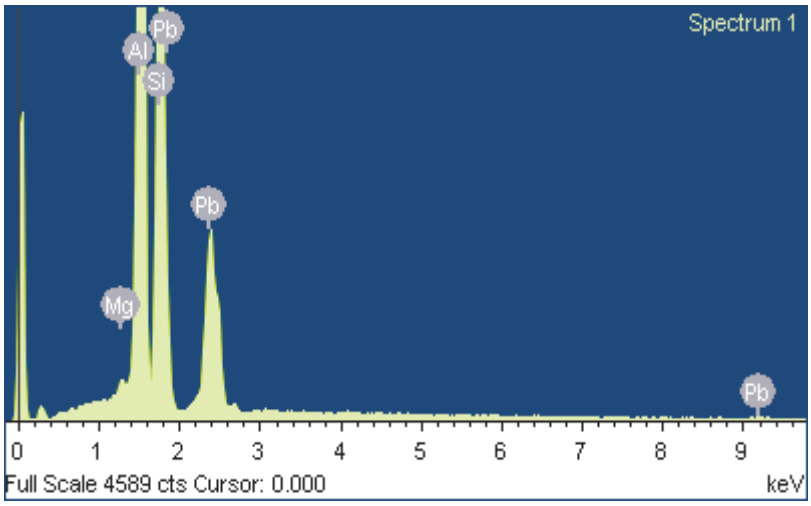

Processing option : All elements analyzed (Normalised)
Number of iterations = 5
Standard :
Mg MgO 1-Jun-1999 12:00 AM
Al Al2O3 1-Jun-1999 12:00 AM
Si SiO2 1-Jun-1999 12:00 AM
Pb PbF2 1-Jun-1999 12:00 AM

Element	Weight%	Atomic%
Mg K	0.43	0.63
Al K	37.16	49.72
Si K	34.89	44.85
Pb M	27.53	4.80
Totals	100.00	

Fig. 4.1.32: SEM BSE image and corresponding spectrum of elements at the selected point for the as-cast MHD A356 alloy.

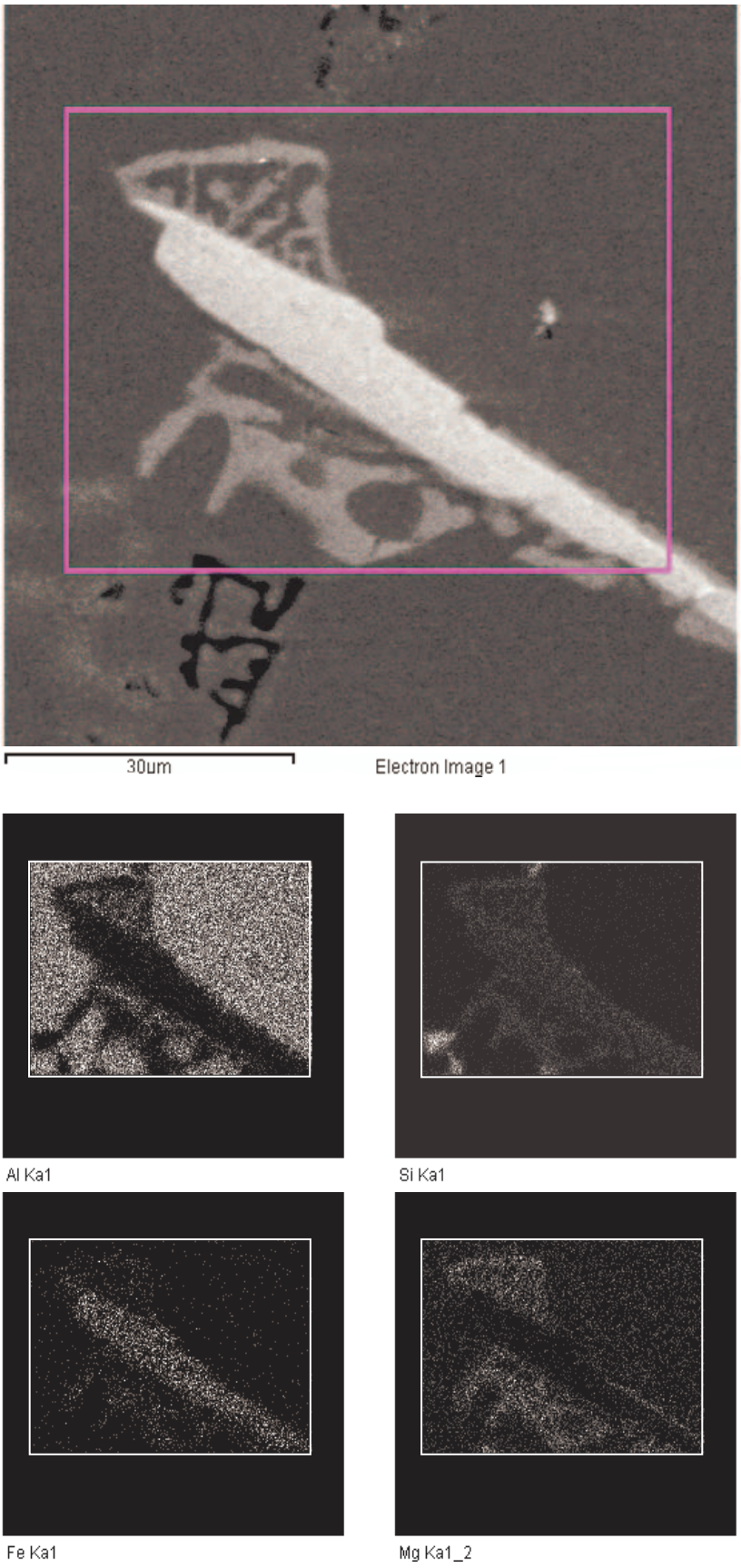

Fig. 4. 1.33: SEM BSE image and corresponding elemental maps for the selected area for the as-cast MHD A356 alloy.

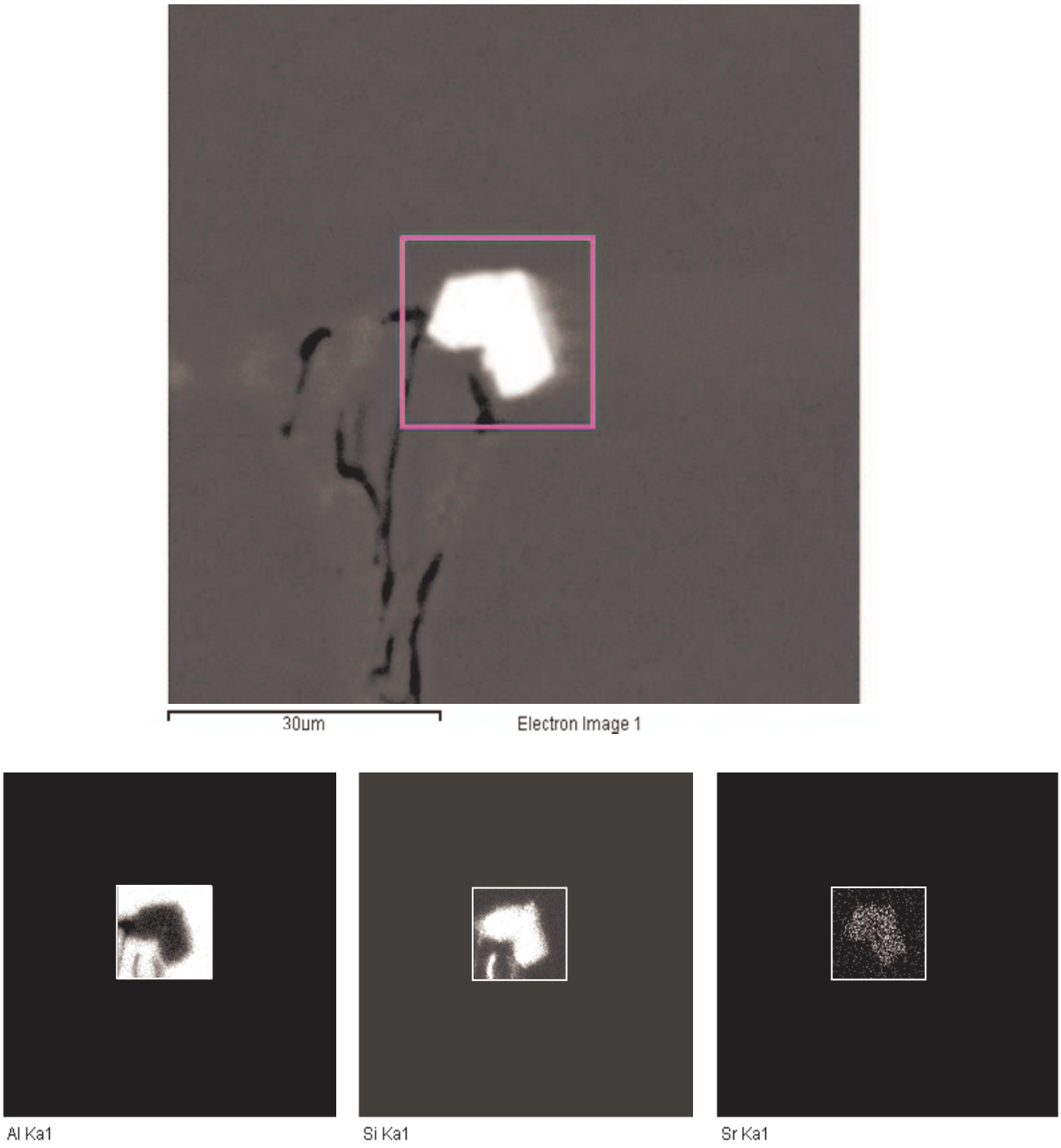

Fig. 4.1.34: SEM BSE image and corresponding elemental maps for the selected area for the as-cast MHD A356 alloy.

4.2. FRACTION SOLID AND FRACTION SOLID SENSITIVITY

In this section the fraction solid was calculated from the DSC heat flow, specific heat and enthalpy data. Calculating the fraction solid from the DSC heat flow and specific heat data is achieved by using the partial area method, whilst that from the enthalpy data requires the enthalpy difference of phases with varying amount of solid as described by Dong et al.[162] and discussed in Section 2.7.2. In the latter part of this section the fraction solid sensitivity and its behaviour with change in temperature has been determined.

4.2.1 Fraction Solid

Using the heat flow data the fraction solid curve was calculated for the NGM AlSi7Mg alloy for both heating and cooling as shown in Fig. 4.2.1(a). It shows the temperature lag and resulting change in fraction solid at a particular temperature. The reproducibility of the results or curves during heating and cooling for the DSC heat flow data for the NGM AlSi7Mg alloy is also visible. The comparison of the heating and cooling curves for the DSC heat flow data for both the COM AlSi7Mg and MHD A356 alloys are shown in Fig. 4.2.1(b) and 4.2.1(c) respectively.

The fraction solid calculated from the specific heat data for the heating and cooling of the NGM AlSi7Mg alloy is given in Fig. 4.2.2(a). The reproducibility which was assessed using different samples could also be observed for both the heating and cooling traces. A comparison of the fraction solid calculated for the heating and cooling of the COM AlSi7Mg and MHD A356 alloy is shown in Figs. 4.2.2(b) and 4.2.2(c), respectively.

The fraction solid which was calculated from the enthalpy data is given in Fig. 4.2.3(a) for both heating and cooling, of the NGM AlSi7Mg alloy. The reproducibility was assessed using different samples and a comparison for heating and cooling has also been made in Fig. 4.2.3(a). A comparison of the fraction solid

calculated for heating and cooling of the COM AlSi7Mg and MHD A356 alloy is shown in Figs. 4.2.3(b) and 4.2.3(c), respectively.

It can be observed in Figs. 4.2.1 to 4.2.3 that the curves change suddenly when the eutectic phase starts to solidify on cooling or melt on heating. This change occurs over a temperature range during heating or cooling.

The variation in transition temperature and corresponding fraction solid within samples for the NGM AlSi7Mg, COM AlSi7Mg and MHD A356 alloys, calculated on the basis of DSC heat flow, specific heat and enthalpy data are given in Tables 4.2.1, 4.2.2 and 4.2.3, respectively. The average temperature range and corresponding fraction solid range is given in Table 4.2.4 and discussed below.

Based on the DSC heat flow data for the NGM AlSi7Mg alloy the temperature ranges are: from 583.3 to 585.2 °C for a fraction solid change from 0.393 to 0.378 during heating, and, from 573.3 to 574.2 °C for a fraction solid change from 0.447 to 0.439 during cooling. The transition temperature ranges for the COM AlSi7Mg alloy are: from 578.4 to 581.5 °C for a fraction solid change from 0.433 to 0.420 during heating; and, from 566.3 to 568.0 °C for a fraction solid change from 0.480 to 0.465 during cooling. Similarly the transition occurs for the MHD A356 alloy at temperatures from 579.8 to 581.5 °C for a fraction solid change from 0.435 to 0.414 during heating and 566.5 to 568.2 °C for a fraction solid change from 0.493 to 0.473 during cooling (see Table 4.2.4).

Based on the DSC specific heat data, the transition temperature for the NGM AlSi7Mg alloy occurred between 583.11 and 585.2 °C for a fraction solid change of 0.409 to 0.392 during heating and over a temperature range from 573.9 to 574.3 °C for a fraction solid change from 0.441 to 0.443 for cooling. For the COM AlSi7Mg alloy the transition occurred from 578.5 to 581.0 °C for a fraction solid of 0.433 to 0.428 on heating and from 566.0 to 568.0 °C for a fraction solid of 0.484 to 0.480 on cooling. Similarly, for the MHD A356 alloy, transition occurred from 579.3 to 581.6 °C for a fraction solid of 0.434 to 0.426 on heating and over a temperature range from 566.4 to 568.2 °C for a fraction solid change of 0.490 to 0.468 on cooling (see Table 4.2.4).

Based on the DSC enthalpy data, for the NGM AlSi7Mg alloy the transition occurred from 583.3 to 584.9 °C over a fraction solid change of 0.405 to 0.401 during heating and from 573.1 to 574.1 °C over a fraction solid change of 0.450 to 0.414 during cooling. This transformation occurred for the COM AlSi7Mg alloy from 578.6 to 581.1 °C for a fraction solid of 0.450 to 0.430 during heating and from 566.1 to 566.4 °C for a fraction solid of 0.508 to 0.464 during cooling. Similarly for the MHD A356 alloy the transition occurred from 579.6 to 581.5 °C for a fraction solid from 0.441 to 0.438 during heating and from 566.4 to 568.1 °C for a fraction solid of 0.496 to 0.446 during cooling (see Table 4.2.4).

4.2.2 Fraction Solid Sensitivity

The change in fraction solid with the change in temperature within a specific interval is called fraction solid sensitivity (see Section 2.7). It can be denoted as $\left(df_s/dT\right)_x$ where x is the mid point of the fraction solid range i.e. in this study $\left(df_s/dT\right)_{0.2}$ is the ratio of change in fraction solid between the 0.1 to 0.3 fraction solid with its corresponding change in temperature, for which 0.2 is the middle point. The fraction solid sensitivity gives an indication of how much the fraction solid value is sensitive to the operating temperature fluctuations in an industrial set-up. The lower the sensitivity of the fraction solid in a particular range, the greater will be the flexibility in the processing of the alloy within that particular temperature and fraction solid range.

For DSC Heat Flow Data

The temperature corresponding to the specific fraction solid calculated on the basis of DSC heat flow data for the NGM AlSi7Mg alloy shown in Fig. 4.2.1(a), is given in Table 4.2.5 and the corresponding fraction solid sensitivity, is given in Table 4.2.6 for heating and in Tables 4.2.7 and 4.2.8 for cooling, respectively. The data given below is analysed on the basis of average values.

For the NGM AlSi7Mg alloy, when analyzing the DSC heat flow data for heating, the fraction solid sensitivity value decreases from 0.0123 at a fraction solid of 0.2 to 0.0097 at a fraction solid of 0.3. It then increases to 0.1044 at a fraction solid of 0.6 and decreases again to 0.0597 for a fraction solid of 0.8. However, for the cooling of the NGM AlSi7Mg alloy the fraction solid sensitivity value based on the DSC heat flow data, decreases from 0.0163 for a fraction solid of 0.2 to 0.0094 for a fraction solid of 0.3. It then increased to 0.0756 for a fraction solid of 0.7 and then again decreased to 0.0655 for a fraction solid of 0.8.

The temperature corresponding to the specific fraction solid calculated on the basis of DSC heat flow data for the COM AlSi7Mg alloy shown in Fig. 4.2.1(b), is given in Table 4.2.9 and the corresponding fraction solid sensitivity, is given in Table 4.2.10 for heating and in Tables 4.2.11 and 4.2.12 for cooling respectively. The data given below is analysed on the basis of average values.

For the COM AlSi7Mg alloy the fraction solid sensitivity during heating based on the heat flow data shows that, the sensitivity value decreases from 0.0120 for a fraction solid of 0.2 to 0.0088 for a fraction solid of 0.3 which increases to 0.1248 for a fraction solid of 0.6 and then again decreases to 0.0506 for a fraction solid of 0.8. On cooling, the sensitivity value decreases from 0.0124 for a fraction solid of 0.2 fraction solid to 0.0074 for a fraction solid of 0.4 which increased to 0.0916 for a fraction solid of 0.6 fraction solid and again decreased to 0.0558 for a fraction solid of 0.8.

The temperature corresponding to the specific fraction solid calculated on the basis of DSC heat flow data for the MHD A356 alloy shown in Fig. 4.2.1(c), is given in Table 4.2.13 and the corresponding fraction solid sensitivity, is given in Table 4.2.14 for heating and in Tables 4.2.15 and 4.2.16 for cooling respectively. The data given below is analysed on the basis of average values.

On heating of the MHD A356 alloy the fraction solid sensitivity, based on the DSC heat flow data, showed a decrease in value from 0.0124 to 0.0092 for a fraction solid of 0.2 to 0.3 respectively, then increased to 0.960 at a fraction solid of 0.6 and again decreased to 0.0491 at a fraction solid of 0.8. On cooling, the sensitivity value decreased from 0.0137 at 0.2 to 0.0074 at 0.4 fraction solid, which then increased to

0.0748 at a fraction solid of 0.7 and again decreased to 0.0592 at a fraction solid of 0.8.

The fraction solid sensitivity with respect to fraction solid and temperature calculated on the basis of DSC heat flow data both for heating and cooling for all the three alloys is compared in Figs. 4.2.4(a) and 4.2.5(a) respectively. The figures also show and compare different criteria suggested by Fan et al.[166,167] and Liu et al.[23].

For Specific Heat Flow data

The temperature corresponding to the specific fraction solid calculated on the basis of specific heat data for the NGM AlSi7Mg alloy shown in Fig. 4.2.2(a), is given in Table 4.2.17 and the corresponding fraction solid sensitivity, is given in Table 4.2.18 for heating and in Tables 4.2.19 and 4.2.20 for cooling respectively. The data given below is analysed on the basis of average values.

The fraction solid sensitivity based on the specific heat for heating shows that values for the NGM AlSi7Mg alloy decreased from 0.0125 at a fraction solid of 0.2 to 0.0097 at a fraction solid of 0.3, which then increased to 0.1072 at a fraction solid of 0.6 and then decreased to 0.590 at a fraction solid of 0.8. However, on cooling the sensitivity value decreased from 0.0163 at a fraction solid of 0.2 to 0.0093 at a fraction solid of 0.3, which then increased to 0.0721 at a fraction solid of 0.7 and again decreased to 0.0646 at a fraction solid of 0.8.

The temperature corresponding to the specific fraction solid calculated on the basis of specific heat data for the COM AlSi7Mg alloy shown in Fig. 4.2.2(b), is given in Table 4.2.21 and the corresponding fraction solid sensitivity, is given in Table 4.2.22 for heating and in Tables 4.2.23 and 4.2.24 for cooling respectively. The data given below is analysed on the basis of average values.

The fraction solid sensitivity of the COM AlSi7Mg alloy, during heating up, shows that a sensitivity value which decreased from 0.0125 at a fraction solid of 0.2 to 0.0092 at a fraction solid of 0.3, before increasing to 0.0879 at a fraction solid of 0.6 and again decreased to 0.0460 at a fraction solid of 0.8. On cooling the value decreased from 0.0124 at a fraction solid of 0.2 to 0.0074 at a fraction solid of 0.4,

which then increased to 0.0750 at a fraction solid of 0.7 and again decreased to 0.0446 at a fraction solid of 0.8.

The temperature corresponding to the specific fraction solid calculated on the basis of specific heat data for the MHD A356 alloy shown in Fig. 4.2.2(c), is given in Table 4.2.25 and the corresponding fraction solid sensitivity, is given in Table 4.2.26 for heating and in Tables 4.2.27 and 4.2.28 for cooling respectively. The data given below is analysed on the basis of average values.

The fraction solid sensitivity calculated, based on the specific heat data for the MHD A356 alloy during heating showed that the sensitivity value decreased from 0.0125 at a fraction solid of 0.2 to 0.0092 at a fraction solid of 0.3, then increased to 0.0947 at a fraction solid of 0.6 and then again decreased to 0.0492 at a fraction solid of 0.8. Similarly on cooling the value decreased from 0.0135 at a fraction solid of 0.2 to 0.0075 at a fraction solid of 0.4, it then increased to 0.0768 at a fraction solid of 0.7 and again decreased to 0.0571 at a fraction solid of 0.8.

The fraction solid sensitivity with respect to fraction solid and temperature calculated on the basis of specific heat data both for heating and cooling for all the three alloys is compared in Figs. 4.2.4(b) and 4.2.5(b) respectively. The figures also show and compare different criteria suggested by Fan et al.[166,167] and Liu et al.[2].

For Enthalpy Data

The temperature corresponding to the specific fraction solid calculated on the basis of enthalpy data for the NGM AlSi7Mg alloy shown in Fig. 4.2.3(a), is given in Table 4.2.29 and the corresponding fraction solid sensitivity, is given in Table 4.2.30 for heating and in Tables 4.2.31 and 4.2.32 for cooling respectively. The data given below is analysed on the basis of average values.

The enthalpy based data for the NGM AlSi7Mg alloy shows that on heating, the fraction solid sensitivity value decreased from 0.0131 at a fraction solid of 0.2 to 0.0099 at a fraction solid of 0.3, then increased to 0.1015 at a fraction solid of 0.6 which then decreased to 0.0595 at a fraction solid of 0.8. While on cooling the sensitivity value decreased from 0.0159 at a fraction solid of 0.2 to 0.0089 at a

fraction solid of 0.3, which then increased to 0.0738 at a fraction solid of 0.7 and then again decreased to 0.0631 at for a fraction solid of 0.8.

The temperature corresponding to the specific fraction solid calculated on the basis of enthalpy data for the COM AlSi7Mg alloy shown in Fig. 4.2.3(b), is given in Table 4.2.33 and the corresponding fraction solid sensitivity, is given in Table 4.2.34 for heating and in Tables 4.2.35 and 4.2.36 for cooling respectively. The data given below is analysed on the basis of average values.

The enthalpy data showed that the fraction solid sensitivity value for the COM AlSi7Mg alloy decreased from 0.0129 at a fraction solid of 0.2 to 0.0096 at a fraction solid of 0.3, which then increased to 0.0888 at a fraction solid of 0.6 and again decreased to 0.0455 at a fraction solid of 0.8, based on the enthalpy data. Similarly on cooling the sensitivity value decreased from 0.0105 at a fraction solid of 0.2 to 0.0087 at a fraction solid of 0.3, which then increased to 0.0745 at a fraction solid of 0.7 and then decreased again to 0.0465 at a fraction solid of 0.8.

The temperature corresponding to the specific fraction solid calculated on the basis of enthalpy data for the MHD A356 alloy shown in Fig. 4.2.3(c), is given in Table 4.2.37 and the corresponding fraction solid sensitivity, is given in Table 4.2.38 for heating and in Tables 4.2.39 and 4.2.40 for cooling respectively. The data given below is analysed on the basis of average values.

On heating the sensitivity value at first decreased from 0.0130 at a fraction solid of 0.2 to 0.0095 at a fraction solid of 0.3, and then increased to 0.0939 at a fraction solid of 0.6 and again decreased to 0.0493 at a fraction solid of 0.8. While on cooling the sensitivity value first decreased to 0.0133 at a fraction solid of 0.2 to 0.0076 at a fraction solid of 0.4, and then increased to 0.0747 at a fraction solid of 0.7 and again decreased to 0.0579 at a fraction solid of 0.8.

The fraction solid sensitivity with respect to fraction solid and temperature calculated on the basis of enthalpy data both for heating and cooling for all the three alloys is compared in Figs. 4.2.4(c) and 4.2.5(c) respectively. The figures also show and compare different criteria suggested by Fan et al.[166,167] and Liu et al.[2].

With regard to the above mentioned criteria, which are necessary for the processing of different materials (as proposed by the different authors and discussed above), the fraction solid sensitivity criteria were used in this study to determine the suitability and calculate the processing temperature range of the alloys. The data obtained from Figs. 4.2.4 to 4.2.5 is given in Tables 4.2.41 and 4.2.42.

The data in Tables 4.2.41 and 4.2.42 showed that the lower limit for the processing of the NGM AlSi7Mg and the MHD A356 alloy corresponds to a lower fraction solid and higher processing temperature, whilst the COM AlSi7Mg alloy can be processed at a relatively higher fraction solid and lower temperature for both the 0.015 and 0.03 fraction solid sensitivity criteria. However, the minimum working temperature does not differ too much for these alloys either in heating or in cooling. The maximum limit for fraction solid shown in Tables 4.2.41 and 4.2.42 give the mid value of ± 0.1 fraction solid as used for the calculation of fraction solid sensitivity, that is, the fraction solid sensitivity at 0.4 fraction solid represents a trend over a range of 0.3 to 0.5 fraction solid. So, for a fraction solid sensitivity criterion of 0.15, the working range for the temperature can be lowered by up to 50% fraction solid, whilst increasing the fraction solid sensitivity to 0.03 results in a decrease in the lower temperature limit to a fraction solid of 60%.

4.2.3 Summary

The fraction solid, as calculated from the DSC traces for the heat flow, specific heat and enthalpy data showed that:

1. The temperature for the same fraction solid differs by up to 5 °C in the primary phase melting temperature range on heating and cooling, while it varies by up to 15 °C during solidification of the eutectic on heating and cooling due to the temperature lag during DSC measurement due to imposed heating/cooling rate for all the alloys.
2. For the cooling data a sudden drop in the fraction solid curves was observed at: ~ 0.20 fraction solid for the NGM AlSi7Mg alloy; ~ 0.05 fraction solid for the COM AlSi7Mg alloy; and ~ 0.10 fraction solid for the MHD A356 alloy. The phenomenon may be due undercooling.

3. The fraction solid sensitivity criterion of a value of 0.03 provides a wider processing range as compared to a value of 0.015 with respect to the fraction solid, both for heating and cooling data, for all alloys.
4. The fraction solid sensitivity criterion of a value of 0.03 provides a wider processing temperature range as compared to a value of 0.015 with respect to the fraction solid, for cooling data for the NGM AlSi7Mg alloy. For the other alloys a wider temperature range was observed during heating.
5. At a fraction solid of < 0.4 all the alloys showed similar fraction solid sensitivity.
6. The fraction solid sensitivity for the NGM AlSi7Mg alloy is higher than that for other alloys at a given fraction solid during both heating and cooling with the difference being greater during heating.
7. The lower workable fraction solid limit for the NGM AlSi7Mg alloy is less than that of the COM AlSi7Mg and MHD A356 alloys.
8. The lower working temperature limit of the NGM AlSi7Mg alloy is higher than that of the other alloys.
9. During heating, the lower working temperature limit for the NGM AlSi7Mg alloy appears to be constant for both a fraction solid sensitivity criteria of 0.03 and 0.015. However, on cooling the lower working temperature limit is reduced by ~ 5 °C for a fraction solid sensitivity criterion of 0.03 compared to a fraction solid sensitivity criterion of 0.05. The COM AlSi7Mg and MHD AlSi7Mg alloys showed an opposite behaviour.
10. The lowest working temperature limit for the NGM AlSi7Mg alloy was found to be ~ 585 °C for reheating.

4.2.4 Tables

Table 4.2.1: The transition temperature and corresponding fraction solid, based on the DSC heat flow data.

Alloy	Sample	Heating		Cooling	
		Temperature range (℃)	Fraction solid	Temperature Range ℃)	Fraction solid
NGM	1	584.4 - 585.2	0.398 - 0.385	574.0 - 574.2	0.439 - 0.440
AlSi7Mg	2	583.4 - 584.2	0.393 - 0.378	573.3 - 573.6	0.443 - 0.438
	3	583.3 - 584.4	0.413 - 0.392	573.4 - 573.9	0.453 - 0.447
COM	1	579.2 - 580.7	0.421 - 0.397	566.3 - 567.1	0.485 - 0.477
AlSi7Mg	2	580.6 - 581.5	0.425 - 0.412	566.2 - 566.3	0.482 - 0.480
	3	579.2 - 579.6	0.420 - 0.410	567.3 - 568.0	0.473 - 0.468
	4	578.4 - 579.0	0.450 - 0.433	566.7 - 567.3	0.465 - 0.452
MHD	1	581.2 - 581.5	0.414 - 0.408	567.9 - 568.2	0.474 - 0.464
A356	2	579.6 - 580.3	0.432 - 0.414	567.1 - 567.4	0.473 - 0.469
	3	579.9 - 580.4	0.441 - 0.435	566.5 - 567.0	0.500 - 0.493
	4	579.8 - 580.4	0.443 - 0.432	566.8 - 567.2	0.496 - 0.487

Table 4.2.2: The transition temperature and corresponding fraction solid, based on the DSC specific heat data.

Alloy	Sample	Heating		Cooling	
		Temperature range (℃)	Fraction solid	Temperature Range ℃)	Fraction solid
NGM	1	584.1 - 585.2	0.417 - 0.392	573.9 - 574.3	0.442 - 0.438
AlSi7Mg	2	583.1 - 584.1	0.409 - 0.386	573.2 - 573.8	0.441 - 0.434
	3	583.1 - 584.4	0.420 - 0.392	573.5 - 573.9	0.448 - 0.443
COM	1	579.3 - 580.3	0.442 - 0.425	566.1 - 566.7	0.491 - 0.480
AlSi7Mg	2	580.1 - 581.0	0.428 - 0.419	566.1 - 567.0	0.484 - 0.475
	3	579.1 - 579.5	0.429 - 0.413	566.9 - 568.0	0.488 - 0.466
	4	578.5 - 579.0	0.441 - 0.433	566.4 - 567.2	0.485 - 0.469
MHD	1	580.6 - 581.6	0.426 - 0.405	567.7 - 568.2	0.472 - 0.462
A356	2	579.6 - 580.2	0.429 - 0.411	566.9 - 567.2	0.468 - 0.463
	3	579.6 - 580.4	0.447 - 0.434	566.4 - 567.0	0.500 - 0.490
	4	579.3 - 580.1	0.458 - 0.434	566.5 - 566.9	0.499 - 0.490

Table 4.2.3: The transition temperature and corresponding fraction solid, based on the DSC enthalpy data.

Alloy	Sample	Heating		Cooling	
		Temperature range (℃)	Fraction solid	Temperature Range ℃)	Fraction solid
NGM	1	584.7 - 584.9	0.405 - 0.401	573.9 - 574.1	0.452 - 0.450
AlSi7Mg	2	583.3 - 584.3	0.426 - 0.407	573.3 - 573.7	0.414 - 0.409
	3	583.7 - 584.0	0.418 - 0.413	573.1 - 573.8	0.443 - 0.431
COM	1	579.7 - 580.1	0.430 - 0.424	566.2 - 566.4	0.512 - 0.508
AlSi7Mg	2	580.3 - 581.1	0.445 - 0.429	566.1 - 566.7	0.467 - 0.462
	3	579.3 - 579.7	0.456 - 0.450	566.7 - 567.4	0.464 - 0.440
	4	578.6 - 579.2	0.444 - 0.431	566.7 - 567.4	0.464 - 0.450
MHD	1	580.8 - 581.5	0.439 - 0.422	567.7 - 568.1	0.446 - 0.440
A356	2	579.6 - 580.2	0.438 - 0.419	566.8 - 567.6	0.468 - 0.458
	3	579.9 - 580.4	0.447 - 0.441	566.4 - 566.9	0.505 - 0.496
	4	579.8 - 580.2	0.443 - 0.436	566.6 - 567.1	0.499 - 0.488

Table 4.2.4: The average transition temperature and corresponding fraction solid, based on the data given in tables 4.2.1 to 4.2.3.

	Alloy	Heating		Cooling	
		Temperature range (℃)	Fraction solid	Temperature range ℃)	Fraction solid
Heat flow	NGM AlSi7Mg	583.3 - 585.2	0.393 - 0.378	573.3 - 574.2	0.447 - 0.439
	COM AlSi7Mg	578.4 - 581.5	0.433 - 0.420	566.3 - 568.0	0.480 - 0.465
	MHD A356	579.8 - 581.5	0.435 - 0.414	566.5 - 568.2	0.493 - 0.473
Specific heat	NGM AlSi7Mg	583.1 - 585.2	0.409 - 0.392	573.9 - 574.3	0.443 - 0.441
	COM AlSi7Mg	578.5 - 581.0	0.433 - 0.428	566.0 - 568.0	0.484 - 0.480
	MHD A356	579.3 - 581.6	0.434 - 0.426	566.4 - 568.2	0.490 - 0.468
Enthalpy	NGM AlSi7Mg	583.3 - 584.9	0.405 - 0.401	573.1 - 574.1	0.450 - 0.414
	COM AlSi7Mg	578.6 - 581.1	0.450 - 0.430	566.1 - 566.4	0.508 - 0.464
	MHD A356	579.6 - 581.5	0.441 - 0.438	566.4 - 568.1	0.496 - 0.446

Table 4.2.5: The fraction solid calculated for the NGM AlSi7Mg alloy on heating based on the DSC heat flow data presented in Fig. 4.2.1(a).

	Temperature ℃			
Fraction solid	Sample 1	Sample 2	Sample 3	Average
0.1	611.7	610.7	611.7	611.4
0.2	604.7	603.7	604.9	604.4
0.3	595.6	593.8	596.0	595.1
0.4	584.6	583.2	583.9	583.9
0.5	583.0	581.9	582.1	582.4
0.6	582.1	581.1	581.2	581.5
0.7	581.0	580.0	580.3	580.4
0.8	579.7	578.8	578.8	579.1
0.9	577.7	576.7	576.9	577.1

Table 4.2.6: The fraction solid sensitivity for the NGM AlSi7Mg alloy on heating, based on the DSC heat flow data given in Table 4.2.5.

Fraction solid sensitivity	Sample1	Sample 2	Sample3	Average
$\left(df_s/dT\right)_{0.2}$	0.0124	0.0118	0.0127	0.0123
$\left(df_s/dT\right)_{0.3}$	0.0100	0.0097	0.0095	0.0097
$\left(df_s/dT\right)_{0.4}$	0.0159	0.0169	0.0145	0.0157
$\left(df_s/dT\right)_{0.5}$	0.0800	0.0930	0.0735	0.0822
$\left(df_s/dT\right)_{0.6}$	0.1020	0.1031	0.1081	0.1044
$\left(df_s/dT\right)_{0.7}$	0.0826	0.0866	0.0866	0.0853
$\left(df_s/dT\right)_{0.8}$	0.0593	0.0610	0.0588	0.0597

Table 4.2.7: The fraction solid calculated for the NGM AlSi7Mg alloy on cooling, based on the DSC heat flow data presented in Fig. 4.2.1(a).

	Temperature °C			
Fraction solid	Sample 1	Sample 2	Sample 3	Average
0.1	603.7	606.3	606.2	605.4
0.2	601.6	601.5	602.6	601.9
0.3	592.9	592.3	593.9	593.0
0.4	580.5	579.6	581.5	580.5
0.5	572.7	572.0	572.3	572.3
0.6	571.1	570.3	571.0	570.8
0.7	569.6	569.0	569.6	569.4
0.8	568.5	567.6	568.4	568.1
0.9	566.6	565.7	566.7	566.3

Table 4.2.8: The fraction solid sensitivity for the NGM AlSi7Mg alloy on cooling, based on the DSC heat flow data given in table 4.2.7.

Fraction solid sensitivity	Sample1	Sample 2	Sample3	Average
$\left(df_s/dT\right)_{0.2}$	0.0184	0.0143	0.0162	0.0163
$\left(df_s/dT\right)_{0.3}$	0.0095	0.0091	0.0095	0.0094
$\left(df_s/dT\right)_{0.4}$	0.0099	0.0098	0.0093	0.0097
$\left(df_s/dT\right)_{0.5}$	0.0213	0.0215	0.0191	0.0206
$\left(df_s/dT\right)_{0.6}$	0.0645	0.0667	0.0735	0.0683
$\left(df_s/dT\right)_{0.7}$	0.0766	0.0735	0.0766	0.0756
$\left(df_s/dT\right)_{0.8}$	0.0669	0.0608	0.0687	0.0655

Table 4.2.9: The fraction solid calculated for the COM AlSi7Mg alloy on heating, based on the DSC heat flow data presented in Fig. 4.2.1(b).

	Temperature ℃				
Fraction solid	Sample 1	Sample 2	Sample 3	Sample 4	Average
0.1	611.4	612.3	611.9	612.1	611.9
0.2	604.3	605.1	604.7	605.2	604.8
0.3	594.0	596.0	594.9	596.2	595.3
0.4	580.4	583.0	581.1	583.8	582.1
0.5	578.3	579.2	578.1	577.8	578.3
0.6	577.3	579.2	577.0	576.8	577.6
0.7	576.0	578.4	575.9	575.5	576.4
0.8	574.2	577.0	574.2	573.8	574.8
0.9	571.5	575.3	571.7	571.2	572.4

Table 4.2.10: The fraction solid sensitivity for the COM AlSi7Mg alloy on heating, based on the DSC heat flow data given in table 4.2.9.

Fraction solid sensitivity	Sample 1	Sample 2	Sample 3	Sample 4	Average
$\left(df_s/dT\right)_{0.2}$	0.0115	0.0123	0.0118	0.0126	0.0120
$\left(df_s/dT\right)_{0.3}$	0.0084	0.0090	0.0085	0.0093	0.0088
$\left(df_s/dT\right)_{0.4}$	0.0127	0.0119	0.0118	0.0109	0.0118
$\left(df_s/dT\right)_{0.5}$	0.0645	0.0529	0.0490	0.0287	0.0488
$\left(df_s/dT\right)_{0.6}$	0.0855	0.2298	0.0943	0.0897	0.1248
$\left(df_s/dT\right)_{0.7}$	0.0645	0.0897	0.0714	0.0662	0.0730
$\left(df_s/dT\right)_{0.8}$	0.0449	0.0645	0.0468	0.0460	0.0506

Table 4.2.11: The fraction solid calculated for the COM AlSi7Mg alloy on cooling, based on the DSC heat flow data presented in Fig. 4.2.1(b).

	Temperature ℃				
Fraction solid	Sample 1	Sample 2	Sample 3	Sample 4	Average
0.1	609.3	609.1	609.3	609.1	609.2
0.2	602.5	602.5	602.4	602.4	602.4
0.3	593.2	593.4	592.9	592.5	593.0
0.4	580.4	580.4	580.3	577.8	579.7
0.5	565.7	565.6	566.7	565.8	566.0
0.6	563.9	565.7	565.4	564.8	564.9
0.7	562.8	564.0	564.2	563.6	563.7
0.8	560.8	562.7	562.9	562.4	562.2
0.9	557.9	561.2	560.1	560.4	559.9

Table 4.2.12: The fraction solid sensitivity for the COM AlSi7Mg alloy on cooling, based on the DSC heat flow data given in table 4.2.11.

Fraction solid sensitivity	Sample 1	Sample 2	Sample 3	Sample 4	Average
$\left(df_s/dT\right)_{0.2}$	0.0124	0.0127	0.0122	0.0121	0.0124
$\left(df_s/dT\right)_{0.3}$	0.0090	0.0091	0.0090	0.0081	0.0088
$\left(df_s/dT\right)_{0.4}$	0.0073	0.0072	0.0076	0.0075	0.0074
$\left(df_s/dT\right)_{0.5}$	0.0121	0.0136	0.0134	0.0154	0.0136
$\left(df_s/dT\right)_{0.6}$	0.0687	0.1290	0.0791	0.0897	0.0916
$\left(df_s/dT\right)_{0.7}$	0.0645	0.0669	0.0791	0.0858	0.0741
$\left(df_s/dT\right)_{0.8}$	0.0413	0.0714	0.0481	0.0623	0.0558

Table 4.2.13: The fraction solid calculated for the MHD A356 alloy on heating based on the DSC heat flow data presented in Fig. 4.2.1(c).

	Temperature ℃				
Fraction solid	Sample 1	Sample 2	Sample 3	Sample 4	Average
0.1	611.6	611.3	613.3	613.3	612.4
0.2	604.5	604.3	606.7	606.4	605.5
0.3	594.9	595.0	597.6	597.6	596.3
0.4	582.0	582.0	585.4	584.9	583.6
0.5	579.7	578.7	578.9	578.8	579.0
0.6	579.0	577.9	578.0	577.9	578.2
0.7	577.8	576.6	576.8	576.7	577.3
0.8	575.9	574.8	575.3	575.1	575.3
0.9	573.4	572.2	572.9	572.9	572.9

Table 4.2.14: The fraction solid sensitivity for the MHD A356 alloy on heating, based on the DSC heat flow data given in table 4.2.13.

Fraction solid sensitivity	Sample 1	Sample 2	Sample 3	Sample 4	Average
$\left(df_s/dT\right)_{0.2}$	0.0120	0.0123	0.0127	0.0128	0.0124
$\left(df_s/dT\right)_{0.3}$	0.0089	0.0090	0.0094	0.0093	0.0092
$\left(df_s/dT\right)_{0.4}$	0.0131	0.0123	0.0107	0.0106	0.0117
$\left(df_s/dT\right)_{0.5}$	0.0669	0.0482	0.0271	0.0286	0.0427
$\left(df_s/dT\right)_{0.6}$	0.1036	0.0930	0.0943	0.0930	0.0960
$\left(df_s/dT\right)_{0.7}$	0.0639	0.0662	0.0717	0.0707	0.0681
$\left(df_s/dT\right)_{0.8}$	0.0460	0.0460	0.0514	0.053	0.0491

Table 4.2.15: The fraction solid calculated for the MHD A356 alloy on cooling, based on the DSC heat flow data presented in Fig. 4.2.1(c).

	Temperature ℃				
Fraction solid	Sample 1	Sample 2	Sample 3	Sample 4	Average
0.1	607.0	606.0	609.5	609.8	608.1
0.2	601.6	601.4	603.6	603.9	602.6
0.3	592.3	592.3	594.6	594.8	593.5
0.4	579.5	579.6	582.6	582.6	581.1
0.5	567.0	566.2	566.4	566.7	566.6
0.6	565.5	564.5	564.4	564.7	564.8
0.7	564.1	563.0	563.0	563.2	563.3
0.8	562.8	561.9	561.7	562.0	562.1
0.9	560.5	559.8	559.5	560.0	559.9

Table 4.2.16: The fraction solid sensitivity for the MHD A356 alloy on cooling based on the DSC heat flow data given in table 4.2.15.

Fraction solid sensitivity	Sample 1	Sample 2	Sample 3	Sample 4	Average
$\left(df_s/dT\right)_{0.2}$	0.0136	0.0146	0.0134	0.0134	0.0137
$\left(df_s/dT\right)_{0.3}$	0.0090	0.0092	0.0095	0.0094	0.0093
$\left(df_s/dT\right)_{0.4}$	0.0079	0.0077	0.0071	0.0071	0.0074
$\left(df_s/dT\right)_{0.5}$	0.0143	0.0132	0.0110	0.0112	0.0124
$\left(df_s/dT\right)_{0.6}$	0.0690	0.0623	0.0588	0.0570	0.0618
$\left(df_s/dT\right)_{0.7}$	0.0758	0.0766	0.0732	0.0735	0.0748
$\left(df_s/dT\right)_{0.8}$	0.0557	0.0629	0.0557	0.0625	0.0592

Table 4.2.17: The fraction solid calculated for the NGM AlSi7Mg alloy on heating, based on the DSC specific heat data presented in Fig. 4.2.2(a).

	Temperature ℃			
Fraction solid	Sample 1	Sample 2	Sample 3	Average
0.1	612.1	610.9	611.6	611.5
0.2	605.1	603.8	604.9	604.6
0.3	596.1	594.6	595.8	595.5
0.4	584.6	583.4	583.9	584.0
0.5	583.0	581.9	582.1	582.4
0.6	582.1	581.2	581.2	581.5
0.7	581.2	580.1	580.2	580.5
0.8	579.7	578.8	578.9	579.1
0.9	577.7	576.7	576.9	577.1

Table 4.2.18: The fraction solid sensitivity for the NGM AlSi7Mg alloy on heating based on the DSC specific heat data given in table 4.2.17.

Fraction solid sensitivity	Sample1	Sample 2	Sample3	Average
$\left(df_s/dT\right)_{0.2}$	0.0125	0.0123	0.0127	0.0125
$\left(df_s/dT\right)_{0.3}$	0.0098	0.0098	0.0095	0.0097
$\left(df_s/dT\right)_{0.4}$	0.0153	0.0157	0.0147	0.0152
$\left(df_s/dT\right)_{0.5}$	0.08	0.0897	0.0735	0.0811
$\left(df_s/dT\right)_{0.6}$	0.1081	0.1099	0.1036	0.1072
$\left(df_s/dT\right)_{0.7}$	0.0826	0.0826	0.0897	0.0850
$\left(df_s/dT\right)_{0.8}$	0.0575	0.0588	0.0608	0.0590

Table 4.2.19: The fraction solid calculated for the NGM AlSi7Mg alloy on cooling, based on the DSC specific heat data presented in Fig. 4.2.2(a).

	Temperature ℃			
Fraction solid	Sample 1	Sample 2	Sample 3	Average
0.1	603.7	606.3	606.3	605.4
0.2	601.4	601.3	602.3	601.7
0.3	593.0	592.4	593.7	593.0
0.4	580.2	579.5	581.1	580.3
0.5	572.6	571.9	572.3	572.3
0.6	571.1	570.4	571.1	570.9
0.7	569.6	569.0	569.6	569.4
0.8	568.4	567.6	568.3	568.1
0.9	566.5	565.8	566.6	566.3

Table 4.2.20: The fraction solid sensitivity for the NGM AlSi7Mg alloy on cooling, based on the DSC specific heat data given in table 4.2.19.

Fraction solid sensitivity	Sample1	Sample 2	Sample3	Average
$\left(df_s/dT\right)_{0.2}$	0.0186	0.0144	0.0159	0.0163
$\left(df_s/dT\right)_{0.3}$	0.0094	0.0092	0.0094	0.0093
$\left(df_s/dT\right)_{0.4}$	0.0098	0.0097	0.0094	0.0096
$\left(df_s/dT\right)_{0.5}$	0.0220	0.0220	0.0201	0.0213
$\left(df_s/dT\right)_{0.6}$	0.0669	0.0687	0.0735	0.0697
$\left(df_s/dT\right)_{0.7}$	0.0743	0.0714	0.0704	0.0721
$\left(df_s/dT\right)_{0.8}$	0.0645	0.0623	0.0669	0.0646

Table 4.2.21: The fraction solid calculated for the COM AlSi7Mg alloy on heating, based on the DSC specific heat data presented in Fig. 4.2.2(b).

	Temperature ℃				
Fraction solid	Sample 1	Sample 2	Sample 3	Sample 4	Average
0.1	612.3	612.1	612.3	612.2	612.2
0.2	605.3	605.1	605.2	605.1	605.2
0.3	596.3	595.9	596.1	596.4	596.2
0.4	583.6	583.2	582.8	583.8	583.4
0.5	578.5	579.2	578.2	577.8	578.4
0.6	577.5	578.4	577.1	576.7	577.4
0.7	576.2	577.0	575.8	575.6	576.2
0.8	574.4	575.1	574.1	573.8	574.4
0.9	571.6	572.2	571.7	571.4	571.8

Table 4.2.22: The fraction solid sensitivity for the COM AlSi7Mg alloy on heating, based on the DSC specific heat data given in table 4.2.21.

Fraction solid sensitivity	Sample 1	Sample 2	Sample 3	Sample 4	Average
$\left(df_s/dT\right)_{0.2}$	0.0125	0.0124	0.0124	0.0127	0.0125
$\left(df_s/dT\right)_{0.3}$	0.0092	0.0091	0.0089	0.0094	0.0092
$\left(df_s/dT\right)_{0.4}$	0.0113	0.0120	0.0112	0.0108	0.0113
$\left(df_s/dT\right)_{0.5}$	0.0327	0.0413	0.0350	0.0283	0.0343
$\left(df_s/dT\right)_{0.6}$	0.0866	0.0897	0.0855	0.0897	0.0879
$\left(df_s/dT\right)_{0.7}$	0.0645	0.0623	0.0667	0.0687	0.0656
$\left(df_s/dT\right)_{0.8}$	0.0457	0.0420	0.0481	0.0481	0.0460

Table 4.2.23: The fraction solid calculated for the COM AlSi7Mg alloy on cooling, based on the DSC specific heat data presented in Fig. 4.2.2(b).

	Temperature ℃				
Fraction solid	Sample 1	Sample 2	Sample 3	Sample 4	Average
0.1	609.3	609.1	609.2	609.7	609.2
0.2	602.4	602.2	602.2	602.1	602.2
0.3	593.4	593.4	592.7	592.5	593.0
0.4	580.6	580.5	579.4	579.3	580.0
0.5	565.8	565.5	566.6	566.1	566.0
0.6	564.0	564.1	565.3	564.8	564.5
0.7	562.7	562.6	564.2	563.6	563.3
0.8	561.1	561.2	562.9	562.3	561.9
0.9	557.8	558.1	559.9	559.3	558.8

Table 4.2.24: The fraction solid sensitivity for the COM AlSi7Mg alloy on cooling, based on the DSC specific heat data given in table 4.2.23.

Fraction solid sensitivity	Sample 1	Sample 2	Sample 3	Sample 4	Average
$\left(df_s/dT\right)_{0.2}$	0.0126	0.0127	0.0121	0.0120	0.0124
$\left(df_s/dT\right)_{0.3}$	0.0091	0.0092	0.0088	0.0088	0.0090
$\left(df_s/dT\right)_{0.4}$	0.0072	0.0072	0.0077	0.0076	0.0074
$\left(df_s/dT\right)_{0.5}$	0.0121	0.0122	0.0141	0.0137	0.0130
$\left(df_s/dT\right)_{0.6}$	0.0645	0.0687	0.0826	0.0791	0.0737
$\left(df_s/dT\right)_{0.7}$	0.0687	0.0687	0.0826	0.080	0.0750
$\left(df_s/dT\right)_{0.8}$	0.0413	0.0444	0.0468	0.0460	0.0446

Table 4.2.25: The fraction solid calculated for the MHD A356 alloy on heating, based on the DSC specific heat data presented in Fig. 4.2.2(c).

	Temperature ℃				
Fraction solid	Sample 1	Sample 2	Sample 3	Sample 4	Average
0.1	611.5	611.2	613.3	613.2	612.3
0.2	604.2	604.0	606.4	606.4	605.3
0.3	594.9	594.8	597.7	597.6	596.3
0.4	582.0	581.5	585.4	585.2	583.5
0.5	579.7	578.8	578.8	578.8	579.0
0.6	578.8	577.8	577.9	577.9	578.1
0.7	577.7	576.6	576.8	576.6	576.9
0.8	575.9	574.8	575.1	575.1	575.2
0.9	573.4	572.3	572.7	572.9	572.8

Table 4.2.26: The fraction solid sensitivity for the MHD A356 alloy on heating, based on the DSC specific heat data given in table 4.2.25.

Fraction solid sensitivity	Sample 1	Sample 2	Sample 3	Sample 4	Average
$\left(df_s/dT\right)_{0.2}$	0.0121	0.0122	0.012837	0.0127	0.0125
$\left(df_s/dT\right)_{0.3}$	0.0090	0.0089	0.009551	0.0094	0.0092
$\left(df_s/dT\right)_{0.4}$	0.0132	0.0124	0.010582	0.0107	0.0117
$\left(df_s/dT\right)_{0.5}$	0.0629	0.0545	0.026455	0.0271	0.0427
$\left(df_s/dT\right)_{0.6}$	0.0980	0.0930	0.098039	0.0897	0.0947
$\left(df_s/dT\right)_{0.7}$	0.0687	0.0662	0.071429	0.0714	0.0694
$\left(df_s/dT\right)_{0.8}$	0.0468	0.0468	0.04902	0.0541	0.0492

Table 4.2.27: The faction solid calculated for the MHD A356 alloy on cooling, based on the DSC specific heat data presented in Fig. 4.2.2(c).

	Temperature ℃				
Fraction solid	Sample 1	Sample 2	Sample 3	Sample 4	Average
0.1	606.9	606.1	609.5	609.8	608.1
0.2	601.6	601.2	603.5	603.6	602.5
0.3	592.2	591.5	594.7	594.6	593.3
0.4	579.2	578.3	582.2	582.6	580.6
0.5	567.0	566.0	566.3	566.6	566.5
0.6	565.5	564.4	564.3	564.5	564.7
0.7	564.1	563.0	562.9	563.3	563.4
0.8	562.9	561.8	561.6	562.0	562.1
0.9	560.6	559.7	559.3	559.8	559.8

Table 4.2.28: The fraction solid sensitivity for the MHD A356 alloy on cooling, based on the DSC specific heat data given in table 4.2.27.

Fraction solid sensitivity	Sample 1	Sample 2	Sample 3	Sample 4	Average
$\left(df_s/dT\right)_{0.2}$	0.0136	0.0138	0.0136	0.0132	0.0135
$\left(df_s/dT\right)_{0.3}$	0.0089	0.0087	0.0094	0.0095	0.0091
$\left(df_s/dT\right)_{0.4}$	0.0079	0.0078	0.0070	0.0071	0.0075
$\left(df_s/dT\right)_{0.5}$	0.0145	0.0144	0.0112	0.0110	0.0128
$\left(df_s/dT\right)_{0.6}$	0.0687	0.0687	0.0588	0.0610	0.0643
$\left(df_s/dT\right)_{0.7}$	0.0766	0.0769	0.0735	0.0800	0.0768
$\left(df_s/dT\right)_{0.8}$	0.0575	0.0593	0.0544	0.0570	0.0571

Table 4.2.29: The fraction solid calculated for the NGM AlSi7Mg alloy on heating, based on the DSC enthalpy data presented in Fig. 4.2.3(a).

	Temperature ℃			
Fraction solid	Sample 1	Sample 2	Sample 3	Average
0.1	612.0	611.4	612.1	611.8
0.2	605.3	604.9	605.4	605.2
0.3	596.4	596.4	597.0	596.6
0.4	585.0	584.7	585.0	584.9
0.5	583.2	582.2	582.3	582.6
0.6	582.3	581.3	581.5	581.7
0.7	581.3	580.3	580.3	580.6
0.8	579.8	578.8	579.0	579.2
0.9	577.9	576.9	577.0	577.3

Table 4.2.30: The fraction solid sensitivity for the NGM AlSi7Mg alloy on heating, based on the DSC enthalpy data given in table 4.2.29.

Fraction solid sensitivity	Sample1	Sample 2	Sample3	Average
$\left(df_s/dT\right)_{0.2}$	0.0128	0.0133	0.0132	0.0131
$\left(df_s/dT\right)_{0.3}$	0.0099	0.0099	0.0098	0.0099
$\left(df_s/dT\right)_{0.4}$	0.0152	0.0141	0.0137	0.0143
$\left(df_s/dT\right)_{0.5}$	0.0735	0.0575	0.0570	0.0627
$\left(df_s/dT\right)_{0.6}$	0.1031	0.1020	0.0995	0.1015
$\left(df_s/dT\right)_{0.7}$	0.0791	0.0826	0.0826	0.0814
$\left(df_s/dT\right)_{0.8}$	0.0590	0.0593	0.0602	0.0595

Table 4.2.31: The fraction solid calculated for the NGM AlSi7Mg alloy on cooling based on the DSC enthalpy data presented in Fig. 4.2.3(a).

	Temperature ℃			
Fraction solid	Sample 1	Sample 2	Sample 3	Average
0.1	603.6	606.1	606.1	605.3
0.2	601.8	600.2	601.7	601.3
0.3	594.0	589.8	592.4	592.1
0.4	582.0	575.3	578.8	578.7
0.5	572.8	571.4	572.0	572.1
0.6	571.2	569.8	570.7	570.6
0.7	569.8	568.4	569.5	569.2
0.8	568.5	567.0	568.1	567.9
0.9	566.8	565.0	566.3	566.0

Table 4.2.32: The fraction solid sensitivity for the NGM AlSi7Mg alloy on cooling based on the DSC enthalpy data given in table 4.2.31.

Fraction solid sensitivity	Sample1	Sample 2	Sample3	Average
$\left(df_s/dT\right)_{0.2}$	0.0207	0.0123	0.0146	0.0159
$\left(df_s/dT\right)_{0.3}$	0.0101	0.0080	0.0087	0.0089
$\left(df_s/dT\right)_{0.4}$	0.0095	0.0109	0.0098	0.0100
$\left(df_s/dT\right)_{0.5}$	0.0185	0.0368	0.0248	0.0267
$\left(df_s/dT\right)_{0.6}$	0.0662	0.0662	0.08	0.0708
$\left(df_s/dT\right)_{0.7}$	0.0735	0.0712	0.0766	0.0738
$\left(df_s/dT\right)_{0.8}$	0.0667	0.0588	0.0639	0.0631

Table 4.2.33: The fraction solid calculated for the COM AlSi7Mg alloy on heating, based on the DSC enthalpy data presented in Fig. 4.2.3(b).

	Temperature ℃				
Fraction solid	Sample 1	Sample 2	Sample 3	Sample 4	Average
0.1	612.3	612.5	612.9	612.2	612.4
0.2	605.4	605.8	606.4	605.1	605.7
0.3	596.1	597.1	598.3	596.2	596.9
0.4	583.5	584.9	586.9	583.8	584.8
0.5	578.6	579.4	578.4	577.8	578.6
0.6	577.5	578.5	577.4	576.8	577.6
0.7	576.2	577.2	576.1	575.7	576.3
0.8	574.4	575.4	574.5	573.8	574.5
0.9	571.8	572.5	572.0	571.3	571.9

Table 4.2.34: The fraction solid sensitivity for the COM AlSi7Mg alloy on heating, based on the DSC enthalpy data given in table 4.2.33.

Fraction solid sensitivity	Sample 1	Sample 2	Sample 3	Sample 4	Average
$\left(df_s/dT\right)_{0.2}$	0.0124	0.0130	0.0137	0.0125	0.0129
$\left(df_s/dT\right)_{0.3}$	0.0091	0.0096	0.0103	0.0094	0.0096
$\left(df_s/dT\right)_{0.4}$	0.0114	0.0113	0.0100	0.0108	0.0109
$\left(df_s/dT\right)_{0.5}$	0.0333	0.0313	0.0210	0.0287	0.0286
$\left(df_s/dT\right)_{0.6}$	0.0826	0.0897	0.0893	0.0935	0.0888
$\left(df_s/dT\right)_{0.7}$	0.0645	0.0641	0.0687	0.0667	0.0660
$\left(df_s/dT\right)_{0.8}$	0.0459	0.0420	0.0481	0.0459	0.0455

Table 4.2.35: The fraction solid calculated for the COM AlSi7Mg alloy on cooling, based on the DSC enthalpy data presented in Fig. 4.2.3(b).

	Temperature ℃				
Fraction solid	Sample 1	Sample 2	Sample 3	Sample 4	Average
0.1	609.7	608.8	608.7	609.0	609.0
0.2	603.8	601.7	600.8	601.4	601.9
0.3	595.7	592.0	590.1	591.4	592.3
0.4	584.6	578.0	574.9	577.5	578.8
0.5	567.7	565.3	566.2	565.8	566.2
0.6	564.4	563.7	565.0	564.6	564.4
0.7	563.0	562.3	563.9	563.5	563.2
0.8	561.5	560.8	562.5	562.2	561.7
0.9	559.1	557.4	559.0	559.7	558.8

Table 4.2.36: The fraction solid sensitivity for the COM AlSi7Mg alloy on cooling, based on the DSC enthalpy data given in table 4.2.35.

Fraction solid sensitivity	Sample 1	Sample 2	Sample 3	Sample 4	Average
$\left(df_s/dT\right)_{0.2}$	0.0142	0.0119	0.0108	0.0114	0.0105
$\left(df_s/dT\right)_{0.3}$	0.0104	0.0084	0.0077	0.0084	0.0087
$\left(df_s/dT\right)_{0.4}$	0.0072	0.0075	0.0084	0.0078	0.0133
$\left(df_s/dT\right)_{0.5}$	0.0099	0.0140	0.0202	0.0155	0.0149
$\left(df_s/dT\right)_{0.6}$	0.0420	0.0662	0.0897	0.0866	0.0711
$\left(df_s/dT\right)_{0.7}$	0.0687	0.0687	0.0791	0.0816	0.0745
$\left(df_s/dT\right)_{0.8}$	0.0514	0.0413	0.0404	0.0529	0.0465

Table 4.2.37: The fraction solid calculated for the MHD A356 alloy on heating, based on the DSC enthalpy data presented in Fig. 4.2.3(c).

	Temperature ℃				
Fraction solid	Sample 1	Sample 2	Sample 3	Sample 4	Average
0.1	611.9	611.3	613.4	613.2	612.5
0.2	605.2	604.3	606.7	606.7	605.7
0.3	596.6	595.2	598.3	598.0	597.0
0.4	584.6	582.3	586.3	585.5	584.7
0.5	579.9	578.9	578.9	579.0	579.2
0.6	579.1	577.9	578.1	578.0	578.3
0.7	578.0	576.7	576.8	576.7	577.0
0.8	576.1	574.8	575.1	575.2	575.3
0.9	573.6	572.4	572.9	572.9	573.0

Table 4.2.38: The fraction solid sensitivity for the MHD A356 alloy on heating, based on the DSC enthalpy data given in table 4.2.37.

Fraction solid sensitivity	Sample 1	Sample 2	Sample 3	Sample 4	Average
$\left(df_s/dT\right)_{0.2}$	0.0131	0.0124	0.0132	0.0132	0.0130
$\left(df_s/dT\right)_{0.3}$	0.0097	0.0091	0.0098	0.0095	0.0095
$\left(df_s/dT\right)_{0.4}$	0.0120	0.0123	0.0103	0.0105	0.0113
$\left(df_s/dT\right)_{0.5}$	0.0368	0.0448	0.0243	0.0265	0.0331
$\left(df_s/dT\right)_{0.6}$	0.1020	0.0897	0.0943	0.0897	0.0939
$\left(df_s/dT\right)_{0.7}$	0.06699	0.0662	0.0687	0.0714	0.0683
$\left(df_s/dT\right)_{0.8}$	0.0460	0.0468	0.0514	0.0529	0.0493

Table 4.2.39: The faction solid calculated for the MHD A356 alloy on cooling, based on the DSC enthalpy data presented in Fig. 4.2.3(c).

	Temperature ℃				
Fraction solid	Sample 1	Sample 2	Sample 3	Sample 4	Average
0.1	606.8	606.0	609.7	609.8	608.0
0.2	600.6	600.7	604.1	603.8	602.3
0.3	590.6	591.2	595.2	594.9	593.0
0.4	575.9	577.8	583.3	582.7	579.9
0.5	566.5	565.8	566.6	566.6	566.4
0.6	565.2	564.3	564.4	564.6	564.6
0.7	563.8	562.9	562.9	563.2	563.2
0.8	562.6	561.7	561.5	562.0	561.9
0.9	560.4	559.3	559.5	559.9	559.8

Table 4.2.40: The fraction solid sensitivity for the MHD A356 alloy on cooling based on the DSC enthalpy data given in table 4.2.39.

Fraction solid sensitivity	Sample 1	Sample 2	Sample 3	Sample 4	Average
$\left(df_s/dT\right)_{0.2}$	0.0123	0.0136	0.0138	0.0135	0.0133
$\left(df_s/dT\right)_{0.3}$	0.0081	0.0087	0.0096	0.0095	0.0090
$\left(df_s/dT\right)_{0.4}$	0.0083	0.0079	0.0070	0.0070	0.0076
$\left(df_s/dT\right)_{0.5}$	0.0186	0.0149	0.0106	0.0110	0.0138
$\left(df_s/dT\right)_{0.6}$	0.0735	0.0687	0.0541	0.0602	0.0641
$\left(df_s/dT\right)_{0.7}$	0.0766	0.0766	0.0687	0.0766	0.0747
$\left(df_s/dT\right)_{0.8}$	0.0590	0.0545	0.0575	0.0608	0.0579

Table 4.2.41: The fraction solid and temperature range based on a fraction solid sensitivity criteria of 0.015, for the data shown in Figs. 4.2.4 to 4.2.5. (m.p. stands for melting point)

Data Type	Alloy	Fraction Solid Range		Temperature Range (℃)	
		Heating	Cooling	Heating	Cooling
DSC Heat Flow	NGM AlSi7Mg	0.390 – 0	0-450 – 0.217	585.3 – m.p.	576.5 – 600.2
	COM AlSi7Mg	0.409 – 0	0.502 – 0	583.1 – m.p.	566.5 – m.p.
	MHD A356	0.411 – 0	0.506 – 0	581.7 – m.p.	566 0 – m.p.
Specific Heat	NGM AlSi7Mg	0.400 – 0	0.447 – 0.216	584.0 – m.p.	576.5 – 600.4
	COM AlSi7Mg	0.411 – 0	0.503 – 0	583.0 – m.p.	566.4 – m.p.
	MHD A356	0.417 – 0	0.505 – 0	582.5 – m.p.	566.0 – m.p.
Enthalpy	NGM AlSi7Mg	0.402 – 0	0.431 – 0.210	584.9 – m.p.	576-7 – 600.1
	COM AlSi7Mg	0.418 – 0	0.501 – 0	583.7 – m.p.	566.3 – m.p.
	MHD A356	0.424 – 0	0.503 – 0	583.3 – m.p.	566.2 – m.p.

Table 4.2.42: The fraction solid and temperature range based on a fraction solid sensitivity criteria of 0.03, for the data shown in Figs. 4.2.4 to 4.2.5. (m.p. stands for melting point)

Data Type	Alloy	Fraction Solid Range		Temperature Range (℃)	
		Heating	Cooling	Heating	Cooling
DSC Heat Flow	NGM AlSi7Mg	0.421 – 0	0.519 – 0	583.6 – m.p.	572.0 – m.p.
	COM AlSi7Mg	0.449 – 0	0.521 – 0	581.7 – m.p.	565.9 – m.p.
	MHD A356	0.459 – 0	0.536 – 0	580.2 – m.p.	565.8 – m.p.
Specific Heat	NGM AlSi7Mg	0.423 – 0	0.518 – 0	583.6 – m.p.	572.0 – m.p.
	COM AlSi7Mg	0.459 – 0	0.528 – 0	580.9 – m.p.	565.9 – m.p.
	MHD A356	0.481 – 0	0.534 – 0	579.3 – m.p.	565.6 – m.p.
Enthalpy	NGM AlSi7Mg	0.434 – 0	0.509 – 0	584.2 – m.p.	572.0 – m.p.
	COM AlSi7Mg	0.488 – 0	0.528 – 0	580.0 – m.p.	565.8 – m.p.
	MHD A356	0.503 – 0	0.533 – 0	578.5 – m.p.	565.7 – m.p.

4.2.5 Figures

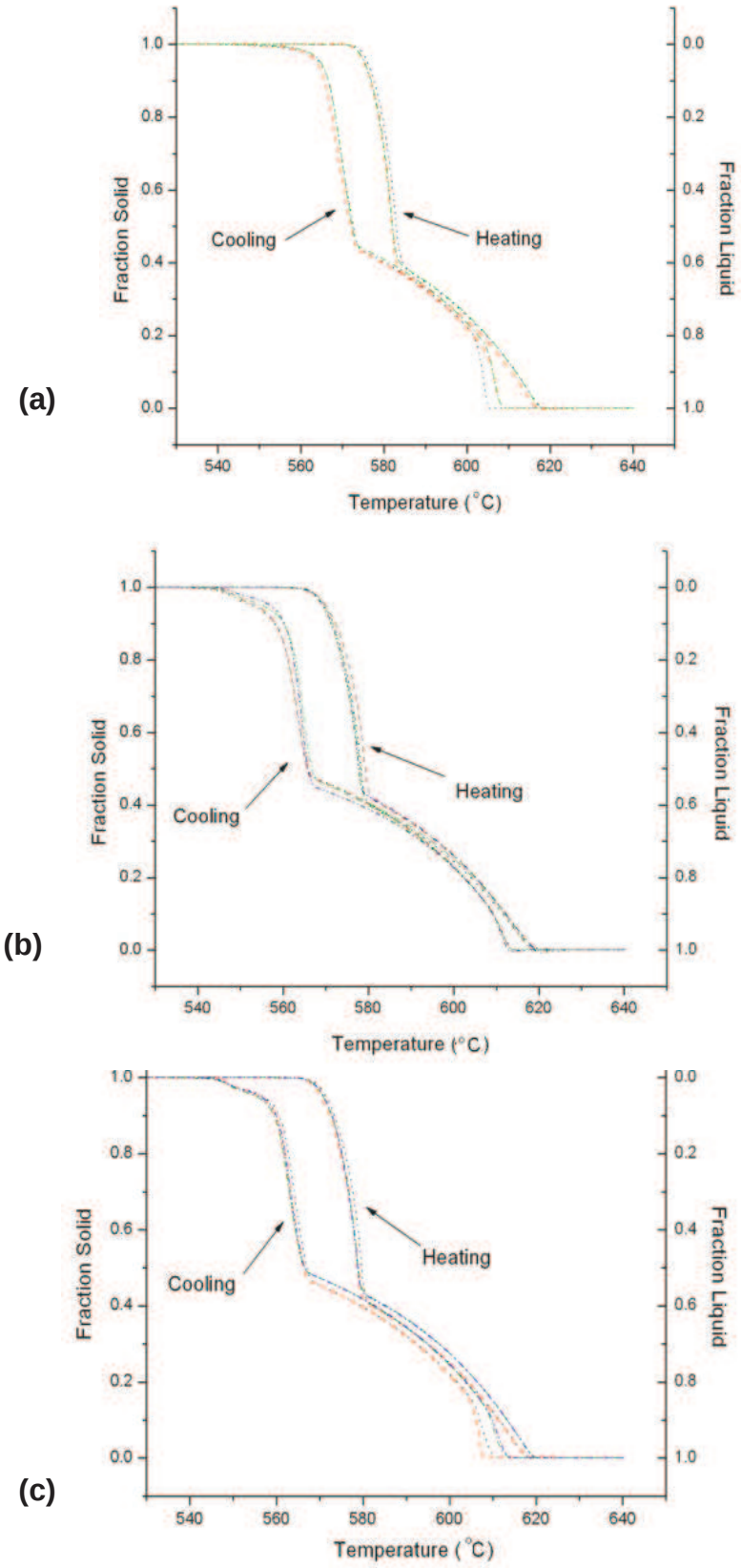

Fig. 4.2.1: The fraction solid change with respect to temperature for (a) the NGM AlSi7Mg alloy, (b) the COM AlSi7Mg alloy and (c) the MHD A356 alloy, as calculated from the DSC heat flow data; ..... shows data for sample 1, - - - - - - for sample 2, - . - . - . for sample 3 and _ _ _ _ for sample 4.

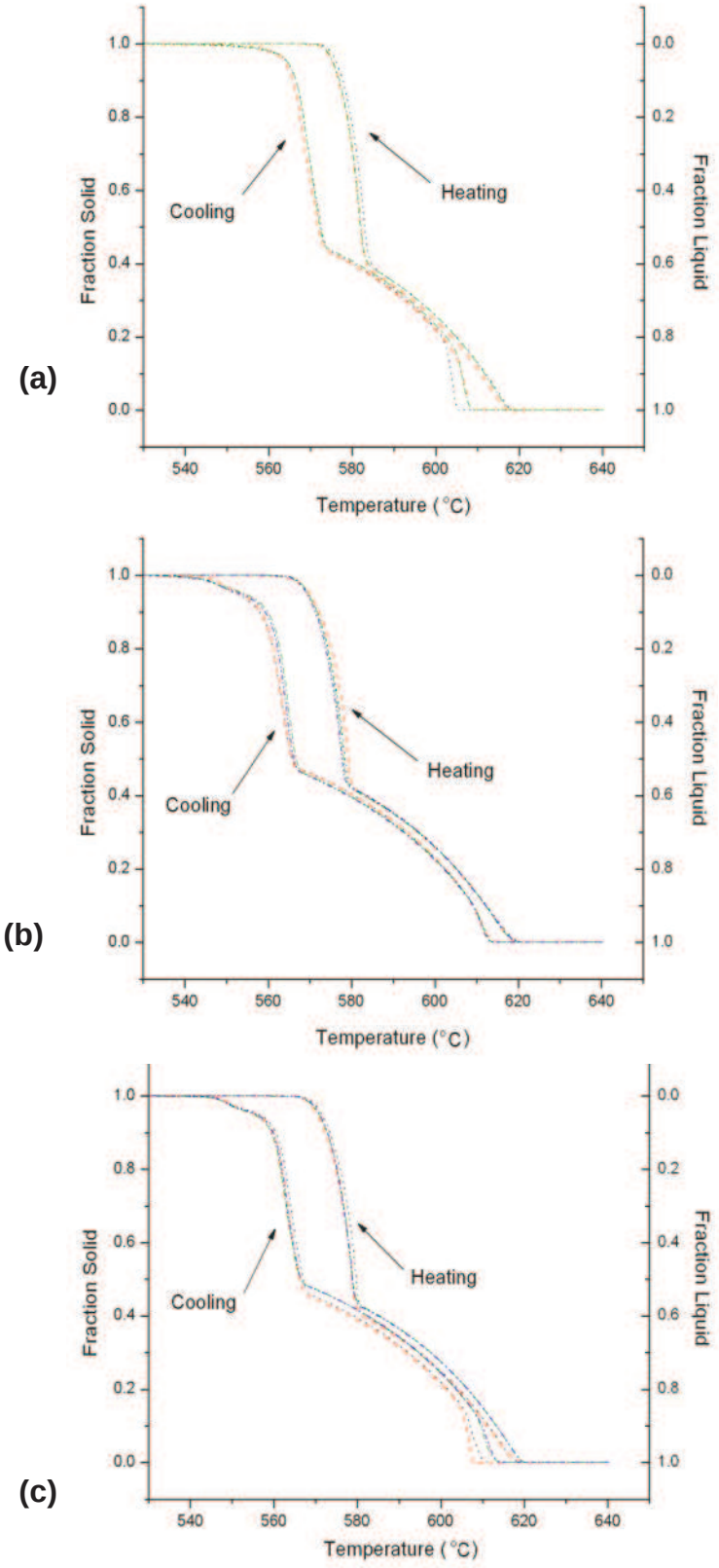

Fig. 4.2.2: The fraction solid change with respect to temperature for (a) the NGM AlSi7Mg alloy, (b) the COM AlSi7Mg alloy and (c) the MHD A356 alloy, as calculated from the DSC specific heat data; ..... shows data for sample 1, - - - - - - for sample 2, -·-·-·- for sample 3 and —··—··— for sample 4.

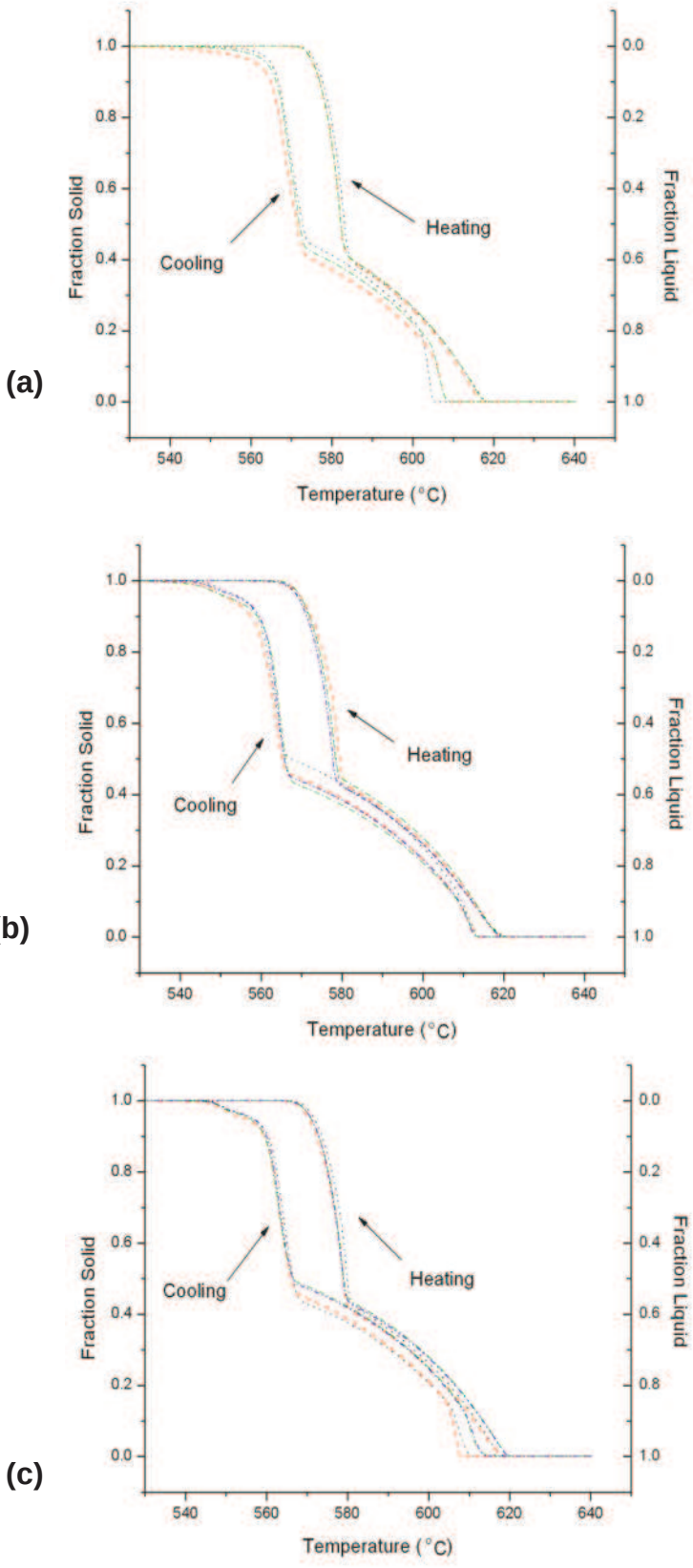

Fig. 4.2.3: The fraction solid change with respect to temperature for (a) the NGM AlSi7Mg alloy, (b) the COM AlSi7Mg alloy and (c) the MHD A356 alloy, as calculated from the DSC enthalpy data; ..... shows data for sample 1, - - - - - - for sample 2, -.-.-.-.- for sample 3 and _ _ . _ . _ for sample 4.

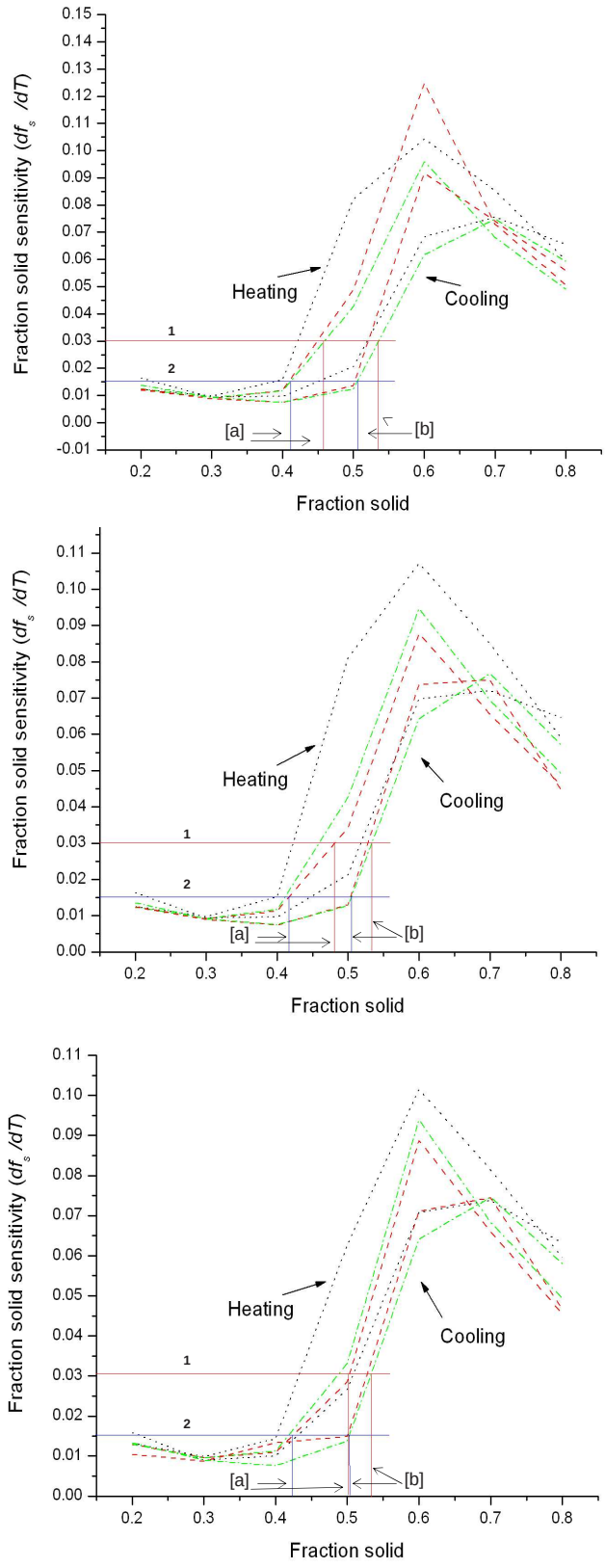

Fig. 4.2.4 : Graphical plots showing the fraction solid sensitivity value vs. the fraction solid for the NGM AlSi7Mg, COM AlSi7Mg and MHD AlSi7Mg alloys, calculated on the basis of the DSC (a) heat flow, (b) specific heat and (c) enthalpy data. The line ..... is for NGM AlSi7Mg alloy, - - - - - - - - for COM AlSi7Mg alloy and _._._._._ for MHD AlSi7Mg alloy. Horizontal lines show the limit: No. 1 shows the limit line suggested by Liu et. al.[23] and No. 2 shows the limit line suggested by Fan et al.[166,167]. [a] shows the lower limit of fraction solid for heating and [b] for cooling.

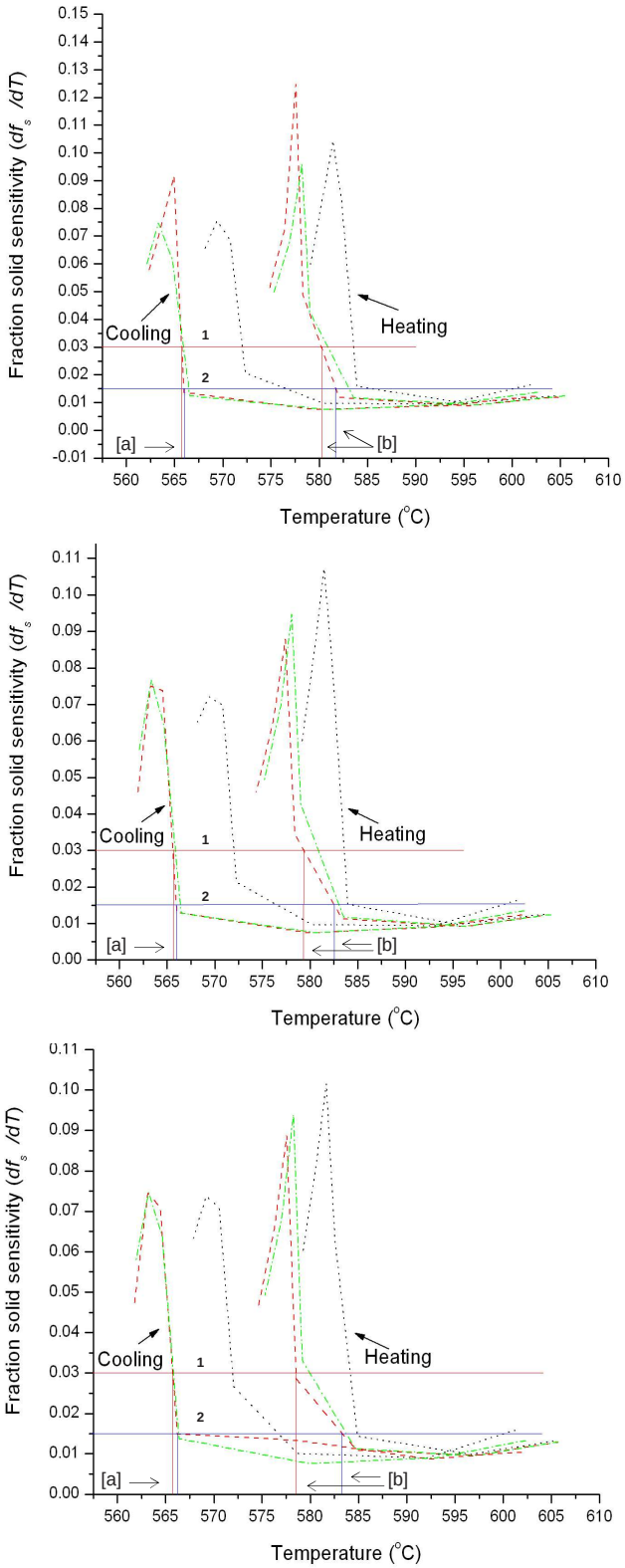

Fig. 4.2.5 : Graphical plots showing the fraction solid sensitivity value vs. the temperature for the NGM AlSi7Mg, COM AlSi7Mg and MHD AlSi7Mg alloys, calculated on the basis of the DSC (a) heat flow, (b) specific heat and (c) enthalpy data. The line ..... is for NGM AlSi7Mg alloy, - - - - - - - - for COM AlSi7Mg alloy and _ . _ . _ for MHD AlSi7Mg alloy. Horizontal lines show the limit: No. 1 shows the limit line suggested by Liu et. al.[23] and No. 2 shows the limit line suggested by Liu et al.[166,167]. [a] shows the lower limit of fraction solid for heating and [b] for cooling.

4.3. EFFECT OF PROCESSING PARAMETERS

In this section the effect of processing parameters such as pouring temperature, inclination angle and melt-plate contact time has been discussed.

4.3.1 Introduction

4.3.1.1 Microstructure Characteristics and their Measurement

The samples obtained by semi-solid processing using the cooling slope technique, were cut, ground and polished and anodized according to the procedure mentioned in Section 3.7. The microstructure was investigated using optical microscopy with cross-polarized light and Lamda (λ) filter as described in Section 3.8. Images were taken and analysed using software as detailed in Section 3.9.

The characteristic features such as: grain size, circularity and aspect ratio were measured according to the assumptions and formulae mentioned in Section 2.5.2.

4.3.1.2 Data Distribution and Analysis

A minimum of 50 grains were observed from an area for statistical analysis. It was found that the smallest and the largest grains were also contained within this size of data set. Also when the data was sorted, sequentially increasing, it was found that the trend was not consistent and varied from sample to sample. In Fig. 4.3.1, it can be seen that the distribution of the data is significantly different for each sample. Similarly the frequency of grains was also different for each sample (Fig. 4.3.2). From the Fig. 4.3.2 it can be observed that the data contained a small number of grains with very high grain size at any sample position. Taking an average of this data, includes these grains, can dramatically influence the true value of the data. To avoid this, the

median of the data was calculated, which represents the maximum population of the data.

It was also observed that grain circularity values remained approximately constant for most of the data, but increased for the grains having a larger grain size as shown in Fig. 4.3.3. Similarly the difference between the maximum and minimum Feret diameter values remained approximately the same for the majority of smaller grains (see Fig. 4.3.4). Although this value increased with an increase in grain size as it should, the variation in the data also increased because of these larger grains. The elongation value also changed markedly for grains with an abnormally large size as shown in Fig. 4.3.4. Analysis of the statistical distribution for the given size supports the use of a median as the representative value for the data set.

The effect of processing parameters such as pouring temperature, contact time and inclination angle on the grain characteristics such as grain size, grain circularity and grain elongation were analysed and reported in the following sections. In semi-solid processing a material exhibiting the smallest grain size, highest grain circularity and smallest grain elongation shows better thixotropic properties. The highest grain circularity obtainable is “1” which represents a complete circle and the smallest grain elongation is also “1” which represents a completely equiaxed grain.

4.3.2 Effect of Pouring Temperature

The effect of pouring temperature was assessed with respect to different melt-plate contact times and inclination angles.

4.3.2.1 Constant Contact Time

The data for the effect of pouring temperature at a specific contact time for different inclination angles for grain size is given in Table 4.3.1, for grain circularity in Table 4.3.2 and for grain elongation in Table 4.3.3.

Grain Size

Contact Time of 0.04 s

At a contact time of 0.04 s, results showed no evidence of a clear trend with a change in pouring temperature from 689 °C to 640 °C (see Table 4.3.1). At the highest and lowest pouring temperatures, 680 °C and 640 °C, the grain size decreased from 161 μm to 147 μm at an inclination angle of 40° and from 181 μm to 98 μm at an inclination angle of 60°. The smallest grain size 89 μm was observed at an inclination angle of 40° angle for a pouring temperature of 660 °C.

Contact Time of 0.09 s

At a contact time of 0.09 s, the grain size increased from 136 μm to 146 μm at an inclination angle of 20° and from 87 μm to 148 μm at an inclination angle of 40° with a decrease in pouring temperature from 680 °C to 640 °C (see Table 4.3.1). At the highest and the lowest pouring temperatures, 680 °C and 640 °C, the grain size increased from 87 μm to 148 μm at an inclination angle of 40° and from 100 μm to 115 μm at an inclination angle of 60°. The smallest grain size 87 μm was observed at inclination angle of 40° for a pouring temperature of 680 °C.

Contact Time of 0.13 s

At a contact time of 0.13 s, the grain size increased from 124 μm to 159 μm at an inclination angle of 20° and from 91 μm to 105 μm at an inclination angle of 60° with a decrease in pouring temperature from 680 °C to 640 °C (see Table 4.3.1). The smallest grain sizes 91 μm, 91 μm and 105 μm were observed at pouring temperatures of 680 °C, 660 °C and 640 °C, respectively, at an inclination angle of 60°. At the highest and lowest pouring temperatures 680 °C and 640 °C, the grain size increased from 87 μm to 145 μm at an inclination angle of 40° from 91 μm to 105 μm at an inclination angle of 60°. The minimum grain size 87 μm was observed at an inclination angle of 40° for a pouring temperature of 680 °C.

Grain Circularity

Contact Time of 0.04 s

At a contact time of 0.04 s, the grain circularity did not exhibit any trend with a decrease in pouring temperature at any inclination angle (see Table 4.3.2). However,

at the highest and lowest pouring temperatures, 680 °C and 640 °C, the grain circularity decreased from 0.67 to 0.58 at an inclination angle of 20° and from 0.66 to 0.64 at an inclination angle of 40° but increased from 0.61 to 0.77 at an inclination angle of 60°. The maximum grain circularity 0.64 was obtained at an inclination angle of 60° for a pouring temperature of 660°C.

Contact Time of 0.09 s

At a contact time of 0.09 s, the grain circularity decreased from 0.86 to 0.65 at an inclination angle of 40°, and from 0.81 to 0.60 at an inclination angle of 60°, and increased from 0.62 to 0.63 at an inclination angle of 20° with a decrease in pouring temperature from 680 °C to 640°C (see Table 4.3.2). The maximum grain circularity 0.86 was obtained at an inclination angle of 40° for a pouring temperature of 680 °C.

Contact Time of 0.13 s

At a contact time of 0.13 s, the grain circularity decreased from 0.79 to 0.59 at an inclination angle of 20° and from 0.86 to 0.71 at an inclination angle of 60° with a decrease in pouring temperature from 680 °C to 640 °C (see Table 4.3.2). The grain circularity values were the highest at an inclination angle of 60° for each pouring temperature. The maximum grain circularity 0.86 was obtained at an inclination angle of 60° for a pouring temperature of 680 °C.

Grain Elongation

Contact Time of 0.04 s

At a contact time of 0.04 s, the grain elongation decreased from 1.11 to 1.05 at an inclination angle of 20°, from 1.08 to 1.07 at an inclination angle of 40° and from 1.12 to 1.08 at an inclination angle of 60° with a decrease in pouring temperature from 680 °C to 640 °C (see Table 4.3.3). The minimum grain elongation 1.05 was obtained at an inclination angle of 20° for a pouring temperature of 640 °C.

Contact Time of 0.09 s

At a contact time of 0.09 s, the grain elongation increased from 1.06 to 1.11 at an inclination angle of 40° with a decrease in pouring temperature from 680 °C to 640 °C (see Table 4.3.3). At the highest and lowest pouring temperatures, 680 °C and 640 °C, the grain elongation increased from 1.06 to 1.11 at an inclination angle of 40° and

from 1.07 to 1.08 at an inclination angle of 60°. The minimum grain elongation value 1.05 was obtained at an inclination angle of 40° for a pouring temperature of 660 °C.

Contact Time of 0.13 s

At a contact time of 0.13 s, the grain elongation did not exhibit a clear trend with a decrease in pouring temperature. At the highest and lowest pouring temperatures, 680 °C and 640 °C, the grain elongation decreased from 1.10 to 1.08 at an inclination angle of 20° and from 1.05 to 1.04 at an inclination angle of 40° (see Table 4.3.3). The minimum grain elongation 1.04 was obtained at an inclination angle of 40° for a pouring temperature of 640 °C.

4.3.2.2 Constant Inclination Angle

The data for the effect of pouring temperature at a specific inclination angle for different contact times for grain size is given in Table 4.3.4, for grain circularity in Table 4.3.5 and for grain elongation in Table 4.3.6.

Grain Size

Inclination Angle of 20°

At an inclination angle of 20°, the grain size increased from 136 μm to 146 μm for a contact time of 0.09 s and 124 μm to 159 μm for a contact time of 0.13 s with a decrease in pouring temperature from 680 °C to 640 °C (see Table 4.3.4). At the highest and lowest pouring temperatures, 680 °C and 640 °C, the grain size increased from 145 μm to 166 μm at a contact time of 0.04 s, from 136 μm to 146 μm at a contact time of 0.09 s and from 124 μm to 159 μm for a contact time of 0.13 s, respectively. The grain size also decreased from 145 μm to 124 μm at a pouring temperature of 680 °C with an increase in contact time from 0.04 s to 0.13 s. The minimum grain size of 111 μm was observed at a contact time of 0.04 s for a pouring temperature of 660 °C.

Inclination Angle of 40°

At an inclination angle of 40°, the grain size increased from 87 μm to 148 μm for a contact time of 0.09 s with a decrease in pouring temperature (see Table 4.3.4). At the

highest and lowest pouring temperatures, 680 °C and 640 °C, the grain size increased from 87 μm to 148 μm at a contact time of 0.04 s and from 87 μm to 145 μm at a contact time of 0.09 s, respectively. The grain size decreased from 161 μm to 87 μm at a pouring temperature of 680 °C and increased from 89 μm to 147 μm at a pouring temperature of 660 °C with increase in contact time from 0.04s to 0.13 s. The minimum grain size of 87 μm was observed at contact times of 0.09 s and 0.13 s for a pouring temperature of 680 °C.

Inclination Angle of 60°

At an inclination angle of 60°, the grain size increased from 91 μm to 105 μm for 0.13 s contact time with a decrease in pouring temperature from 680 °C to 640 °C (see Table 4.3.4). At the highest and lowest pouring temperatures, 680 °C and 640 °C, grain size decreased from 181 μm to 98 μm for a contact time of 0.04 s, while it increased from 100 μm to 115 μm for a contact time of 0.09 s and from 91 μm to 105 μm for a contact time of 0.13 s. The grain size decreased from 181 μm to 91 μm at a pouring temperature of 680 °C with an increase in contact time from 0.04 s to 0.13 s. The grain size remained nearly constant, 93 / 91 μm, for a pouring temperature of 660 °C with an increase in contact time. The minimum grain size of 91 μm was observed at a contact time of 0.13 s at a pouring temperature of 680 °C and 660 °C.

Grain Circularity

Inclination Angle of 20°

At an inclination angle of 20°, the grain circularity decreased from 0.79 to 0.59 for a contact time of 0.13 s and remained approximately constant to about 0.62 for a contact time of 0.09 s with a decrease in pouring temperature from 680 °C to 640 °C (see Table 4.3.5). At the highest and lowest pouring temperatures, 680 °C and 640 °C, the grain circularity decreased from 0.67 to 0.58 for a contact time of 0.04 s and from 0.79 to 0.59 for a contact time of 0.13 s at pouring temperatures 680 °C and of 640 °C, respectively. The highest grain circularity value of 0.79 was obtained for a contact time of 0.13 s at a pouring temperature of 680 °C.

Inclination Angle of 40°

At an inclination angle of 40°, the grain circularity decreased from 0.86 to 0.65 for a contact time of 0.09 s with a decrease in pouring temperature from 680°C to 640 °C

(see Table 4.3.5). The grain circularity at the highest and lowest pouring temperatures, 680 °C and 640 °C, decreased from 0.66 to 0.64 for a contact time of 0.04 s, from 0.86 to 0.65 for a contact time of 0.09 s and from 0.82 to 0.62 for a contact time of 0.13 s at pouring temperatures of 680 °C and 640 °C, respectively. The maximum grain circularity value of 0.86 was obtained for a contact time of 0.09 s at a pouring temperature of 660 °C.

Inclination Angle of 60°

At an inclination angle of 60°, the grain circularity decreased from 0.82 to 0.60 for a contact time of 0.09 s and from 0.86 to 0.71 for a contact time of 0.13 s with a decrease in pouring temperature from 680 °C to 640 °C (see Table 4.3.5). The maximum grain circularity value of 0.86 was obtained for a contact time of 0.13 s at a pouring temperature of 680 °C.

Grain Elongation

Inclination Angle of 20°

At an inclination angle of 20°, the grain elongation decreased from 1.11 to 1.05 for a contact time of 0.04 s with a decrease in pouring temperature from 680 °C to 640 °C (see Table 4.3.6). At the highest and lowest pouring temperature, 680 °C and 640 °C, the grain elongation decreased from 1.11 to 1.05 for a contact time of 0.04 s, from 1.11 to 1.08 for a contact time of 0.09 s and from 1.10 to 1.08 for a contact time of 0.13 s at pouring temperatures of 680 °C and 640 °C, respectively. The minimum grain elongation of 1.05 was obtained for a contact time of 0.04 s of at a pouring temperature of 640 °C.

Inclination Angle of 40°

At an inclination angle of 40°, the grain elongation decreased from 1.08 to 1.07 for a contact time of 0.04 s and from 1.06 to 1.11 for a contact time of 0.09 s with a decrease in pouring temperature from 680 °C to 640 °C (see Table 4.3.6). At the highest and lowest pouring temperatures, 680 °C and 640 °C, the grain elongation decreased from 1.05 to 1.04 for a contact time of 0.13 s. The minimum grain elongation value of 1.04 was obtained for a contact time of 0.13 s at a pouring temperature of 640 °C.

Inclination Angle of 60°

At an inclination angle of 60°, the grain elongation decreased from 1.12 to 1.08 for a contact time of 0.04 s with a decrease in pouring temperature from 680 °C to 640 °C (see Table 4.3.6). At the highest and lowest pouring temperatures, 680 °C and 640 °C, the grain elongation value increased from 1.07 to 1.08 for a contact time of 0.09 s and from 1.05 to 1.07 for a contact time of 0.13 s at pouring temperatures of 680 °C and 640 °C, respectively. The minimum grain elongation value of 1.05 was obtained for a contact time of 0.13 s at a pouring temperature of 680 °C.

4.3.3 Effect of Contact Time

The effect of contact time on the grain size, grain circularity and grain elongation values has been assessed at different pouring temperatures and contact times.

4.3.3.1 Constant Pouring Temperature

The data for the effect of contact time at a specific pouring temperature for different inclination angles for grain size is given in Table 4.3.7, for grain circularity in Table 4.3.8 and for grain elongation in Table 4.3.9.

Grain Size

Pouring Temperature of 680 °C

At a pouring temperature of 680 °C, the grain size decreased from 145 μm to 124 μm at an inclination angle of 20°, 161 μm to 87 μm at an inclination angle of 40° and 181 μm to 91 μm at an inclination angle of 60° with an increase in contact time from 0.04 s to 0.13 s (see Table 4.3.7). The minimum grain size of 87 μm was observed at an inclination angle of 40° for contact times of 0.09 s and 0.13 s.

Pouring Temperature of 660 °C

At a pouring temperature of 660 °C, the grain size increased from 89 μm to 147 μm at an inclination angle of 40°, but decreased from 93 μm to 91 μm at an inclination angle of 60° with an increase in contact time from 0.04 s to 0.13 s (see Table 4.3.7). The grain size remained approximately unchanged at ~ 91 μm and 93 μm at an inclination angle of 60° with an increase in contact time. At the lowest and highest contact times, 0.04 s and 0.13 s, the grain size increased from 111 μm to 137 μm for an inclination angle of 20° and from 89 μm to 147 μm for an inclination angle of 40°, respectively. The minimum grain size of 89 μm was obtained at an inclination angle of 40° for a contact time of 0.04 s.

Pouring Temperature of 640 °C

At a pouring temperature of 640 °C, the minimum grain size was observed for an inclination angle of 60° at each contact time (see Table 4.3.7). At the lowest and highest contact times, 0.04 s and 0.13 s, the grain size decreased from 166 μm to 159 μm for an inclination angle of 20° and 147 μm to 145 μm for an inclination angle of 40°, respectively. The minimum grain size of 98 μm was observed at an inclination angle of 60° for a contact time of 0.04 s.

Grain Circularity

Pouring Temperature of 680 °C

At a pouring temperature 680 °C, the grain circularity increased from 0.61 to 0.86 for an inclination angle of 60° with increase in contact time from 0.04 to 0.13 s (see Table 4.3.8). At the lowest and highest contact times, 0.04 s and 0.13 s, the grain circularity increased from 0.67 to 0.79 for an inclination angle of 20°, from 0.66 to 0.82 for an inclination angle of 40° and 0.61 to 0.86 for an inclination angle of 60° with an increase in contact time. The maximum grain circularity of 0.86 was obtained at an inclination angle of 40° for a contact time of 0.09 s and at an inclination angle of 60° for a contact time of 0.13 s.

Pouring Temperature of 660 °C

At a pouring temperature of 660 °C, the grain circularity decreased from 0.83 to 0.61 at an inclination angle of 40° with an increase in contact time from 0.04 s to 0.13 s (see Table 4.3.8). The grain circularity was the maximum at an inclination angle of

60° for each contact time. At the lowest and highest contact time, 0.04 s and 0.13 s, the grain circularity decreased from 0.76 to 0.65 at an inclination angle of 20°, from 0.83 to 0.61 at an inclination angle of 40° and from 0.84 to 0.79 at an inclination angle of 60°, respectively. The grain circularity was the maximum for a contact time of 0.04 s at each inclination angle. The maximum grain circularity value of 0.84 was obtained at an inclination angle of 60° for a contact time of 0.04 s.

Pouring Temperature of 640 °C

At a pouring temperature of 640 °C, the grain circularity decreased at the maximum and minimum contact time, 0.04 s and 0.13 s, from 0.64 to 0.62 at an inclination angle of 40° and from 0.77 to 0.71 at an inclination angle of 60°, respectively (see Table 4.3.8). The maximum grain circularity value of 0.77 was obtained at an iclination angle of 60° for a contact time of 0.04 s.

Grain Elongation

Pouring Temperature of 680 °C

At a pouring temperature of 680 °C, the grain elongation decreased from 1.11 to 1.10 at an inclination angle of 20°, from 1.8 to 1.05 at an inclination angle of 40° and from 1.12 to 1.05 at an inclination angle of 60° with an increase in contact time from 0.04 s to 0.13 s (see Table 4.3.9). The grain elongation values for an inclination angle of 40° were the minimum for each contact time. The minimum grain elongation value of 1.05 was obtained at inclination angles of 40° and 60° for a contact time of 0.13 s.

Pouring Temperature of 660 °C

At a pouring temperature of 660 °C, the grain elongation increased from 1.08 to 1.14 at an inclination angle of 40° with an increase in contact time from 0.04 s to 0.13 s (see Table 4.3.9). At the lowest and highest contact times, 0.04 s and 0.13 s, the grain elongation increased from 1.08 to 1.11 at an inclination angle of 20°, from 1.08 to 1.14 at an inclination angle of 40° and from 1.08 to 1.10 at an inclination angle of 60°. The minimum grain elongation value of 1.06 was obtained at an inclination angle of 60° for a contact time of 0.09 s.

Pouring Temperature of 640 °C

At a pouring temperature of 640 °C, the grain elongation increased from 1.05 to 1.08 at an inclination angle of 20°, but decreased from 1.08 to 1.07 at an inclination angle of 60° with an increase in contact time from 0.04 s to 0.13 s (see Table 4.3.9). The lowest grain elongation value of 1.04 was obtained at an inclination angle of 40° for a contact time of 0.13 s.

4.3.3.2 Constant Inclination Angle

The data for the effect of contact time at a specific inclination angle for different pouring temperatures for grain size is given in Table 4.3.10, for grain circularity in Table 4.3.11 and for grain elongation in Table 4.3.12.

Grain Size

Inclination Angle of 20°

At an inclination angle of 20°, the grain size decreased from 145 μm to 124 μm at a pouring temperature of 680 °C with an increase in contact time from 0.04 s to 0.13 s (see Table 4.3.10). At the lowest and highest contact times, 0.04 s and 0.13 s, the grain size decreased from 145 μm to 124 μm for a pouring temperature of 680 °C and from166 μm to 159 μm for a pouring temperature of 640 °C, respectively. The minimum grain size of 111 μm was obtained at 660 °C for a contact time of 0.04s.

Inclination Angle of 40°

At an inclination angle of 40°, the grain size decreased from 161 μm to 87 μm for a pouring temperature of 680 °C and from 147 μm to 145 μm for a pouring temperature of 640 °C but increased from 89 μm to 147 μm for a pouring temperature of 660 °C with an increase in contact time from 0.04 s to 0.13 s (see Table 4.3.10). The minimum grain size of 87 μm was obtained for a pouring temperature of 680 °C at contact times of 0.09 s and 0.13 s.

Inclination Angle of 60°

At an inclination angle of 60°, the grain size decreased from 181 μm to 91 μm for a pouring temperature of 680 °C and 93 μm to 91 μm for a pouring temperature of

660 °C with an increase in contact time from 0.04 s to 0.13 s (see Table 4.3.10). The minimum grain size of 91 μm was obtained at a contact time of 0.13 s for pouring temperatures of 680 °C and 660 °C. The smallest grain size was obtained for a pouring temperature of 660 °C for each contact time.

Grain Circularity

Inclination Angle of 20°

At an inclination angle of 20°, the grain circularity decreased from 0.76 to 0.65 for a pouring temperature of 660 °C with an increase in contact time from 0.04 s to 0.13 s (see Table 4.3.11). At the lowest and highest contact times, 0.04 s and 0.13 s, the grain circularity increased from 0.67 to 0.79 for a pouring temperature of 680 °C and 0.58 to 0.59 for a pouring temperature of 640 °C. The maximum grain circularity value of 0.79 was obtained at a pouring temperature of 680 °C for a contact time of 0.13 s.

Inclination Angle of 40°

At an inclination angle of 40°, the grain circularity decreased from 0.83 to 0.61 for a pouring temperature of 660 °C with an increase in contact time from 0.04 s to 0.13 s (see Table 4.3.11). At the lowest and highest contact time, 0.04 and 0.13 s, the grain circularity decreased from 0.83 to 0.61 at a pouring temperature of 660 °C and from 0.64 to 0.62 at a pouring temperature of 640 °C. The maximum grain circularity value of 0.86 was obtained at a pouring temperature of 680 °C for a contact time of 0.09 s.

Inclination Angle of 60°

At an inclination angle of 60°, the grain circularity increased from 0.61 to 0.86 for a pouring temperature of 680 °C with an increase in contact time from 0.04 s to 0.13 s (see Table 4.3.11). At the lowest and highest contact times, 0.04 s and 0.13 s, the grain circularity decreased from 0.84 to 0.79 for a pouring temperature of 660 °C and from 0.77 to 0.71 for a pouring temperature of 640 °C. The maximum grain circularity value of 0.86 was obtained at a pouring temperature of 680 °C for a contact time of 0.13 s.

Grain Elongation

Inclination Angle of 20°

At an inclination angle of 20°, the grain elongation decreased from 1.11 to 1.10 at a pouring temperature of 680 °C, but increased from 1.05 to 1.08 at a pouring temperature of 640 °C with an increase in contact time from 0.04 s to 0.13 s (see Table 4.3.12). At the lowest and highest contact times, 0.04 s and 0.13 s, the grain elongation increased from 1.08 to 1.11 at a pouring temperature of 660 °C and from 1.05 to 1.08 at a pouring temperature of 640 °C. The minimum grain elongation value of 1.05 was obtained at a pouring temperature of 640 °C for a contact time of 0.04 s.

Inclination Angle of 40°

At an inclination angle of 40°, the grain elongation decreased from 1.08 to 1.05 for a pouring temperature of 680 °C, while it increased from 1.08 to 1.14 at a pouring temperature of 660 °C with an increase in contact time from 0.04 s to 0.13 s (see Table 4.3.12). The minimum grain elongation value of 1.04 was obtained at a pouring temperature of 640 °C for a contact time of 0.13 s.

Inclination Angle of 60°

At an inclination angle of 60°, the grain elongation decreased from 1.12 to 1.05 for a pouring temperature of 680 °C and from 1.08 to 1.07 for a pouring temperature of 640 °C with an increase in contact time from 0.04 s to 0.13 s (see Table 4.3.12). The minimum grain elongation value of 1.05 was obtained at a pouring temperature of 680 °C for a contact time of 0.13 s.

4.3.4 Effect of Inclination Angle

The effect of inclination angle on grain characteristics such as grain size, grain circularity and grain elongation was assessed for different contact times and pouring temperatures.

4.3.4.1 Constant Contact Time

The data for the effect of inclination angle at a specific contact time for different pouring temperatures for grain size is given in Table 4.3.13, for grain circularity in Table 4.3.14 and for grain elongation in Table 4.3.15.

Grain Size

Contact Time of 0.04 s

At a contact time of 0.04 s, the grain size increased from 145 μm to 181 μm for a pouring temperature of 680 °C and decreased from 166 μm to 98 μm for a pouring temperature of 640 °C with an increase in inclination angle from 20° to 60° (see Table 4.3.13). The grain size was the minimum for 660 °C for each inclination angle at this contact time. The minimum grain size of 89 μm was obtained for a pouring temperature of 660 °C at an inclination angle of 40°.

Contact Time of 0.09 s

At a contact time of 0.09 s, the grain size decreased from 140 μm to 93 μm for a pouring temperature of 660 °C with an increase in inclination angle from 20° to 60° (see Table 4.3.13). At the lowest and highest inclination angles, 20° and 60°, the grain size decreased from 136 μm to 100 μm for a pouring temperature of 680 °C, from 140 μm to 93 μm for a pouring temperature of 660 °C and from 146 μm to 115 μm for a pouring temperature of 640 °C. The minimum grain size of 87 μm was obtained for a pouring temperature of 680 °C at an inclination angle of 40°.

Contact Time of 0.13 s

At a contact time of 0.13 s, the grain size decreased from 159 μm to 105 μm for a pouring temperature of 640 °C with an increase in inclination angle from 20° to 60° (see Table 4.3.13). The grain size was found to be a minimum for a pouring temperature of 680 °C for each inclination angle. The grain size was found to be 91 μm both for pouring temperature of 680 °C and 660 °C at an inclination angle of 60°. The minimum grain size of 87 μm was found for a pouring temperature of 680 °C at an inclination angle of 40°.

Grain Circularity

Contact Time of 0.04 s

At a contact time of 0.04 s, the grain circularity decreased from 0.67 to 0.61 for a pouring temperature of 680 °C and increased from 0.76 to 0.84 for a pouring temperature of 660 °C and from 0.58 to 0.77 for a pouring temperature of 640 °C with an increase in inclination angle from 20° to 60° (see Table 4.3.14). The grain circularity was the highest for a pouring temperature of 660 °C for each inclination angle. The highest grain circularity of 0.84 was obtained for a pouring temperature of 660 °C at an inclination angle of 60°.

Contact Time of 0.09 s

At a contact time of 0.09 s, the grain circularity increased from 0.62 to 0.76 for a pouring temperature of 660 °C with an increase in inclination angle from 20° to 60° (see Table 4.3.14). At the lowest and highest inclination angles, 20° and 60°, the grain circularity increased from 0.62 to 0.81 for a pouring temperature of 680 °C and from 0.62 to 0.76 for a pouring temperature of 660 °C. The maximum grain circularity value of 0.86 was obtained at an inclination angle of 40° for a pouring temperature of 680 °C.

Contact Time of 0.13 s

At a contact time of 0.13 s, the grain circularity increased from 0.79 to 0.85 for a pouring temperature of 680 °C and from 0.59 to 0.71 for a pouring temperature of 640 °C with an increase in inclination angle from 20° to 60° (see Table 4.3.14). At the lowest and highest inclination angles, 20° and 60°, the grain circularity increased from 0.65 to 0.79 for a pouring temperature of 660 °C. The grain circularity values for a pouring temperature of 680 °C were higher for each inclination angle. The maximum grain circularity value of 0.86 was obtained for a pouring temperature of 680 °C at an inclination of 60°.

Grain Elongation

Contact Time of 0.04 s

At a contact time of 0.0.4 s, the grain elongation increased from 1.05 to 1.08 at a pouring temperature of 680 °C and remained approximately 1.08 for a pouring

temperature of 660 °C with an increase in inclination angle from 20° to 60° (see Table 4.3.15). The lowest grain elongation value of 1.05 was obtained for a pouring temperature of 640 °C at an inclination of 20°.

Contact Time of 0.09 s

At a contact time of 0.09 s, the grain elongation values at the lowest and highest inclination angles, 20° and 60°, decrease from 1.11 to 1.07 at a pouring temperature of 680 °C, from 1.07 to 1.06 at a pouring temperature of 660 °C and from reamin 1.08 at a pouring temperature of 640 °C (see Table 4.3.15). The minimum grain elongation value of 1.06 was obtained for a pouring temperature of 680 °C at an inclination angle of 40°.

Contact Time of 0.13 s

At a contact time of 0.13 s, the grain elongation decreased from 1.10 to 1.05 for a pouring temperature of 680 °C with an increase in inclination from 20° to 60° (see Table 4.3.15). At the lowest and highest inclinations; 20° and 60°, the grain elongation decreased from 1.10 to 1.05 for 680°C pouring temperature, from 1.11 to 1.10 for a pouring temperature of 660 °C and from 1.08 to 1.07 at a pouring temperature of 640 °C. The minimum grain elongation value of 1.04 was obtained for a pouring temperature of 640 °C at an inclination of 40°.

4.3.4.2 Constant Pouring Temperature

The data for the effect of inclination angle at a specific pouring temperature for different contact times for grain size is given in Table 4.3.16, for grain circularity in Table 4.3.17 and for grain elongation in Table 4.3.18.

Grain Size

Pouring temperature of 680 °C

At a pouring temperature of 680 °C, the grain size increased from 145 μm to 181 μm at a contact time of 0.04 s with an increase in inclination angle from 20° to 60° (see Table 4.3.16). The grain size was the minimum for a contact time of 0.13 s for

each inclination angle. The grain size decreased from 145 μm to 124 μm at an inclination angle of 20° and 181 μm to 91 μm at an inclination angle of 60° with an increase in contact time from 0.04 to 0.13 s. At the lowest and highest inclination angles, 20° and 60°, the grain size decreased from 136 μm to 100 μm for a contact time of 0.09 s and 124 μm to 91 μm for a contact time of 0.13 s, respectively. The minimum grain size of 87 μm was obtained at an inclination angle of 40° for contact times of 0.09 s and 0.13 s.

Pouring Temperature of 660 °C

At a pouring temperature of 660 °C, the grain size decreased from 140 μm to 93 μm for a contact time of 0.09 s with an increase in inclination angle from 20° to 60° (see Table 4.3.16). The grain size was the minimum for a contact time of 0.04 s for each inclination angle. The grain size was coarser at an inclination angle of 20° than those at an inclination angle of 60° for each contact time. The minimum grain size of 86 μm was obtained at an inclination angle of 40° for a contact time of 0.04 s.

Pouring Temperature of 640 °C

At a pouring temperature of 640 °C, the grain size decreased from 166 μm to 98 μm for a contact time of 0.04 s, from 146 μm to 115 μm for a contact time of 0.09 s and from 159 μm to 105 μm for a contact time of 0.13 s with an increase in inclination angle from 20° to 60° (see Table 4.3.16). The minimum grain size of 98 μm was obtained for a contact time of 0.04 s at an inclination angle of 60°.

Grain Circularity

Pouring Temperature of 680 °C

At a pouring temperature of 680 °C, the grain circularity decreased from 0.67 to 0.61 for a contact time of 0.04 s and increased from 0.79 to 0.86 for a contact time of 0.13 s with an increase in inclination angle from 20° to 60° (see Table 4.3.17). At the lowest and highest inclination angles, 20° and 60°, the grain circularity increased from 0.62 to 0.81 for a contact time of 0.09 s and from 0.79 to 0.86 for a contact time of 0.13 s. The highest grain circularity value of 0.86 was obtained for a contact time of 0.09 s at an inclination of 40° and for a contact time of 0.13 s at an inclination of 60°.

Pouring Temperature of 660 °C

At a pouring temperature of 660 °C, the grain circularity increased from 0.76 to 0.84 for a contact time of 0.04 s and from 0.62 to 0.76 for a contact time of 0.09 s with an increase in inclination angle from 20° to 60°. At the lowest and highest inclination angles, 20° and 60°, the grain circularity increased from 0.65 to 0.79 for a contact time of 0.13 s (see Table 4.3.17). The grain circularity was higher for a contact time of 0.04 s for each inclination angle. The highest grain circularity value of 0.84 was obtained for a contact time of 0.04 s at an inclination of 60°.

Pouring Temperature of 640 °C

At a pouring temperature of 640 °C, the grain circularity increased from 0.58 to 0.77 for a contact time of 0.04 s and from 0.59 to 0.71 for a contact time of 0.13 s with an increase in inclination angle from 20° to 60°. At the lowest and highest inclinations, 20° and 60°, the grain circularity decreased from 0.63 to 0.60 for a contact time of 0.09 s (see Table 4.3.17). The highest grain circularity value of 0.77 was obtained for a contact time of 0.04 s at an inclination of 60°.

Grain Elongation

Pouring Temperature of 680 °C

At a pouring temperature of 680 °C, the grain elongation decreased from 1.10 to 1.05 for a contact time of 0.13 s with an increase in inclination angle from 20° to 60° (see Table 4.3.18). The minimum grain elongation value of 1.05 was obtained for a contact time of 0.13 s for inclination angles of 40° and 60°.

Pouring Temperature of 660 °C

At a pouring temperature of 660 °C, the grain elongation of 1.08 remained the same for a contact time of 0.04 s with an increase in inclination angle from 20° to 60° (see Table 4.3.18). The minimum grain elongation value of 1.06 was obtained for a contact time of 0.09 s at an inclination of 60°.

Pouring Temperature of 640 °C

At a pouring temperature of 640 °C, the grain elongation increased from 1.05 to 1.08 for a contact time of 0.04 s with an increase in inclination angle from 20° to 60°

(see Table 4.3.18). The minimum grain elongation value of 1.04 was obtained for a contact time of 0.13 s at an inclination angle of 40°.

4.3.5 Summary

Considering the effect of processing parameters on the cooling slope process and the final microstructure, the results can be summarised as:

1. A minimum grain size of 87 μm with circularity of 0.86 and elongation of 1.05 was obtained, showing a fine, globular and equiaxed grain morphology, suiTable for semi-solid processing.
2. At an inclination angle of 60° with a contact time of 0.13 s, a similar grain size was obtained for all pouring temperatures (680, 660 and 640 °C).
3. In general, a pouring temperature of 660 °C gave a relatively finer grain size with globular and equiaxed morphology for all inclinations and contact times.
4. At higher contact times and inclination angles the process becomes sTable and showed a regular decreasing or increasing trend with a change in pouring temperature.
5. At each contact time and pouring temperature, an increase in inclination angle produced a finer grain size due to an increase in effective shear force thereby producing a higher number of nuclei to grow.
6. With a change in inclination angle, the grain size remained nearly unaffected for a pouring temperature of 680 °C at an inclination angle of 20°, at a pouring temperature of 660 °C at an inclination angle of 60 ° and at a pouring temperature of 640 °C at inclination angles of 40° and 60°.
7. Grain circularity and elongation data showed that the microstructure was nearly globular and equiaxed in nature for all conditions.

4.3.6 Tables

Table 4.3.1: Effect of pouring temperature on grain size (μm) at different contact times for different inclination angles.

Contact Time (s)	Pouring Temperature (℃)	Inclination angle (°)		
		20	40	60
0.04	680	145	161	181
	660	111	89	93
	640	166	147	98
0.09	680	136	87	100
	660	140	120	93
	640	146	148	115
0.13	680	124	87	91
	660	137	147	91
	640	159	145	105

Table 4.3.2: Effect of pouring temperature on grain circularity at different contact times for different inclination angles.

Contact Time (s)	Pouring Temperature (℃)	Inclination angle (°)		
		20	40	60
0.04	680	0.67	0.66	0.61
	660	0.76	0.83	0.84
	640	0.58	0.64	0.77
0.09	680	0.62	0.86	0.81
	660	0.62	0.72	0.76
	640	0.63	0.65	0.60
0.13	680	0.79	0.82	0.86
	660	0.65	0.61	0.79
	640	0.59	0.62	0.71

Table 4.3.3: Effect of pouring temperature on grain elongation at different contact times for different inclination angles.

Contact Time (s)	Pouring Temperature (℃)	Inclination angle (°)		
		20	40	60
0.04	680	1.11	1.08	1.12
	660	1.08	1.08	1.08
	640	1.05	1.07	1.08
0.09	680	1.11	1.06	1.07
	660	1.07	1.11	1.06
	640	1.08	1.11	1.08
0.13	680	1.10	1.05	1.05
	660	1.11	1.14	1.10
	640	1.08	1.04	1.07

Table 4.3.4: Effect of pouring temperature on grain size (μm) at different inclination angles for different contact times.

Inclination Angle (°)	Pouring Temperature (°C)	Contact Time (s)		
		0.04	0.09	0.13
20	680	145	136	124
	660	111	140	137
	640	166	146	159
40	680	161	87	87
	660	89	120	147
	640	147	148	145
60	680	181	100	91
	660	93	93	91
	640	98	115	105

Table 4.3.5: Effect of pouring temperature on grain circularity at different inclination angles for different contact times.

Inclination Angle (°)	Pouring Temperature (°C)	Contact Time (s)		
		0.04	0.09	0.13
20	680	0.67	0.62	0.79
	660	0.76	0.62	0.65
	640	0.58	0.63	0.59
40	680	0.66	0.86	0.82
	660	0.83	0.72	0.61
	640	0.64	0.65	0.62
60	680	0.61	0.81	0.86
	660	0.84	0.76	0.79
	640	0.77	0.60	0.71

Table 4.3.6: Effect of pouring temperature on grain elongation at different inclination angles for different contact times.

Inclination Angle (°)	Pouring Temperature (°C)	Contact Time (s)		
		0.04	0.09	0.13
20	680	1.11	1.11	1.10
	660	1.08	1.07	1.11
	640	1.05	1.08	1.08
40	680	1.08	1.06	1.05
	660	1.08	1.11	1.14
	640	1.07	1.11	1.04
60	680	1.12	1.07	.05
	660	1.08	1.06	1.10
	640	1.08	1.08	1.07

Table 4.3.7: Effect of contact time on grain size (μm) at different pouring temperatures for different inclination angles.

Pouring Temperature (℃)	Contact Time (s)	Inclination Angle (°)		
		20	40	60
680	0.04	145	161	181
	0.09	136	87	100
	0.13	124	87	91
660	0.04	111	89	93
	0.09	140	120	93
	0.13	137	147	91
640	0.04	166	147	98
	0.09	146	148	115
	0.13	159	145	105

Table 4.3.8: Effect of contact time on grain circularity at different pouring temperatures for different inclination angles.

Pouring Temperature (℃)	Contact Time (s)	Inclination Angle (°)		
		20	40	60
680	0.04	0.67	0.66	0.61
	0.09	0.62	0.86	0.81
	0.13	0.79	0.82	0.86
660	0.04	0.76	0.83	0.84
	0.09	0.62	0.72	0.76
	0.13	0.65	0.61	0.79
640	0.04	0.58	0.64	0.77
	0.09	0.63	0.65	0.60
	0.13	0.59	0.62	0.71

Table 4.3.9: Effect of contact time on grain elongation at different pouring temperatures for different inclination angles.

Pouring Temperature (℃)	Contact Time (s)	Inclination Angle (°)		
		20	40	60
680	0.04	1.11	1.08	1.12
	0.09	1.11	1.06	1.07
	0.13	1.10	1.05	1.05
660	0.04	1.08	1.08	1.08
	0.09	1.07	1.11	1.06
	0.13	1.11	1.14	1.10
640	0.04	1.05	1.07	1.08
	0.09	1.08	1.11	1.08
	0.13	1.08	1.04	1.07

Table 4.3.10: Effect of contact time on grain size (μm) at different inclination angles for different pouring temperatures.

Inclination Angle(°)	Contact Time (s)	Pouring Temperature (℃)		
		680	660	640
20	0.04	145	111	166
	0.09	136	140	146
	0.13	124	137	159
40	0.04	161	89	147
	0.09	87	120	148
	0.13	87	147	145
60	0.04	181	93	98
	0.09	100	93	115
	0.13	91	91	105

Table 4.3.11: Effect of contact time on grain circularity at different inclination angles for different pouring temperatures.

Inclination Angle(°)	Contact Time (s)	Pouring Temperature (℃)		
		680	660	640
20	0.04	0.67	0.76	0.58
	0.09	0.62	0.62	0.63
	0.13	0.79	0.65	0.59
40	0.04	0.66	0.83	0.64
	0.09	0.86	0.72	0.65
	0.13	0.82	0.61	0.62
60	0.04	0.61	0.84	0.77
	0.09	0.81	0.76	0.60
	0.13	0.86	0.79	0.71

Table 4.3.12: Effect of contact time on grain elongation at different inclination angles for different pouring temperatures.

Inclination Angle(°)	Contact Time (s)	Pouring Temperature (℃)		
		680	660	640
20	0.04	1.11	1.08	1.05
	0.09	1.11	1.07	1.08
	0.13	1.10	1.11	1.08
40	0.04	1.08	1.08	1.07
	0.09	1.06	1.11	1.11
	0.13	1.05	1.14	1.04
60	0.04	1.12	1.08	1.08
	0.09	1.07	1.06	1.08
	0.13	1.05	1.10	1.07

Table 4.3.13: Effect of inclination angle on grain size (μm) at different contact times for different pouring temperatures.

Contact Time (s)	Inclination Angle(°)	Pouring temperature (℃)		
		680	660	640
0.04	20	145	111	166
	40	161	89	147
	60	181	93	98
0.09	20	136	140	146
	40	87	120	148
	60	100	93	115
0.13	20	124	137	159
	40	87	147	145
	60	91	91	105

Table 4.3.14: Effect of inclination angle on grain circularity at different contact times for different pouring temperatures.

Contact Time (s)	Inclination Angle(°)	Pouring temperature (℃)		
		680	660	640
0.04	20	0.67	0.76	0.58
	40	0.66	0.83	0.64
	60	0.61	0.84	0.77
0.09	20	0.62	0.62	0.63
	40	0.86	0.72	0.65
	60	0.81	0.76	0.60
0.13	20	0.79	0.65	0.59
	40	0.82	0.61	0.62
	60	0.86	0.79	0.71

Table 4.3.15: Effect of inclination angle on grain elongation at different contact times for different pouring temperatures.

Contact Time (s)	Inclination Angle(°)	Pouring temperature (℃)		
		680	660	640
0.04	20	1.11	1.08	1.05
	40	1.08	1.08	1.07
	60	1.12	1.08	1.08
0.09	20	1.11	1.07	1.08
	40	1.06	1.11	1.11
	60	1.07	1.06	1.08
0.13	20	1.10	1.11	1.08
	40	1.05	1.14	1.04
	60	1.05	1.10	1.07

Table4.3.16: Effect of inclination angle on grain size (μm) at different pouring temperatures for different contact times.

Pouring Temperature (℃)	Inclination Angle(°)	Contact Time (s)		
		0.04	0.09	0.13
680	20	145	136	124
	40	161	87	87
	60	181	100	91
660	20	111	140	137
	40	89	120	147
	60	93	93	91
640	20	166	146	159
	40	147	148	145
	60	98	115	105

Table 4.3.17: Effect of inclination angle on grain circularity at different pouring temperatures for different contact times.

Pouring Temperature (℃)	Inclination Angle(°)	Contact Time (s)		
		0.04	0.09	0.13
680	20	0.67	0.62	0.79
	40	0.66	0.86	0.82
	60	0.61	0.81	0.86
660	20	0.76	0.62	0.65
	40	0.83	0.72	0.61
	60	0.84	0.76	0.79
640	20	0.58	0.63	0.59
	40	0.64	0.65	0.62
	60	0.77	0.60	0.71

Table 4.3.18: Effect of inclination angle on grain elongation at different pouring temperatures for different contact times.

Pouring Temperature (℃)	Inclination Angle(°)	Contact Time (s)		
		0.04	0.09	0.13
680	20	1.11	1.11	1.10
	40	1.08	1.06	1.05
	60	1.12	1.07	1.05
660	20	1.08	1.07	1.11
	40	1.08	1.11	1.14
	60	1.08	1.06	1.10
640	20	1.05	1.08	1.08
	40	1.07	1.11	1.04
	60	1.08	1.08	1.07

4.3.7 Figures

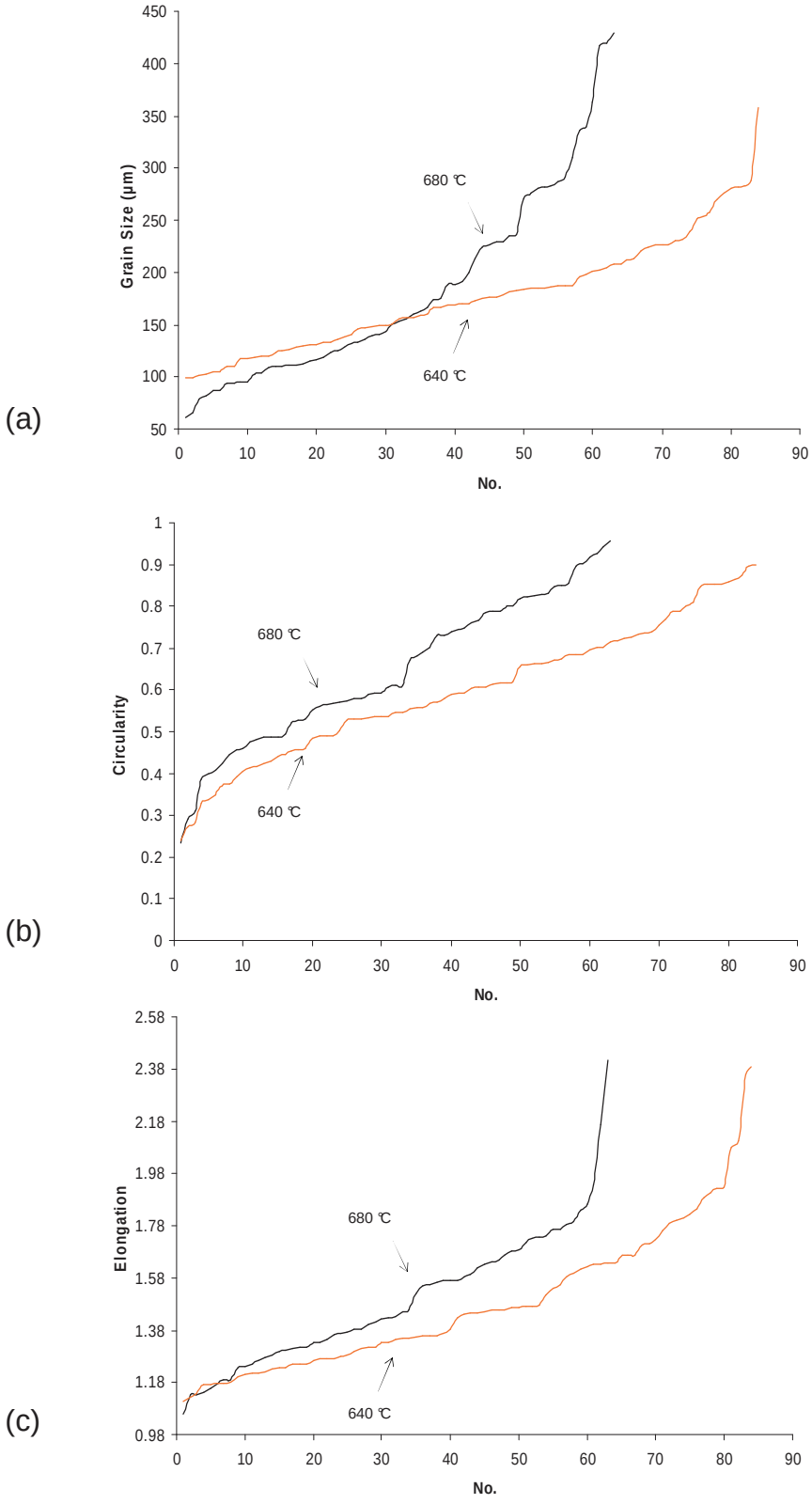

Fig. 4.3.1: Variation of data for samples processed at pouring temperatures of 680 °C and 640 °C on an inclination angle of 20° and a contact time of 0.04 s : (a) grain size; (b) circularity; and, (c) elongation. The ——— line shows data for 680 °C and ——— for 640 °C.

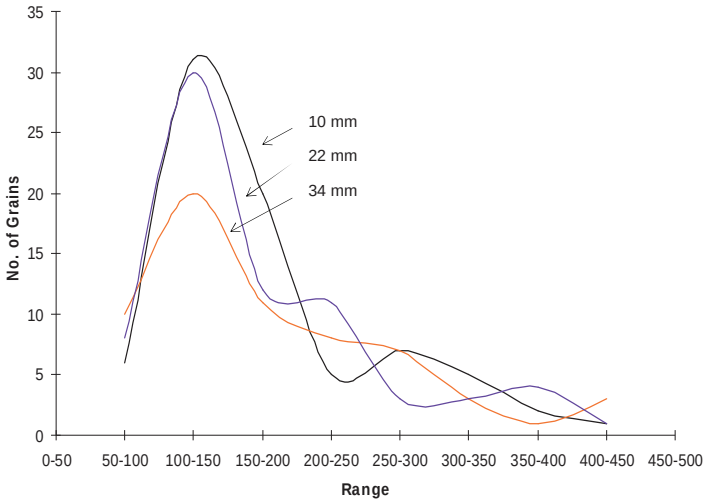

Fig. 4.3.2: Distribution of grain size for samples processed at a pouring temperature of 680 °C for an inclination angle of 20° and a contact time of 0.04 s for different sample thicknesses. The _____ line for 10mm, _____ for 22 mm and _____ for 34 mm thick sections.

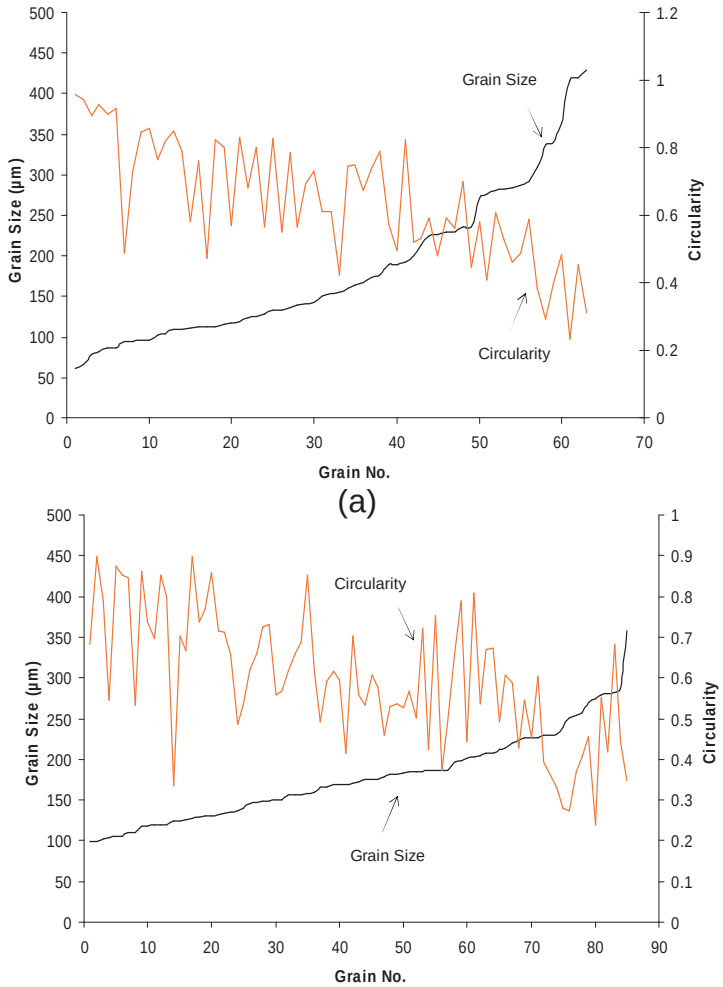

Fig. 4.3.3: Variation of corresponding circularity data with increase in grain size for samples processed for an inclination angle of 20° and a contact time of 0.04 s : (a) 680 °C; and, (b) 640 °C. The _____ line shows grain size and _____ circularity.

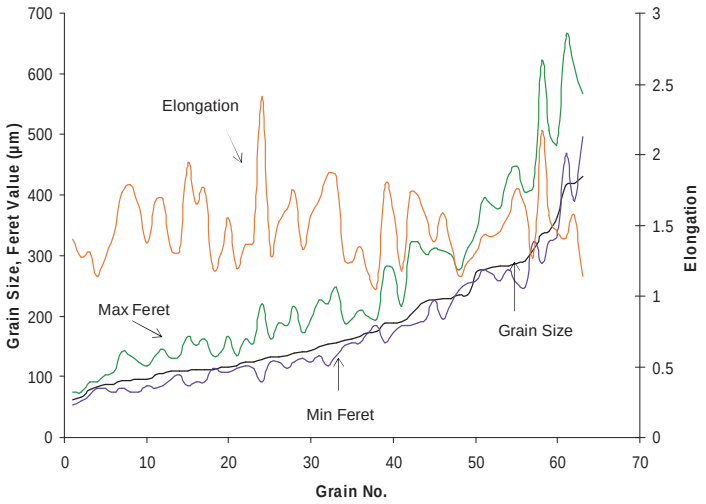

(a)

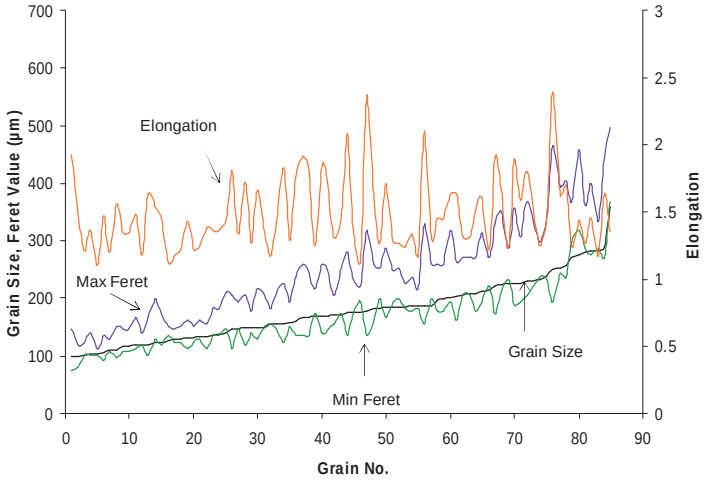

(b)

Fig. 4.3.4: Variation of corresponding Feret diameter and elongation data with increase in grain size for samples processed at an inclination angle of 20° and a contact time of 0.04 s for: (a) 680 °C; and, (b) 640 °C. The ——— line shows grain size, ——— maximum Feret diameter, minimum Feret diameter and ——— elongation.

4.4. EFFECT OF SAMPLE THICKNESS

In this section the effect of pouring temperature, inclination angle and contact time on the NGM AlSi7Mg alloy, processed on a water cooled graphite coated cooling slope and cast into a sand mould, was investigated. The sand cast samples were sectioned and examined. Position "1" describes the point at the sand wall edge of the sample, position "2" represents the point just inside the surface of the sample, position "3" represents the mid point of the sample section at a wall thickness of 10 mm. Point "4" represents the centre of the 22 mm thick section and point "5" represents the centre of 34 mm thick section of the sand cast sample (see Fig. 4.4.1).

4.4.1 Effect of Processing Parameters Combined with the Effect of Position in 10 mm Thick Sample (Wall to Centre)

In this section the effect of processing parameters such as a pouring temperature, contact time and inclination on the microstructure characteristics of the NGM AlSi7Mg alloy, using the cooling slope technique with sand mould, for a sample thickness of 10 mm was reported.

4.4.1.1 Effect of Pouring Temperature

Contact Time of 0.04 s

At a contact time of 0.04 s, for an inclination angle of 20°, the grain size decreased from 137 μm to 122 μm at a pouring temperature of 660 °C and from 194 μm to 179 μm for a pouring temperature of 640 °C, between positions 1 and 3 in the sand cast sample (see Table 4.4.1). For an inclination angle of 40°, the grain size increased from 133 μm to 151 μm at a pouring temperature of 640 °C between positions 1 and 3 in the sand cast sample. For an inclination angle of 60°, the grain size increased from 169 μm to 213 μm at a pouring temperature of 680 °C, from 94 μm to 100 μm at a

pouring temperature of 660 °C and from 76 μm to 117 μm at a pouring temperature of 640 °C between positions 1 and 3 in the sand cast sample.

Contact Time of 0.09 s

At a contact time of 0.09 s, for an inclination angle of 20°, the grain size increased from 125 μm to 152 μm at a pouring temperature of 680 °C and from 123 μm to 189 μm at a pouring temperature of 640 °C between positions 1 and 3 in the sand cast sample (see Table 4.4.1). For an inclination angle of 40°, the grain size decreased from 123 μm to 86 μm at a pouring temperature of 680 °C and from 104 μm to 97 μm at a pouring temperature of 640 °C but increased from 114 μm to 115 μm at a pouring temperature of 660 °C between positions 1 and 3 in the sand cast sample. For an inclination angle of 60°, the grain size decreased from 100 μm to 98 μm at a pouring temperature of 680 °C and from 103 μm to 91 μm at a pouring temperature of 660 °C but increased from 169 μm to 179 μm at a pouring temperature of 640 °C between positions 1 and 3 in the sand cast sample.

Contact Time of 0.13 s

At a contact time of 0.13 s, for an inclination angle of 20°, the grain size increased from 129 μm to 165 μm at a pouring temperature of 680 °C between positions 1 and 3 in the sand cast sample (see Table 4.4.1). For an inclination angle of 40°, the grain size increased from 87 μm to 96 μm at a pouring temperature of 680 °C and from 119 μm to 124 μm at a pouring temperature of 640 °C between positions 1 and 3 in the sand cast sample. For an inclination angle of 60°, the grain size 98 μm remained at a pouring temperature of 680 °C but increased from 83 μm to 95 μm at a pouring temperature of 640 °C between positions 1 and 3 in the sand cast sample.

In general at a contact time of 0.04 s, a finer grains size was obtained for an inclination angle of 60° at a pouring temperature of 660 °C. At a contact time of 0.09 s a finer grain size was obtained for an inclination angle of 40° at pouring temperatures of 680 °C and 640 °C and for an inclination angle of 60° at pouring temperatures of 680 °C and 660 °C. At a contact time of 0.13 s a finer grain size was obtained for an inclination angle of 40° at a pouring temperature of 680 °C and for an inclination angle of 60° at each pouring temperature.

Grain Circularity

Contact Time of 0.04 s

At a contact time of 0.04 s, for an inclination angle of 20°, the grain circularity increased from 0.49 to 0.58 at a pouring temperature of 640 °C between positions 1 and 3 in the sand cast sample (see Table 4.4.2). For an inclination angle of 40°, the grain circularity decreased from 0.67 to 0.62 at a pouring temperature of 640 °C between positions 1 and 3 in the sand cast sample. For an inclination angle of 60°, the grain circularity decreased from 0.60 to 0.51 at a pouring temperature of 680 °C and from 0.82 to 0.72 at a pouring temperature of 640 °C but remained unchanged at 0.78 at a pouring temperature of 660 °C between positions 1 and 3 in the sand cast sample.

Contact Time of 0.09 s

At a contact time of 0.09 s, for an inclination angle of 20°, the grain circularity decreased from 0.67 to 0.53 at a pouring temperature of 640 °C between positions 1 and 3 in the sand cast sample (see Table 4.4.2). For an inclination angle of 40°, the grain circularity increased from 0.73 to 0.84 at a pouring temperature of 680 °C, from 0.69 to 0.71 at a pouring temperature of 660 °C and from 0.70 to 0.76 at a pouring temperature of 640 °C between positions 1 and 3 in the sand cast sample. For an inclination angle of 60°, the grain circularity decreased from 0.76 to 0.80 at a pouring temperature of 680 °C, from 0.71 to 0.74 at a pouring temperature of 660 °C and from 0.51 to 0.57 at a pouring temperature of 640 °C between positions 1 and 3 in the sand cast sample.

Contact Time of 0.13 s

At a contact time of 0.13 s, for an inclination angle of 20°, the grain circularity decreased from 0.70 to 0.68 at a pouring temperature of 680 °C between positions 1 and 3 in the sand cast sample (see Table 4.4.2). For an inclination angle of 40°, the grain circularity decreased from 0.81 to 0.78 at a pouring temperature of 680 °C, from 0.72 to 0.67 at a pouring temperature of 660 °C and from 0.67 to 0.65 at a pouring temperature of 640 °C between positions 1 and 3 in the sand cast sample. For an inclination angle of 60°, the grain circularity increased from 0.76 to 0.81 at a pouring temperature of 680 °C and decreased from 0.76 to 0.73 at a pouring temperature of 640 °C between positions 1 and 3 in the sand cast sample.

In general at a contact time of 0.04 s the highest grains circularity was obtained for an inclination angle of 20° at a pouring temperature of 660 °C, for an inclination angle of 40° at a pouring temperature of 660 °C and for an inclination angle of 60° at pouring temperatures of 660 °C and 640 °C. At contact times of 0.09 s and 0.13 s the highest grain circularity was obtained at a pouring temperature of 680 °C for each inclination angle.

Grain Elongation

Contact Time of 0.04 s

At a contact time of 0.04 s, for an inclination angle of 20°, the grain elongation decreased from 1.11 to 1.08 at a pouring temperature of 680 °C, from 1.13 to 1.08 at a pouring temperature of 660 °C and from 1.15 to 1.09 at a pouring temperature of 640 °C between positions 1 and 3 in the sand cast sample (see Table 4.4.3). For an inclination angle of 40°, the grain elongation decreased from 1.15 to 1.10 at a pouring temperature of 680 °C, from 1.11 to 1.10 at a pouring temperature of 660 °C and from 1.13 to 1.08 at a pouring temperature of 640 °C between positions 1 and 3 in the sand cast sample. For an inclination angle of 60°, the grain elongation increased from 1.10 to 1.12 at a pouring temperature of 680 °C, decreased from 1.11 to 1.06 at a pouring temperature of 660 °C and remained constant at 1.00 at a pouring temperature of 640 °C between positions 1 and 3 in the sand cast sample.

Contact Time of 0.09 s

At a contact time of 0.09 s, for an inclination angle of 20°, the grain elongation increased from 1.09 to 1.10 at a pouring temperature of 680 °C, decreased from 1.13 to 1.08 at a pouring temperature of 660 °C and remained unchanged at 1.10 at a pouring temperature of 640 °C between positions 1 and 3 in the sand cast sample (see Table 4.4.3). For an inclination angle of 40°, the grain elongation decreased from 1.09 to 1.06 at a pouring temperature of 680 °C and from 1.10 to 1.08 at a pouring temperature of 640 °C but increased from 1.08 to 1.11 at a pouring temperature of 660 °C between positions 1 and 3 in the sand cast sample. For an inclination angle of 60°, the grain elongation decreased from 1.08 to 1.06 at a pouring temperature of 680 °C but increased from 1.11 to 1.18 at a pouring temperature of 640 °C between positions 1 and 3 in the sand cast sample.

Contact Time of 0.13 s

At a contact time of 0.13 s, for an inclination angle of 20°, the grain elongation decreased from 1.14 to 1.05 at a pouring temperature of 680 °C, from 1.10 to 1.08 at a pouring temperature of 660 °C and from 1.13 to 1.12 at a pouring temperature of 640 °C between positions 1 and 3 in the sand cast sample (see Table 4.4.3). For an inclination angle of 40°, the grain elongation increased from 1.00 to 1.09 at a pouring temperature of 680 °C but remained unchanged at 1.08 at a pouring temperature of 640 °C between positions 1 and 3 in the sand cast sample. For an inclination angle of 60°, the grain elongation increased from 1.05 to 1.12 at a pouring temperature of 680 °C, from 1.00 to 1.11 at a pouring temperature of 660 °C and from 1.00 to 1.10 at a pouring temperature of 640 °C between positions 1 and 3 in the sand cast sample.

In general at a contact time of 0.04 s the lowest elongation was obtained for an inclination angle of 20° at a pouring temperature of 660 °C, for an inclination angle of 40° at a pouring temperature of 640 °C and at an inclination angle of 60° at a pouring temperature of 640 °C. At a contact time of 0.09 s the lowest elongation was obtained for an inclination angle of 20° at a pouring temperature of 660 °C, for an inclination angle of 40° at a pouring temperature of 680 °C and for an inclination angle of 60° at pouring temperatures of 680 °C and 660 °C. At a contact time of 0.13 s the lowest elongation was obtained for an inclination angle of 20° at a pouring temperature of 660 °C, for an inclination angle of 40° at a pouring temperature of 640 °C and for an inclination angle of 20° at a pouring temperature of 660 °C.

4.4.1.2 Effect of Contact Time

Grain Size

Inclination Angle of 20°

At an inclination of 20°, for a pouring temperature of 680 °C, the grain size increased from 125 μm to 152 μm at a contact time of 0.09 s and from 129 μm to 165 μm at a contact time of 0.13 s between positions 1 and 3 in the sand cast sample (see Table 4.4.4). For a pouring temperature of 660 °C, the grain size decreased from 137 μm to 122 μm at a contact time of 0.04 s between positions 1 and 3 in the sand cast sample. For a pouring temperature of 640 °C, the grain size decreased from 194 μm to 179 μm

at a contact time of 0.04 s but increased from 123 μm to 189 μm at a contact time of 0.09 s between positions 1 and 3 in the sand cast sample.

Inclination Angle of 40°

At an inclination of 40°, for a pouring temperature of 680 °C, the grain size decreased from 103 μm to 86 μm at a contact time of 0.09 s but increased from 87 μm to 96 μm at a contact time of 0.13 s between positions 1 and 3 in the sand cast sample (see Table 4.4.4). For a pouring temperature of 660 °C, the grain size increased from 114 μm to 115 μm at a contact time of 0.09 s between positions 1 and 3 in the sand cast sample. For a pouring temperature of 640 °C, the grain size increased from 133 μm to 151 μm at a contact time of 0.04 s and from 118 μm to 124 μm at a contact time of 0.13 s but decreased from 104 μm to 97 μm at a contact time of 0.09 s between positions 1 and 3 in the sand cast sample.

Inclination Angle of 60°

At an inclination of 60°, for a pouring temperature of 680 °C, the grain size increased from 169 μm to 213 μm at a contact time of 0.04 s, decreased from 100 μm to 89 μm at a contact time of 0.09 s and remained constant to 98 μm at a contact time of 0.13 s between positions 1 and 3 in the sand cast sample (see Table 4.4.4). For a pouring temperature of 660 °C, the grain size increased from 94 μm to 100 μm at a contact time of 0.04 s and decreased from 103 μm to 91 μm at a contact time of 0.09 s between positions 1 and 3 in the sand cast sample. For a pouring temperature of 640 °C, the grain size increased from 76 μm to 117 μm at a contact time of 0.04 s, from 169 μm to 179 μm at a contact time of 0.09 s and from 83 μm to 95 μm at a contact time of 0.13 s between positions 1 and 3 in the sand cast sample.

In general at an inclination angle of 20° a relatively finer grain size was obtained for a pouring temperature of 660 °C at a contact time of 0.04 s. At an inclination angle of 40° a relatively finer grains size was obtained for a pouring temperature of 680 °C at contact times of 0.09 s and 0.13 s, for a pouring temperature of 660 °C at a contact time of 0.13 s and for a pouring temperature of 640 °C at a contact time of 0.09 s. At an inclination angle of 60° a relatively finer grains size was obtained for a pouring temperature of 680 °C at contact times of 0.09 s and 0.13 s, for a pouring temperature of 660 °C at each a contact time and for a pouring temperature of 640 °C at contact times of 0.04 s and 0.13 s.

Grain Circularity

Inclination Angle of 20°

At an inclination angle of 20°, for a pouring temperature of 680 °C, the grain circularity decreased from 0.70 to 0.68 at a contact time of 0.04 s between positions 1 and 3 in the sand cast sample (see Table 4.4.5). For a pouring temperature of 660 °C, the grain circularity increased from 0.68 to 0.71 at a contact time of 0.04 s between positions 1 and 3 in the sand cast sample. For a pouring temperature of 640 °C, the grain circularity increased from 0.49 to 0.58 at a contact time of 0.04 s and decreased from 0.67 to 0.53 at a contact time of 0.09 s between positions 1 and 3 in the sand cast sample.

Inclination Angle of 40°

At an inclination of 40°, for a pouring temperature of 680 °C, the grain circularity increased from 0.73 to 0.84 at a contact time of 0.09 s and decreased from 0.81 to 0.78 at a contact time of 0.13 s between positions 1 and 3 in the sand cast sample (see Table 4.4.5). For a pouring temperature of 660 °C, the grain circularity increased from 0.69 to 0.71 at a contact time of 0.09 s and decreased from 0.72 to 0.67 at a contact time of 0.13 s between positions 1 and 3 in the sand cast sample. For a pouring temperature of 640 °C, the grain circularity decreased from 0.67 to 0.62 at a contact time of 0.04 s and from 0.67 to 0.65 at a contact time of 0.13 s but increased from 0.70 to 0.76 at a contact time of 0.09 s between positions 1 and 3 in the sand cast sample.

Inclination Angle of 60°

At an inclination of 60°, for a pouring temperature of 680 °C, the grain circularity decreased from 0.60 to 0.51 at a contact time of 0.04 s but increased from 0.76 to 0.80 at a contact time of 0.09 s and from 0.76 to 0.81 at a contact time of 0.13 s between positions 1 and 3 in the sand cast sample (see Table 4.4.5). For a pouring temperature of 660 °C, the grain circularity remained unchanged at 0.78 at a contact time of 0.04 s and increased from 0.71 to 0.74 at a contact time of 0.09 s between positions 1 and 3 in the sand cast sample. For a pouring temperature of 640 °C, the grain circularity decreased from 0.82 to 0.72 at a contact time of 0.04 s and from 0.76 to 0.73 at a

contact time of 0.13 s but increased from 0.51 to 0.57 at a contact time of 0.09 s between positions 1 and 3 in the sand cast sample.

In general at an inclination angle of 20° the highest grain circularity was obtained for pouring temperatures of 680 °C and 640 °C at a contact time of 0.13 s and for a pouring temperature of 660 °C at a contact time of 0.04 s. At an inclination angle of 40° the highest circularity was obtained for a pouring temperature of 680 °C at contact times of 0.09 s and 0.13 s and for pouring temperatures of 660 °C and 640 °C at a contact time of 0.09 s.

Grain Elongation

Inclination Angle of 20°

At an inclination angle of 20°, for a pouring temperature of 680 °C, the grain elongation decreased from 1.11 to 1.08 at a contact time of 0.04 s and from 1.14 to 1.05 at a contact time of 0.13 s, between positions 1 and 3 in the sand cast sample (see Table 4.4.6). For a pouring temperature of 660 °C, the grain elongation decreased from 1.13 to 1.08 at a contact time of 0.09 s and from 1.10 to 1.08 at a contact time of 0.13 s between positions 1 and 3 in the sand cast sample. For a pouring temperature of 640 °C, the grain elongation decreased from 1.15 to 1.09 at a contact time of 0.04 s and from 1.13 to 1.12 at a contact time of 0.13 s but remained unchanged at 1.10 at a contact time of 0.09 s between positions 1 and 3 in the sand cast sample.

Inclination Angle of 40°

At an inclination of 40°, for a pouring temperature of 680 °C, the grain elongation decreased from 1.15 to 1.10 at a contact time of 0.04 s and from 1.09 to 1.06 at a contact time of 0.09 s but increased from 1.00 to 1.09 at a contact time of 0.13 s between positions 1 and 3 in the sand cast sample (see Table 4.4.6). For a pouring temperature of 660 °C, the grain elongation decreased from 1.08 to 1.11 at a contact time of 0.09 s between positions 1 and 3 in the sand cast sample. For a pouring temperature of 640 °C, the grain elongation decreased from 1.13 to 1.08 at a contact time of 0.04 s and from 1.10 to 1.08 at a contact time of 0.09 s and remained unchanged at 1.08 at a contact time of 0.13 s between positions 1 and 3 in the sand cast sample.

Inclination Angle of 60°

At an inclination of 60°, for a pouring temperature of 680 °C, the grain elongation increased from 1.10 to 1.12 at a contact time of 0.04 s and from 1.05 to 1.12 at a contact time of 0.13 s, but decreased from 1.08 to 1.06 at a contact time of 0.09 s between positions 1 and 3 in the sand cast sample (see Table 4.4.6). For a pouring temperature of 660 °C, the grain elongation decreased from 1.11 to 1.06 at a contact time of 0.04 s but increased from 1.00 to 1.11 at a contact time of 0.13 s between positions 1 and 3 in the sand cast sample. For a pouring temperature of 640 °C, the grain elongation increased from 1.11 to 1.18 at a contact time of 0.09 s and from 1.00 to 1.10 at a contact time of 0.13 s, and remained unchanged at 1.00 at a contact time of 0.04 s between positions 1 and 3 in the sand cast sample.

In general at an inclination angle of 20°, the grain elongation was the lowest for pouring temperatures of 680 °C and 660 °C at a contact time of 0.09 s and for a pouring temperature of 640 °C at a contact time of 0.04 s. At an inclination angle of 40° the grain elongation was the lowest for pouring temperatures of 680 °C and 660 °C at a contact time of 0.09 s and for a pouring temperature of 640 °C at a contact time of 0.13 s. At an inclination angle of 60° the lowest grain elongation for pouring temperatures of 680 °C and 660 °C at a contact time of 0.09 s and for a pouring temperature of 640 °C at a contact time of 0.04 s.

4.4.1.3 Effect of Inclination Angle

Grain Size

Pouring Temperature of 680 °C

At a pouring temperature of 680 °C, for a contact time of 0.04 s, the grain size increased from 169 μm to 213 μm at an inclination angle of 60° between positions 1 and 3 in the sand cast sample (see Table 4.4.7). For a contact time of 0.09 s, the grain size increased from 125 μm to 152 μm at an inclination angle of 20° and decreased from 103 μm to 86 μm at an inclination angle of 40° and from 100 μm to 89 μm at an inclination angle of 60° between positions 1 and 3 in the sand cast sample. For a contact time of 0.13 s, the grain size increased from 129 μm to 165 μm at an inclination angle of 20° and from 87 μm to 96 μm at an inclination angle of 40°, but

remained unchanged at 98 μm at an inclination angle of 60° between positions 1 and 3 in the sand cast sample.

Pouring Temperature of 660 °C

At a pouring temperature of 660 °C, for a contact time of 0.04 s, the grain size decreased from 137 μm to 122 μm at an inclination angle of 20° but increased from 94 μm to 100 μm at an inclination angle of 60° between positions 1 and 3 in the sand cast sample (see Table 4.4.7). For a contact time of 0.09 s, the grain size increased from 114 μm to 115 μm at an inclination angle of 40° but decreased from 103 μm to 91 μm at an inclination angle of 60° between positions 1 and 3 in the sand cast sample. For a contact time of 0.13 s, the grain size did not exhibit a clear trend between positions 1 and 3 in the sand cast sample.

Pouring Temperature of 640 °C

At a pouring temperature of 640 °C, for a contact time of 0.04 s, the grain size decreased from 194 μm to 179 μm at an inclination angle of 20° but increased from 76 μm to 117 μm at an inclination angle of 60° between positions 1 and 3 in the sand cast sample (see Table 4.4.7). For a contact time of 0.09 s, the grain size increased from 123 μm to 189 μm at an inclination angle of 20° and from 169 μm to 179 μm at an inclination angle of 60° but decreased from 104 μm to 97 μm at an inclination angle of 40° between positions 1 and 3 in the sand cast sample. For a contact time of 0.13 s, the grain size increased from 118 μm to 124 μm at an inclination angle of 40° and from 83 μm to 95 μm at an inclination angle of 60° between positions 1 and 3 in the sand cast sample.

In general at a pouring temperature of 680 °C, the finest grain size for a contact time of 0.04 s was obtained at an inclination angle of 20° and for contact times of 0.09 s and 0.13 s at inclination angles of 40° and 60°. At a pouring temperature of 660 °C the finest grain size was obtained for contact times of 0.04 s and 0.09 s at an inclination angle of 60° and for a contact time of 0.13 s at inclination angles of 40° and 60°. At a pouring temperature of 640 °C, the finest grain size was obtained for contact times of 0.04 s and 0.13 s at an inclination angle of 60° and for a contact time of 0.09 s at an inclination angle of 40°.

Grain Circularity

Pouring Temperature of 680 °C

At a pouring temperature of 680 °C, for a contact time of 0.04 s, the grain circularity decreased from 0.60 to 0.51 at an inclination angle of 60° between positions 1 and 3 in the sand cast sample (see Table 4.4.8). For a contact time of 0.09 s, the grain circularity increased from 0.73 to 0.84 at an inclination angle of 40° and from 0.76 to 0.80 at an inclination angle of 60° between positions 1 and 3 in the sand cast sample. For a contact time of 0.13 s, the grain circularity decreased from 0.70 to 0.68 at an inclination angle of 20° and from 0.81 to 0.78 at an inclination angle of 40° but increased from 0.76 to 0.81 at an inclination angle of 60° between positions 1 and 3 in the sand cast sample.

Pouring Temperature of 660 °C

At a pouring temperature of 660 °C, for a contact time of 0.09 s, the grain circularity increased from 0.68 to 0.71 at an inclination angle of 20° and remained unchanged at 0.78 at an inclination angle of 60° between positions 1 and 3 in the sand cast sample (see Table 4.4.8). For a contact time of 0.09 s, the grain circularity increased from 0.69 to 0.71 at an inclination angle of 40° and from 0.71 to 0.74 at an inclination angle of 60° between positions 1 and 3 in the sand cast sample. For a contact time of 0.13 s, the grain circularity decreased from 0.72 to 0.67 at an inclination angle of 40° between positions 1 and 3 in the sand cast sample.

Pouring Temperature of 640 °C

At a pouring temperature of 640 °C, for a contact time of 0.13 s, the grain circularity increased from 0.49 to 0.58 at an inclination angle of 20° but decreased from 0.67 to 0.62 at an inclination angle of 40° and from 0.82 to 0.72 at an inclination angle of 60° between positions 1 and 3 in the sand cast sample (see Table 4.4.8). For a contact time of 0.09 s, the grain circularity decreased from 0.67 to 0.53 at an inclination angle of 20° but increased from 0.70 to 0.76 at an inclination angle of 40° and from 0.51 to 0.57 at an inclination angle of 60° between positions 1 and 3 in the sand cast sample. For a contact time of 0.13 s, the grain circularity decreased from 0.67 to 0.65 at an inclination angle of 40° and from 0.76 to 0.73 at an inclination angle of 60° between positions 1 and 3 in the sand cast sample.

In general at a pouring temperature of 680 °C, the highest grain circularity for a contact time of 0.04 s was obtained at inclination angles of 20° and for contact times of 0.09 s and 0.13 s at inclination angles of 40° and 60°. At a pouring temperature of 660 °C the highest grain circularity was obtained for contact times of 0.04 s and 0.09 s at an inclination angle of 60° and for a contact time of 0.13 s at inclination angles of 40° and 60°. At a pouring temperature of 640 °C, the highest grain circularity was obtained for contact times of 0.04 s and 0.13 s at an inclination angle of 60° and for a contact time of 0.09 s at an inclination angle of 40°.

Grain Elongation

Pouring Temperature of 680 °C

At a pouring temperature of 680 °C, for a contact time of 0.04 s, the grain elongation decreased from 1.11 to 1.08 at an inclination angle of 20° and from 1.15 to 1.10 at an inclination angle of 40° but increased from 1.10 to 1.12 at an inclination angle of 60° between positions 1 and 3 in the sand cast sample (see Table 4.4.9). For a contact time of 0.09 s, the grain elongation decreased from 1.09 to 1.06 at an inclination angle of 40° and from 1.08 to 1.06 at an inclination angle of 60° between positions 1 and 3 in the sand cast sample. For a contact time of 0.13 s, the grain elongation decreased from 1.14 to 1.05 at an inclination angle of 20° but increased from 1.00 to 1.09 at an inclination angle of 40° and from 1.05 to 1.12 at an inclination angle of 60° between positions 1 and 3 in the sand cast sample.

Pouring Temperature of 660 °C

At a pouring temperature of 660 °C, for a contact time of 0.04 s, the grain elongation decreased from 1.11 to 1.06 at an inclination angle of 60° between positions 1 and 3 in the sand cast sample (see Table 4.4.9). For a contact time of 0.09 s, the grain elongation decreased from 1.13 to 1.08 at an inclination angle of 20° but increased from 1.08 to 1.11 at an inclination angle of 40° between positions 1 and 3 in the sand cast sample. For a contact time of 0.13 s, the grain elongation decreased from 1.10 to 1.08 at an inclination angle of 20° but increased from 1.00 to 1.11 at an inclination angle of 60° between positions 1 and 3 in the sand cast sample.

Pouring Temperature of 640 °C

At a pouring temperature of 640 °C, for a contact time of 0.04 s, the grain elongation decreased from 1.15 to 1.09 at an inclination angle of 20° and from 1.13 to 1.08 at an inclination angle of 40°, and remained unchanged at 1.00 at an inclination angle of 60° between positions 1 and 3 in the sand cast sample (see Table 4.4.9). For a contact time of 0.09 s, the grain elongation decreased from 1.10 to 1.08 at an inclination angle of 40° but increased from 1.11 to 1.18 at an inclination angle of 60°, and remained unchanged at 1.10 at an inclination angle of 20° between positions 1 and 3 in the sand cast sample. For a contact time of 0.13 s, the grain elongation decreased from 1.13 to 1.12 at an inclination angle of 20° but increased from 1.00 to 1.10 at an inclination angle of 60°, and remained unchanged at 1.08 at an inclination angle of 40° between positions 1 and 3 in the sand cast sample.

In general at a pouring temperature of 680 °C, the lowest grain elongation for a contact time of 0.04 s was obtained at an inclination angle of 20°, for a contact time of 0.09 s at inclination angles of 40 and 60° and for a contact time of 0.13 s at an inclination angle of 40°. At a pouring temperature of 660 °C the lowest grain elongation was obtained at an inclination angle of 60° for each contact time. At a pouring temperature of 640 °C, the lowest grain elongation was obtained for a contact time of 0.04 s at an inclination angle of 60° and for contact times of 0.09 s and 0.13 s at an inclination angle of 40°.

4.4.2 Effect of Processing Parameters Combined with Sample Thickness Variation from 10 mm to 34 mm

In this section the effect of processing parameters such as pouring temperature, contact time and inclination on the microstructure characteristics of the NGM AlSi7Mg alloy using the cooling slope technique with sand mould for different a sample thickness was investigated.

4.4.2.1 Effect of Pouring Temperature

Grain Size

Contact Time of 0.04 s

At a contact time of 0.04 s, for an inclination angle of 20°, the grain size did not exhibit any trend with an increase in section thickness from 10 mm to 34 mm in the sand cast sample (see Table 4.4.10). For an inclination angle of 40°, the grain size decreased from 151 μm to 147 μm at a pouring temperature of 640 °C with an increase in section thickness from 10 mm to 34 mm in the sand cast sample. For an inclination angle of 60°, the grain size decreased from 100 μm to 93 μm at a pouring temperature of 660 °C and from 117 μm to 98 μm at a pouring temperature of 640 °C with an increase in section thickness from 10 mm to 34 mm in the sand cast sample.

Contact Time of 0.09 s

At a contact time of 0.09 s, for an inclination angle of 20°, the grain size decreased from 189 μm to 146 μm at a pouring temperature of 640 °C with an increase in section thickness from 10 mm to 34 mm in the sand cast sample (see Table 4.4.10). For an inclination angle of 40°, the grain size increased from 97 μm to 148 μm at a pouring temperature of 640 °C with an increase in section thickness from 10 mm to 34 mm in the sand cast sample. For an inclination angle of 60°, the grain size increased from 89 μm to 100 μm at a pouring temperature of 680 °C with an increase in section thickness from 10 mm to 34 mm in the sand cast sample.

Contact Time of 0.13 s

At a contact time of 0.13 s, for an inclination angle of 20°, the grain size decreased from 165 μm to 124 μm at a pouring temperature of 680 °C but increased from 120 μm to 137 μm at a pouring temperature of 660 °C with an increase in section thickness from 10 mm to 34 mm in the sand cast sample (see Table 4.4.10). For an inclination angle of 40°, the grain size increased from 107 μm to 147 μm at a pouring temperature of 660 °C with an increase in section thickness from 10 mm to 34 mm in the sand cast sample. For an inclination angle of 60°, the grain size increased from 95 μm to 105 μm at a pouring temperature of 640 °C with an increase in section thickness from 10 mm to 34 mm in the sand cast sample.

In general, at a contact time of 0.04 s, the finest grain size was obtained for inclination angles of 20° and 40° at a pouring temperature of 660 °C and for an inclination angle of 60° at pouring temperatures of 660 °C and 640 °C. At a contact time of 0.09 s, a relatively fine grain size was obtained for an inclination angle of 20° at a pouring temperature of 680 °C, but the finest grain size was obtained for an inclination angle of 40° at a pouring temperature of 680 °C and for an inclination angle of 60° at pouring temperatures of 680 °C and 660 °C. At a contact time of 0.13 s, a relatively fine grain size was obtained for an inclination angle of 20° at a pouring temperature of 660 °C, however, the finest grain size was obtained for an inclination angle of 40° at a pouring temperature of 680 °C and for an inclination angle of 60° at each pouring temperature.

Grain Circularity

Contact Time of 0.04 s

At a contact time of 0.04 s, for an inclination angle of 20°, the grain circularity did not exhibit any clear trend with an increase in section thickness from 10 mm to 34 mm in the sand cast sample (see Table 4.4.11). For an inclination angle of 40°, the grain circularity increased from 0.54 to 0.66 at a pouring temperature of 680 °C and from 0.65 to 0.83 at a pouring temperature of 640 °C with an increase in section thickness from 10 mm to 34 mm in the sand cast sample. For an inclination angle of 60°, the grain circularity increased from 0.78 to 0.8 at a pouring temperature of 660 °C and from 0.72 to 0.77 at a pouring temperature of 640 °C with an increase in section thickness from 10 mm to 34 mm in the sand cast sample.

Contact Time of 0.09 s

At a contact time of 0.09 s, for an inclination angle of 20°, the grain circularity did not exhibit a clear trend with an increase in section thickness from 10 mm to 34 mm in the sand cast sample (see Table 4.4.11). For an inclination angle of 40°, the grain circularity decreased from 0.76 to 0.65 at a pouring temperature of 640 °C with an increase in section thickness from 10 mm to 34 mm in the sand cast sample. For an inclination angle of 60°, the grain circularity increased from 0.74 to 0.76 at a pouring temperature of 660 °C with an increase in section thickness from 10 mm to 34 mm in the sand cast sample.

Contact Time of 0.13 s

At a contact time of 0.13 s, for inclination angles of 20° and 40°, the grain circularity did not exhibit a clear trend with an increase in section thickness from 10 mm to 34 mm in the sand cast sample (see Table 4.4.11). For an inclination angle of 60°, the grain circularity increased from 0.81 to 0.86 at a pouring temperature of 680 °C and from 0.75 to 0.79 at a pouring temperature of 660 °C with an increase in section thickness from 10 mm to 34 mm in the sand cast sample.

In general, at a contact time of 0.04 s, the highest grain circularity was obtained for inclination angles of 20° and 40° at a pouring temperature of 660 °C and for an inclination angle of 60° at pouring temperature of 660 °C and 640 °C. At a contact time of 0.09 s, the highest grain circularity was obtained for an inclination angle of 20° at a pouring temperature of 680 °C and for inclination angles of 40° and 60° at pouring temperature of 680 °C and 660 °C. At a contact time of 0.13 s, the highest grain circularity was obtained for inclination angles of 20° and 40° at a pouring temperature of 680 °C and for an inclination angle of 60° at each pouring temperature.

Grain Elongation

Contact Time of 0.04 s

At a contact time of 0.04 s, for an inclination angle of 20°, the grain elongation did not exhibit a trend with an increase in section thickness from 10 mm to 34 mm in the sand cast sample (see Table 4.4.12). For an inclination angle of 40°, the grain elongation decreased from 1.10 to 1.08 at a pouring temperature of 660 °C and from 1.08 to 1.07 at a pouring temperature of 640 °C with an increase in section thickness from 10 mm to 34 mm in the sand cast sample. For an inclination angle of 60°, the grain elongation increased from 1.06 to 1.08 at a pouring temperature of 660 °C and from 1.00 to 1.08 at a pouring temperature of 640 °C with an increase in section thickness from 10 mm to 34 mm in the sand cast sample.

Contact Time of 0.09 s

At a contact time of 0.09 s, for an inclination angle of 20°, the grain elongation decreased from 1.10 to 1.08 at a pouring temperature of 640 °C with an increase in section thickness from 10 mm to 34 mm in the sand cast sample (see Table 4.4.12).

For an inclination angle of 40°, the grain elongation increased from 1.08 to 1.11 at a pouring temperature of 640 °C with an increase in section thickness from 10 mm to 34 mm in the sand cast sample. For an inclination angle of 60°, the grain elongation did not exhibit a clear trend with an increase in section thickness from 10 mm to 34 mm in the sand cast sample.

Contact Time of 0.13 s

At a contact time of 0.13 s, for an inclination angle of 20°, the grain elongation decreased from 1.05 to 1.10 at a pouring temperature of 680 °C and from 1.08 to 1.11 at a pouring temperature of 660 °C but decreased from 1.12 to 1.08 for a pouring temperature of 640 °C with an increase in section thickness from 10 mm to 34 mm in the sand cast sample (see Table 4.4.12). For an inclination angle of 40°, the grain elongation decreased from 1.08 to 1.04 at a pouring temperature of 640 °C with an increase in section thickness from 10 mm to 34 mm in the sand cast sample. For an inclination angle of 60°, the grain elongation decreased from 1.12 to 1.05 at a pouring temperature of 680 °C and from 1.10 to 1.07 at a pouring temperature of 640 °C with an increase in section thickness from 10 mm to 34 mm in the sand cast sample.

In general, at a contact time of 0.04 s, the lowest grain elongation was obtained for an inclination angle of 20° at a pouring temperature of 660 °C, for an inclination angle of 40° at a pouring temperature of 640 °C and for an inclination angle of 60° at pouring temperatures of 660 °C and 640 °C. At a contact time of 0.09 s, the lowest grain elongation was obtained for an inclination angle of 20° at a pouring temperature of 660 °C and an inclination angle of 60° at pouring temperatures of 680 °C and 660 °C, while for an inclination angle of 40° no clear trend was obtained. At a contact time of 0.13 s, the lowest grain elongation was obtained for an inclination angle of 20° at a pouring temperature of 680 °C and for inclination angles of 40° and 60° at a pouring temperature of 640 °C.

4.4.2.2 Effect of Contact Time

Grain Size

Inclination Angle of 20°

At an inclination angle of 20°, for a pouring temperature of 680 °C, the grain size decreased from 165 μm to 124 μm at a contact time of 0.13 s with an increase in section thickness from 10 mm to 34 mm in the sand cast sample (see Table 4.4.13). For a pouring temperature of 660 °C, the grain size increased from 120 μm to 137 μm at a contact time of 0.13 s with an increase in section thickness from 10 mm to 34 mm in the sand cast sample. For a pouring temperature of 640 °C, the grain size decreased from 179 μm to 166 μm at a contact time of 0.04 s and from 189 μm to 146 μm at a contact time of 0.09 s with an increase in section thickness from 10 mm to 34 mm in the sand cast sample.

Inclination Angle of 40°

At an inclination angle of 40°, for a pouring temperature of 680 °C, the grain size exhibited a clear trend with an increase in section thickness from 10 mm to 34 mm in the sand cast sample (see Table 4.4.13). For a pouring temperature of 660 °C, the grain size increased from 107 μm to 147 μm at a contact time of 0.13 s with an increase in section thickness from 10 mm to 34 mm in the sand cast sample. For a pouring temperature of 640 °C, the grain size decreased from 151 μm to 147 μm at a contact time of 0.04 s but increased from 97 μm to 148 μm at a contact time of 0.09 s with an increase in section thickness from 10 mm to 34 mm in the sand cast sample.

Inclination Angle of 60°

At an inclination angle of 60°, for a pouring temperature of 680 °C, the grain size increased from 89 μm to 100 μm at a contact time of 0.09 s with an increase in section thickness from 10 mm to 34 mm in the sand cast sample (see Table 4.4.13). For a pouring temperature of 660 °C, the grain size decreased from 100 μm to 93 μm at a contact time of 0.04 s with an increase in section thickness from 10 mm to 34 mm in the sand cast sample. For a pouring temperature of 640 °C, the grain size decreased from 117 μm to 98 μm at a contact time of 0.04 s but increased from 95 μm to 105 μm

at a contact time of 0.13 s with an increase in section thickness from 10 mm to 34 mm in the sand cast sample.

In general at an inclination angle of 20°, for a pouring temperature of 660 °C a relatively finer grain size was obtained at a contact time of 0.04 s and for a pouring temperature of 640 °C at a contact time of 0.13 s. At an inclination angle of 40°, the finest grain size was obtained for a pouring temperature of 680 °C at a contact time of 0.09 s, for a pouring temperature of 660 °C at a contact time of 0.09 s and for a pouring temperature of 640 °C a relatively finer grain size was obtained at a contact time of 0.09 s. At an inclination angle of 60°, the finest grain size was obtained for a pouring temperature of 680 °C at a contact time of 0.09 s, for a pouring temperature of 660 °C at each contact time and for a pouring temperature of 640 °C at contact times of 0.04 s and 0.13 s.

Grain Circularity

Inclination Angle of 20°

At an inclination angle of 20°, for a pouring temperature of 680 °C, 660 °C and 640 °C, the grain circularity did not exhibit a clear trend, however the value did not vary significantly with an increase in section thickness from 10 mm to 34 mm in the sand cast sample (see Table 4.4.14).

Inclination Angle of 40°

At an inclination angle of 40°, for a pouring temperature of 680 °C, the grain circularity increased from 0.54 to 0.66 at a contact time of 0.04 s with an increase in section thickness from 10 mm to 34 mm in the sand cast sample (see Table 4.4.14). For a pouring temperature of 660 °C, the grain circularity decreased from 0.65 to 0.83 at a contact time of 0.04 s with an increase in section thickness from 10 mm to 34 mm in the sand cast sample. For a pouring temperature of 640 °C, the grain circularity did not exhibit a clear trend with an increase in section thickness from 10 mm to 34 mm in the sand cast sample.

Inclination Angle of 60°

At an inclination angle of 60°, for a pouring temperature of 680 °C, the grain circularity increased from 0.81 to 0.86 at a contact time of 0.13 s with an increase in

section thickness from 10 mm to 34 mm in the sand cast sample (see Table 4.4.14). For a pouring temperature of 660 °C, the grain circularity decreased from 0.78 to 0.84 at a contact time of 0.04 s, from 0.74 to 0.76 at a contact time of 0.09 s and from 0.75 to 0.79 at a contact time of 0.13 s with an increase in section thickness from 10 mm to 34 mm in the sand cast sample. For a pouring temperature of 640 °C, the grain circularity decreased from 0.72 to 0.77 at a contact time of 0.04 s with an increase in section thickness from 10 mm to 34 mm in the sand cast sample.

In general at an inclination angle of 20°, a relatively higher grain circularity was obtained for pouring temperatures of 680 °C and 640 °C at a contact time of 0.13 s, while the highest grain circularity was obtained for a pouring temperature of 660 °C at a contact time of 0.04 s. At an inclination angle of 40°, the highest grain circularity was obtained for a pouring temperature of 680 °C at contact times of 0.09 s and 0.13 s and for a pouring temperature of 660 °C at a contact time of 0.09 s while a relatively higher grain circularity was obtained for a pouring temperature of 640 °C at a contact time of 0.09 s. At an inclination angle of 60°, the highest grain circularity was obtained for a pouring temperature of 680 °C at contact times of 0.09 s and 0.13 s, while a relatively higher grain circularity was obtained for a pouring temperature of 660 °C at each a contact time and for a pouring temperature of 640 °C at contact times of 0.04 s and 0.13 s.

Grain Elongation

Inclination Angle of 20°

At an inclination angle of 20°, for a pouring temperature of 680 °C, the grain elongation increased from 1.05 to 1.10 at a contact time of 0.13 s with an increase in section thickness from 10 mm to 34 mm in the sand cast sample (see Table 4.4.15). For a pouring temperature of 660 °C, the grain elongation increased from 1.08 to 1.11 at a contact time of 0.13 s with an increase in section thickness from 10 mm to 34 mm in the sand cast sample. For a pouring temperature of 640 °C, the grain elongation decreased from 1.10 to 1.08 at a contact time of 0.09 s, decreased from 1.12 to 1.08 at a contact time of 0.13 s with an increase in section thickness from 10 mm to 34 mm in the sand cast sample.

Inclination Angle of 40°

At an inclination angle of 40°, for a pouring temperature of 680 °C, the grain elongation did not exhibit a clear trend with an increase in section thickness from 10 mm to 34 mm in the sand cast sample (see Table 4.4.15). For a pouring temperature of 660 °C, the grain elongation decreased from 1.10 to 1.08 at a contact time of 0.04 s with an increase in section thickness from 10 mm to 34 mm in the sand cast sample. For a pouring temperature of 640 °C, the grain elongation decreased from 1.08 to 1.07 at a contact time of 0.04 s and from 1.08 to 1.04 at a contact time of 0.13 s, but increased from 1.08 to 1.11 at a contact time of 0.09 s with an increase in section thickness from 10 mm to 34 mm in the sand cast sample.

Inclination Angle of 60°

At an inclination angle of 60°, for a pouring temperature of 680 °C, the grain elongation decreased from 1.12 to 1.05 at a contact time of 0.13 s with an increase in section thickness from 10 mm to 34 mm in the sand cast sample (see Table 4.4.15). For a pouring temperature of 660 °C, the grain elongation increased from 1.06 to 1.08 at a contact time of 0.04 s with an increase in section thickness from 10 mm to 34 mm in the sand cast sample. For a pouring temperature of 640 °C, the grain elongation increased from 1.00 to 1.08 at a contact time of 0.04 s, but decreased from 1.10 to 1.07 at a contact time of 0.04 s with an increase in section thickness from 10 mm to 34 mm in the sand cast sample.

In general at an inclination angle of 20°, a relatively lower grain elongation was obtained for a pouring temperature of 680 °C at a contact time of 0.13 s, for a pouring temperature of 660 °C at a contact time of 0.04 s and for a pouring temperature of 640 °C at a contact time of 0.09 s. At an inclination angle of 40°, a relatively lower grain elongation was obtained for a pouring temperature of 680 °C at a contact time of 0.13 s, for a pouring temperature of 660 °C at a contact time of 0.04 s and for a pouring temperature of 640 °C at contact times of 0.04 s and 0.13 s. At an inclination angle of 60°, a relatively lower grain elongation was obtained for a pouring temperature of 680 °C at contact times of 0.09 s and 0.13 s and for pouring temperatures of 660 °C and 640 °C at each contact time.

4.4.2.3 Effect of Inclination Angle

Grain Size

Pouring Temperature of 680 °C

At a pouring temperature of 680 °C, for a contact time of 0.04 s, the grain size did not exhibit a clear trend with an increase in section thickness from 10 mm to 34 mm in the sand cast sample (see Table 4.4.16). For a contact time of 0.09 s, the grain size increased from 89 μm to 100 μm at an inclination angle of 60° with an increase in section thickness from 10 mm to 34 mm in the sand cast sample. For a contact time of 0.13 s, the grain size decreased from 165 μm to 124 μm at an inclination angle of 20° with an increase in section thickness from 10 mm to 34 mm in the sand cast sample.

Pouring Temperature of 660 °C

At a pouring temperature of 660 °C, for a contact time of 0.04 s, the grain size decreased from 100 μm to 93 μm at an inclination angle of 60° with an increase in section thickness from 10 mm to 34 mm in the sand cast sample (see Table 4.4.16). For a contact time of 0.09 s, the grain size did not exhibit a clear trend with an increase in section thickness from 10 mm to 34 mm in the sand cast sample. For a contact time of 0.13 s, the grain size increased from 120 μm to 137 μm at an inclination angle of 20° and from 107 μm to 147 μm at an inclination angle of 40° with an increase in section thickness from 10 mm to 34 mm in the sand cast sample.

Pouring Temperature of 640 °C

At a pouring temperature of 640 °C, for a contact time of 0.04 s, the grain size decreased from 179 μm to 166 μm at an inclination angle of 20°, from 151 μm to 147 μm at an inclination angle of 40° and from 117 μm to 98 μm at an inclination angle of 60° with an increase in section thickness from 10 mm to 34 mm in the sand cast sample (see Table 4.4.16). For a contact time of 0.09 s, the grain size decreased from 189 μm to 146 μm at an inclination angle of 20° but increased from 97 μm to 148 μm at an inclination angle of 40° with an increase in section thickness from 10 mm to 34 mm in the sand cast sample. For a contact time of 0.13 s, the grain size increased from 95 μm to 105 μm at an inclination angle of 60° with an increase in section thickness from 10 mm to 34 mm in the sand cast sample.

In general, at a pouring temperature of 680 °C a relatively finer grain size was obtained for a contact time of 0.04 s at an inclination angle of 20°, while the finest grain size was obtained for contact times of 0.09 s and 0.13 s at an inclination angle of 60°. At a pouring temperature of 660 °C the finest grain size was obtained for each contact time at an inclination angle of 60°. At a pouring temperature of 640 °C a relatively finer grain size was obtained for contact times of 0.04 s and 0.13 s at an inclination angle of 60°.

Grain Circularity

Pouring Temperature of 680 °C

At a pouring temperature of 680 °C, for a contact time of 0.04 s, the grain circularity increased from 0.54 to 0.66 at an inclination angle of 20° with an increase in section thickness from 10 mm to 34 mm in the sand cast sample (see Table 4.4.17). For a contact time of 0.09 s, the grain circularity did not exhibit a clear trend, however, the grain elongation values did not differ significantly at an inclination angle of 40° and 60° with an increase in section thickness from 10 mm to 34 mm in the sand cast sample. For a contact time of 0.13 s, the grain circularity increased from 0.81 to 0.86 for an inclination angle of 20° with an increase in section thickness from 10 mm to 34 mm in the sand cast sample.

Pouring Temperature of 660 °C

At a pouring temperature of 660 °C, for a contact time of 0.04 s, the grain circularity increased from 0.65 to 0.83 at an inclination angle of 40° and from 0.78 to 0.84 at an inclination angle of 60° with an increase in section thickness from 10 mm to 34 mm in the sand cast sample (see Table 4.4.17). For a contact time of 0.09 s, the grain circularity increased from 0.74 to 0.76 at an inclination angle of 60° with an increase in section thickness from 10 mm to 34 mm in the sand cast sample. For a contact time of 0.13 s, the grain circularity increased from 0.75 to 0.79 at an inclination angle of 60° with an increase in section thickness from 10 mm to 34 mm in the sand cast sample.

Pouring Temperature of 640 °C

At a pouring temperature of 640 °C, for a contact time of 0.09 s, the grain circularity increased from 0.72 to 0.77 at an inclination angle of 60° with an increase in section thickness from 10 mm to 34 mm in the sand cast sample (see Table 4.4.17). For contact times of 0.09 s and 0.13 s, the grain circularity did not exhibit a clear trend with an increase in section thickness from 10 mm to 34 mm in the sand cast sample.

In general, at a pouring temperature of 680 °C a relatively higher grain circularity was obtained for a contact time of 0.04 s at an inclination angle of 20°, while the highest grain circularity was obtained for a contact time of 0.09 s and 0.13 s at inclination angles of 40° and 60°. At a pouring temperature of 660 °C the highest grain circularity was obtained for a contact time of 0.04 s at an inclination angle of 60°. A relatively higher grain circularity was obtained for a contact time of 0.04 s at an inclination angle of 20° and for contact times of 0.09 s and 0.13 s at an inclination angle of 60°. At a pouring temperature of 640 °C relatively higher grain circularity was obtained for contact times of 0.04 s and 0.13 s at an inclination angle of 60°.

Grain Elongation

Pouring Temperature of 680 °C

At a pouring temperature of 680 °C, the grain elongation did not exhibit a clear trend for a contact time of 0.04 s and 0.09 s with an increase in section thickness from 10 mm to 34 mm in the sand cast sample (see Table 4.4.18). For a contact time of 0.13 s, the grain elongation increased from 1.05 to 1.10 at an inclination angle of 20° but decreased from 1.12 to 1.05 at an inclination angle of 60° with an increase in section thickness from 10 mm to 34 mm in the sand cast sample.

Pouring Temperature of 660 °C

At a pouring temperature of 660 °C, for a contact time of 0.04 s, the grain elongation decreased from 1.10 to 1.08 at an inclination angle of 40° but increased from 1.06 to 1.08 at an inclination angle of 60° with an increase in section thickness from 10 mm to 34 mm in the sand cast sample (see Table 4.4.18). For a contact time of 0.13 s, the grain elongation increased from 1.08 to 1.11 at an inclination angle of 20° with an increase in section thickness from 10 mm to 34 mm in the sand cast sample. For a contact time of 0.09 s, the grain elongation did not exhibit a clear trend with an increase in section thickness from 10 mm to 34 mm in the sand cast sample.

Pouring Temperature of 640 °C

At a pouring temperature of 640 °C, for a contact time of 0.04 s, the grain elongation decreased from 1.08 to 1.07 at an inclination angle of 40° but increased from 1.00 to 1.08 at an inclination angle of 60° with an increase in section thickness from 10 mm to 34 mm in the sand cast sample (see Table 4.4.18). For a contact time of 0.09 s, the grain elongation decreased from 1.10 to 1.08 at an inclination angle of 20° but increased from 1.08 to 1.11 at an inclination angle of 40° with an increase in section thickness from 10 mm to 34 mm in the sand cast sample. For a contact time of 0.13 s, the grain elongation decreased from 1.12 to 1.08 at an inclination angle of 20°, from 1.08 to 1.04 at an inclination angle of 20° and from 1.10 to 1.07 at an inclination angle of 60° with an increase in section thickness from 10 mm to 34 mm in the sand cast sample.

In general, at a pouring temperature of 680 °C a relatively lower grain elongation was obtained for a contact time of 0.09 s at an inclination angle of 60° and for a contact time of 0.13 s at each inclination angle. At a pouring temperature of 660 °C the lowest grain elongation was obtained for contact time of 0.04 s and 0.09 s at an inclination angle of 60°, while for a contact time of 0.04 s a relatively lower grain elongation was obtained at inclination angles of 20° and 60°. At a pouring temperature of 640 °C a relatively lower grain elongation was obtained for a contact time of 0.04 s at an inclination angle of 60°, for a contact time of 0.09 s at inclination angles of 20° and 60° and for a contact time of 0.13 s at inclination angles of 20° and 60°.

4.4.3 Summary

The above mentioned results for the effect of sample thickness in the sand mould on the final microstructure can be summarised as follows:

1. At an inclination angle of 60° and a contact time of 0.13 s, the grain size was the finest (~ 100 μm) and was similar throughout the casting regardless of its thickness.
2. In general, the decrease in grain size with an increase in sample thickness, may be due to the transport of a large number of nuclei/grains, continued

nucleation multiplication of root melting or equiaxed growth due to an isothermal temperature distribution.

3. The grain size obtained under most of the processing conditions was less than 200 μm having high circularity and minimum elongation values, thus showing the effectiveness of the cooling slope in obtaining near globular, equiaxed grains.

4.4.4. Tables

Table 4.4.1: Effect of pouring temperature on grain size (μm) with change in sample thickness (within the 10 mm thick section) at different inclination angles for different contact times.

0.04 s Contact Time									
Position	20° Inclination			40° Inclination			60° Inclination		
	680 (℃)	660 (℃)	640 (℃)	680 (℃)	660 (℃)	640 (℃)	680 (℃)	660 (℃)	640 (℃)
1	152	137	194	212	132	133	169	94	76
2	163	123	179	215	115	147	213	96	117
3	151	122	179	208	121	151	213	100	117
0.09 s Contact Time									
1	125	160	123	103	114	104	100	103	169
2	139	137	189	86	114	97	89	103	179
3	152	147	189	86	115	97	89	91	179
0.13 s Contact Time									
1	129	131	120	87	104	118	98	83	83
2	141	154	204	96	112	124	98	98	95
3	165	120	141	96	107	124	98	95	95

Table 4.4.2: Effect of pouring temperature on grain circularity with change in sample thickness (within the 10 mm thick section) at different inclination angles for different contact times.

0.04 s Contact Time									
Position	20° Inclination			40° Inclination			60° Inclination		
	680 (℃)	660 (℃)	640 (℃)	680 (℃)	660 (℃)	640 (℃)	680 (℃)	660 (℃)	640 (℃)
1	0.66	0.68	0.49	0.56	0.66	0.67	0.60	0.78	0.82
2	0.62	0.71	0.58	0.52	0.72	0.64	0.51	0.78	0.72
3	0.65	0.71	0.58	0.54	0.65	0.62	0.51	0.78	0.72
0.09 s Contact Time									
1	0.68	0.53	0.67	0.73	0.69	0.70	0.76	0.71	0.51
2	0.71	0.65	0.53	0.84	0.70	0.76	0.80	0.72	0.57
3	0.67	0.60	0.53	0.84	0.71	0.76	0.80	0.74	0.57
0.13 s Contact Time									
1	0.70	0.67	0.72	0.81	0.72	0.67	0.76	0.75	0.76
2	0.68	0.64	0.54	0.78	0.68	0.65	0.81	0.71	0.73
3	0.68	0.69	0.62	0.78	0.67	0.65	0.81	0.75	0.73

Table 4.4.3: Effect of pouring temperature on grain elongation with change in sample thickness (within the 10 mm thick section) at different inclination angles for different contact times.

0.04 s Contact Time									
Position	20° Inclination			40° Inclination			60° Inclination		
	680 (℃)	660 (℃)	640 (℃)	680 (℃)	660 (℃)	640 (℃)	680 (℃)	660 (℃)	640 (℃)
1	1.11	1.13	1.15	1.15	1.11	1.13	1.10	1.11	1.00
2	1.10	1.07	1.09	1.14	1.08	1.08	1.12	1.09	1.00
3	1.08	1.08	1.09	1.10	1.10	1.08	1.12	1.06	1.00
0.09 s Contact Time									
1	1.09	1.13	1.10	1.09	1.08	1.10	1.08	1.07	1.11
2	1.08	1.08	1.10	1.06	1.11	1.08	1.06	1.11	1.18
3	1.10	1.08	1.10	1.06	1.11	1.08	1.06	1.00	1.18
0.13 s Contact Time									
1	1.14	1.10	1.13	1.00	1.10	1.08	1.05	1.00	1.00
2	1.13	1.10	1.12	1.09	1.12	1.08	1.12	1.00	1.10
3	1.05	1.08	1.12	1.09	1.09	1.08	1.12	1.11	1.10

Table 4.4.4: Effect of contact time on grain size (μm) with change in sample thickness (within the 10 mm thick section) at different pouring temperature for different inclination angles.

20° Inclination									
Position	680 ℃ pouring temperature			660 ℃ pouring temperature			640 ℃ pouring temperature		
	0.04 s	0.09 s	0.13 s	0.04 s	0.09 s	0.13 s	0.04 s	0.09 s	0.13 s
1	152	125	129	137	160	131	194	123	120
2	163	139	141	123	137	154	179	189	204
3	151	152	165	122	147	120	179	189	141
40° Inclination									
1	212	103	87	132	114	104	133	104	118
2	215	86	96	115	114	112	147	97	124
3	208	86	96	121	115	107	151	97	124
60° Inclination									
1	169	100	98	94	103	83	76	169	83
2	213	89	98	96	103	98	117	179	95
3	213	89	98	100	91	95	117	179	95

Table 4.4.5: Effect of contact time on grain circularity with change in sample thickness (within the 10 mm thick section) at different pouring temperature for different inclination angles.

20° Inclination									
Position	680 ℃ pouring temperature			660 ℃ pouring temperature			640 ℃ pouring temperature		
	0.04 s	0.09 s	0.13 s	0.04 s	0.09 s	0.13 s	0.04 s	0.09 s	0.13 s
1	0.66	0.68	0.70	0.68	0.53	0.67	0.49	0.67	0.72
2	0.62	0.71	0.68	0.71	0.65	0.64	0.58	0.53	0.54
3	0.65	0.67	0.68	0.71	0.60	0.69	0.58	0.53	0.62
40° Inclination									
1	0.56	0.73	0.81	0.66	0.69	0.72	0.67	0.70	0.67
2	0.52	0.84	0.78	0.72	0.70	0.68	0.64	0.76	0.65
3	0.54	0.84	0.78	0.65	0.71	0.67	0.62	0.76	0.65
60° Inclination									
1	0.60	0.76	0.76	0.78	0.71	0.75	0.82	0.51	0.76
2	0.51	0.80	0.81	0.78	0.72	0.71	0.72	0.57	0.73
3	0.51	0.80	0.81	0.78	0.74	0.75	0.72	0.57	0.73

Table 4.4.6: Effect of contact time on grain elongation with change in sample thickness (within the 10 mm thick section) at different pouring temperature for different inclination angles.

20° Inclination									
Position	680 ℃ pouring temperature			660 ℃ pouring temperature			640 ℃ pouring temperature		
	0.04 s	0.09 s	0.13 s	0.04 s	0.09 s	0.13 s	0.04 s	0.09 s	0.13 s
1	1.11	1.09	1.14	1.13	1.13	1.10	1.15	1.10	1.13
2	1.10	1.08	1.13	1.07	1.08	1.10	1.09	1.10	1.12
3	1.08	1.10	1.05	1.08	1.08	1.08	1.09	1.10	1.12
40° Inclination									
1	1.15	1.09	1.00	1.11	1.08	1.10	1.13	1.10	1.08
2	1.14	1.06	1.09	1.08	1.11	1.12	1.08	1.08	1.08
3	1.10	1.06	1.09	1.10	1.11	1.09	1.08	1.08	1.08
60° Inclination									
1	1.10	1.08	1.05	1.11	1.07	1.00	1.00	1.11	1.00
2	1.12	1.06	1.12	1.09	1.11	1.00	1.00	1.18	1.10
3	1.12	1.06	1.12	1.06	1.00	1.11	1.00	1.18	1.10

Table 4.4.7: Effect of inclination angle on grain size (μm) with change in sample thickness (within the 10 mm thick section) at different contact times for different pouring temperature.

680 ℃ Pouring Temperature									
Position	0.04 s Contact Time			0.09 s Contact Time			0.13 s Contact Time		
	20°	40°	60°	20°	40°	60°	20°	40°	60°
1	152	212	169	125	103	100	129	87	98
2	163	215	213	139	86	89	141	96	98
3	151	208	213	152	86	89	165	96	98
660 ℃ Pouring Temperature									
1	137	132	94	160	114	103	131	104	83
2	123	115	96	137	114	103	154	112	98
3	122	121	100	147	115	91	120	107	95
640 ℃ Pouring Temperature									
1	194	133	76	123	104	169	120	118	83
2	179	147	117	189	97	179	204	124	95
3	179	151	117	189	97	179	141	124	95

Table 4.4.8: Effect of inclination angle on grain circularity with change in sample thickness (within the 10 mm thick section) at different contact times for different pouring temperature.

680 ℃ Pouring Temperature									
Position	0.04 s Contact Time			0.09 s Contact Time			0.13 s Contact Time		
	20°	40°	60°	20°	40°	60°	20°	40°	60°
1	0.66	0.56	0.60	0.68	0.73	0.76	0.70	0.81	0.76
2	0.62	0.52	0.51	0.71	0.84	0.80	0.68	0.78	0.81
3	0.65	0.54	0.51	0.67	0.84	0.80	0.68	0.78	0.81
660 ℃ Pouring Temperature									
1	0.68	0.66	0.78	0.53	0.69	0.71	0.67	0.72	0.75
2	0.71	0.72	0.78	0.65	0.70	0.72	0.64	0.68	0.71
3	0.71	0.65	0.78	0.60	0.71	0.74	0.69	0.67	0.75
640 ℃ Pouring Temperature									
1	0.49	0.67	0.82	0.67	0.70	0.51	0.72	0.67	0.76
2	0.58	0.64	0.72	0.53	0.76	0.57	0.54	0.65	0.73
3	0.58	0.62	0.72	0.53	0.76	0.57	0.62	0.65	0.73

Table 4.4.9: Effect of inclination angle on grain circularity with change in sample thickness (within the 10 mm thick section) at different contact times for different pouring temperature.

680 ℃ Pouring Temperature									
Position	0.04 s Contact Time			0.09 s Contact Time			0.13 s Contact Time		
	20°	40°	60°	20°	40°	60°	20°	40°	60°
1	1.11	1.15	1.10	1.09	1.09	1.08	1.14	1.00	1.05
2	1.10	1.14	1.12	1.08	1.06	1.06	1.13	1.09	1.12
3	1.08	1.10	1.12	1.10	1.06	1.06	1.05	1.09	1.12
660 ℃ Pouring Temperature									
1	1.13	1.11	1.11	1.13	1.08	1.07	1.10	1.10	1.00
2	1.07	1.08	1.09	1.08	1.11	1.11	1.10	1.12	1.00
3	1.08	1.10	1.06	1.08	1.11	1.00	1.08	1.09	1.11
640 ℃ Pouring Temperature									
1	1.15	1.13	1.00	1.10	1.10	1.11	1.13	1.08	1.00
2	1.09	1.08	1.00	1.10	1.08	1.18	1.12	1.08	1.10
3	1.09	1.08	1.00	1.10	1.08	1.18	1.12	1.08	1.10

Table 4.4.10: Effect of pouring temperature on grain size (μm) with change in sample thickness at different inclination angles for different contact times.

0.04 s Contact Time									
Position	20° Inclination			40° Inclination			60° Inclination		
	680 (℃)	660 (℃)	640 (℃)	680 (℃)	660 (℃)	640 (℃)	680 (℃)	660 (℃)	640 (℃)
3	151	122	179	208	121	151	213	100	117
4	153	106	171	160	123	149	168	94	102
5	145	111	166	161	89	147	181	93	98
0.09 s Contact Time									
3	152	147	189	86	115	97	89	91	179
4	132	151	178	93	101	116	92	100	180
5	136	140	146	87	120	148	100	93	115
0.13 s Contact Time									
3	165	120	141	96	107	124	98	95	95
4	143	131	171	110	109	119	105	89	100
5	124	137	159	87	147	145	91	91	105

Table: 4.4.11: Effect of pouring temperature on grain circularity with change in sample thickness at different inclination angles for different contact times.

0.04 s Contact Time									
Position	20° Inclination			40° Inclination			60° Inclination		
	680 (℃)	660 (℃)	640 (℃)	680 (℃)	660 (℃)	640 (℃)	680 (℃)	660 (℃)	640 (℃)
3	0.65	0.71	0.58	0.54	0.65	0.62	0.51	0.78	0.72
4	0.61	0.77	0.60	0.62	0.69	0.61	0.66	0.82	0.76
5	0.67	0.76	0.58	0.66	0.83	0.64	0.62	0.84	0.77
0.09 s Contact Time									
3	0.67	0.60	0.53	0.84	0.71	0.76	0.80	0.74	0.57
4	0.71	0.63	0.51	0.82	0.73	0.64	0.83	0.76	0.49
5	0.62	0.62	0.63	0.86	0.72	0.65	0.81	0.76	0.60
0.13 s Contact Time									
3	0.68	0.69	0.62	0.78	0.67	0.65	0.81	0.75	0.73
4	0.67	0.64	0.58	0.72	0.72	0.70	0.82	0.77	0.75
5	0.79	0.65	0.59	0.82	0.61	0.62	0.86	0.79	0.71

Table 4.4.12: Effect of pouring temperature on grain elongation with change in sample thickness at different inclination angles for different contact times.

0.04 s Contact Time									
Position	20° Inclination			40° Inclination			60° Inclination		
	680 (℃)	660 (℃)	640 (℃)	680 (℃)	660 (℃)	640 (℃)	680 (℃)	660 (℃)	640 (℃)
3	1.08	1.08	1.09	1.10	1.10	1.08	1.12	1.06	1.00
4	1.06	1.06	1.11	1.12	1.08	1.07	1.13	1.07	1.06
5	1.11	1.08	1.05	1.08	1.08	1.07	1.12	1.08	1.08
0.09 s Contact Time									
3	1.10	1.08	1.10	1.06	1.11	1.08	1.06	1.00	1.18
4	1.14	1.10	1.08	1.13	1.08	1.11	1.00	1.07	1.06
5	1.11	1.07	1.08	1.06	1.11	1.11	1.07	1.06	1.08
0.13 s Contact Time									
3	1.05	1.08	1.12	1.09	1.09	1.08	1.12	1.11	1.10
4	1.09	1.10	1.12	1.10	1.06	1.08	1.05	1.09	1.07
5	1.10	1.11	1.08	1.05	1.14	1.04	1.05	1.10	1.07

Table 4.4.13: Effect of contact time on grain size (μm) with change in sample thickness at different pouring temperatures for different inclination angles.

Position	680 ℃ pouring temperature			660 ℃ pouring temperature			640 ℃ pouring temperature		
	0.04 s	0.09 s	0.13 s	0.04 s	0.09 s	0.13 s	0.04 s	0.09 s	0.13 s
20° Inclination									
3	151	152	165	122	147	120	179	189	141
4	153	132	143	106	151	131	171	178	171
5	145	136	124	111	140	137	166	146	159
40° Inclination									
3	208	86	96	121	115	107	151	97	124
4	160	93	110	123	101	109	149	116	119
5	161	87	87	89	120	147	147	148	145
60° Inclination									
3	213	89	98	100	91	95	117	179	95
4	168	92	105	94	100	89	102	1780	100
5	181	100	91	93	93	91	98	115	105

Table 4.4.14: Effect of contact time on grain circularity with change in sample thickness at different pouring temperatures for different inclination angles.

Position	680 ℃ pouring temperature			660 ℃ pouring temperature			640 ℃ pouring temperature		
	0.04 s	0.09 s	0.13 s	0.04 s	0.09 s	0.13 s	0.04 s	0.09 s	0.13 s
20° Inclination									
3	0.65	0.67	0.68	0.71	0.60	0.69	0.58	0.53	0.62
4	0.61	0.71	0.67	0.77	0.63	0.64	0.60	0.51	0.58
5	0.67	0.62	0.79	0.76	0.62	0.65	0.58	0.63	0.59
40° Inclination									
3	0.54	0.84	0.78	0.65	0.71	0.67	0.62	0.76	0.65
4	0.62	0.82	0.72	0.69	0.73	0.72	0.61	0.64	0.70
5	0.66	0.86	0.82	0.83	0.72	0.61	0.64	0.65	0.62
60° Inclination									
3	0.51	0.80	0.81	0.78	0.74	0.75	0.72	0.57	0.73
4	0.66	0.83	0.82	0.82	0.76	0.77	0.76	0.49	0.75
5	0.61	0.81	0.86	0.84	0.76	0.79	0.77	0.60	0.71

Table 4.4.15: Effect of contact time on grain elongation with change in sample thickness at different pouring temperatures for different inclination angles.

Position	680 ℃ pouring temperature			660 ℃ pouring temperature			640 ℃ pouring temperature		
	0.04 s	0.09 s	0.13 s	0.04 s	0.09 s	0.13 s	0.04 s	0.09 s	0.13 s
20° Inclination									
3	1.08	1.10	1.05	1.08	1.08	1.08	1.09	1.10	1.12
4	1.06	1.14	1.09	1.06	1.10	1.10	1.11	1.08	1.12
5	1.11	1.11	1.10	1.08	1.07	1.11	1.05	1.08	1.08
40° Inclination									
3	1.10	1.06	1.09	1.10	1.11	1.09	1.08	1.08	1.08
4	1.12	1.13	1.10	1.08	1.08	1.06	1.07	1.11	1.08
5	1.08	1.06	1.05	1.08	1.11	1.14	1.07	1.11	1.04
60° Inclination									
3	1.12	1.06	1.12	1.06	1.00	1.11	1.00	1.18	1.10
4	1.13	1.00	1.05	1.07	1.07	1.09	1.06	1.06	1.07
5	1.12	1.07	1.05	1.08	1.06	1.10	1.08	1.08	1.07

Table 4.4.16: Effect of inclination angle on grain size (μm) with change in sample thickness at different contact time for different pouring temperatures.

680 ℃ Pouring Temperature									
Position	0.04 s Contact Time			0.09 s Contact Time			0.13 s Contact Time		
	20°	40°	60°	20°	40°	60°	20°	40°	60°
3	151	208	213	152	86	89	165	96	98
4	153	160	168	132	93	92	143	110	105
5	145	161	181	136	87	100	124	87	91
660 ℃ Pouring Temperature									
3	122	121	100	147	115	91	120	107	95
4	106	123	94	151	101	100	131	109	89
5	111	89	93	140	120	93	137	147	91
640 ℃ Pouring Temperature									
3	179	151	117	189	97	179	141	124	95
4	171	149	102	178	116	180	171	119	100
5	166	147	98	146	148	115	159	145	105

Table 4.4.17: Effect of inclination angle on grain circularity with change in sample thickness at different contact time for different pouring temperatures.

680 ℃ Pouring Temperature									
Position	0.04 s Contact Time			0.09 s Contact Time			0.13 s Contact Time		
	20°	40°	60°	20°	40°	60°	20°	40°	60°
3	0.65	0.54	0.51	0.67	0.84	0.80	0.68	0.78	0.81
4	0.61	0.62	0.66	0.71	0.82	0.83	0.67	0.72	0.82
5	0.67	0.66	0.61	0.62	0.86	0.81	0.79	0.82	0.86
660 ℃ Pouring Temperature									
3	0.71	0.65	0.78	0.60	0.71	0.74	0.69	0.67	0.75
4	0.77	0.69	0.82	0.63	0.73	0.76	0.64	0.72	0.77
5	0.76	0.83	0.84	0.62	0.72	0.76	0.65	0.61	0.79
640 ℃ Pouring Temperature									
3	0.58	0.62	0.72	0.53	0.76	0.57	0.62	0.65	0.73
4	0.60	0.61	0.76	0.51	0.64	0.49	0.58	0.70	0.75
5	0.58	0.64	0.77	0.63	0.65	0.60	0.59	0.62	0.71

Table 4.4.18: Effect of inclination angle on grain elongation with change in sample thickness at different contact time for different pouring temperatures.

680 ℃ Pouring Temperature									
Position	0.04 s Contact Time			0.09 s Contact Time			0.13 s Contact Time		
	20°	40°	60°	20°	40°	60°	20°	40°	60°
3	1.08	1.10	1.12	1.10	1.06	1.06	1.05	1.09	1.12
4	1.06	1.12	1.13	1.14	1.13	1.00	1.09	1.10	1.05
5	1.11	1.08	1.12	1.11	1.06	1.07	1.10	1.05	1.05
660 ℃ Pouring Temperature									
3	1.08	1.10	1.06	1.08	1.11	1.00	1.08	1.09	1.11
4	1.06	1.08	1.07	1.10	1.08	1.07	1.10	1.06	1.09
5	1.08	1.08	1.08	1.07	1.11	1.06	1.11	1.14	1.10
640 ℃ Pouring Temperature									
3	1.09	1.08	1.00	1.10	1.08	1.18	1.12	1.08	1.10
4	1.11	1.07	1.06	1.08	1.11	1.06	1.12	1.08	1.07
5	1.05	1.07	1.08	1.08	1.11	1.08	1.08	1.04	1.07

4.4.5 Figures

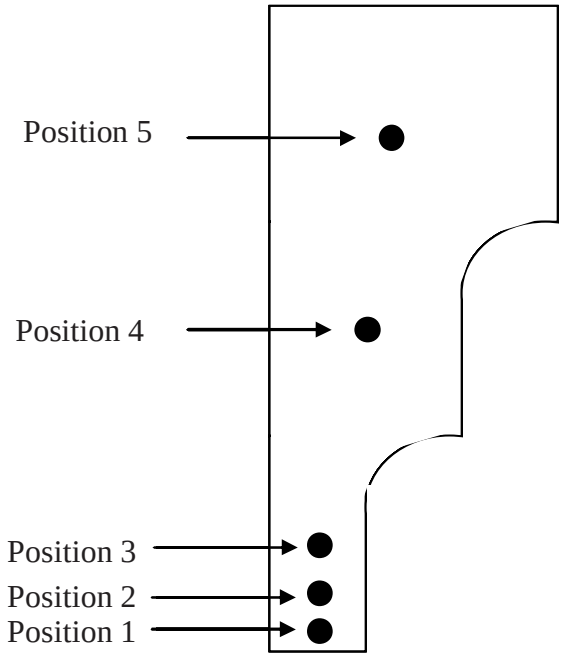

Fig. 4.4.1: Schematic of sampling and their relative position in the sand cast sample.

4.5. EFFECT OF MOULD MATERIAL ON FINAL GRAIN CHARACTERISTICS

In this section, the effect of pouring temperature, melt contact time on the cooling slope and inclination angle on the final grain size, and grain characteristics such as circularity and elongation values, obtained for samples cast in CO_2-hardend water glass bonded sand moulds were compared with those for the water cooled metallic mould.

4.5.1 Effect of Pouring Temperature

4.5.1.1 Constant Contact Time

Grain Size

Contact Time of 0.04 s

At a contact time of 0.04 s and an inclination angle of 20°, the grain size did not exhibit a clear trend both for the sand cast and metallic mould cast samples with a decrease in pouring temperature from 680 °C to 640 °C. The grain size for the metallic mould cast samples was finer than those for the sand cast samples at each pouring temperature (see Table 4.5.1). At an inclination angle of 40°, the grain size did not exhibit a clear trend both for the sand cast and metallic mould cast samples with a decrease in pouring temperature from 680 °C to 640 °C. The grain size for the metallic mould cast samples was finer than those for the sand cast samples at pouring temperatures of 660 °C and 640 °C. At an inclination angle of 60°, the grain size did not exhibit a clear trend for the sand cast samples but it increased from 85 µm to 144 µm for the metallic mould cast samples with a decrease in pouring temperature from 680 °C to 640 °C. The grain size for the metallic mould cast samples was finer than those for the sand cast samples at pouring temperatures of 680 °C and 640 °C.

Contact Time of 0.09 s

At a contact time of 0.09 s and an inclination angle of 20°, the grain size did not exhibit a clear trend for the sand cast samples but it increased from 87 μm to 134 μm for the metallic mould cast samples with a decrease in pouring temperature from 680 °C to 640 °C. The grain size for the metallic mould cast samples was finer than those for the sand cast samples at each pouring temperature (see Table 4.5.1). At an inclination angle of 40°, the grain size did not exhibit a clear trend for the sand cast samples but it increased from 89 μm to 124 μm for the metallic mould cast samples with a decrease in pouring temperature from 680 °C to 640 °C. The grain size for the metallic mould cast samples was coarser than those for the sand cast samples at each pouring temperature. At an inclination angle of 60°, the grain size increased from 89 μm to 179 μm for the sand cast samples and from 80 μm to 179 μm for the metallic mould cast samples with a decrease in pouring temperature from 680 °C to 640 °C. The grain size for the metallic mould cast samples was finer than those for the sand cast samples at a pouring temperature of 680 °C and was the same at a pouring temperature of 640 °C.

Contact Time of 0.13 s

At a contact time of 0.13 s and an inclination angle of 20°, the grain size did not exhibit a clear trend for the sand cast samples but it increased for 85 μm to 189 μm for the metallic mould cast samples with a decrease in pouring temperature from 680 °C to 640 °C. The grain size for the metallic mould cast samples was finer than those for the sand cast samples at pouring temperatures of 680 °C and 660 °C (see Table 4.5.1). At an inclination angle of 40°, the grain size increased from 96 μm to 124 μm for the sand cast samples and from 101 μm to 124 μm for the metallic mould cast samples with a decrease in pouring temperature from 680 °C to 640 °C. The grain size for the metallic mould cast samples was coarser than those for the sand cast samples at each pouring temperature. At an inclination angle of 60°, the grain size decreased from 98 μm to 95 μm for the sand cast samples but it increased from 92 μm to 134 μm for the metallic mould cast samples with a decrease in pouring temperature from 680 °C to 640 °C. The grain size for the metallic mould cast samples was finer than those for the sand cast samples only at a pouring temperature of 680 °C.

Grain Circularity

Contact Time of 0.04 s

At a contact time of 0.04 s and an inclination angle of 20°, the grain circularity did not exhibit a clear trend both for the sand cast and the metallic mould cast samples with a decrease in pouring temperature from 680 °C to 640 °C. The grain circularity for metallic mould cast samples was higher than those for the sand cast samples at pouring temperatures of 680 °C and 660 °C (see Table 4.5.2). At an inclination angle of 40°, the grain circularity did not exhibit a clear trend both for the sand cast and the metallic mould cast samples with a decrease in pouring temperature from 680 °C to 640 °C. The grain circularity for the metallic mould cast samples was higher than those for the sand cast samples at a pouring temperature of 660 °C. At an inclination angle of 60°, the grain circularity did not exhibit a clear trend both for the sand cast and the metallic mould cast samples with a decrease in pouring temperature from 680 °C to 640 °C. The grain circularity for the metallic mould cast samples was lower than those for the sand cast samples at each pouring temperature.

Contact Time of 0.09 s

At a contact time of 0.09 s and an inclination angle of 20°, the grain circularity decreased from 0.67 to 0.53 for the sand cast samples but it did not exhibit a clear trend for the metallic mould cast samples with a decrease in pouring temperature from 680 °C to 640 °C. The grain circularity for the metallic mould cast samples was higher than those for the sand cast samples at pouring temperatures of 660 °C and 640 °C (see Table 4.5.2). At an inclination angle of 40°, the grain circularity did not exhibit a clear trend both for the sand cast and the metallic mould cast samples with a decrease in pouring temperature from 680 °C to 640 °C. The grain circularity for the metallic mould cast samples was lower than those for the sand cast samples at each pouring temperature. At an inclination angle of 60°, the grain circularity did not exhibit a clear trend both for the sand cast and the metallic mould cast samples with a decrease in pouring temperature from 680 °C to 640 °C. The grain circularity for the metallic mould cast samples was lower than those for the sand cast samples at each pouring temperature.

Contact Time of 0.13 s

At a contact time of 0.13 s and an inclination angle of 20°, the grain circularity did not exhibit a clear trend for the sand cast and the metallic mould cast samples with a decrease in pouring temperature from 680 °C to 640 °C. The grain circularity for the metallic mould cast samples was lower than those for the sand cast samples for each pouring temperature (see Table 4.5.2). At an inclination angle of 40°, the grain circularity decreased from 0.78 to 0.65 for the sand cast samples and it did not exhibit a clear trend for the metallic mould cast samples with a decrease in pouring temperature from 680 °C to 640 °C. The grain circularity for the metallic mould cast samples was lower than those for the sand cast samples at each pouring temperature. At an inclination angle of 60°, the grain circularity decreased from 0.81 to 0.73 for the sand cast samples and it did not exhibit a clear trend for the metallic mould cast samples with a decrease in pouring temperature from 680 °C to 640 °C. The grain circularity for the metallic mould cast samples was lower than those for the sand cast samples at each pouring temperature.

Grain Elongation

Contact Time of 0.04 s

At a contact time of 0.04 s and an inclination angle of 20°, the grain elongation increased from 1.08 to 1.09 for the sand cast samples and it did not exhibit a clear trend for the metallic mould cast samples with a decrease in pouring temperature from 680 °C to 640 °C. The grain elongation for the metallic mould cast samples was lower than those for the sand cast samples at a pouring temperature of 680 °C (see Table 4.5.3). At an inclination angle of 40°, the grain elongation decreased from 1.10 to 1.08 for the sand cast samples and it increased from 1.11 to 1.44 for the metallic mould cast samples with a decrease in pouring temperature from 680 °C to 640 °C. The grain elongation for the metallic mould cast samples was higher than those for the sand cast samples at each pouring temperature. At an inclination angle of 60°, the grain elongation decreased from 1.12 to 1.00 for the sand cast samples but it did not exhibit a clear trend for the metallic mould cast samples with a decrease in pouring temperature from 680 °C to 640 °C. The grain elongation for the metallic mould cast samples was lower than those for the sand cast samples at a pouring temperature of 680 °C.

Contact Time of 0.09 s

At a contact time of 0.09 s and an inclination angle of 20°, the grain elongation did not exhibit a clear trend for the sand cast samples but it increased from 1.06 to 1.39 for the metallic mould cast samples with a decrease in pouring temperature from 680 °C to 640 °C. The grain elongation for the metallic mould cast samples was lower than those for the sand cast samples at a pouring temperature of 680 °C (see Table 4.5.3). At an inclination angle of 40°, the grain elongation did not exhibit a clear trend both for the sand cast and the metallic mould cast samples with a decrease in pouring temperature from 680 °C to 640 °C. The grain elongation for the metallic mould cast samples was higher than those for the sand cast samples at each pouring temperature. At an inclination angle of 60°, the grain elongation did not exhibit a clear trend for the sand cast and the metallic mould cast samples with a decrease in pouring temperature from 680 °C to 640 °C. The grain elongation for the metallic mould cast samples was higher than those for the sand cast samples at each pouring temperature.

Contact Time of 0.13 s

At a contact time of 0.13 s and an inclination angle of 20°, the grain elongation did not exhibit a clear trend both for the sand cast and the metallic mould cast samples with a decrease in pouring temperature from 680 °C to 640 °C. The grain elongation for the metallic mould cast samples was lower than those for the sand cast samples at a pouring temperature of 640 °C (see Table 4.5.3). At an inclination angle of 40°, the grain elongation decreased from 1.09 to 1.08 for the sand cast samples but it increased from 1.00 to 1.50 for the metallic mould cast samples with a decrease in pouring temperature from 680 °C to 640 °C. The grain elongation for the metallic mould cast samples was lower than those for the sand cast samples at a pouring temperature of 680 °C. At an inclination angle of 60°, the grain elongation decreased from 1.12 to 1.10 for the sand cast samples but it increased from 1.00 to 1.45 for the metallic mould cast samples with a decrease in pouring temperature from 680 °C to 640 °C. The grain elongation for the metallic mould cast samples was lower than those for the sand cast samples at a pouring temperature of 680 °C.

4.5.1.2 Constant Inclination Angle

Grain Size

Inclination Angle of 20°

At an inclination angle of 20° and a contact time of 0.04 s, the grain size did not exhibit a clear trend both for the sand cast and the metallic mould cast samples with a decrease in pouring temperature from 680 °C to 640 °C. The grain size for the metallic mould cast samples was finer than those for the sand cast samples at each pouring temperature (see Table 4.5.4). For a contact time of 0.09 s, the grain size did not exhibit a clear trend for the sand cast samples but it increased from 87 μm to 134 μm for the metallic mould cast samples with a decrease in pouring temperature from 680 °C to 640 °C. The grain size for the metallic mould cast samples was finer than those for the sand cast samples at each pouring temperature. For a contact time of 0.13 s, the grain size did not exhibit a clear trend for the sand cast samples but it increased from 85 μm to 189 μm for the metallic mould cast samples with a decrease in pouring temperature from 680 °C to 640 °C. The grain size for the metallic mould cast samples was finer than those for the sand cast samples at pouring temperatures of 680 °C and 660 °C.

Inclination Angle of 40°

At an inclination angle of 40° and a contact time of 0.04 s, the grain size did not exhibit a clear trend both for the sand cast samples and the metallic mould cast samples with a decrease in pouring temperature from 680 °C to 640 °C. The grain size for the metallic mould cast samples was finer than those for the sand cast samples at pouring temperatures of 660 °C and 640 °C (see Table 4.5.4). For a contact time of 0.09 s, the grain size did not exhibit a clear trend for the sand cast samples but it increased from 89 μm to 124 μm for the metallic mould cast samples with a decrease in pouring temperature from 680 °C to 640 °C. The grain size for the metallic mould cast samples was coarser than those for the sand cast samples at each pouring temperature. For a contact time of 0.13 s, the grain size did not exhibit a clear trend for the sand cast samples but it increased from 101 μm to 124 μm for the metallic mould cast samples with a decrease in pouring temperature from 680 °C to 640 °C. The grain size for the metallic mould cast samples was coarser than those for the sand

cast samples at pouring temperatures of 680 °C, 660 °C, and was similar to the sand cast samples at a pouring temperature of 640 °C.

Inclination Angle of 60°

At an inclination angle of 60° and a contact time of 0.04 s, the grain size did not exhibit a clear trend for the sand cast samples but increased from 85 μm to 144 μm for the metallic mould cast samples with a decrease in pouring temperature from 680 °C to 640 °C. The grain size for the metallic mould cast samples was finer than those for the sand cast samples at pouring temperatures of 680 °C and 660 °C (see Table 4.5.4). For a contact time of 0.09 s, the grain size increased from 89 μm to 179 μm for the sand cast samples and from 80 μm to 179 μm for the metallic mould cast samples with a decrease in pouring temperature from 680 °C to 640 °C. The grain size for the metallic mould cast samples was finer than those for the sand cast samples at a pouring temperature of 680 °C. For a contact time of 0.13 s, the grain size did not exhibit a clear trend for the sand cast samples but it increased from 92 μm to 134 μm for the metallic mould cast samples with a decrease in pouring temperature from 680 °C to 640 °C. The grain size for the metallic mould cast samples was finer than those for the sand cast samples at a pouring temperature of 680 °C.

Grain Circularity

Inclination Angle of 20°

At an inclination angle of 20° and a contact time of 0.04 s, the grain circularity did not exhibit a clear trend for the sand cast and the metallic mould cast samples with a decrease in pouring temperature from 680 °C to 640 °C. The grain circularity for the metallic mould cast samples was higher than those for the sand cast samples at pouring temperatures of 660 °C and 640 °C (see Table 4.5.5). For a contact time of 0.09 s, the grain circularity decreased from 0.67 to 0.53 for the sand cast samples but it did not exhibit a clear trend for the metallic mould cast samples with a decrease in pouring temperature from 680 °C to 640 °C. The grain circularity for the metallic mould cast samples was higher than those for the sand cast samples at pouring temperatures of 660 °C and 640 °C. For a contact time of 0.13 s, the grain circularity did not exhibit a clear trend both for the sand cast and the metallic mould cast samples with a decrease in pouring temperature from 680 °C to 640 °C. The grain circularity

for the metallic mould cast samples was lower than those for the sand cast samples at each pouring temperature.

Inclination Angle of 40°

At an inclination angle of 40° and a contact time of 0.04 s, the grain circularity did not exhibit a clear trend both for the sand cast and the metallic mould cast samples with a decrease in pouring temperature from 680 °C to 640 °C. The grain circularity for the metallic mould cast samples was higher than those for the sand cast samples at a pouring temperature of 660 °C (see Table 4.5.5). For a contact time of 0.09 s, the grain circularity did not exhibit a clear trend both for the sand cast and for the metallic mould cast samples with a decrease in pouring temperature from 680 °C to 640 °C. The grain circularity for the metallic mould cast samples was lower than those for the sand cast samples at each pouring temperature. For a contact time of 0.13 s, the grain circularity decreased from 0.78 to 0.65 for the sand cast samples but it did not exhibit a clear trend for the metallic mould cast samples with a decrease in pouring temperature from 680 °C to 640 °C. The grain circularity for the metallic mould cast samples was lower than those for the sand cast samples at each pouring temperature.

Inclination Angle of 60°

At an inclination angle of 60° and a contact time of 0.04 s, the grain circularity did not exhibit a clear trend both for the sand cast and the metallic mould cast samples with a decrease in pouring temperature from 680 °C to 640 °C. The grain circularity for metallic mould cast samples was lower than those for the sand cast samples at each pouring temperature (see Table 4.5.5). For a contact time of 0.09 s, the grain circularity decreased from 0.80 to 0.57 for the sand cast samples but it did not exhibit a clear trend for the metallic mould cast samples with a decrease in pouring temperature from 680 °C to 640 °C. The grain circularity for the metallic mould cast samples was lower than those for the sand cast samples at each pouring temperature. For a contact time of 0.13 s, the grain circularity decreased from 0.81 to 0.73 for the sand cast samples but it did not exhibit a clear trend for the metallic mould cast samples with a decrease in pouring temperature from 680 °C to 640 °C. The grain circularity for the metallic mould cast samples was lower than those for the sand cast samples at each pouring temperature.

Grain Elongation

Inclination Angle of 20°

At an inclination angle of 20° and a contact time of 0.04 s, the grain elongation increased from 1.08 to 1.09 for the sand cast samples but it did not exhibit a clear trend for the metallic mould cast samples with a decrease in pouring temperature from 680 °C to 640 °C. The grain elongation for the metallic mould cast samples was lower than those for the sand cast samples at a pouring temperature of 680 °C (see Table 4.5.6). For a contact time of 0.09 s, the grain elongation did not exhibit a clear trend for the sand cast samples but it increased from 1.06 to 1.39 for the metallic mould cast samples with a decrease in pouring temperature from 680 °C to 640 °C. The grain elongation for the metallic mould cast samples was lower than those for the sand cast samples at a pouring temperature of 680 °C. For a contact time of 0.13 s, the grain elongation increased from 1.05 to 1.12 for the sand cast samples but it did not exhibit a clear trend for the metallic mould cast samples with a decrease in pouring temperature from 680 °C to 640 °C. The grain elongation for the metallic mould cast samples was lower than those for the sand cast samples at a pouring temperature of 640 °C.

Inclination Angle of 40°

At an inclination angle of 40° and a contact time of 0.04 s, the grain elongation decreased from 1.10 to 1.08 for the sand cast samples but it increased from 1.11 to 1.44 for the metallic mould cast samples with a decrease in pouring temperature from 680 °C to 640 °C. The grain elongation for the metallic mould cast samples was higher than those for the sand cast samples at each pouring temperature (see Table 4.5.6). For a contact time of 0.09 s, the grain size did not exhibit a clear trend both for the sand cast and the metallic mould cast samples with a decrease in pouring temperature from 680 °C to 640 °C. The grain elongation for the metallic mould cast samples was higher than those for the sand cast samples at each pouring temperature. For a contact time of 0.13 s, the grain elongation decreased from 1.09 to 1.08 for the sand cast samples but it increased from 1.00 to 1.50 for the metallic mould cast samples with a decrease in pouring temperature from 680 °C to 640 °C. The grain elongation for the metallic mould cast samples was lower than those for the sand cast samples at a pouring temperature of 680 °C.

Inclination Angle of 60°

At an inclination angle of 60° and a contact time of 0.04 s, the grain elongation decreased from 1.12 to 1.00 for the sand cast samples but it did not exhibit a clear trend for the metallic mould cast samples with a decrease in pouring temperature from 680 °C to 640 °C. The grain elongation for the metallic mould cast samples was lower than those for the sand cast samples at a pouring temperature of 680 °C (see Table 4.5.6). For a contact time of 0.09 s, the grain elongation did not exhibit a clear trend both for the sand cast and the metallic mould cast samples with a decrease in pouring temperature from 680 °C to 640 °C. The grain elongation for the metallic mould cast samples was higher than those for the sand cast samples at each pouring temperature. For a contact time of 0.13 s, the grain elongation decreased from 1.12 to 1.10 for the sand cast samples but it increased from 1.00 to 1.45 for the metallic mould cast samples with a decrease in pouring temperature from 680 °C to 640 °C. The grain elongation for the metallic mould cast samples was lower than those for the sand cast samples at a pouring temperature of 680 °C.

4.5.2 Effect of Contact Time

4.5.2.1 Constant Pouring Temperature

Grain Size

Pouring Temperature of 680 °C

At a pouring temperature of 680 °C and an inclination angle of 20°, the grain size increased from 151 μm to 165 μm for the sand cast samples and it decreased from 114 μm to 85 μm for the metallic mould cast samples with a decrease in contact time from 0.04 s to 0.13 s. The grain size for the metallic mould cast samples was finer than those for the sand cast samples for each contact time (see Table 4.5.7). At an inclination angle of 40°, the grain size did not exhibit a clear trend both for the sand cast and the metallic mould cast samples with a decrease in contact time from 0.04 s to 0.13 s. The grain size for the metallic mould cast samples was finer than those for the sand cast samples for contact times of 0.09 s and 0.13 s. At an inclination angle of

60°, the grain size did not exhibit a clear trend both for the sand cast and the metallic mould cast samples with a decrease in contact time from 0.04 s to 0.13 s. The grain size for the metallic mould cast samples was finer than those for the sand cast samples for each contact time.

Pouring Temperature of 660 °C

At a pouring temperature of 660 °C and inclination angle of 20°, the grain size did not exhibit a clear trend both for the sand cast and the metallic mould cast samples with a decrease in contact time from 0.04 s to 0.13 s. The grain size for the metallic mould cast samples was finer than those for the sand cast samples for a contact time of 0.04 s (see Table 4.5.7). At an inclination angle of 40°, the grain size did not exhibit a clear trend for the sand cast samples but it increased from 104 μm to 122 μm for the metallic mould cast samples with a decrease in contact time from 0.04 s to 0.13 s. The grain size for the metallic mould cast samples was finer than those for the sand cast samples for a contact time of 0.04 s. At an inclination angle of 60°, the grain size did not exhibit a clear trend for the sand cast samples but it increased from 99 μm to 124 μm for the metallic mould cast samples with a decrease in contact time from 0.04 s to 0.13 s. The grain size for the metallic mould cast samples was finer than those for the sand cast samples for a contact time of 0.04 s.

Pouring Temperature of 640 °C

At a pouring temperature of 640 °C and an inclination angle of 20°, the grain size did not exhibit a clear trend for the sand cast samples but it increased from 121 μm to 189 μm for the metallic mould cast samples with a decrease in contact time from 0.04 s to 0.13 s. The grain size for the metallic mould cast samples was finer than those for the sand cast samples for a contact time of 0.04 s (see Table 4.5.7). At an inclination angle of 40°, the grain size did not exhibit a clear trend for the sand cast samples but it increased from 122 μm to 124 μm for the metallic mould cast samples with a decrease in contact time from 0.04 s to 0.13 s. The grain size for the metallic mould cast samples was coarser than those for the sand cast samples for each contact time. At an inclination angle of 60°, the grain size did not exhibit a clear trend both for the sand cast and the metallic mould cast samples with a decrease in contact time from 0.04 s to 0.13 s. The grain size for the metallic mould cast samples was coarser than those for the sand cast samples for each contact time.

Grain Circularity

Pouring Temperature of 680 °C

At a pouring temperature of 680 °C and an inclination angle of 20°, the grain circularity increased from 0.65 to 0.68 for the sand cast samples but it did not exhibit a clear trend for the metallic mould cast samples with a decrease in contact time from 0.04 s to 0.13 s. The grain circularity for the metallic mould cast samples was lower than those for the sand cast samples for each contact time (see Table 4.5.8). At an inclination angle of 40°, the grain circularity did not exhibit a clear trend for the sand cast samples but it increased from 0.24 to 0.34 for the metallic mould cast samples with a decrease in contact time from 0.04 s to 0.13 s. The grain circularity for the metallic mould cast samples was lower than those for the sand cast samples for each contact time. At an inclination angle of 60°, the grain circularity did not exhibit a clear trend both for the sand cast and the metallic mould cast samples with a decrease in contact time from 0.04 s to 0.13 s. The grain circularity for the metallic mould cast samples was lower than those for the sand cast samples for each contact time.

Pouring Temperature of 660 °C

At a pouring temperature of 660 °C and an inclination angle of 20°, the grain circularity did not exhibit a clear trend both for the sand cast and the metallic mould cast samples with a decrease in contact time from 0.04 s to 0.13 s. The grain circularity for the metallic mould cast samples was higher than those for the sand cast samples for a contact time of 0.04 s (see Table 4.5.8). At an inclination angle of 40°, the grain circularity did not exhibit a clear trend for the sand cast samples but it decreased from 0.71 to 0.62 for the metallic mould cast samples with a decrease in contact time from 0.04 s to 0.13 s. The grain circularity for the metallic mould cast samples was higher than those for the sand cast samples for a contact time of 0.04 s. At an inclination angle of 60°, the grain circularity did not exhibit a clear trend for the sand cast samples but it decreased from 0.70 to 0.66 for the metallic mould cast samples with a decrease in contact time from 0.04 s to 0.13 s. The grain circularity for the metallic mould cast samples was finer than those for the sand cast samples for contact times of 0.04 s and 0.13 s.

Pouring Temperature of 640 °C

At a pouring temperature of 640 °C and an inclination angle of 20°, the grain circularity increased from 0.51 to 0.81 for the sand cast samples but it decreased from 0.65 to 0.46 for the metallic mould cast samples with a decrease in contact time from 0.04 s to 0.13 s. The grain circularity for the metallic mould cast samples was higher than those for the sand cast samples for a contact time of 0.04 s (see Table 4.5.8). At an inclination angle of 40°, the grain circularity did not exhibit a clear trend both for the sand cast and the metallic mould cast samples with a decrease in contact time from 0.04 s to 0.13 s. The grain circularity for the metallic mould cast samples was lower than those for the sand cast samples for each contact time. At an inclination angle of 60°, the grain circularity did not exhibit a clear trend both for the sand cast and the metallic mould cast samples with a decrease in contact time from 0.04 s to 0.13 s. The grain circularity for the metallic mould cast samples was lower than those for the sand cast samples for each contact time.

Grain Elongation

Pouring Temperature of 680 °C

At a pouring temperature of 680 °C and an inclination angle of 20°, the grain elongation did not exhibit a clear trend for the sand cast samples but it increased from 1.06 to 1.08 for the metallic mould cast samples with a decrease in contact time from 0.04 s to 0.13 s. The grain elongation for the metallic mould cast samples was lower than those for sand cast samples for contact times of 0.04 s and 0.09 s (see Table 4.5.9). At an inclination angle of 40°, the grain elongation remained unchanged to 1.08 for the sand cast samples but it decreased from 1.11 to 1.00 for the metallic mould cast samples with a decrease in contact time from 0.04 s to 0.13 s. The grain elongation for the metallic mould cast samples was lower than those for the sand cast samples for a contact time of 0.13 s. At an inclination angle of 60°, the grain elongation increased from 1.09 to 1.12 for the sand cast samples but it decreased from 1.10 to 1.00 for the metallic mould cast samples with a decrease in contact time from 0.04 s to 0.13 s. The grain elongation for the metallic mould cast samples was lower than those for the sand cast samples for contact times of 0.09 s and 0.13 s.

Pouring Temperature of 660 °C

At a pouring temperature of 660 °C qnd an inclination angle of 20°, the grain elongation did not exhibit a clear trend both for the sand cast and the metallic mould cast samples with a decrease in contact time from 0.04 s to 0.13 s. The grain elongation for the metallic mould cast samples was higher than those for the sand cast samples for each contact time (see Table 4.5.9). At an inclination angle of 40°, the grain elongation did not exhibit a clear trend for the sand cast samples but it increased from 1.41 to 1.44 for the metallic mould cast samples with a decrease in contact time from 0.04 s to 0.13 s. The grain elongation for the metallic mould cast samples was higher than those for the sand cast samples for each contact time. At an inclination angle of 60°, the grain elongation remained unchanged to 1.08 for the sand cast samples but it decreased from 1.46 to 1.41 for the metallic mould cast samples with a decrease in contact time from 0.04 s to 0.13 s. The grain elongation for the metallic mould cast samples was higher than those for the sand cast samples for each contact time.

Pouring Temperature of 640 °C

At a pouring temperature of 640 °C at an inclination angle of 20°, the grain elongation did not exhibit a clear trend for the sand cast samples but it increased from 1.36 to 1.54 for the metallic mould cast samples with a decrease in contact time from 0.04 s to 0.13 s. The grain elongation for the metallic mould cast samples was higher than those for the sand cast samples for each contact time (see Table 4.5.9). At an inclination angle of 40°, the grain elongation did not exhibit a clear trend both for the sand cast and the metallic mould cast samples with a decrease in the contact time from 0.04 s to 0.13 s. The grain elongation for the metallic mould cast samples was higher than those for the sand cast samples for each contact time. At an inclination angle of 60°, the grain elongation did not exhibit a clear trend both for the sand cast and the metallic mould cast samples with a decrease in contact time from 0.04 s to 0.13 s. The grain elongation for the metallic mould cast samples was higher than those for the sand cast samples for each contact time.

4.5.2.2 Constant Inclination Angle

Grain Size

Inclination Angle of 20°

At an inclination angle of 20° and a pouring temperature of 680 °C, the grain size increased from 151 μm to 165 μm for the sand cast samples but it decreased from 114 μm to 85 μm for the metallic mould cast samples with a decrease in contact time from 0.04 s to 0.13 s. The grain size for the metallic mould cast samples was finer than those for the sand cast samples for each contact time (see Table 4.5.10). At a pouring temperature of 660 °C, the grain size did not exhibit a clear trend both for the sand cast and the metallic mould cast samples with a decrease in contact time from 0.04 s to 0.13 s. The grain size for the metallic mould cast samples was finer than those for the sand cast samples for a contact time of 0.04 s. At a pouring temperature of 640 °C, the grain size decreased from 213 μm to 98 μm for the sand cast samples but it increased from 121 μm to 189 μm for the metallic mould cast samples with a decrease in contact time from 0.04 s to 0.13 s. The grain size for the metallic mould cast samples was finer than those for the sand cast samples for a contact time of 0.04 s.

Inclination Angle of 40°

At an inclination angle of 40° and a pouring temperature of 680 °C, the grain size did not exhibit a clear trend both for the sand cast and the metallic mould cast samples with a decrease in contact time from 0.04 s to 0.13 s. The grain size for the metallic mould cast samples was finer than those for the sand cast samples for contact times of 0.09 s and 0.13 s (see Table 4.5.10). At a pouring temperature of 660 °C, the grain size decreased from 121 μm to 107 μm for the sand cast samples but it increased from 104 μm to 122 μm for the metallic mould cast samples with a decrease in contact time from 0.04 s to 0.13 s. The grain size for the metallic mould cast samples was finer than those for the sand cast samples for contact times of 0.04 s and 0.09 s. At a pouring temperature of 640 °C, the grain size did not exhibit a clear trend for the sand cast samples but it increased from 122 μm to 124 μm for the metallic mould cast samples with a decrease in contact time from 0.04 s to 0.13 s. The grain size for the metallic mould cast samples was coarser than those for the sand cast samples for each contact time.

Inclination Angle of 60°

At an inclination angle of 60° and a pouring temperature of 680 °C, the grain size did not exhibit a clear trend for the sand cast samples but it increased from 85 μm to 92 μm for the metallic mould cast samples with a decrease in contact time from 0.04 s to 0.13 s. The grain size for the metallic mould cast samples was finer than those for the sand cast samples for each contact time (see Table 4.5.10). At a pouring temperature of 660 °C, the grain size did not exhibit a clear trend for the sand cast samples but it increased from 99 μm to 124 μm for the metallic mould cast samples with a decrease in contact time from 0.04 s to 0.13 s. The grain size for the metallic mould cast samples was finer than those for the sand cast samples for each contact time. At a pouring temperature of 640 °C, the grain size did not exhibit a clear trend both for the sand cast and the metallic mould cast samples with a decrease in contact time from 0.04 s to 0.13 s. The grain size for the metallic mould cast samples was coarser than those for the sand cast samples for each contact time.

Grain Circularity

Inclination Angle of 20°

At an inclination angle of 20° and a pouring temperature of 680 °C, the grain circularity increased from 0.65 to 0.68 for the sand cast samples but it did not exhibit a clear trend for the metallic mould cast samples with a decrease in contact time from 0.04 s to 0.13 s. The grain circularity for the metallic mould cast samples was lower than those for the sand cast for each contact time (see Table 4.5.11). At a pouring temperature of 660 °C, the grain circularity did not exhibit a clear trend both for the sand cast and the metallic mould cast samples with a decrease in contact time from 0.04 s to 0.13 s. The grain circularity for the metallic mould cast samples was higher than those for the sand cast samples for a contact time of 0.04 s. At a pouring temperature of 640 °C, the grain circularity increased from 0.51 to 0.81 for the sand cast samples but it decreased from 0.65 to 0.46 for the metallic mould cast samples with a decrease in contact time from 0.04 s to 0.13 s. The grain circularity for the metallic mould cast samples was higher than those for the sand cast samples for a contact time of 0.04 s.

Inclination Angle of 40°

At an inclination angle of 40° and a pouring temperature of 680 °C, the grain circularity did not exhibit a clear trend for the sand cast samples but it increased from 0.24 to 0.34 for the metallic mould cast samples with a decrease in contact time from 0.04 s to 0.13 s. The grain circularity for the metallic mould cast samples was lower than those for the sand cast for each contact time (see Table 4.5.11). At a pouring temperature of 660 °C, the grain circularity did not exhibit a clear trend for the sand cast samples but it decreased from 0.71 to 0.62 for the metallic mould cast samples with a decrease in contact time from 0.04 s to 0.13 s. The grain circularity for the metallic mould cast samples was higher than those for the sand cast samples for a contact time of 0.04 s. At a pouring temperature of 640 °C, the grain circularity did not exhibit a clear trend both for the sand cast and the metallic mould cast samples with a decrease in contact time from 0.04 s to 0.13 s. The grain circularity for the metallic mould cast samples was lower than those for the sand cast samples for each contact time.

Inclination Angle of 60°

At an inclination angle of 60° and a pouring temperature of 680 °C, the grain circularity did not exhibit a clear trend both for the sand cast and the metallic mould cast samples with a decrease in contact time from 0.04 s to 0.13 s. The grain circularity for the metallic mould cast samples was lower than those for the sand cast for each contact time (see Table 4.5.11). At a pouring temperature of 660 °C, the grain circularity did not exhibit a clear trend for the sand cast samples but it decreased from 0.70 to 0.66 for the metallic mould cast samples with a decrease in contact time from 0.04 s to 0.13 s. The grain circularity for the metallic mould cast samples was higher than those for the sand cast samples for contact times of 0.04 s and 0.13 s. At a pouring temperature of 640 °C, the grain circularity did not exhibit a clear trend both for the sand cast and the metallic mould cast samples with a decrease in contact time from 0.04 s to 0.13 s. The grain circularity for the metallic mould cast samples was lower than those for the sand cast samples for each contact time.

Grain Elongation

Inclination Angle of 20°

At an inclination angle of 20° and a pouring temperature of 680 °C, the grain elongation did not exhibit a clear trend for the sand cast samples but it increased from 1.06 to 1.08 for the metallic mould cast samples with a decrease in contact time from 0.04 s to 0.13 s. The grain elongation for the metallic mould cast samples was lower than those for the sand cast samples for contact times of 0.04 s and 0.09 s (see Table 4.5.12). At a pouring temperature of 660 °C, the grain elongation did not exhibit a clear trend both for the sand cast and the metallic mould cast samples with a decrease in contact time from 0.04 s to 0.13 s. The grain elongation for the metallic mould cast samples was higher than those for the sand cast samples for each contact time. At a pouring temperature of 640 °C, the grain elongation did not exhibit a clear trend for the sand cast samples but it increased from 1.36 to 1.54 for the metallic mould cast samples with a decrease in contact time from 0.04 s to 0.13 s. The grain elongation for the metallic mould cast samples was higher than those for the sand cast samples for each contact time.

Inclination Angle of 40°

At an inclination angle of 40° and a pouring temperature of 680 °C, the grain elongation remained unchanged at 1.08 for the sand cast samples but it decreased from 1.11 to 1.00 for the metallic mould cast samples with a decrease in contact time from 0.04 s to 0.13 s. The grain elongation for the metallic mould cast samples was lower than those for the sand cast samples for a contact time of 0.13 s (see Table 4.5.12). At a pouring temperature of 660 °C, the grain elongation did not exhibit a clear trend for the sand cast samples but it increased from 1.41 to 1.44 for the metallic mould cast samples with a decrease in contact time from 0.04 s to 0.13 s. The grain elongation for the metallic mould cast samples was higher than those for the sand cast samples for each contact time. At a pouring temperature of 640 °C, the grain elongation did not exhibit a clear trend both for the sand cast and the metallic mould cast samples with a decrease in contact time from 0.04 s to 0.13 s. The grain elongation for the metallic mould cast samples was higher than those for the sand cast samples for each contact time.

Inclination Angle of 60°

At an inclination angle of 60° and a pouring temperature of 680 °C, the grain elongation increased from 1.09 to 1.12 for the sand cast samples but it decreased from 1.10 to 1.00 for the metallic mould cast samples with a decrease in contact time from 0.04 s to 0.13 s. The grain elongation for the metallic mould cast samples was lower than those for the sand cast samples at contact times of 0.09 s and 0.13 s (see Table 4.5.12). At a pouring temperature of 660 °C, the grain elongation remained unchanged at 1.08 for the sand cast samples but it decreased from 1.46 to 1.41 for the metallic mould cast samples with a decrease in contact time from 0.04 s to 0.13 s. The grain elongation for the metallic mould cast samples was higher than those for the sand cast samples at each contact time. At a pouring temperature of 640 °C, the grain elongation did not exhibit a clear trend both for the sand cast and the metallic mould cast samples with a decrease in contact time from 0.04 s to 0.13 s. The grain elongation for the metallic mould cast samples was higher than those for the sand cast samples for each contact time.

4.5.3 Effect of Inclination Angle

4.5.3.1 Constant Pouring Temperature

Grain Size

Pouring Temperature of 680 °C

At a pouring temperature of 680 °C and a contact time of 0.04 s, the grain size increased from 151 μm to 213 μm for the sand cast samples but it did not exhibit a clear trend for the metallic mould cast samples with a decrease in inclination angle from 20° to 60°. The grain size for the metallic mould cast samples was finer than those for the sand cast samples at inclination angles of 20° and 60° (see Table 4.5.13). For a contact time of 0.09 s, the grain size decreased from 122 μm to 100 μm for the sand cast samples but did not exhibit a clear trend for the metallic mould cast samples with a decrease in inclination angle from 20° to 60°. The grain size for the metallic mould cast samples was finer than those for the sand cast samples at each inclination

angle. For a contact time of 0.13 s, the grain size decreased from 179 μm to 117 μm for the sand cast samples but did not exhibit a clear trend for the metallic mould cast samples with a decrease in inclination angle from 20° to 60°. The grain size for the metallic mould cast samples was finer than those for the sand cast samples at each inclination angle.

Pouring Temperature of 660 °C

At a pouring temperature of 660 °C and a contact time of 0.04 s, the grain size did not exhibit a clear trend both for the sand cast and the metallic mould cast samples with a decrease in inclination angle from 20° to 60°. The grain size for metallic mould cast samples was finer than those for the sand cast samples at an inclination angle of 20° (see Table 4.5.13). For a contact time of 0.09 s, the grain size decreased from 147 μm to 91 μm for the sand cast samples but it decreased from 122 μm to 102 μm for the metallic mould cast samples with a decrease in inclination angle from 20° to 60°. The grain size for the metallic mould cast samples was finer than those for the sand cast samples at inclination angles of 20° and 40°. For a contact time of 0.13 s, the grain size for the sand cast samples but it increased from 119 μm to 124 μm for the metallic mould cast samples with a decrease in inclination angle from 20° to 60°. The grain size for metallic mould cast samples was finer than those for the sand cast samples at an inclination angle of 20°.

Pouring Temperature of 640 °C

At a pouring temperature of 640 °C and contact time of 0.04 s, the grain size did not exhibit a clear trend for the sand cast samples but it increased from 121 μm to 144 μm for the metallic mould cast samples with a decrease in inclination angle from 20° to 60°. The grain size for the metallic mould cast samples was finer than those for the sand cast samples at an inclination angle of 20° (see Table 4.5.13). For a contact time of 0.09 s, the grain size decreased from 120 μm to 95 μm for the sand cast samples but it did not exhibit a clear trend for the metallic mould cast samples with a decrease in inclination angle from 20° to 60°. The grain size for the metallic mould cast samples was coarser than those for the sand cast samples at each inclination angle. For a contact time of 0.13 s, the grain size decreased from 141 μm to 95 μm for the sand cast samples but did not exhibit a clear trend for the metallic mould cast samples with a decrease in inclination angle from 20° to 60°. The grain size for the metallic mould

cast samples was coarser than those for the sand cast samples at each inclination angle.

Grain Circularity

Pouring Temperature of 680 °C

At a pouring temperature of 680 °C and contact time of 0.04 s, the grain circularity decreased from 0.65 to 0.51 for the sand cast samples but did not exhibit a clear trend for the metallic mould cast samples with a decrease in inclination angle from 20° to 60°. The grain circularity for the metallic mould cast samples was lower than those for the sand cast samples for each inclination angle (see Table 4.5.14). For a contact time of 0.09 s, the grain circularity did not exhibit a clear trend both for the sand cast and the metallic mould cast samples with a decrease in inclination angle from 20° to 60°. The grain circularity for the metallic mould cast samples was lower than those for the sand cast samples for each inclination angle. For a contact time of 0.13 s, the grain circularity increased from 0.58 to 0.72 for the sand cast samples but did not exhibit a clear trend for the metallic mould cast samples with a decrease in inclination angle from 20° to 60°. The grain circularity for the metallic mould cast samples was lower than those for the sand cast samples at each inclination angle.

Pouring Temperature of 660 °C

At a pouring temperature of 660 °C and contact time of 0.04 s, the grain circularity did not exhibit a clear trend for the sand cast samples but decreased from 0.74 to 0.70 for the metallic mould cast samples with a decrease in inclination angle from 20° to 60°. The grain circularity for the metallic mould cast samples was higher than those for the sand cast samples at an inclination angle of 20° (see Table 4.5.14). For a contact time of 0.09 s, the grain circularity increased from 0.60 to 0.74 for the sand cast samples and from 0.65 to 0.69 for the metallic mould cast samples with a decrease in inclination angle from 20° to 60°. The grain circularity for the metallic mould cast samples was higher than those for the sand cast samples at an inclination angle of 20°. For a contact time of 0.13 s, the grain circularity did not exhibit a clear trend both for the sand cast and the metallic mould cast samples with a decrease in inclination angle from 20° to 60°. The grain circularity for the metallic mould cast samples was higher than those for the sand cast samples at inclination angles of 20° and 60°.

Pouring Temperature of 640 °C

At a pouring temperature of 640 °C and contact time of 0.04 s, the grain circularity increased from 0.68 to 0.81 for the sand cast samples but decreased from 0.65 to 0.57 for the metallic mould cast samples with a decrease in the inclination angle from 20° to 60°. The grain circularity for the metallic mould cast samples was lower than those for the sand cast samples at each inclination angle (see Table 4.5.14). For a contact time of 0.09 s, the grain circularity did not exhibit a clear trend both for the sand cast and the metallic mould cast samples with a decrease in inclination angle from 20° to 60°. The grain circularity for the metallic mould cast samples was lower than those for the sand cast samples at each inclination angle. For a contact time of 0.13 s, the grain circularity increased from 0.62 to 0.73 for the sand cast samples and from 0.46 to 0.55 for the metallic mould cast samples with a decrease in inclination angle from 20° to 60°. The grain circularity for the metallic mould cast samples was lower than those for the sand cast samples at each inclination angle.

Grain Elongation

Pouring Temperature of 680 °C

At a pouring temperature of 640 °C and contact time of 0.04 s, the grain elongation increased from 1.08 to 1.12 for the sand cast samples but did not exhibit a clear trend for the metallic mould cast samples with a decrease in inclination angle from 20° to 60°. The grain elongation for the metallic mould cast samples was lower than those for the sand cast samples at inclination angles of 20° and 60° (see Table 4.5.15). For a contact time of 0.09 s, the grain elongation did not exhibit a clear trend both for the sand cast and the metallic mould cast samples with a decrease in inclination angle from 20° to 60°. The grain elongation for the metallic mould cast samples was finer than those for the sand cast samples at inclination angles of 20° and 40°. For a contact time of 0.13 s, the grain elongation decreased from 1.09 to 1.00 for the sand cast samples and from 1.08 to 1.00 for the metallic mould cast samples with a decrease in inclination angle from 20° to 60°. The grain elongation for the metallic mould cast samples was finer than those for the sand cast samples at each inclination angle.

Pouring Temperature of 660 °C

At a pouring temperature of 640 °C and contact time of 0.04 s, the grain elongation decreased from 1.10 to 1.06 for the sand cast samples but increased from 1.40 to 1.46 for the metallic mould cast samples with a decrease in inclination angle from 20° to 60°. The grain elongation for the metallic mould cast samples was higher than those for the sand cast samples at each inclination angle (see Table 4.5.15). For a contact time of 0.09 s, the grain elongation did not exhibit a clear trend for the sand cast samples but it increased from 1.39 to 1.46 for the metallic mould cast samples with a decrease in inclination angle from 20° to 60°. The grain elongation for the metallic mould cast samples was higher than those for the sand cast samples at each inclination angle. For a contact time of 0.13 s, the grain elongation did not exhibit a clear trend both for the sand cast and the metallic mould cast samples with a decrease in inclination angle from 20° to 60°. The grain elongation for the metallic mould cast samples was higher than those for the sand cast samples at each inclination angle.

Pouring Temperature of 640 °C

At a pouring temperature of 640 °C and contact time of 0.04 s, the grain elongation increased from 1.05 to 1.12 for the sand cast samples but did not exhibit a clear trend for the metallic mould cast samples with a decrease in inclination angle from 20° to 60°. The grain elongation for the metallic mould cast samples was higher than those for the sand cast samples at each inclination angle (see Table 4.5.15). For a contact time of 0.09 s, the grain elongation increased from 1.08 to 1.11 for the sand cast samples and from 1.39 to 1.41 for the metallic mould cast samples with a decrease in inclination angle from 20° to 60°. The grain elongation for the metallic mould cast samples was higher than those for the sand cast samples at each inclination angle. For a contact time of 0.13 s, the grain elongation did not exhibit a clear trend for the sand cast samples but it decreased from 1.54 to 1.45 for the metallic mould cast samples with a decrease in inclination angle from 20° to 60°. The grain elongation for the metallic mould cast samples was higher than those for the sand cast samples at each inclination angle.

4.5.3.3 Constant Contact Time

Grain Size

Contact Time of 0.04 s

At a contact time of 0.04 s and pouring temperature of 680 °C, the grain size increased from 151 μm to 213 μm for the sand cast samples but did not exhibit a clear trend for the metallic mould cast samples with a decrease in inclination angle from 20° to 60°. The grain size for the metallic mould cast samples was finer than those for the sand cast samples for inclination angles of 20° and 60° (see Table 4.5.16). At a pouring temperature of 660 °C, the grain size did not exhibit a clear trend both for the sand cast and the metallic mould cast samples with a decrease in inclination angle from 20° to 60°. The grain size for the metallic mould cast samples was finer than those for the sand cast samples at an inclination angle of 20°. At a pouring temperature of 640 °C, the grain size did not exhibit a clear trend for the sand cast samples but it increased from 121 μm to 144 μm for the metallic mould cast samples with a decrease in inclination angle from 20° to 60°. The grain size for the metallic mould cast samples was finer than those for the sand cast samples at an inclination angle of 20°.

Contact Time of 0.09 s

At a contact time of 0.09 s and pouring temperature of 680 °C, the grain size decreased from 122 μm to 100 μm for the sand cast samples but did not exhibit a clear trend for the metallic mould cast samples with a decrease in inclination angle from 20° to 60°. The grain size for the metallic mould cast samples was finer than those for the sand cast samples at each inclination angle (see Table 4.5.16). At a pouring temperature of 660 °C, the grain size decreased from 147 μm to 91 μm for the sand cast samples and from 122 μm to 102 μm for the metallic mould cast samples with a decrease in inclination angle from 20° to 60°. The grain size for the metallic mould cast samples was finer than those for the sand cast samples for an inclination angle of 20°. At a pouring temperature of 640 °C, the grain size decreased from 120 μm to 95 μm for the sand cast samples but did not exhibit a clear trend for the metallic mould cast samples with a decrease in inclination angle from 20° to 60°. The grain size for the metallic mould cast samples was coarser than those for the sand cast samples at each inclination angle.

Contact Time of 0.13 s

At a contact time of 0.13 s and pouring temperature of 680 °C, the grain size decreased from 179 μm to 117 μm for the sand cast samples but did not exhibit a clear trend for the metallic mould cast samples with a decrease in inclination angle from 20° to 60°. The grain size for the metallic mould cast samples was finer than those for the sand cast samples at each inclination angle (see Table 4.5.16). At a pouring temperature of 660 °C, the grain size did not exhibit a clear trend for the sand cast samples but it increased from 119 μm to 124 μm for the metallic mould cast samples with a decrease in inclination angle from 20° to 60°. The grain size for the metallic mould cast samples was finer than those for the sand cast samples at inclination angles of 20° and 60°. At pouring temperature of 640 °C, the grain size decreased from 141 μm to 95 μm for the sand cast samples but did not exhibit a clear trend for the metallic mould cast samples with a decrease in inclination angle from 20° to 60°. The grain size for the metallic mould cast samples was coarser than those for the sand cast samples at each inclination angle.

Grain Circularity

Contact Time of 0.04 s

At a contact time of 0.04 s and pouring temperature of 680 °C, the grain circularity decreased from 0.65 to 0.51 for the sand cast samples but did not exhibit a clear trend for the metallic mould cast samples with a decrease in inclination angle from 20° to 60°. The grain circularity for the metallic mould cast samples was lower than those for the sand cast samples at each inclination angle (see Table 4.5.17). At a pouring temperature of 660 °C, the grain circularity did not exhibit a clear trend for the sand cast samples but it decreased from 0.74 to 0.70 for the metallic mould cast samples with a decrease in inclination angle from 20° to 60°. The grain circularity for the metallic mould cast samples was higher than those for the sand cast samples at an inclination angle of 20°. At a pouring temperature of 640 °C, the grain circularity increased from 0.68 to 0.81 for the sand cast samples but it decreased from 0.65 to 0.57 for the metallic mould cast samples with a decrease in inclination angle from 20° to 60°. The grain circularity for the metallic mould cast samples was lower than those for the sand cast samples at each inclination angle.

Contact Time of 0.09 s

At a contact time of 0.09 s and pouring temperature of 680 °C, the grain circularity did not exhibit a clear trend both for the sand cast and the metallic mould cast samples with a decrease in inclination angle from 20° to 60°. The grain circularity for the metallic mould cast samples was lower than those for the sand cast samples at each inclination angle (see Table 4.5.17). At a pouring temperature of 660 °C, the grain circularity increased from 0.60 to 0.74 for the sand cast samples and from 0.65 to 0.69 for the metallic mould cast samples with a decrease in inclination angle from 20° to 60°. The grain circularity for the metallic mould cast samples was higher than those for the sand cast samples at an inclination angle of 20°. At a pouring temperature of 640 °C, the grain circularity did not exhibit a clear trend both for the sand cast and the metallic mould cast samples with a decrease in inclination angle from 20° to 60°. The grain circularity for the metallic mould cast samples was lower than those for the sand cast samples at each inclination angle.

Contact Time of 0.13 s

At a contact time of 0.13 s and pouring temperature of 680 °C, the grain circularity increased from 0.58 to 0.72 for the sand cast samples but did not exhibit a clear trend for the metallic mould cast samples with a decrease in inclination angle from 20° to 60°. The grain circularity for the metallic mould cast samples was lower than those for the sand cast samples at each inclination angle (see Table 4.5.17). At a pouring temperature of 660 °C, the grain circularity did not exhibit a clear trend both for the sand cast and the metallic mould cast samples with a decrease in inclination angle from 20° to 60°. The grain circularity for the metallic mould cast samples was higher than those for the sand cast samples at inclination angles of 20° and 60°. At a pouring temperature of 640 °C, the grain circularity increased from 0.62 to 0.73 for the sand cast samples and from 0.46 to 0.55 for the metallic mould cast samples with a decrease in inclination angle from 20° to 60°. The grain circularity for the metallic mould cast samples was lower than those for the sand cast samples at each inclination angle.

Grain Elongation

Contact Time of 0.04 s

At a contact time of 0.04 s and pouring temperature of 680 °C, the grain elongation increased from 1.08 to 1.12 for the sand cast samples but did not exhibit a clear trend for the metallic mould cast samples with a decrease in inclination angle from 20° to 60°. The grain elongation for the metallic mould cast samples was lower than those for the sand cast samples at inclination angles of 20° and 60° (see Table 4.5.18). At a pouring temperature of 660 °C, the grain elongation decreased from 1.10 to 1.06 for the sand cast samples but it increased from 1.40 to 1.46 for the metallic mould cast samples with a decrease in inclination angle from 20° to 60°. The grain elongation for the metallic mould cast samples was higher than those for the sand cast samples for each inclination angle. At a pouring temperature of 640 °C, the grain elongation increased from 1.05 to 1.12 for the sand cast samples but it did not exhibit a clear trend for the metallic mould cast samples with a decrease in inclination angle from 20° to 60°. The grain elongation for the metallic mould cast samples was higher than those for the sand cast samples at each inclination angle.

Contact Time of 0.09 s

At a contact time of 0.09 s and pouring temperature of 680 °C, the grain elongation did not exhibit a clear trend both for the sand cast and the metallic mould cast samples with a decrease in inclination angle from 20° to 60°. The grain elongation for the metallic mould cast samples was finer than those for the sand cast samples at inclination angles of 20° and 40° (see Table 4.5.18). At a pouring temperature of 660 °C, the grain elongation did not exhibit a clear trend for the sand cast samples but it increased from 1.39 to 1.45 for the metallic mould cast samples with a decrease in inclination angle from 20° to 60°. The grain elongation for the metallic mould cast samples was higher than those for the sand cast samples for each inclination angle. At a pouring temperature of 640 °C, the grain elongation increased from 1.08 to 1.11 for the sand cast samples and from 1.39 to 1.41 for the metallic mould cast samples with a decrease in inclination angle from 20° to 60°. The grain elongation for the metallic mould cast samples was higher than those for the sand cast samples at each inclination angle.

Contact Time of 0.13 s

At a contact time of 0.13 s and pouring temperature of 680 °C, the grain elongation decreased from 1.09 to 1.00 for the sand cast samples and from 1.08 to 1.00 for the metallic mould cast samples with a decrease in inclination angle from 20° to 60°. The grain elongation for the metallic mould cast samples was lower than those for the sand cast samples at each inclination angle (see Table 4.5.18). At a pouring temperature of 660 °C, the grain elongation did not exhibit a clear trend both for the sand cast and the metallic mould cast samples with a decrease in inclination angle from 20° to 60°. The grain elongation for the metallic mould cast samples was higher than those for the sand cast samples at each inclination angle. At a pouring temperature of 640 °C, the grain elongation did not exhibit a clear trend for the sand cast samples but it decreased from 1.54 to 1.45 for the metallic mould cast samples with a decrease in inclination angle from 20° to 60°. The grain elongation for the metallic mould cast samples was higher than those for the sand cast samples at each inclination angle.

4.5.4 Summary

With respect to the effect of mould material (sand and metallic), which alter the imposed thermal gradient, it was found that:

1. At lower contact times and inclination angles, the grain size of the metallic mould was relatively finer than that for the sand mould.
2. At higher contact times and inclination angles the grain size for the sand moulds was similar or finer than that for the metallic mould.
3. At an inclination angle of 60° and a contact time of 0.13 s, the grain size was similar (~ 95 μm) at all the pouring temperatures (680, 660 and 640 °C) for the sand mould.
4. In general at a pouring temperature of 660 °C a relatively finer grain size was obtained both for the sand and metallic mould. This may be due to an optimum undercooling of the melt suitable for the existence of nuclei floating in the bulk and their subsequent growth.
5. The grain size obtained, when using a metallic mould in general, was relatively non-globular and non-equiaxed in nature in comparison to the sand mould.

6. In the metallic mould, when analyzing the microstructure obtained at pouring temperatures of 660 °C and 640 °C, the circularity values increased indicating a smoother surface of the grains but higher elongation values indicated a more columnar structure.
7. In the metallic mould samples poured at a pouring temperature of 680 °C, fine, equiaxed grains with very low circularity (rosette-like morphology) were obtained.

4.5.5 Tables

Table 4.5.1: Effect of pouring temperature on grain size (μm) for sand and metallic mould cast samples with different inclination angles for different contact times.

0.04 s Contact Time						
Pouring Temperature (℃)	20° Inclination		40° Inclination		60° Inclin ation	
	Sand Mould	Metallic Mould	Sand Mould	Metallic Mould	Sand Mould	Metallic Mould
680	151	114	208	211	213	85
660	122	83	121	104	100	99
640	179	121	151	122	117	144
0.09 s Contact Time						
680	152	87	86	89	89	80
660	147	122	115	119	91	102
640	189	134	97	124	179	179
0.13 s Contact Time						
680	165	85	96	101	98	92
660	120	119	107	122	95	124
640	141	189	124	124	95	134

Table 4.5.2: Effect of pouring temperature on grain circularity for sand and metallic mould cast samples with different inclination angles for different contact times.

0.04 s Contact Time						
Pouring Temperature (℃)	20° Inclination		40° Inclination		60° Inclin ation	
	Sand Mould	Metallic Mould	Sand Mould	Metallic Mould	Sand Mould	Metallic Mould
680	0.65	0.37	0.54	0.24	0.51	0.27
660	0.71	0.74	0.65	0.71	0.78	0.70
640	0.58	0.65	0.62	0.58	0.72	0.57
0.09 s Contact Time						
680	0.67	0.44	0.84	0.44	0.80	0.51
660	0.60	0.65	0.71	0.65	0.74	0.69
640	0.53	0.60	0.76	0.60	0.57	0.49
0.13 s Contact Time						
680	0.68	0.29	0.78	0.34	0.81	0.29
660	0.69	0.67	0.67	0.62	0.75	0.66
640	0.62	0.46	0.65	0.55	0.73	0.55

Table 4.5.3: Effect of pouring temperature on grain elongation for sand and metallic mould cast samples with different inclination angles for different contact times.

0.04 s Contact Time						
Pouring Temperature (℃)	20° Inclination		40° Inclination		60° Inclin ation	
	Sand Mould	Metallic Mould	Sand Mould	Metallic Mould	Sand Mould	Metallic Mould
680	1.08	1.06	1.10	1.11	1.12	1.10
660	1.08	1.40	1.10	1.41	1.06	1.45
640	1.09	1.36	1.08	1.44	1.00	1.42
0.09 s Contact Time						
680	1.10	1.06	1.06	1.08	1.06	1.07
660	1.08	1.39	1.11	1.44	1.00	1.45
640	1.10	1.39	1.08	1.41	1.18	1.41
0.13 s Contact Time						
680	1.05	1.10	1.09	1.00	1.12	1.00
660	1.08	1.11	1.09	1.44	1.11	1.41
640	1.12	1.08	1.08	1.50	1.10	1.45

Table 4.5.4: Effect of pouring temperature on grain size (μm) for sand and metallic mould cast samples with different contact times for different inclination angles.

20° Inclination						
Pouring Temperature (℃)	0.04 s Contact Time		0.09 s Contact Time		0.13 s Contact Time	
	Sand Mould	Metallic Mould	Sand Mould	Metallic Mould	Sand Mould	Metallic Mould
680	151	114	152	87	165	85
660	122	83	147	122	120	119
640	179	121	189	134	141	189
40° Inclination						
680	208	211	86	89	96	101
660	121	104	115	119	107	122
640	151	122	97	124	124	124
60° Inclination						
680	213	85	89	80	98	92
660	100	99	91	102	95	124
640	117	144	179	179	95	134

Table 4.5.5: Effect of pouring temperature on grain circularity for sand and metallic mould cast samples with different contact times for different inclination angles.

20° Inclination						
Pouring Temperature (℃)	0.04 s Contact Time		0.09 s Contact Time		0.13 s Contact Time	
	Sand Mould	Metallic Mould	Sand Mould	Metallic Mould	Sand Mould	Metallic Mould
680	0.65	0.37	0.67	0.44	0.68	0.29
660	0.71	0.74	0.60	0.65	0.69	0.67
640	0.58	0.65	0.53	0.60	0.62	0.46
40° Inclination						
680	0.54	0.24	0.84	0.44	0.78	0.34
660	0.65	0.71	0.71	0.65	0.67	0.62
640	0.62	0.58	0.76	0.60	0.65	0.55
60° Inclination						
680	0.51	0.27	0.80	0.51	0.81	0.29
660	0.78	0.70	0.74	0.69	0.75	0.66
640	0.72	0.57	0.57	0.49	0.73	0.55

Table 4.5.6: Effect of pouring temperature on grain elongation for sand and metallic mould cast samples with different contact times for different inclination angles.

20° Inclination						
Pouring Temperature (℃)	0.04 s Contact Time		0.09 s Contact Time		0.13 s Contact Time	
	Sand Mould	Metallic Mould	Sand Mould	Metallic Mould	Sand Mould	Metallic Mould
680	1.08	1.06	1.10	1.06	1.05	1.10
660	1.08	1.40	1.08	1.39	1.08	1.11
640	1.09	1.36	1.10	1.39	1.12	1.08
40° Inclination						
680	1.10	1.11	1.06	1.08	1.09	1.00
660	1.10	1.41	1.11	1.44	1.09	1.44
640	1.08	1.44	1.08	1.41	1.08	1.50
60° Inclination						
680	1.12	1.10	1.06	1.07	1.12	1.00
660	1.06	1.45	1.00	1.45	1.11	1.41
640	1.00	1.42	1.18	1.41	1.10	1.45

Table 4.5.7: Effect of contact time on grain size (μm) for sand and metallic mould cast samples with different inclination angles for different pouring temperatures.

680 ℃ Pouring Temperature						
Contact Time (s)	20° Inclination		40° Inclination		60° Inclination	
	Sand Mould	Metallic Mould	Sand Mould	Metallic Mould	Sand Mould	Metallic Mould
0.04	151	114	122	211	179	85
0.09	152	87	147	89	189	80
0.13	165	85	120	101	141	92
660 ℃ Pouring Temperature						
0.04	208	83	121	104	151	99
0.09	86	122	115	119	97	102
0.13	96	119	107	122	124	124
640 ℃ Pouring Temperature						
0.04	213	121	100	122	117	144
0.09	89	134	91	124	179	179
0.13	98	189	95	124	95	134

Table 4.5.8: Effect of contact time on grain circularity for sand and metallic mould cast samples with different inclination angles for different pouring temperatures.

680 ℃ Pouring Temperature						
Contact Time (s)	20° Inclination		40° Inclination		60° Inclination	
	Sand Mould	Metallic Mould	Sand Mould	Metallic Mould	Sand Mould	Metallic Mould
0.04	0.65	0.37	0.71	0.24	0.58	0.27
0.09	0.67	0.44	0.60	0.32	0.53	0.51
0.13	0.68	0.29	0.69	0.34	0.62	0.29
660 ℃ Pouring Temperature						
0.04	0.54	0.74	0.65	0.71	0.62	0.70
0.09	0.84	0.65	0.71	0.69	0.76	0.69
0.13	0.78	0.67	0.67	0.62	0.65	0.66
640 ℃ Pouring Temperature						
0.04	0.51	0.65	0.78	0.58	0.72	0.57
0.09	0.80	0.60	0.74	0.61	0.57	0.49
0.13	0.81	0.46	0.75	0.55	0.73	0.55

Table 4.5.9: Effect of contact time on grain elongation for sand and metallic mould cast samples with different inclination angles for different pouring temperatures.

680 ℃ Pouring Temperature						
Contact Time (s)	20° Inclination		40° Inclination		60° Inclination	
	Sand Mould	Metallic Mould	Sand Mould	Metallic Mould	Sand Mould	Metallic Mould
0.04	1.08	1.06	1.08	1.11	1.09	1.10
0.09	1.10	1.06	1.08	1.08	1.10	1.07
0.13	1.05	1.08	1.08	1.00	1.12	1.00
660 ℃ Pouring Temperature						
0.04	1.10	1.40	1.10	1.41	1.08	1.46
0.09	1.06	1.39	1.11	1.44	1.08	1.45
0.13	1.09	1.43	1.09	1.44	1.08	1.41
640 ℃ Pouring Temperature						
0.04	1.12	1.36	1.06	1.44	1.00	1.42
0.09	1.06	1.39	1.00	1.41	1.18	1.41
0.13	1.12	1.54	1.11	1.50	1.10	1.45

Table 4.5.10: Effect of contact time on grain size (μm) for sand and metallic mould cast samples with different pouring temperatures for different inclination angles.

20° Inclination						
Contact Time (s)	680 ℃ Pouring Temperature		660 ℃ Pouring Temperature		640 ℃ Pouring Temperature	
	Sand Mould	Metallic Mould	Sand Mould	Metallic Mould	Sand Mould	Metallic Mould
0.04	151	114	208	83	213	121
0.09	152	87	86	122	89	134
0.13	165	85	96	119	98	189
40° Inclination						
0.04	122	211	121	104	100	122
0.09	147	89	115	119	91	124
0.13	120	101	107	122	95	124
60° Inclination						
0.04	179	85	151	99	117	144
0.09	189	80	97	102	179	179
0.13	141	92	124	124	95	134

Table 4.5.11: Effect of contact time on grain circularity for sand and metallic mould cast samples with different pouring temperatures for different inclination angles.

20° Inclination						
Contact Time (s)	680 ℃ Pouring Temperature		660 ℃ Pouring Temperature		640 ℃ Pouring Temperature	
	Sand Mould	Metallic Mould	Sand Mould	Metallic Mould	Sand Mould	Metallic Mould
0.04	0.65	0.37	0.54	0.74	0.51	0.65
0.09	0.67	0.44	0.84	0.65	0.80	0.60
0.13	0.68	0.29	0.78	0.67	0.81	0.46
40° Inclination						
0.04	0.71	0.24	0.65	0.71	0.78	0.58
0.09	0.60	0.32	0.71	0.69	0.74	0.61
0.13	0.69	0.34	0.67	0.62	0.75	0.55
60° Inclination						
0.04	0.58	0.27	0.62	0.70	0.72	0.57
0.09	0.53	0.51	0.76	0.69	0.57	0.49
0.13	0.62	0.29	0.65	0.66	0.73	0.55

Table 4.5.12: Effect of contact time on grain elongation for sand and metallic mould cast samples with different pouring temperatures for different inclination angles.

20° Inclination						
Contact Time (s)	680 ℃ Pouring Temperature		660 ℃ Pouring Temperature		640 ℃ Pouring Temperature	
	Sand Mould	Metallic Mould	Sand Mould	Metallic Mould	Sand Mould	Metallic Mould
0.04	1.08	1.06	1.10	1.40	1.12	1.36
0.09	1.10	1.06	1.06	1.39	1.06	1.39
0.13	1.05	1.08	1.09	1.43	1.12	1.54
40° Inclination						
0.04	1.08	1.11	1.10	1.41	1.06	1.44
0.09	1.08	1.08	1.11	1.44	1.00	1.41
0.13	1.08	1.00	1.09	1.44	1.11	1.50
60° Inclination						
0.04	1.09	1.10	1.08	1.46	1.00	1-42
0.09	1.10	1.07	1.08	1.45	1.18	1.41
0.13	1.12	1.00	1.08	1.41	1.10	1.45

Table 4.5.13: Effect of inclination angle on grain size (μm) for sand and metallic mould cast samples with different contact times for different pouring temperatures.

680 ℃ Pouring Temperature						
Inclination Angle (°)	0.04 s Contact Time		0.09 s Contact Time		0.13 s Contact Time	
	Sand Mould	Metallic Mould	Sand Mould	Metallic Mould	Sand Mould	Metallic Mould
20	151	114	122	87	179	85
40	208	211	121	89	151	101
60	213	85	100	80	117	92
660 ℃ Pouring Temperature						
20	152	83	147	122	189	119
40	86	104	115	119	97	122
60	89	99	91	102	179	124
640 ℃ Pouring Temperature						
20	165	121	120	134	141	189
40	96	122	107	124	124	124
60	98	144	95	179	95	134

Table 4.5.14: Effect of inclination angle on grain circularity for sand and metallic mould cast samples with different contact times for different pouring temperatures.

680 ℃ Pouring Temperature						
Inclination Angle (°)	0.04 s Contact Time		0.09 s Contact Time		0.13 s Contact Time	
	Sand Mould	Metallic Mould	Sand Mould	Metallic Mould	Sand Mould	Metallic Mould
20	0.65	0.37	0.71	0.44	0.58	0.29
40	0.54	0.24	0.65	0.32	0.62	0.34
60	0.51	0.27	0.78	0.51	0.72	0.29
660 ℃ Pouring Temperature						
20	0.67	0.74	0.60	0.65	0.53	0.67
40	0.84	0.71	0.71	0.69	0.76	0.62
60	0.80	0.70	0.74	0.69	0.57	0.66
640 ℃ Pouring Temperature						
20	0.68	0.65	0.69	0.60	0.62	0.46
40	0.78	0.58	0.67	0.61	0.65	0.55
60	0.81	0.57	0.75	0.49	0.73	0.55

Table 4.5.15: Effect of inclination angle on grain elongation for sand and metallic mould cast samples with different contact times for different pouring temperatures.

680 ℃ Pouring Temperature						
Inclination Angle (°)	0.04 s Contact Time		0.09 s Contact Time		0.13 s Contact Time	
	Sand Mould	Metallic Mould	Sand Mould	Metallic Mould	Sand Mould	Metallic Mould
20	1.08	1.06	1.08	1.06	1.09	1.08
40	1.10	1.11	1.10	1.08	1.08	1.00
60	1.12	1.10	1.06	1.07	1.00	1.00
660 ℃ Pouring Temperature						
20	1.10	1.40	1.08	1.39	1.10	1.43
40	1.06	1.41	1.11	1.44	1.08	1.44
60	1.06	1.46	1.00	1.45	1.18	1.41
640 ℃ Pouring Temperature						
20	1.05	1.36	1.08	1.39	1.12	1.54
40	1.09	1.44	1.09	1.41	1.08	1.50
60	1.12	1.42	1.11	1.41	1.10	1.45

Table 4.5.16: Effect of inclination angle on grain size (μm) for sand and metallic mould cast samples with different pouring temperatures for different contact times.

0.04 s Contact Time						
Inclination Angle (°)	680 ℃ Pouring Temperature		660 ℃ Pouring Temperature		640 ℃ Pouring Temperature	
	Sand Mould	Metallic Mould	Sand Mould	Metallic Mould	Sand Mould	Metallic Mould
20	151	114	152	83	165	121
40	208	211	86	104	96	122
60	213	85	89	99	98	144
0.09 s Contact Time						
20	122	87	147	122	120	134
40	121	89	115	119	107	124
60	100	80	91	102	95	179
0.13 s Contact Time						
20	179	85	189	119	141	189
40	151	101	97	122	124	124
60	117	92	179	124	95	134

Table 4.5.17: Effect of inclination angle on grain circularity for sand and metallic mould cast samples with different pouring temperatures for different contact times.

0.04 s Contact Time						
Inclination Angle (°)	680 ℃ Pouring Temperature		660 ℃ Pouring Temperature		640 ℃ Pouring Temperature	
	Sand Mould	Metallic Mould	Sand Mould	Metallic Mould	Sand Mould	Metallic Mould
20	0.65	0.37	0.67	0.74	0.68	0.65
40	0.54	0.24	0.84	0.71	0.78	0.58
60	0.51	0.27	0.80	0.70	0.81	0.57
0.09 s Contact Time						
20	0.71	0.44	0.60	0.65	0.69	0.60
40	0.65	0.32	0.71	0.69	0.67	0.61
60	0.78	0.51	0.74	0.69	0.75	0.49
0.13 s Contact Time						
20	0.58	0.29	0.53	0.67	0.62	0.46
40	0.62	0.34	0.76	0.62	0.65	0.55
60	0.72	0.29	0.57	0.66	0.73	0.55

Table 4.5.18: Effect of inclination angle on grain elongation for sand and metallic mould cast samples with different pouring temperatures for different contact times.

0.04 s Contact Time						
Inclination Angle (°)	680 ℃ Pouring Temperature		660 ℃ Pouring Temperature		640 ℃ Pouring Temperature	
	Sand Mould	Metallic Mould	Sand Mould	Metallic Mould	Sand Mould	Metallic Mould
20	1.08	1.06	1.10	1.40	1.05	1.36
40	1.10	1.11	1.06	1.41	1.09	1.44
60	1.12	1.10	1.06	1.46	1.12	1.42
0.09 s Contact Time						
20	1.08	1.06	1.08	1.39	1.08	1.39
40	1.10	1.08	1.11	1.44	1.09	1.41
60	1.06	1.07	1.00	1.45	1.11	1.41
0.13 s Contact Time						
20	1.09	1.08	1.10	1.43	1.12	1.54
40	1.08	1.00	1.08	1.44	1.08	1.50
60	1.00	1.00	1.18	1.41	1.10	1.45

4.6 EFFECT OF COATING MATERIAL

To observe the effect of coating, the graphite and boron nitride (BN) coatings were applied to the cooling slope. The coatings were also applied partially i.e. the melt was poured onto an uncoated part of the cooling slope and flowed over the coated part of the cooling slope. In all cases the metallic mould was used.

4.6.1 Full Coating

The melt was poured on to the water cooled cooling slope for a contact time of 0.107 s at pouring temperatures of 660 °C and 640 °C for inclination angles of 40° and 60°. The resultant melt was subsequently quenched in a water cooled metallic mould.

Grain Size

Pouring Temperature of 660 °C

At a pouring temperature of 660 °C and a contact time of 0.107 s the grain size decreased from 242 μm to 179 μm for the graphite coating and from 206 μm to 158 μm for the BN coating with a decrease in inclination angle from 60° to 40° (see Table 4.6.1). The grain size for the BN coating was finer than that of the graphite for all inclination angles.

Pouring Temperature of 640 °C

At a pouring temperature of 640 °C and a contact time of 0.107 s the grain size decreased from 176 μm to 174 μm for the graphite coating and from 195 μm to 116 μm for the BN coating with a decrease in inclination angle from 60° to 40° (see Table 4.6.1). The grain size for the BN coating was finer than that of the graphite at an inclination angle of 40°.

Grain Circularity

Pouring Temperature of 660 °C

At a pouring temperature of 660 °C and a contact time of 0.107 s the grain circularity decreased from 0.51 to 0.49 for the graphite coating and from 0.53 to 0.51 for the BN coating with a decrease in inclination angle from 60° to 40° (see Table 4.6.1). The grain circularity for the BN coating was higher than that of the graphite for each inclination.

Pouring Temperature of 640 °C

At a pouring temperature of 660 °C and a contact time of 0.107 s the grain circularity decreased from 0.55 to 0.52 for the graphite coating but increased from 0.50 to 0.68 for the BN coating with a decrease in inclination angle from 60° to 40° (see Table 4.6.1). The grain circularity for the BN coating was higher than that of the graphite at an inclination angle of 40°.

Grain Elongation

Pouring Temperature of 660 °C

At a pouring temperature of 660 °C and a contact time of 0.107 s the grain elongation increased from 1.33 to 1.45 for the graphite coating and from 1.32 to 1.48 for the BN coating with a decrease in inclination angle from 60° to 40° (see Table 4.6.1). The grain elongation for the BN coating was lower than that of the graphite at an inclination angle of 60°.

Pouring Temperature of 640 °C

At a pouring temperature of 660 °C and a contact time of 0.107 s the grain elongation decreased from 1.50 to 1.48 for the graphite coating and from 1.48 to 1.46 for the BN coating with a decrease in inclination angle from 60° to 40° (see Table 4.6.1). The grain elongation for the BN coating was lower than that of the graphite at each inclination angle.

4.6.2 Partial Coating

The melt was poured on to the water cooled cooling slope for a contact time of 0.107 s at a pouring temperature of 640 °C with a graphite or BN coated slope having a 1:3 ratio (1 part uncoated and 3 parts coated). The melt was subsequently quenched in a a water cooled metallic mould.

Grain Size

At a pouring temperature of 640 °C and a contact time of 0.107 s, the grain size increased from 158 μm to 183 μm for the partial graphite coating and from 175 μm to 181 μm for the partial BN coating with a decrease in inclination angle from 60° to 40° (see Table 4.6.2). The grain size for the BN partial coating was finer than that of the graphite at an inclination angle of 40°.

Grain Circularity

At a pouring temperature of 640 °C and a contact time of 0.107 s, the grain circularity decreased from 0.56 to 0.55 for the partial graphite coating and from 0.59 to 0.56 for the partial BN coating with a decrease in inclination angle from 60° to 40° (see Table 4.6.2). The grain circularity for the BN coating was higher than that of the graphite at each inclination angle.

Grain Elongation

At a pouring temperature of 660 °C and a contact time of 0.107 s, the grain elongation decreased from 1.44 to 1.37 for the partial graphite coating but increased from 1.36 to 1.39 for the partial BN coating with a decrease in inclination angle from 60° to 40° (see Table 4.6.2). The grain elongation for the BN coating was lower than that of the graphite at an inclination angle of 60°.

4.6.3 Cooling of Slope

The melt at a pouring temperature of 640°C was poured on to the cooling slope, partially and fully coated with graphite and BN, inclined at an angle of 60° for a contact time of 0.107 s. The resultant melt was allowed to solidify in the metallic mould under non-cooled and water cooled conditions.

Grain Size

At a pouring temperature of 640 °C, for a contact time of 0.107 s and inclination angle of 60°, the grain size decreased from 179 μm to 158 μm for the graphite coating but it increased from 158 μm to 175 μm for the BN coating with a change from full coating to partial coating in the cooled condition, while it increased from 123 μm to 193 μm for the graphite coating but it decreased from 159 μm to 157 μm for the BN coating with a change from full coating to partial coating in the non-cooling condition (see Table 4.6.3). The grain size for the BN coating was finer for the full coating under cooling conditions and for partial coating under non-cooling conditions.

Grain Circularity

At a pouring temperature of 640 °C, for a contact time of 0.107 s and inclination angle of 60°, the grain circularity increased from 0.49 to 0.56 for the graphite coating and from 0.51 to 0.59 for the BN coating with a change from full coating to partial coating in the cooled condition, while it decreased from 0.60 to 0.46 for the graphite coating but it increased from 0.56 to 0.57 for the BN coating with a change from full coating to partial coating in the non-cooling condition (see Table 4.6.3). The grain circularity for the BN coating was higher both for the full and partial coating in the cooling condition and for the partial coating in non-cooling condition.

Grain Elongation

At a pouring temperature of 640 °C, for a contact time of 0.107 s and inclination angle of 60°, the grain elongation decreased from 1.45 to 1.44 for the graphite coating and from 1.48 to 1.36 for the BN coating with a change from the full coating to the partial coating in the cooled condition, while it increased from 1.48 to 1.50 for the graphite

coating but it decreased from 1.44 to 1.35 for the BN coating with a change from full coating to partial coating in the non-cooling condition (see Table 4.6.3). The grain elongation for the BN coating was lower for the partial coating in the cooling condition and for both the full and partial coating in the non-cooling condition.

4.6.4 Summary

The effect of the application of graphite and Boron Nitride (the BN) coatings on the final microstructure obtained using the cooling slope has been investigated and the results are summarised as follows:

1. With a BN coating, a slightly finer grain size than that for graphite coating, was obtained at higher pouring temperatures for all studied inclination angles while at lower pouring temperatures a finer grain size was obtained for lower inclination angle.
2. A similar trend was observed when the cooling slope was partially coated (3/4 of the contact length) with graphite and BN.
3. Under air cooling the fully coated graphite coating resulted in a finer grain size, whilst a BN coating resulted in a finer grain size for the partial coating of the cooling slope.
4. A grain size less than 200 μm with lower circularity and with non-equiaxed morphology was obtained using a metallic mould, thus showing the effect of mould material on heat extraction from the melt.
5. The elongation values for the water cooled cooling slope were slightly higher than those for the air cooled.

4.6.5 Tables

Table 4.6.1: Effect of different coatings on the grain characteristics for different pouring temperatures at different inclination angles for a contact time of 0.107s.

Parameters	Angle (°)	660 °C		640 °C	
		Graphite	BN	Graphite	BN
Grain Size (μm)	60	242	206	176	195
	40	179	158	174	116
Circularity	60	0.51	0.53	0.55	0.50
	40	0.49	0.51	0.52	0.68
Elongation	60	1.33	1.32	1.50	1.48
	40	1.45	1.48	1.48	1.46

Table 4.6.2: Effect of partial coating (1:3) of different coatings on grain characteristics for different inclination angles when the melt was poured at 640 °C for a contact time of 0.107 s.

Parameters	Angle (°)	Graphite	BN
Grain Size (μm)	60	158	175
	40	183	181
Circularity	60	0.56	0.59
	40	0.55	0.56
Elongation	60	1.44	1.36
	40	1.37	1.39

Table 4.6.3: Effect of water cooling on grain characteristics when the melt is poured at 640 °C on a fully or partially coated coo ling slope inclined at 60° for a contact time of 0.107 s.

Parameters	Conditions	Cooling		No cooling	
		Graphite	BN	Graphite	BN
Grain Size (μm)	Full coating	179	158	123	159
	Partial coating	158	175	193	157
Circularity	Full coating	0.49	0.51	0.60	0.56
	Partial coating	0.56	0.59	0.46	0.57
Elongation	Full coating	1.45	1.48	1.48	1.44
	Partial coating	1.44	1.36	1.50	1.35

4.7. COMPARISON OF ALLOYS

In this section the NGM AlSi7Mg and COM AlSi7Mg alloys are compared with respect to graphite and BN coatings, full or partial coatings, and also the effect of water cooling on their microstructures. The NGM AlSi7Mg, COM AlSi7Mg and as-cast alloys are also compared to their as-received state and the semi-solid processed MHD A356 alloy.

4.7.1 Comparison of the NGM AlSi7Mg and the COM AlSi7Mg Alloys

In this section the NGM AlSi7Mg and COM AlSi7Mg alloys are compared with respect to their grain characteristics for the effect of full graphite and BN coating, partial coating, and inclination angle of the cooling of slope.

4.7.1.1 Effect of Inclination Angle and Coatings

Grain Size

At a pouring temperature of 640 °C, inclination angle of 60° and contact time of 0.107 s, the grain size decreased from 179 μm to 158 μm for the NGM AlSi7Mg alloy and from 199 μm to 144 μm for the COM AlSi7Mg alloy with a change in coating from graphite to BN (see Table 4.7.1). The grain size for the NGM AlSi7Mg was finer for the graphite coating.

At a pouring temperature of 640 °C, inclination angle of 40° and contact time of 0.13 s, the grain size decreased from 184 μm to 165 μm for the NGM AlSi7Mg alloy and from 200 μm to 154 μm for the COM AlSi7Mg alloy with a change in coating from graphite to BN (see Table 4.7.1). The grain size for the NGM AlSi7Mg was finer for the graphite coating.

Grain Circularity

At a pouring temperature of 640 °C, inclination angle of 60° and contact time of 0.107 s, the grain circularity increased from 0.49 to 0.51 for the NGM AlSi7Mg alloy and from 0.46 to 0.54 for the COM AlSi7Mg alloy with a change in coating from graphite to BN (see Table 4.7.1). The grain circularity for the NGM AlSi7Mg was higher for the graphite coating.

At a pouring temperature of 640 °C, inclination angle of 60° and contact time of 0.107 s, the grain circularity increased from 0.50 to 0.59 for the NGM AlSi7Mg alloy and from 0.48 to 0.57 for the COM AlSi7Mg alloy with a change in coating from graphite to BN (see Table 4.7.1). The grain circularity for the NGM AlSi7Mg was higher for both the graphite and BN coatings.

Grain Elongation

At a pouring temperature of 640 °C, inclination angle of 60° and contact time of 0.107 s, the grain circularity increased from 1.45 to 1.48 for the NGM AlSi7Mg alloy and from 1.40 to 1.45 for the COM AlSi7Mg alloy with a change in coating from graphite to BN (see Table 4.7.1). The grain elongation for the NGM AlSi7Mg was higher for both the graphite and BN coatings.

At a pouring temperature of 640 °C, inclination angle of 60° and contact time of 0.107 s, the grain circularity increased from 1.40 to 1.44 for the NGM AlSi7Mg alloy and from 1.50 to 1.51 for the COM AlSi7Mg alloy with a change in coating from graphite to BN (see Table 4.7.1). The grain elongation for the NGM AlSi7Mg was lower for both the graphite and BN coatings.

4.7.1.2 Cooling of Slope and Coating

Grain Size

At a pouring temperature of 640 °C, inclination angle of 60° and contact time of 0.107 s, the grain size decreased from 179 µm to 123 µm for the NGM AlSi7Mg alloy

and from 199 μm to 169 μm for the COM AlSi7Mg alloy with a change from a cooling to non-cooling graphite coated slope (see Table 4.7.2). The grain size for the NGM AlSi7Mg was finer for both the cooling and non-cooling conditions.

At a pouring temperature of 640 °C, inclination angle of 60° and contact time of 0.107 s, the grain size increased from 158 μm to 159 μm for the NGM AlSi7Mg alloy and from 144 μm to 169 μm for the COM AlSi7Mg alloy with a change from a cooling to non-cooling BN coated slope (see Table 4.7.2). The grain size for the NGM AlSi7Mg was finer for the non-cooling condition.

Grain Circularity

At a pouring temperature of 640 °C, inclination angle of 60° and contact time of 0.107 s, the grain circularity increased from 0.49 to 0.60 for the NGM AlSi7Mg alloy and from 0.46 to 0.52 for the COM AlSi7Mg alloy with a change from a cooling to non-cooling graphite coated slope (see Table 4.7.2). The grain circularity for the NGM AlSi7Mg was higher for both the cooling and non-cooling conditions.

At a pouring temperature of 640 °C, inclination angle of 60° and contact time of 0.107 s, the grain circularity increased from 0.51 to 0.56 for the NGM AlSi7Mg alloy and from 0.54 to 0.59 for the COM AlSi7Mg alloy with a change from a cooling to non-cooling BN coated slope (see Table 4.7.2). The grain circularity for the NGM AlSi7Mg was lower for both the cooling and non-cooling conditions.

Grain Elongation

At a pouring temperature of 640 °C, inclination angle of 60° and contact time of 0.107 s, the grain elongation increased from 1.45 μm to 1.48 μm for the NGM AlSi7Mg alloy and from 1.44 μm to 1.43 μm for the COM AlSi7Mg alloy with a change from a cooling to non-cooling graphite coated slope (see Table 4.7.2). The grain elongation for the NGM AlSi7Mg was higher for both the cooling and non-cooling conditions.

At a pouring temperature of 640 °C, inclination angle of 60° and contact time of 0.107 s, the grain elongation decreased from 1.48 μm to 1.44 μm for the NGM AlSi7Mg alloy but remained approximately the same at 1.45 μm for the

COM AlSi7Mg alloy with a change from a cooling to non-cooling BN coated slope (see Table 4.7.2). The grain elongation for the NGM AlSi7Mg was lower for both the cooling and non-cooling conditions.

4.7.1.3 Effect of Partial Coating

Grain Size

At a pouring temperature of 640 °C, inclination angle of 60° and contact time of 0.107 s, the grain size increased from 154 μm to 190 μm for the NGM AlSi7Mg alloy and from 166 μm to 193 μm for the COM AlSi7Mg alloy with a change from a cooling to non-cooling partially coated BN slope (see Table 4.7.3). The grain size for the NGM AlSi7Mg was finer for both the cooling and non-cooling conditions.

Grain Circularity

At a pouring temperature of 640 °C, inclination angle of 60° and contact time of 0.107 s, the grain circularity decreased from 0.55 to 0.42 for the NGM AlSi7Mg alloy and from 0.50 to 0.45 for the COM AlSi7Mg alloy with a change from a cooling to non-cooling partially coated BN slope (see Table 4.7.3). The grain circularity for the NGM AlSi7Mg was higher for the cooling condition.

Grain Elongation

At a pouring temperature of 640 °C, inclination angle of 60° and contact time of 0.107 s, the grain elongation increased from 1.38 μm to 1.41 μm for the NGM AlSi7Mg alloy and from 1.53 μm to 1.47 μm for the COM AlSi7Mg alloy with a change from a cooling to non-cooling partially coated BN slope (see Table 4.7.3). The grain elongation for the NGM AlSi7Mg was lower for both the cooling and non-cooling conditions.

4.7.2 Comparison of the NGM AlSi7Mg, COM AlSi7Mg and MHD A356 Alloys

Grain Size

The grain size decreased from 184 μm to 165 μm for the NGM AlSi7Mg alloy processed at a pouring temperature of 640 °C, inclination angle of 40° and contact time of 0.13 s, with a change of coating from graphite to BN. These values were much finer than the 520 μm the value obtained for as-received sample (see Table 4.7.4). The grain size decreased from 199 μm to 165 μm for the COM AlSi7Mg alloy processed at a pouring temperature of 640 °C, inclination angle of 40° and contact time of 0.13 s, with a change of coating from graphite to BN. These values were finer than 273 μm, the value obtained for as-received sample. The grain size increased from 166 μm to 183 μm for the MHD A356 alloy processed at a pouring temperature of 640 °C, inclination angle of 40° and contact time of 0.13 s with a change of coating from graphite to BN. These values were similar to 187 μm, the value obtained for as-received sample. The grain size for the NGM AlSi7Mg was coarser than the MHD A356 alloy for the graphite coating and similar to the COM AlSi7Mg alloy for BN coating. It was coarsest in the as-received condition for NGM AlSi7Mg alloy.

Grain Circularity

The grain circularity increased from 0.50 to 0.59 for the NGM AlSi7Mg alloy processed at a pouring temperature of 640 °C, inclination angle of 40° and contact time of 0.13 s, with a change of coating from graphite to BN and these values were much higher than 0.26 the value obtained for the as-received sample (see Table 4.7.4). The grain circularity increased from 0.48 to 0.57 for the COM AlSi7Mg alloy processed at a pouring temperature of 640 °C, inclination angle of 40° and contact time of 0.13 s, with a change of coating from graphite to BN. These values were higher than 0.44, the value obtained for the as-received sample. The grain circularity increased from 0.49 to 0.50 for the MHD A356 alloy processed at a pouring temperature of 640 °C, inclination angle of 40° and contact time of 0.13 s with a change of coating from graphite to BN. These values were similar to 0.49, the value obtained for the as-received sample. The grain circularity for the NGM AlSi7Mg was

the highest for the sample obtained for the graphite and BN coatings but the lowest for the as-received condition.

Grain Elongation

The grain elongation increased from 1.40 μm to 1.44 μm for the NGM AlSi7Mg alloy processed at a pouring temperature of 640 °C, inclination angle of 40° and contact time of 0.13 s, with a change of coating from graphite to BN and these values were much lower than 3.13 the value obtained for the as-received sample (see Table 4.7.4). The grain elongation increased from 1.50 μm to 1.51 μm for the COM AlSi7Mg alloy processed at a pouring temperature of 640 °C, inclination angle of 40° and contact time of 0.13 s, with a change of coating from graphite to BN and these values were higher than 1.49 , the value obtained for the as-received sample. The grain elongation increased from 1.44 to 1.46 for the MHD A356 alloy processed at a pouring temperature of 640 °C, inclination angle of 40° and contact time of 0.13 s with a change of coating from graphite to BN. These values were similar to 1.53, the value obtained for the as-received sample. The grain elongation for the NGM AlSi7Mg was the lowest for the graphite and BN coating, but the highest for the as-received condition.

4.7.3 Summary

A comparison of the NGM AlSi7Mg and COM AlSi7Mg alloys was made with respect to the effect of coating and cooling and a summary of the results is given below:

1. A graphite coating produced a finer grain size for the NGM AlSi7Mg alloy and a BN coating produced a finer grain size for the COM AlSi7Mg alloy, due to their different liquidus temperatures.
2. For both the NGM AlSi7Mg and COM AlSi7Mg alloys, the grain circularity and elongation for the BN coating was higher showing a round but less equiaxed grain morphology.

3. Air cooling resulted in a finer grain size when using a graphite coating and coarser grain size when using a BN coating for the NGM AlSi7Mg alloy. However, the microstructure showed a high circularity although it was more dendritic in nature.
4. In the case of the partial coating, the grain size was higher for air than water cooling with the grains exhibiting a relatively lower circularity but similar dendritic nature (~ 1.4 elongation value).
5. The graphite coating produced a finer structure in the MHD A356 alloy compared to the BN coating.
6. The grain size obtained for the NGM AlSi7Mg, COM AlSi7Mg and MHD A356 alloys obtained using the cooling slope technique and a metal mould was similar to that obtained for magneto-hydrodynamic stirring, observed in as-received grain refined, modified MHD A356 alloy. The grain size obtained using cooling slope was finer than as-received grain refined electromagnetically stirred COM AlSi7Mg alloy and much finer than as-received electromagnetically stirred non-modified non-grain refined NGM AlSi7Mg alloy.

4.7.4. Tables

Table 4.7.1: Comparison of grain characteristics observed for different coatings on the cooling slope at different inclination angles for the NGM AlSi7Mg and COM AlSi7Mg alloys poured at a 640 ℃.

Characteristics	Conditions	60° Inclination, 0.107 s Contact Time		40° Inclination, 0.13 s Contact Time	
		NGM AlSi7Mg	COM AlSi7Mg	NGM AlSi7Mg	COM AlSi7Mg
Grain Size (μm)	graphite coating	179	199	184	200
	BN coating	158	144	165	154
Circularity	graphite coating	0.49	0.46	0.50	0.48
	BN coating	0.51	0.55	0.59	0.57
Elongation	graphite coating	1.45	1.44	1.40	1.50
	BN coating	1.48	1.45	1.44	1.51

Table 4.7.2: Comparison of the effect of cooling for different coatings on grain characteristics for the NGM AlSi7Mg and COM AlSi7Mg alloys poured at 640 ℃ on a cooling slope inclined at 60° for a contact time of 0.107 s.

Characteristics	Condition	graphite		BN	
		NGM AlSi7Mg	COM AlSi7Mg	NGM AlSi7Mg	COM AlSi7Mg
Grain Size (μm)	Cooling	179	199	158	144
	No cooling	123	169	159	169
Circularity	Cooling	0.49	0.46	0.51	0.54
	No cooling	0.60	0.52	0.56	0.59
Elongation	Cooling	1.45	1.44	1.48	1.45
	No cooling	1.48	1.43	1.44	1.45

Table 4.7.3: Comparison of the effect of cooling for partial coating for the NGM AlSi7Mg and COM AlSi7Mg alloys for a pouring temperature of 640 ℃ and inclination angle of 60° for a contact time of 0.107 s on a BN coated cooling slope.

Characteristics	Conditions	NGM AlSi7Mg	COM AlSi7Mg
Grain Size (μm)	Cooling	154	166
	No cooling	190	193
Circularity	Cooling	0.55	0.50
	No cooling	0.42	0.45
Elongation	Cooling	1.38	1.53
	No cooling	1.41	1.47

Table 4.7.4: Comparison of grain characteristics for the NGM AlSi7Mg, COM AlSi7Mg and MHD A356 alloys for the as-received condition and obtained by pouring at 640 ℃ at an inclination angle of 40° for a contact time of 0.13 s on to a cooling slope treated with different coatings.

Characteristics	Coatings	NGM AlSi7Mg	COM AlSi7Mg	SAG A356
Grain Size (μm)	graphite coating	184	200	166
	BN coating	165	165	183
	As received	521	273	187
Circularity	graphite coating	0.50	0.48	0.49
	BN coating	0.59	0.57	0.50
	As received	0.26	0.44	0.49
Elongation	graphite coating	1.40	1.50	1.44
	BN coating	1.44	1.51	1.46
	As received	3.13	1.49	1.53

Chapter 5

Discussion

The results presented in Chapter 4 are discussed and analysed herein with respect to the effect of variation in the alloys, the new contact time parameter, the grain characteristics and cooling slope solidification mechanism.

5.1 VARIATION IN THE ALLOYS

In this section the comparison and relative variation in non-grain refined non-modified AlSi7Mg (NGM AlSi7Mg), commercial grain refined AlSi7Mg (COM AlSi7Mg) and magnetohydrodynamic stirred grain refined modified A356 (MHD A356) alloys in the as-received state, have been discussed with respect to their solidification behaviour, solidification sequence, relative fraction solid range and their response to semi-solid processing. Although all three alloys are generically identical, it is still nevertheless important to acquire a detailed knowledge of the basic characteristics of each to enable improved semi-solid process control.

5.1.1 Characteristic Temperatures

The chemical composition of the three as-received alloys processed i.e. the NGM AlSi7Mg, COM AlSi7Mg and MHD A356 alloys (given in Table 4.1.1), lie within official limits for an A356 and are particularly close to that of an A356.2 alloy (as shown in Table 5.1). However, the Fe, Mn, Zn and Ti content in all three alloys was lower than that suggested for the standard A356.2. The Si content of the NGM AlSi7Mg and COM AlSi7Mg alloys are quite similar, however, the Mg content varies significantly. The MHD A356 alloy revealed similar Mg contents to that of the

COM AlSi7Mg alloy but showed a significantly higher Si content than both the NGM AlSi7Mg and COM AlSi7Mg alloys. As chemical composition can play an important role in determining the characteristics of the alloys, particularly melting point, intermetallic phase formation, the solidification sequence of these phases and the fraction solid over the solidification range, the effect of variations in composition are examined and are subsequently discussed in further detail.

The nucleation temperature, T_N, calculated using the first derivative, *dT/dt*, from the cooling curve data with the help of Origin 7G software was found to be 616.0 °C, 616.7 °C and 612.1 °C for the NGM AlSi7M, COM AlSi7Mg and MHD A356 alloys respectively. The nucleation temperature of the COM AlSi7Mg alloy was marginally higher, in spite of having higher Si and Mg contents which should reduce the solidification temperature. The MHD A356 alloy having both high Si and Mg contents showed this expected lower nucleation temperature. An increase of 0.40 wt% in Si content should decrease the liquidus temperature by about 2.8 °C[227] (see Fig. 5.1(a)) and an increase in Mg content to 0.4 wt% should reduce the liquidus temperature by 1.8 °C[228] (see Fig. 5.1(b)), provided the liquidus line in the phase diagram is assumed to be linear. The unusual behaviour of the COM AlSi7Mg alloy could be due to heterogeneous nucleation on grain refining particles[65] added during the initial processing as shown in Fig. 5.1(c) which shows the total elimination of recalescence on complete refinement[65].

The growth temperature, T_{growth}, where a sustainable growth starts, was found to be 615.5 °C, 616.2 °C and 611.3 °C for the NGM AlSi7Mg, COM AlSi7Mg and MHD A356 alloys respectively, displaying a similar trend to that of the nucleation temperature.

The effect of heterogeneous nucleation on the growth can be determined by studying the degree of undercooling for the nucleation, $\Delta\Phi$ (Fig. 5.1(c))[65]. The undercooling for the nucleation observed was 2.5 °C, 1.3 °C and 2.9 °C for the NGM AlSi7Mg, COM AlSi7Mg and MHD A356 alloys, respectively. A comparison of these undercoolings for the NGM AlSi7Mg and the COM AlSi7Mg alloys clearly reveals the smallest value for the COM AlSi7Mg alloy which confirms the use of heterogeneous grain refiner additions during initial processing and the presence of Ti in the chemical composition is further proof.

The melting temperatures, calculated using DSC heat flow traces with the help of the first derivative (see Section 4.1.4), on heating were 618.4 °C, 620.6 °C and 619.8 °C for the NGM AlSi7Mg, COM AlSi7Mg and MHD A356 alloys, respectively.

Thermo-Calc® simulation was also employed to predict the solidification behaviour. According to Thermo-Calc® simulations the primary Al phase may form at 616.0 °C, 615.5 °C and 614.0 °C for the NGM AlSi7Mg, COM AlSi7Mg and MHD A356 alloys respectively.

In addition to the above techniques empirical formulae based on the chemical composition in wt% were also used. The empirical formula proposed by Drossel[230] is given as:

$$T_{Liq}(°C) = 661 - 4.97Si - 0.15(Si)^2 - 6.13Cu - 17.4Mg + 2.72Zn + 5.08CuMg \qquad \text{Eq. (5.1)}$$

A modified formula presented by Hernandez et al.[229] for hypoeutectic Al-Si alloys, incorporating the "Si equivalent" ($Si_{Eq}^{X_i}$) factor is given as:

$$T_{Liq}^{Al-Si\sum X_i} = 660.452 - 6.110\sum Si_{Eq}^{X_i} - 0.057\sum\left(Si_{Eq}^{X_i}\right)^2 \qquad \text{Eq. (5.2)}$$

and

$$Si_{Eq}^{X_i} = Si\,(wt.\%) - X_i\,(wt.\%) \qquad \text{Eq. (5.3)}$$

The melting temperatures calculated from the DSC data were the highest for all three alloys. However, the difference between the temperatures was most prominent for COM AlSi7Mg and MHD A356 alloys, ~5 to ~10 °C (see Table 5.2). The results indicate the effect of temperature lag in DSC data as well as the influence of the previous thermal histories of these alloys.

The temperature for the dendrite coherency point (*TDCP),* where the dendrite network of the primary phase becomes coherent, was found to be 615.4 °C, 616.2 °C and 611.0 °C for the NGM AlSi7Mg, COM AlSi7Mg and the MHD A356 alloys respectively. This shows that the network of dendrites was formed without any prominent decrease in the growth temperature, however, a delay in the dendrite coherency point (DCP) was observed in the case of MHD A356 alloy when compared to the NGM AlSi7Mg and COM AlSi7Mg alloys. This finding was in accordance

with the literature[112,224,231,232,233,234,235], which states that a reduction in the surface tension due to modifying agents results in an increase in flowability of the melt through the growing dendrites, thus delaying the DCP.

The eutectic temperature and amount of eutectic helps to control a thixoforming process. The processing window is generally slightly higher than the eutectic temperature and the eutectic acts as a lubricant during deformation[23,160]. The eutectic phases are formed when the dendrites of the primary Al phase have grown to the extent that the interdendritic liquid reaches the eutectic composition. For the NGM AlSi7Mg alloy the eutectic nucleated at 577.9 °C, grew at 577.8 °C with a 0.7 °C undercooling for nucleation ($\Delta\Phi$) and the eutectic reaction finished at 536.0 °C. For the COM AlSi7Mg alloy the eutectic nucleated at 564.0 °C, grew at 563.7 °C with an undercooling for nucleation of 2.0 °C. Similarly the eutectic for the MHD A356 alloy nucleated at 566.1 °C, grew at 564.9 °C with an undercooling for nucleation of 0.1 °C and the eutectic reaction finished at 552.35 °C.

The decrease in eutectic growth temperatures both for the COM AlSi7Mg and the MHD A356 alloy may be due to the higher content of Mg, as Mg decreases the start of the Al-Si binary eutectic formation by ~5°C for an increase of 0.3 wt% Mg (see Fig. 5.1(b))[227]. For an Al-Si-Mg system (see Fig. 5.2(a)), the temperature of the eutectic channel between the binary and ternary eutectic decreases by ~23 °C over 5 wt% Mg, according to which a decrease of ~1.84 °C per 0.4 wt% increase in Mg content, is expected in the eutectic growth temperature for the COM AlSi7Mg and MHD A356 alloys[227] provided the liquidus line is assumed to be linear. For an Al-7Si-0.13Fe system a decrease in the binary eutectic temperature for an non-modified alloy of 8 °C[237] to 16 °C[238,239] per 1 wt% increase in Mg, in the range concerned (0 to 0.7 wt%) has been reported[227]. Another reason for this drop in eutectic temperature is the modification of the Si phase in the eutectic as a result of the increase in Mg content in addition to the normal modification agents (see Fig. 5.2(b))[238]. The modification restricts the faceted growth of Si by poisoning the growth faces, which results in a higher undercooling being required to nucleate the Si phase. As a consequence the eutectic temperature is depressed (see Fig. 5.2(b)), and for which a maximum decrease of ~9 °C has been reported[65,186,240,241] (see Fig. 5.2(c)). A higher value of undercooling for the nucleation of the COM AlSi7Mg alloy relative to the NGM AlSi7Mg alloy (2.0 °C as compared to

0.7 °C) is also in accordance with the effect of modification[65]. However, the lower undercooling for nucleation in the MHD A356 alloy with respect to the COM AlSi7Mg alloy (0.1 °C as compared to 2.0 °C) needs to be explained. Normally the greater the modification, the higher the undercooling due to the growth restriction factor[242]. However, the effect of modification on the eutectic temperature can be clearly described in terms of undercooling for growth (*ΔT)* and undercooling for nucleation (*ΔΦ)*, where *ΔT* is the change in eutectic growth temperature and *ΔΦ* is the resulting undercooling for nucleation (Fig. 5.2(b), 5.2(c) and 5.2(d))[65]. According to Bäckerud et al.[186] when the optimum modification is achieved in an alloy either the recalescence or the undercooling is completely or partially removed from the cooling curve. Nafisi et al.[112] have reported that undercooling for nucleation decreases from the modified cooling curve with an increase in Sr content in the melt (see Fig. 5.2(d)), as this increases the availability of nucleation sites on which Si can nucleate and grow. The modifying agents also reduce the surface tension of the melt[112,231,232,233,234,235], enabling the melt to flow through the dendrites and dendrite arms[112,224,233] favouring the ripening of the dendrite arms and establishing a homogenous temperature distribution throughout the melt, which results in lower eutectic temperature[112].

The eutectic temperatures obtained from the DSC data for the NGM AlSi7Mg, COM AlSi7Mg and the MHD A356 alloys were 574.0 °C, 567.1 °C and 567.6 °C, respectively, which were higher than the cooling curve in spite of temperature lag (see Table 5.3). This could be the result of premature fading of the *Sr* due to the very thin specimens which are necessary for DSC analysis[227].

Thermo-Calc® simulation resulted in relatively higher eutectic temperatures for the COM AlSi7Mg and MHD A356 alloys. The Al-Si binary eutectic may form at 575.8 °C, 573.8 °C and 574.8 °C for the NGM AlSi7Mg, COM AlSi7Mg and MHD A356 alloys respectively. A comparison of the eutectic temperatures calculated from different techniques is given in Table 5.3.

5.1.2 Intermetallic Phases

A co-eutectic phase was observed in the temperature range of 553.6 to 536.2 °C for the COM AlSi7Mg alloy and from 552.4 to 540.0 °C for the MHD A356 alloy in the cooling curve (Fig. 4.1.1(d)). This may be due to the formation of a ternary and/or quaternary eutectic phase such as Mg_2Si and/or Fe-bearing intermetallics[227]. According to Bäckerud et al.[186], this corresponds to the formation of the Mg_2Si phase.

However, in DSC results during heating, peak 3, (see Fig. 4.1.4(b)) representing the co-eutectic transformation was only visible for the COM AlSi7Mg alloy within the temperature range of 559.4 to 563.3 °C, while on cooling the peak was visible for the COM AlSi7Mg and MHD A356 alloys in the range of 541.2 to 552.0 °C and from 540.9 to 552.8 °C respectively, which was similar to the range observed in the cooling curves for these two alloys.

Another peak (peak 4) was also observed in the heating and cooling DSC thermograms, which overlapped with the eutectic peak on the DSC traces, which was found. However, this peak was more prominent on cooling. During cooling the transformation was found to be in the temperature range of 564.0 to 565.6 °C, 556.0 to 560.0 °C and 558.2 to 559.9 °C for the NGM AlSi7Mg, COM AlSi7Mg and MHD A356 alloys, respectively.

Thermo-Calc® simulation shows that a ternary eutectic containing a β-*AlFeSi* phase may form at 571.3, 567.5 and 568.6 °C for the NGM AlSi7Mg, COM AlSi7Mg and MHD A356 alloys, respectively. Another ternary eutectic containing a π-*AlFeMgSi* phase may form at 560.5, 561.2 and 561 °C for the NGM AlSi7Mg, COM AlSi7Mg and MHD A356 alloys respectively. A quaternary eutectic containing π-*AlFeMgSi* and Mg_2Si phases may also form at 556.2, 556.8 and 557 °C for the NGM AlSi7Mg, COM AlSi7Mg and the MHD A356 alloys respectively.

According to the expected intermetallic phases predicted in Thermo-Calc® simulations (see Fig. 4.1.6) the β-*AlFeSi* phase may be found in addition to the Al primary phase and the Al-Si eutectic phase in all three alloys, whilst the

π-AlMgFeSi and Mg_2Si phases may be additionally found in the COM AlSi7Mg and MHD A356 alloys.

The SEM results supported these results. The SEM results from the as-received NGM AlSi7Mg alloy (Fig. 4.1.13, 4.1.14) showed the presence of a *π-AlMgFeSi* phase. The as-cast NGM AlSi7Mg samples (Fig. 4.1.22, 4.1.24) showed the presence of the plate-like structure of the Fe based *β-AlFeSi* phase.

Similarly the SEM results for the as-received COM AlSi7Mg alloy showed the presence of a *π-AlMgFeSi* phase (see Fig. 4.1.15), whilst in the as-cast samples a *β-AlFeSi* phase (Fig. 4.1.26) and a *π-AlMgFeSi* phase (Fig. 4.1.25. 4.1.27) were observed.

However, the SEM observations for the as-received MHD A356 alloy showed no traces of *β-AlFeSi* and *π-AlMgFeSi* phases. The SEM micrographs for the as-cast MHD A356 alloy samples showed the presence of the plate-like *β-AlFeSi* phase (Fig. 4.1.28) and *π-AlMgFeSi* phase (Fig. 4.1.30) as well as an Mg_2Si phase (Fig. 4.1.29). The intermetallic phases formed in the different alloys in this study are tabulated in Table 5.4.

The presence of Ti containing particles in the as-received COM AlSi7Mg alloy (Figs. 4.1.16, 4.1.17) indicated grain refiner particles were added to the alloy. Similarly the presence of Sr particles in the as-received MHD A356 alloy samples (see Figs. 4.1.31, 4.1.34) indicated modification, whilst the excess amount of *Sr* in the melt, resulted in the reduction/absence of recalescence during the eutectic reaction.

To determine the solidification reaction corresponding to peak 4 in the DSC trace, SEM results were used. The SEM EDX results confirmed the presence of a *π-AlMgFeSi* phase in all the as-received and as-cast alloys, which may correspond to peak 4 in the DSC traces. Peak 4 was observed for each alloy on heating and cooling in the DSC traces. However, the Mg_2Si phase was not observed in the as-received or the as-cast COM AlSi7Mg samples, but observed only in the as-cast MHD A356 alloy sample. The reason for its absence in the as-received sample may be due to the processing of the alloy i.e. the intensive stirring which results in homogeneous

distribution of solute atoms into the bulk melt resulting in a very small or even absence of intermetallic phases.

5.1.3 Solidification Behaviour

Simulation with Thermo-Calc® suggests a sequence of solidification reactions, for all the three alloys as given in Table 5.5.

Bäckerud et al.[186] has also studied the expected phases, their temperature and their sequence during solidification. To determine the sequence of phase transformations due to solute enrichment, Bäckerud et al.[186] used the Scheil equation and segregation lines obtained from the distribution coefficient of the elements, particularly Fe and Si, to determine the sequence of phase formation. They used an Al-Fe-Si system with constant element level (Mn for an A356.2 alloy system) (see Fig. 5.3) and predicted the sequence of phases for an A356.2 alloy as is given in Table 5.6.

In DSC traces for the alloys under consideration it was noted that peak 4 was observed during heating for all alloys, but peak 3 was only observed in those of the COM AlSi7Mg alloy. This suggests that peak 4 corresponds to the co-eutectic phase which was present in the as-cast samples of all the alloys whilst the SEM EDX analyses of the as-received samples, of all three alloys, show the presence of a *π-AlMgFeSi* phase, thereby implying that peak 4 corresponds to the *π-AlMgFeSi* phase. This could suggest that the transformation, reaction 5 in Table 5.6, is responsible for peak 3 and reaction 3b for peak 4 in the DSC traces (see Fig. 4.1.4). However, on cooling, a *β-AlFeSi* phase was observed in each sample for all the alloys, which suggests that reaction 3a occurred for all the alloys during cooling. The *π-AlMgFeSi* was found in the SEM investigations of the COM AlSi7Mg and the MHD A356 alloys, but not in the NGM AlSi7Mg alloy due to the lower Mg content. The characteristic temperature with no clear evidence of an Mg_2Si phase suggests that reaction 5 was the last reaction to occur before complete solidification. This sequence of reactions is listed in Table 5.6. It is the same sequence predicted by the simulation made by Thermo-Calc® software as given in Table 5.5. Wang et al.[227] and Taylor et al.[242] mentioned that the *π-AlMgFeSi* phase was found independent of Mg

levels and grew in close association with the β-AlFeSi phase. Also the volume fraction of *π-AlMgFeSi* phase does not change much with a change in Mg content, whilst the Mg_2Si phase increases with an increase in Mg level[227,242].

5.1.4 Fraction Solid and Fraction Solid Sensitivity

Semi-solid processing makes use of a suitable fraction solid range to control the processing parameters and end product properties. Fraction solid varies from 0 to 1 in the solidification range of an alloy. The effect of fraction solid on the processing conditions is shown schematically in Fig. 5.4, which shows the forces required to process the material may vary with fraction solid from pressure die casting to forging. The f_s-T graph is usually used to observe the behaviour of a change in fraction solid. Different criteria to select a suitable fraction solid range and corresponding temperature for semi-solid processing has been suggested as discussed in Section 2.5. However, a fraction solid sensitivity with respect to temperature is the most suggested criterion, however, different upper limits of this sensitivity have been suggested[17,23,166,170] as mentioned in Section 2.5. In this study upper limits for the fraction solid sensitivity value of 0.015[166] and 0.03[23] have been used to compare the three alloys.

The f_s-T graphs show a similar trend for all three alloys, gradually changing from a lower fraction solid towards a high fraction solid until a eutectic temperature is reached. At the eutectic temperature, due to the solidification occurring at a constant temperature, a sharp change in the curve is observed and the fraction solid reaches 1 without any significant variation in corresponding temperature. A fraction solid difference occurred in the heating and cooling data during solidification of the primary phase for a given temperature, while a temperature difference occurred during the eutectic solidification for a given fraction solid. This variation clearly shows the effect of temperature lag in the calculations during heating and cooling.

The fraction solid sensitivity change over the fraction range or over the solidification range clearly shows the effect of characteristic temperatures. The variation of fraction

solid data is quite similar for COM AlSi7Mg and MHD A356 alloys, for both cooling and heating.

The highest fraction solid sensitivity criteria of 0.03 for semi-solid processing gives relatively higher upper limit values of fraction solid compared to that for the 0.015 fraction solid sensitivity criteria, for both heating and cooling data. On the other hand the highest upper limit criteria for the 0.03 fraction solid sensitivity for heating and cooling gives a different processing temperature for the lowest limit in comparison to that of the 0.015 fraction solid sensitivity criteria. This is particularly true of a NGM AlSi7Mg alloy on heating however, temperature values for cooling data are similar for both the 0.03 and 0.015 criteria. In general the highest working fraction solid and the lowest working temperature are higher for the NGM AlSi7Mg alloy, ~5°C greater/less than that for the COM AlSi7Mg and MHD A356 alloys.

The above discussion clearly shows the effect of alloy composition on characteristic temperatures, solidification range and corresponding fraction solid at a given temperature; hence a working range for one particular alloy is not suitable for another alloy, even if it is similar.

5.1.5 Response to Semi-solid Processing using the Cooling Slope Technique

5.1.5.1 Comparison of NGM AlSi7Mg and COM AlSi7Mg Alloys

The data showed that the grain size for the COM AlSi7Mg was coarser with graphite coating than with BN coating. However, data for the circularity and elongation showed that the grains obtained for the BN coating were less globular and less equiaxed in nature compared to those with the graphite coating. The non-equiaxed nature increased with a decrease in inclination angle. This phenomenon may be explained by the number of nuclei in the melt which was lower for the graphite coating as a result of the formation of a solid layer on the cooling slope. This resulted in a smaller shear force to shear the nuclei from the surface of the cooling slope due to the lower inclination angle combined with less temperature in the melt needed to start

the nucleation multiplication by root melting and fragmentation. The melt poured into the metallic mould from the cooling slope was marginally cooler for the graphite than for the BN coating and a solid skin formed on the mould wall, which reduced the thermal conductivity. At the same time the imposed higher thermal gradient due to the metallic mould favoured the growth of a non-equiaxed morphology. There may be an additional effect from the different chemical composition of the alloys, which could result in different superheats and undercoolings for the melt poured at the same temperature, due to the difference in liquidus temperature. A similar grain size both for the non-grain refined and non-modified NGM AlSi7Mg and grain refined COM AlSi7Mg alloy was observed under similar processing conditions due to the different nucleation mechanisms as discussed in Section 2.2.2 thereby, supporting the earlier findings[83,89].

5.1.5.2 Comparison of the NGM AlSi7Mg, COM AlSi7Mg and MHD A356 Alloys

The data shows that the grain size for the BN coated cooling slope was finer for the COM AlSi7Mg and NGM AlSi7Mg alloys but coarser for the MHD A356 alloy. However, in each case the grain size of these alloys was finer than that for the as-received, thus showing the effectiveness of the process. Different chemical compositions may also affect the resulting grain size due to the different liquidus temperature and the relative degree of superheat for a melt poured into the mould from the cooling slope. It was observed that under similar conditions the grain size was similar for non-grain refined non-modified NGM AlSi7Mg, grain refined COM AlSi7Mg and semi-solid precursor MHD A356 alloys i.e. an effect of grain refinement was not observed. This is in accordance to the finding of Easton[83], who reported that grain refining was not effective below a superheat of 60 °C and Wang et al.[89] who stated that the wall nucleation was the prominent mechanism in the melt with superheats less than ~65 °C.

5.2 EFFECT OF CONTACT TIME

In all previous studies, as mentioned in Section 2.4 and compared in Table 2.1, a contact length on the cooling slope was used as a processing parameter. In this study a newly devised contact time was used instead to analyze the effect of contact established between the flowing melt and the cooling slope. This adopted parameter has never before been reported or discussed in any semi-solid processing literature.

Significance of Contact Time

The results of this study confirmed our hypothesis that a contact time is a better process controlling parameter. At contact times of 0.09 s and 0.13 s and an inclination angle of 60°, the grain size remained unaffected by a change in pouring temperature from 680 °C to 640°C. Similarly at a contact time of 0.04 s and a pouring temperature of 660°C, the grain size remained unaffected with change in inclination angles from 20° to 60°. However, it should be noted that besides the contact time other factors also contribute to the final microstructure such as inclination angle, pouring temperature, the nature of cooling slope surface etc..

The use of contact time has the following advantages over that of the contact length:

(i) The poured melt flows on the cooling slope with a certain flow velocity. During the flow, heat is extracted from the melt. A contact length does not provide a uniform parameter for the amount of heat extracted if the melt flow velocity has changed on the same inclination angle.

(ii) For the same inclination angle, a change in length does not take into account a change in velocity, which changes with increase in length. However, contact time is independent of change in flow velocity due to gravitational force.

(iii) The contact length at an inclination has no correlation with the contact length at another inclination angle. Similarly the melt flow also changes with change in inclination angle, which also cannot be correlated. However, for a contact time the melt contact with the cooling slope can be correlated and generalized as a similar heat extraction is expected under similar processing conditions.

(iv) On the basis of contact time the nucleation density and heat removal can easily be described and compared to the contact length.

(v) The heat extraction of the melt and the melt contact time combine to obtain the total heat removed from the melt.

(vi) With keeping the contact time constant we can easily investigate the effect of inclination, resulting shear force and degree of undercooling in the melt.

5.3 DETERMINATION OF GRAIN CHARACTERISTICS

Grain Size

Grain size is one of the most basic characteristic in quantifying a microstructure. In this study the samples of all three alloys were anodized using Barker's etch and the microstructure observed under polarized light using a Lambda (λ) filter. Using image analysis software, grains or globules with similar colour intensity were selected manually and the equivalent diameter i.e. the diameter of a circle with the same area as the feature (see Fig. 3.18(a))[115], was used to estimate its size. Mathematically it is given by:

$$Equivalent\ diameter = \left(\frac{4 \times Area}{\pi}\right)^{1/2} \qquad \text{(Eq. 5.7)}$$

As the NGM AlSiSi7Mg alloy is a non-grain refined, non modified alloy, the resultant eutectic structure formed around the primary grain was coarse and acicular in nature (see Fig. 5.5(a)). The silicon plates make it practically impossible to differentiate the grains and determine if they are connected to each other or are separate and Dahle et al.[243] showed that an Al-Si eutectic phase in Al-Si alloys grows from the primary phase in non-modified alloys, but grows independently in the melt in modified alloys[95], hence making it more difficult to analyse the microstructure in a non-modified Al-Si alloy containing eutectic.

The anodizing of the polished samples helps with the determination of the grain sizes. In anodizing instead of being etched, the primary phase is oxidized and the colour remains the same for both macro- or micro-examination. However, small variations

may be observed in gray values if part of the grain is strained during grinding and polishing or bent during processing. The area with the same colour tint and intensity should indicate a single grain (see Fig. 5.5(b)) provided it is not in the same crystallographic orientation as its neighbour/s. The grain size was measured as an equivalent diameter, which was derived from the area of the grain.

Although the linear intercept method[174,244] and secondary arm spacing[174] in cast metals with dendritic microstructure are the most common methods to characterise the grain, the anodizing technique was selected, as the linear intercept method is based on counting grain boundaries which creates erroneous results.

However, in semi-solid processing the primary grains transform from a dendritic to rosette and finally globular morphology due to the processing conditions, such as a high shear force imposed by stirring [1,2,3]. On sectioning, due to the presence of grains having varying morphologies from equiaxed to rosette to fully globular, a globular structure is frequently observed which contrasts to that which would be expected for a dendritic morphology which should display a clear morphology pattern (see Fig. 5.6)[225,245,246]. This transformation has aroused questions about the validity of the normal grain measuring methods in semi-solid processed alloys [35,247]. Figure 5.7[248] clearly shows how sectioning of the sample can affect the grain size in the linear intercept method in a semi-solid processed material. Similarly, in normal grain size evaluation methods over etching can easily change the microstructure as was observed during the selection of a suitable etching reagent (see Fig. 5.8).

Niroumand and Xia[247,249] were the first to report that the smaller round particles which are usually considered as single grains[250,251,252] may be a part of an agglomerate in 3D (also termed as pseudo particles and pseudo cluster[249,253]) as can be seen in Fig. 5.9, where a 3D view obtained from serial sectioning of a sample shows the connectivity of the globules. This agglomeration may result from the slow cooling of the stirred semi-solid melt[254] or from the drop in shear force[55] (see Fig. 5.10). Smeulders et al.[255] showed by isothermal stirring of transparent organic material that primary dendrite arms transformed to a round shape by ripening and coarsening resulting in a pseudo-particle with a “bunches of grapes” morphology and misorientation of <10°. This phenomenon has been simulated by the thermal/solutal advection model proposed by Mullis[256].

Furthermore, Falak and Niroumand[253] found that pseudo-particles can also form on the wall of the crucible and with an increase in stirring may be more spherical, detach earlier from the wall and be transported into the bulk, where due to long shearing time and solidification time they become coarser. Therefore it is possible to find pseudo-particles in the microstructure even when they are least expected.

In addition to the complexity of the microstructure in semi-solid alloys as mentioned above, single particles in 3D may also result in pseudo-particles in 2D view due to sectioning as shown schematically in Fig. 5.11[95].

Considering these problems with the semi-solid alloy structure different researchers worked on methods and techniques to clearly identify the separate grains from pseudo-particles connected together in a pseudo-cluster. Colour microscopy particularly anodizing using Barker's reagent has already been used to identify the dendrites in aluminium alloys by Bäckerud et al.[186]. Inspired by these findings, the anodizing technique was used in this study as particles connected to each other reflect the same colour (see Fig. 5.11) and recently this technique was successfully used to quantify the semi-solid microstructure by Nafisi and co-workers in grain refined and modified Al-Si alloys[95,112,245]. The steps involved in measurement of grain characteristics are shown in Fig. 5.12.

5.4 EVOLUTION OF MICROSTRUCTURE

The grain characteristics such as grain size and grain shape depend on the nucleation events and their subsequent growth during solidification. Processing parameters, such as pouring temperature, inclination angle and contact time, sample thickness, mould material, coating material, and the alloy are the controlling parameters.

5.4.1 Nucleation and Growth on Cooling Slope

No Grain Refiner Addition - NGM AlSi7Mg Alloy

The NGM AlSi7Mg alloy contains no grain refiner or modification additions and on pouring onto the cooling slope an insufficient cellular to equiaxed transition (CET)[257] may occur and consequently the constitutional undercooling plays a key role on the cooling slope. The melt behaves in the following manner:

If the pouring temperature of the melt is low, then a low thermal gradient on the cooling slope leads to high constitutional undercoolings and promotes the formation of highly branched dendrites which grow at an angle against the melt flow on the cooling slope surface. If the inclination angle is large enough, the resulting melt velocities and shear force may be sufficient to break and fragment the highly branched dendrites. These dendritic fragments can be transported into the bulk melt and ultimately into the mould where they can continue to grow resulting in a small grain size (see Fig. 5.13 (a)). On the other hand when the inclination angle is low, the insufficient shear force results in the formation of very few nuclei by fragmentation in the bulk melt before entering the mould which results in a larger grain size (see Fig. 5.13(b)).

With an increase in contact time there is a possibility of an increase in the formation of nuclei by fragmentation, due to the longer contact with the slope. In addition, the melt temperature decreases with an increase in contact time, which limits the remelting of the existing fragmented nuclei in the melt, hence increasing the nuclei number density flowing into the mould. It thus also favours the preservation of the formed nuclei once in the mould and therefore results in a smaller grain size (see Fig. 5.13(c)).

If the pouring temperature of the melt is high, then a high thermal gradient on the cooling slope leads to low constitutional undercoolings and promotes the formation of thick, coarse dendrites on the cooling slope surface. If the inclination angle is large, the resulting shear force although high will still not be sufficient to break and fragment these dendrites. This results in the formation of very few nuclei in the bulk melt before entering the mould and thus a larger grain size (see Figs. 5.14(a) and

5.14(b)). When the inclination angle is low, the insufficient shear force also results in formation of very few nuclei in the bulk melt before entering the mould. However with longer contact time, subsequent thermal and constitutional undercooling in the mould may become dominant and can result in smaller grain size and near globular structure morphology due to the relatively cold melt being poured into the mould (see Fig. 5.14(c)).

In circumstances where no or only a few nuclei are formed in the bulk melt and the heat extracted from the melt is limited, there is no benefit in using the cooling slope technique with respect to obtaining a desirable microstructure for semi-solid processing.

Grain Refiner Addition - COM AlSi7Mg and MHD A356 Alloys

The grain refined and modified COM AlSi7Mg and MHD A356 alloys, when poured onto the cooling slope, exhibited the following behaviour:

If the pouring temperature of the melt is low, then a low thermal gradient on the cooling slope leads to high constitutional undercoolings and promotes the formation of highly branched dendrites which grow at an angle against the melt flow on the cooling slope surface. If the inclination angle is large enough, the shear force may be sufficient to break and fragment the highly branched dendrites. In addition to these fragments heterogeneous boride particles are also present in the bulk melt which promote a columnar to equiaxed transition (CET). If the pouring temperature is excessively high, then the detached fragments cannot survive and even nucleation on boride particles may not occur on the slope. In this case, the cooling slope will only decrease the superheat, which favours heterogeneous nucleation on the boride particles in the mould. On the other hand when the inclination angle is low, the insufficient shear force results in the formation of very few nuclei in the form of fragments. Nevertheless, nuclei are still present in the bulk melt before entering the mould but they are primarily in the form of borides. As a consequence grain sizes are similar under both regimes (see Fig. 5.15).

An increase in the contact time results in a decrease in the superheat of the melt favouring the formation of nuclei in the bulk melt on the cooling slope. This also restricts the remelting of any existing nuclei in the melt.

If the pouring temperature of the melt is high, then a high thermal gradient on the cooling slope leads to low constitutional undercoolings and promotes the formation of thick, coarse dendrites on the cooling slope surface. If the inclination angle is large, the resulting shear force although higher will still not be sufficient to break and fragment these dendrites. This results in the formation of very few nuclei in the form of fragments. Nevertheless, nuclei are still present in the bulk melt before entering the mould but they are primarily in the form of active borides[258]. These heterogeneous particles promote the columnar to equiaxed transition (CET). When the inclination angle is low, the insufficient shear force results in the formation of very few nuclei in the form of fragments. Nevertheless, nuclei are still present in the bulk melt before entering the mould but again they are primarily in the form of borides. These heterogeneous particles promote the columnar to equiaxed transition (CET) which results in grain sizes and shape similar to those previously described in this section.

Cooling Slope Coating

The coating on the cooling slope provides a rough surface with cracks, fishers and particle sizes which can promote nucleation. It also controls the thermal gradient which affects the morphology of the nucleated grains on the cooling slope surface. Graphite being more conductive extracts more heat from the melt, resulting in an increase in thermal gradient, which favours the formation of thick dendritic trunks on the surface. Therefore, the boron nitride (BN) coating is more favourable for the formation of the highly branched dendrites, suitable for easy fragmentation, resulting in a higher number of pre-existing nuclei in the melt being poured into the mould, resulting in finer grain size (see Fig. 5.16).

The coating has manifold effects on the melt being poured onto the cooling slope and the resulting grain population in the melt[259,260]. A coating with higher conductivity and smooth surface can extract more heat than a coating with lower thermal conductivity and a rough surface[259,260].

The roughness is a comparative factor with respect to the melt in consideration (see Fig. 5.17). It is measured by the apex angle (φ) which is composed of the peak to peak distance (S_m) and peak to valley height (R_z).The smaller the apex angle, the rougher the coating and the lower the heat transfer due to a reduced contact between the melt and the mould surface. The presence of insulating air in the grooves/valleys, formed due to the roughness of the coating, further reduces the heat transfer coefficient. The surface roughness also depends on the contact angle of the melt with the surface. If the contact angle is less than the apex angle of the coating, the heat transfer will be greater (see Fig 5.18). As soon as a solid layer is formed on the coated surface, the contact between the coating and the solid further decreases due to solidification shrinkage[14,15,64,261].

The heat transfer through the coated mould surface depends on the alloy thermal properties, wetting of the mould surface and thermal conductivity of the mould wall. In addition to the thermal conductivity, the interface heat transfer coefficient depends on the mould coating, gas layer, and thermal diffusivity of the melt[246,260]. Kim et al.[260] reported that the interfacial heat transfer coefficient increases with increase in pouring temperature in the case of the non-coated mould, whilst it remained approximately unchanged in the case where the mould was coated. The graphite coating is more effective in removing the effect of superheat i.e. no change in interface heat transfer coefficient with increase in superheat. Similar trends have been observed during solidification, where the interface heat transfer coefficient is further decreased and remained ineffective with respect to initial pouring temperature in the case of the coating. The boron nitride (BN) coating is used as an insulating coating and the interface heat transfer of BN is less than that of the graphite coating.

5.4.2 Nucleation, Growth and Coarsening in the Mould

In the mould, constitutional undercooling is dominated by thermal undercooling imposed by thermal gradients, controlling the grain morphology for a given number of pre-existing nuclei created on the cooling slope.

In the sand mould heat extraction is low due to the low heat transfer coefficient, which reduces the thermal gradient in the bulk melt. This lower thermal gradient favours a non-dendritic morphology of the pre-existing and newly formed nuclei in the mould. The final grain size in the sand mould will depend upon the number of active nuclei available for growth. In the case of a melt with a higher superheat poured from the cooling slope, only the growth of stable pre-existing nuclei will occur. If the melt poured from the cooling slope is low in superheat, no remelting of newly formed nuclei in the mould will occur therefore increasing the number of active nuclei in the melt. In addition, the longer solidification times inherent to the sand mould promotes coarsening of the grains which can result in the formation of a globular microstructure (see Fig. 5.19(a)).

In the metallic mould a higher heat transfer coefficient results in a higher thermal gradient in the melt. The higher thermal gradient and thermal undercooling result in higher growth rates. These conditions favour the instability of the growth front as described by Mullins and Sekerka[97] and dendritic growth occurs (see Fig. 5.19(b)).

When a melt with higher superheat flows from the cooling slope into the metallic mould, the high thermal gradient imposed by the mould results in columnar grains at the mould walls. Depending on the pre-existing nuclei in the bulk melt a CET may occur. The high thermal undercooling will promote a dendritic microstructure.

When a melt with low superheat flows into the mould from the cooling slope, the lower superheat results in undercooling of the bulk melt. This will readily facilitate the columnar to equiaxed transition (CET) especially in the presence of grain refiner particles. The survival of the pre-existing nuclei from the cooling slope will assist the CET. Again the high thermal undercoolings will promote a dendritic structure. However, at high nucleation densities dendrites have insufficient space to develop and a fine globular structure may be observed.

Although the findings from the microstructures in the sand and metallic moulds are counter intuitive they may be explained by the above reasoning. It is clear from the results though that the effect of the sand mould may be beneficial in the process and its result is somewhat analogous with results from procedures used to obtain lower thermal gradients in the NRC process[2].

The above explanations help us understand the nucleation and growth mechanisms on the cooling slope thereby elucidating the results obtained and presented in Chapter 4 of this study.

5.5 Tables

Table 5.1: Composition of an AA-standard A356.2 alloy (wt%)[186]

Alloy	Elements						
	Si	Fe	Cu	Mn	Mg	Zn	Ti
A356.2	6.5 – 7.5	0.12	0.10	0.05	0.30 – 0.45	0.05	0.20

Table 5.2: Comparison of growth temperatures for the primary phase during the solidification of the alloys. ( ) shows the values calculated using the formula presented by [229].

Method	Cooling Curve (℃)	DSC Heat Flow Traces (heating) (℃)	Thermo-Calc® Simulations (℃)	Empirical Relationship [229,230] (℃)
NGM AlSi7Mg	615.5	618.4	616.0	615.9 (615.6)
COM AlSi7Mg	616.2	620.6	615.5	611.6 (614.3)
MHD A356	611.3	619.8	614.0	610.3 (611.9)

Table 5.3: Comparison of eutectic temperature during the solidification of the alloys.

Method	Cooling Curve (℃)	DSC Heat Flow Traces (On Cooling) (℃)	Thermo-Calc® Simulations (℃)
NGM AlSi7Mg	577.8	574.0	575.8
COM AlSi7Mg	563.7	567.1	573.8
MHD A356	564.9	567.6	574.8

Table 5.4: The intermetallic phases present in the alloys.

Alloys	SEM Micrographs	Thermo-Calc® Simulation	Bäckerud et al.[186]
NGM AlSi7Mg	*β-AlFeSi* *π- AlMgFeSi*	*β-AlFeSi* *π- AlMgFeSi*	*β-AlFeSi* *π- AlMgFeSi* *Mg_2Si*
COM AlSi7Mg	*β-AlFeSi* *π- AlMgFeSi* *Mg_2Si*	*β-AlFeSi* *π- AlMgFeSi* *Mg_2Si*	*β-AlFeSi* *π- AlMgFeSi* *Mg_2Si*
MHD A356	*β-AlFeSi* *π- AlMgFeSi* *Mg_2Si*	*β-AlFeSi* *π- AlMgFeSi* *Mg_2Si*	*β-AlFeSi* *π- AlMgFeSi* *Mg_2Si*

Table 5.5: Reaction sequence predicted by Thermo-Calc® Simulation.

Reaction No.	Reaction	Temperature (℃)		
		NGM AlSi7Mg	COM AlSi7Mg	MHD A356
1	*Liquid*	616.0	616.5	614.0
2	*Liquid* ⟶ *Al*	616.0	616.5	614.0
3	*Liquid* ⟶ *Al + Si*	575.8	573.8	574.8
4	*Liquid* ⟶ *Al + Si + β-Al_5FeSi*	571.3	567.5	568.6
5	*Liquid* ⟶ *Al + Si + β-Al_5FeSi + π-$Al_8Mg_3FeSi_6$*	-	-	-
6	*Liquid* ⟶ *Al + Si + π-$Al_8Mg_3FeSi_6$*	560.5	561.2	561.0
7	*Liquid* ⟶ *Al + Si + π-$Al_8Mg_3FeSi_6$ + Mg_2Si*	556.2	556.8	557.0

Table 5.6: The sequence of solidification reactions proposed by Bäckerud et al.[186] for A356.2 alloy and corresponding peaks from DSC traces as observed in this study.

Reaction No.	Reaction[186]	Suggested Temperature (℃) [186]	DSC peaks
1	*Development of dendritic network*	615	1
2a	*Liquid* ⟶ *Al + Si*		2
2b	*Liquid* ⟶ *Al + β-Al_5FeSi*		
3a	*Liquid* ⟶ *Al + Si + β-Al_5FeSi*	575	4
3b	*Liquid + β-Al_5FeSi* ⟶ *Al + Si + π-$Al_8Mg_3FeSi_6$*	567	4
4	*Liquid* ⟶ *Al + Si + Mg_2Si*	555	
5	*Liquid* ⟶ *Al + Si + π-$Al_8Mg_3FeSi_6$ + Mg_2Si*	554	3

5.6 Figures

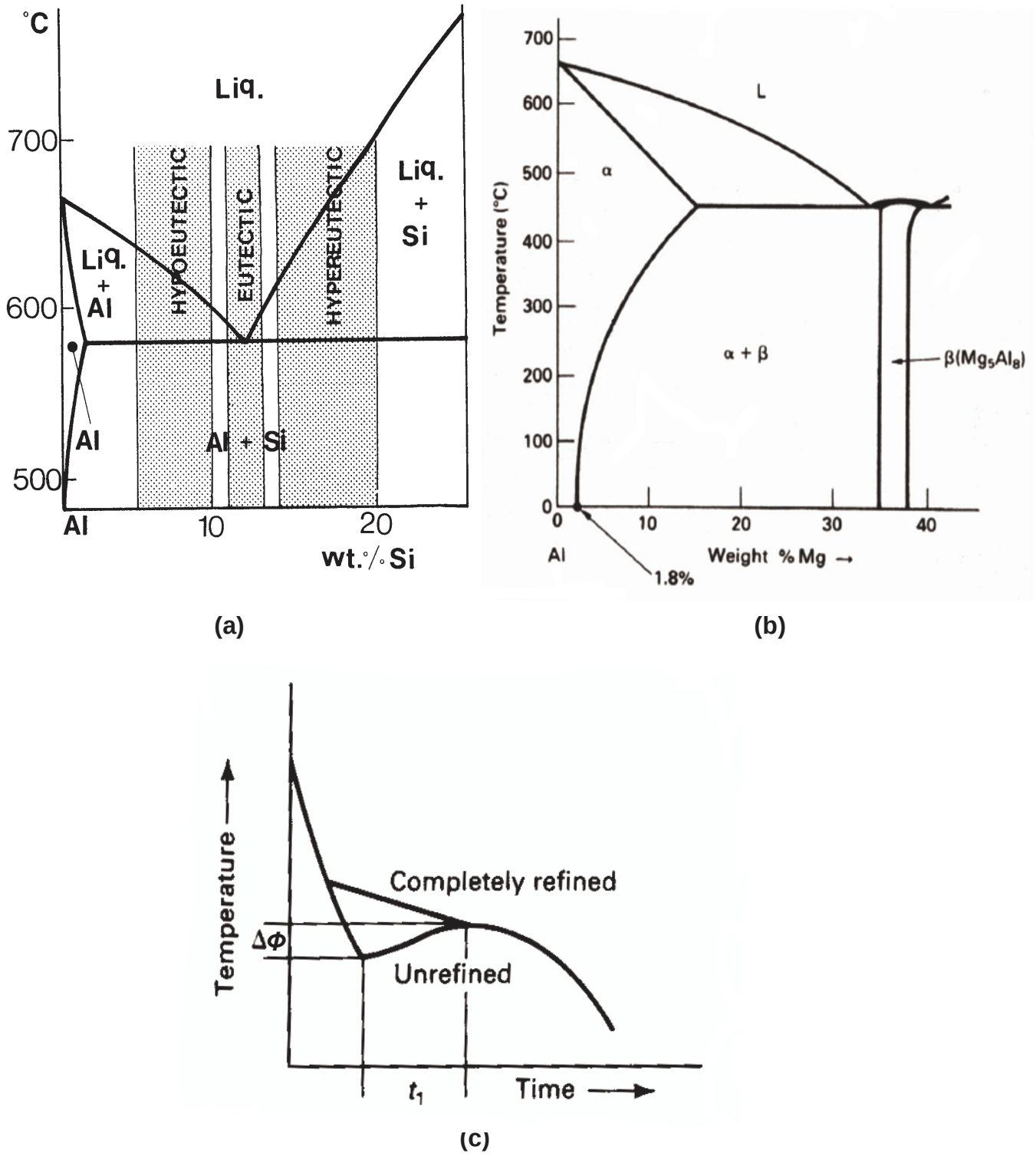

Fig. 5.1: Schematic illustration of: (a) phase diagram for Al-Si binary system[186]; (b) Al rich end of Al-Mg binary phase diagram[228]; and (c) effect of grain refinement on recalescence, $\Delta\Phi$[65].

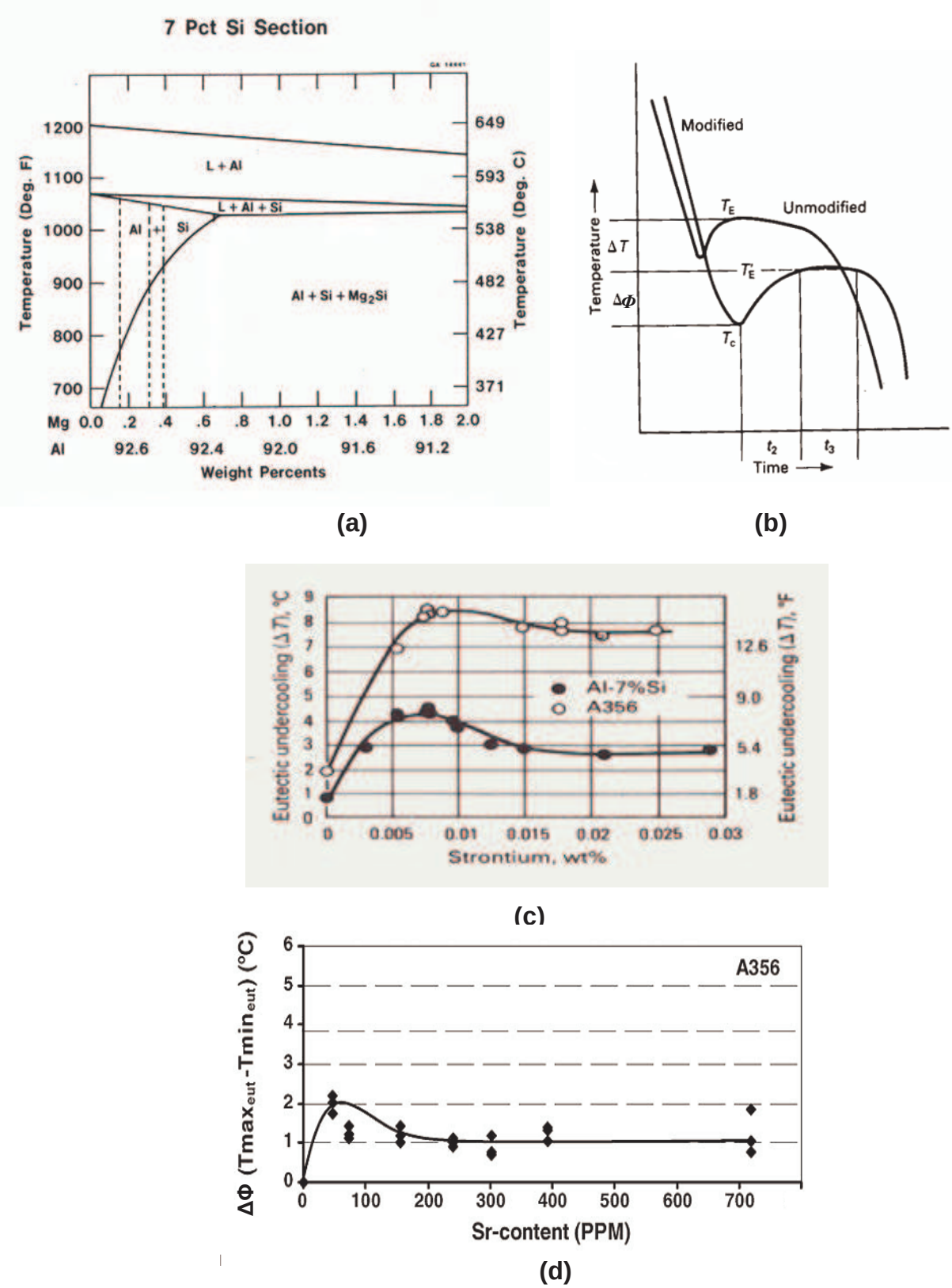

Fig. 5.2: The schematic of: (a) a 7 wt% Si section showing the effect of increase in Mg content on the solidification sequence and expected phases. Dotted lines show the different Mg content[236]; (b) effect of modification on eutectic temperature undercooling, ΔT, and recalescence, $\Delta\Phi$ [65]; (c) effect of Sr addition on eutectic undercooling, ΔT, for Al-7%Si and A356 alloy[65]; and (d) effect of Sr on the recalescence, $\Delta\Phi$, for an A356 alloy[112].

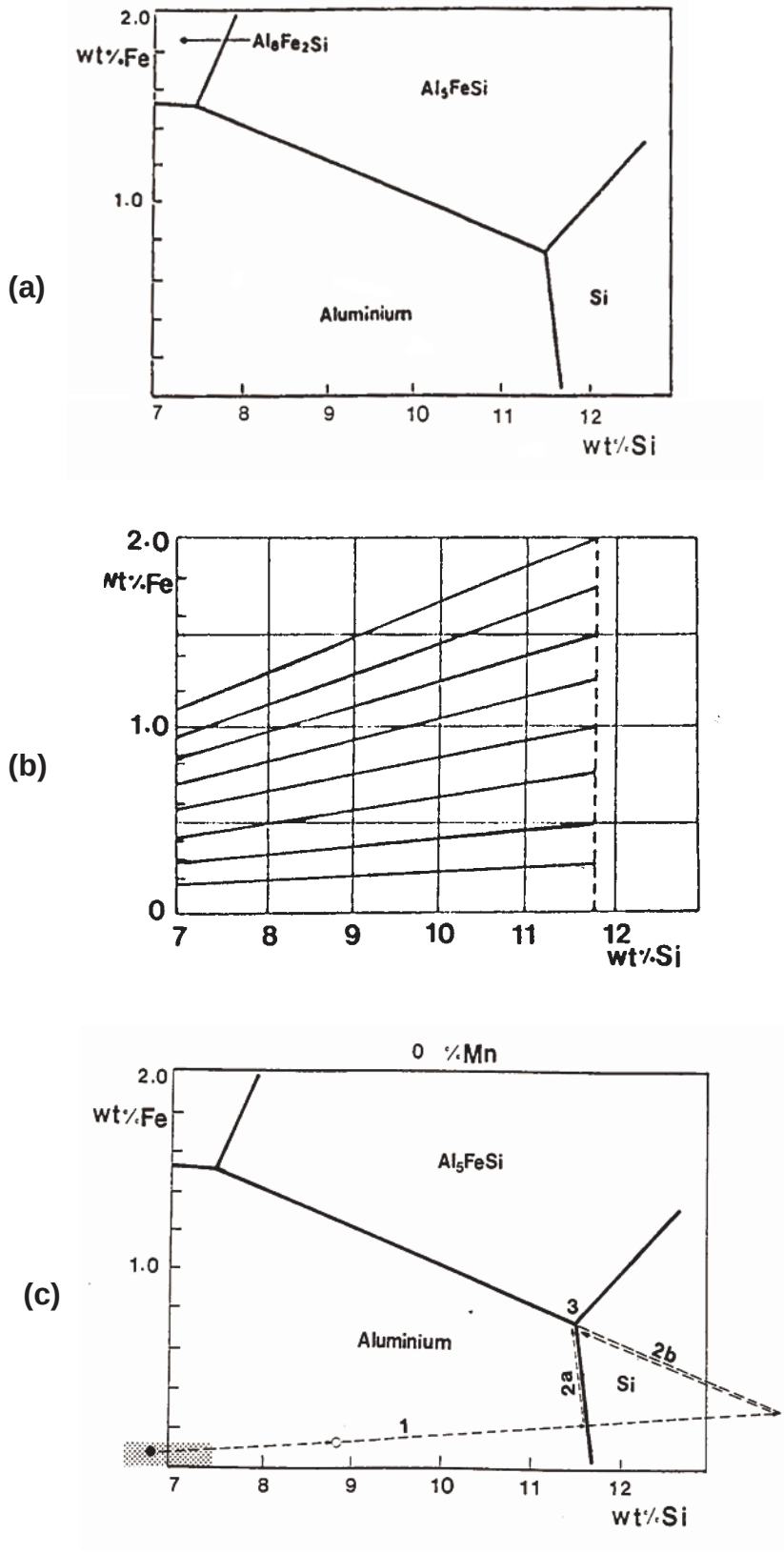

Fig. 5.3: Figures showing: (a) simplified phase diagram of the Al-Fe-Si system with 0 % Mn content; (b) segregation lines calculated according to the Scheil equation for an Al-Si alloy system; and, (c) simplified phase diagram showing the compositional limits of an A356.2 alloy (shaded area) and calculation of sequence of solidification and expected phases for the alloy[186].

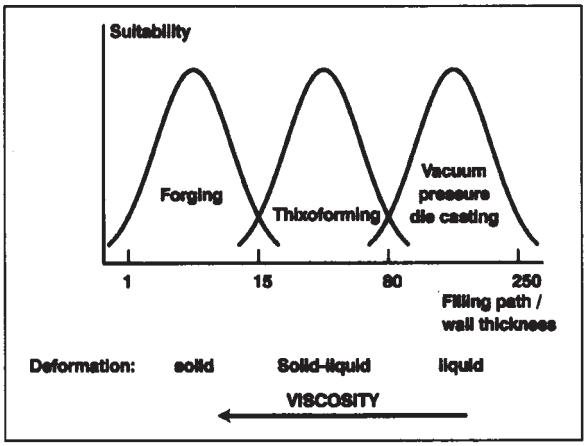

Fig. 5.4: Geometric differentiation of the forging, thixoforming and vacuum pressure die casting based on viscosity, which depends on the fraction solid in the material[190].

(a)

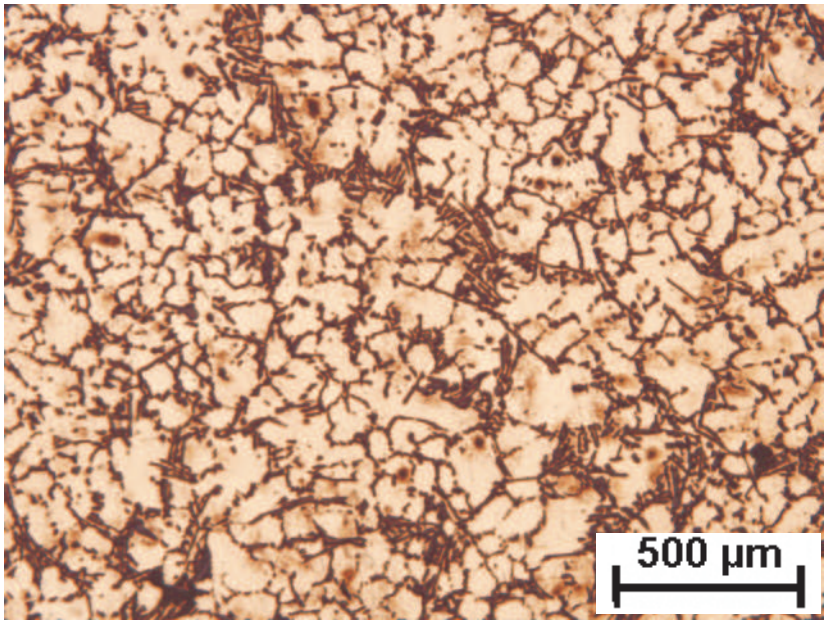

(b)

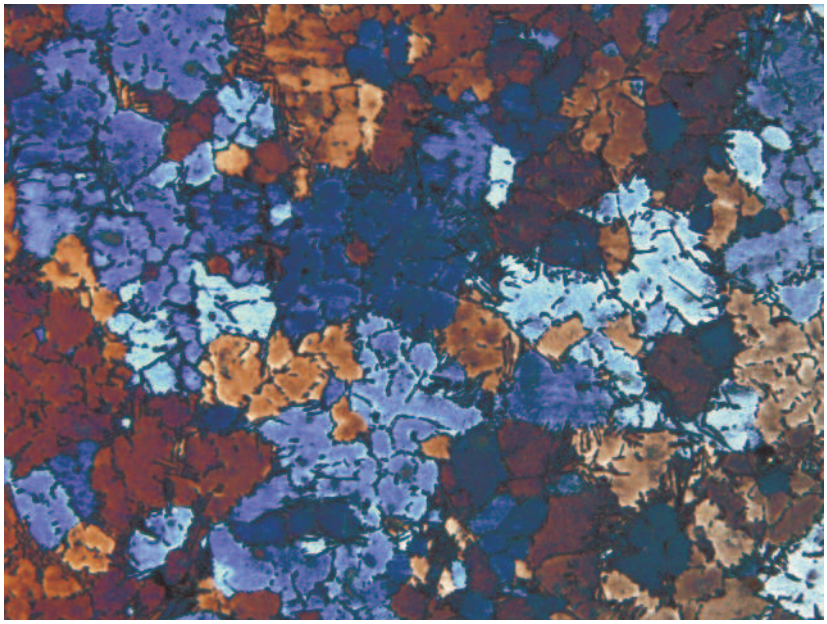

Fig. 5.5: Micrographs from this study; (a) without anodizing and polarized light; and (b) anodized and under polarized light.

(a)

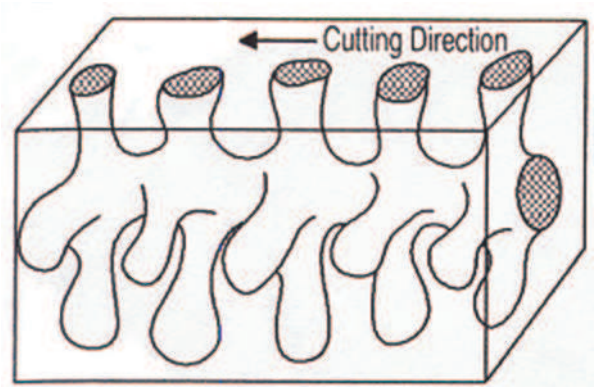

(b)

Fig. 5.6 : Schematic of: (a) a 3D view of a dendrite; (b) a 2D section, showing shortcomings of 2D view [245].

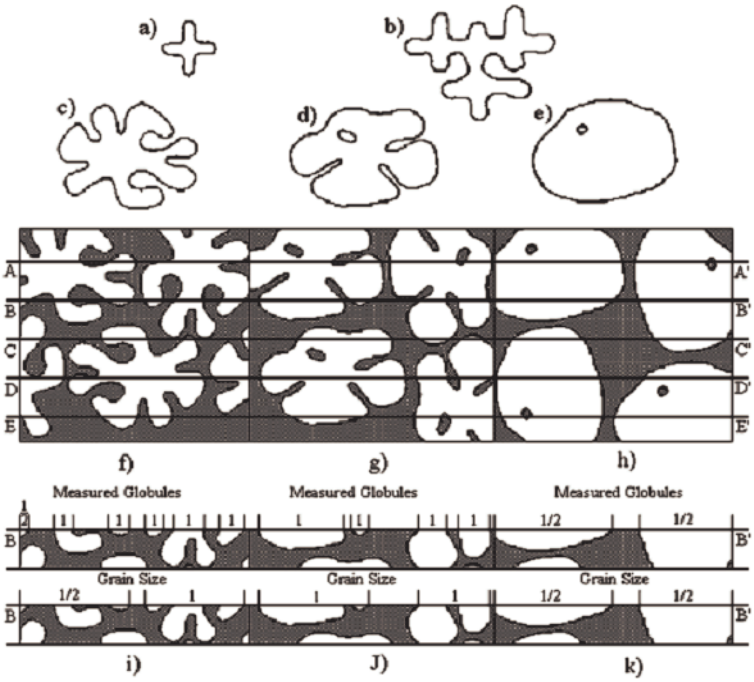

Fig. 5.7: Schematic diagram showing a relation ship between 2D sectioned view and the linear intercept measurement technique: (a-e) morphological evolution; (f-h) counting lines; and (i-k) counting of grains[248].

(a)

(b)

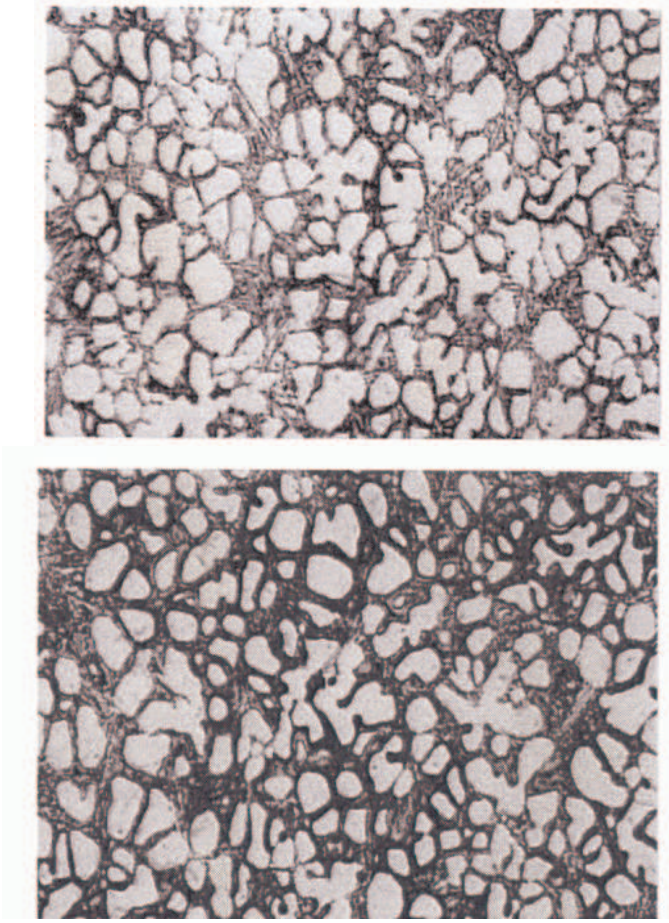

Fig. 5.8: Effect of etching time using Poulton‘s etchant on the microstructure: (a) 28 s; and (b) 52 s at the same magnification.

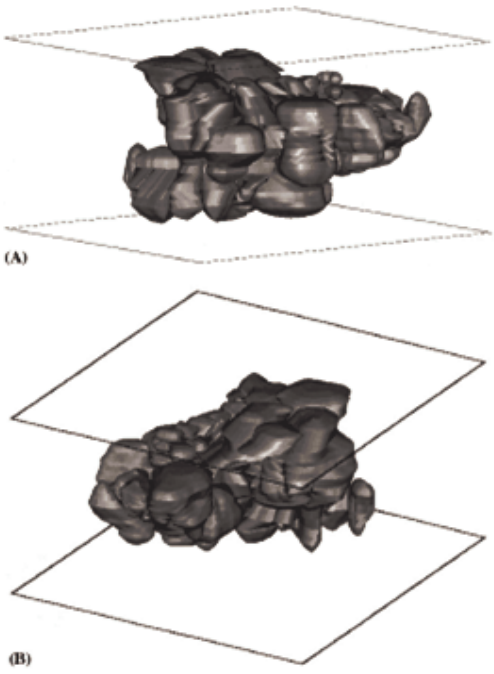

Fig. 5.9: Figures showing an AutoCAD generated 3D view of a pseudo-cluster shown from two different angle to exhibit structure complexity[249] in semi-solid processed alloys.

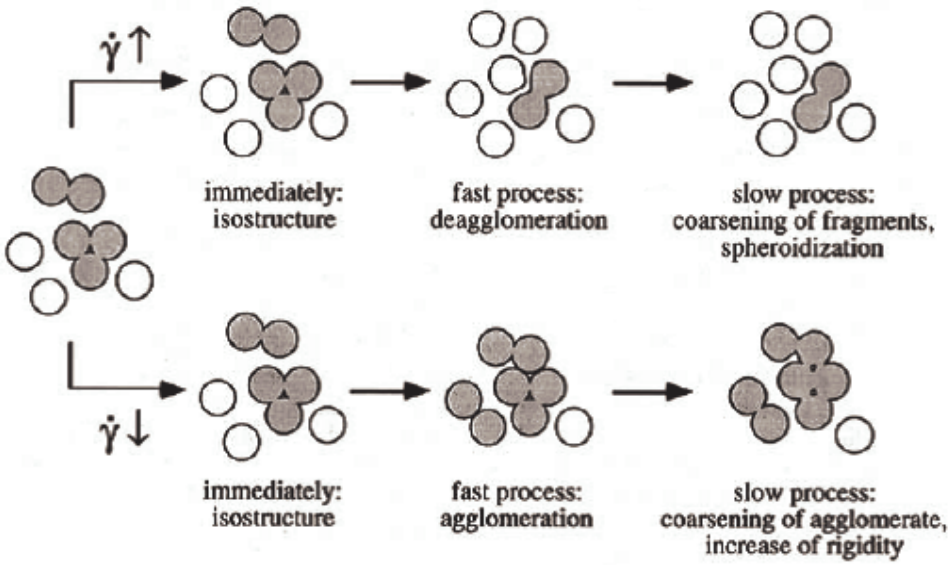

Fig. 5.10: Schematic model describing the fast and slow processes in a semi-solid material's structure after shear rate up and down jumps[55].

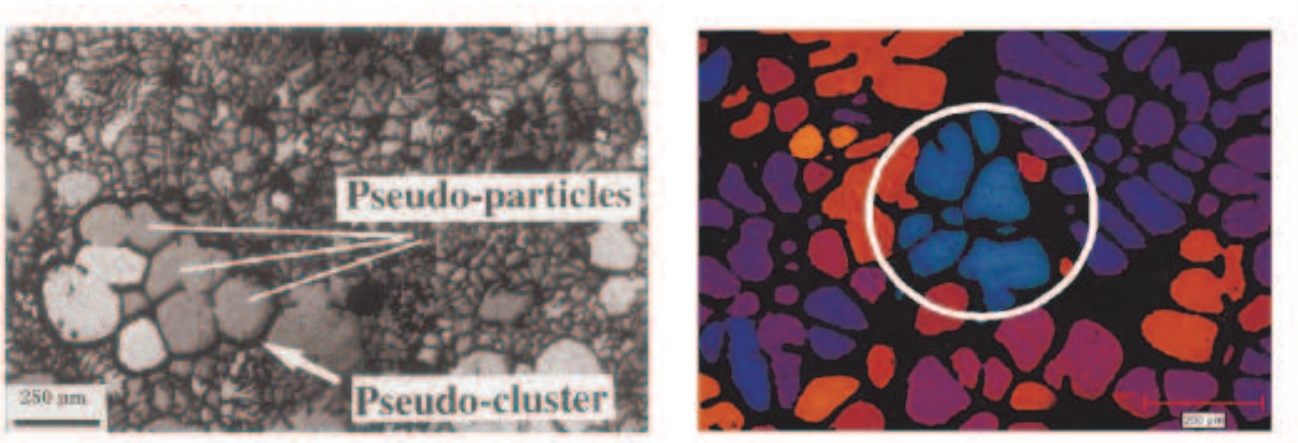

(a) (b)

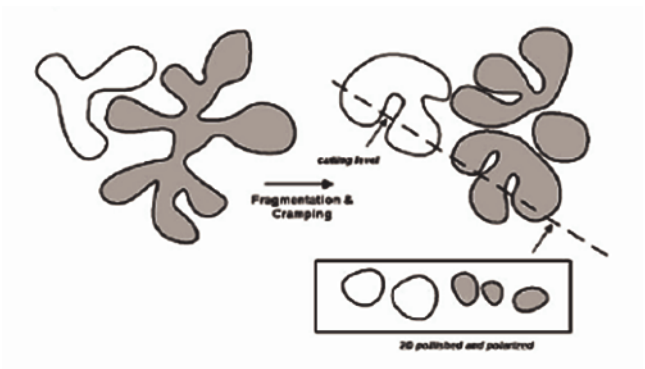

(c)

Fig. 5.11: Schematic showing: (a) a pseudo-particles and pseudo-cluster[253]; (b) Anodized sample under polarized light showing globules connected to single grain, as shown in circle[95]; and, (c) schematic of sectioning of sample across a grain giving pseudo-particles which exhibit the same colour under polarized light [95].

(a)

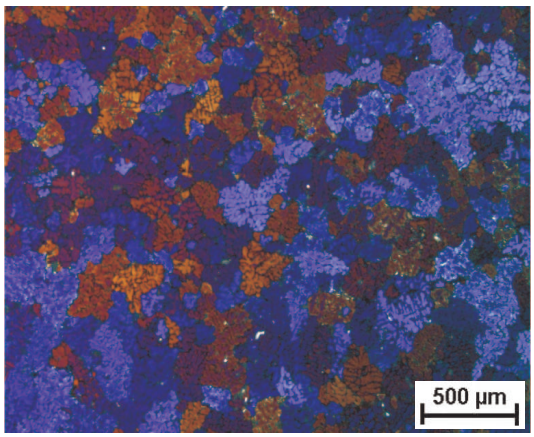

(b)

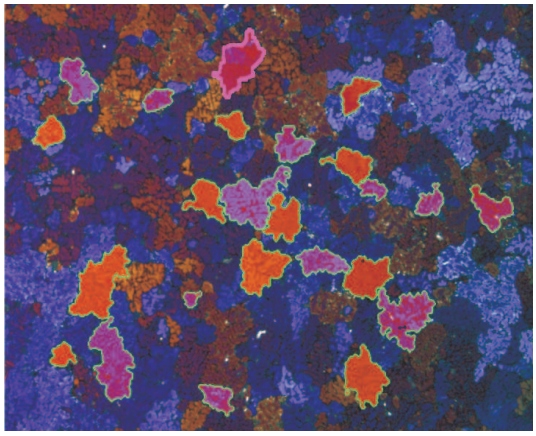

(c)

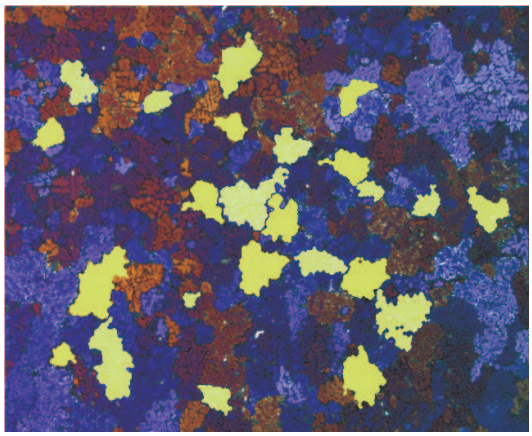

Fig. 5.12: The steps involved in the measurement of grain characteristics : (a) optical micrograph of an anodized sample under polarized light; (b) selection and encircling of objects/grains to measure the perimeter; and, (c) measurement of area with filling of the grain borders.

(a)

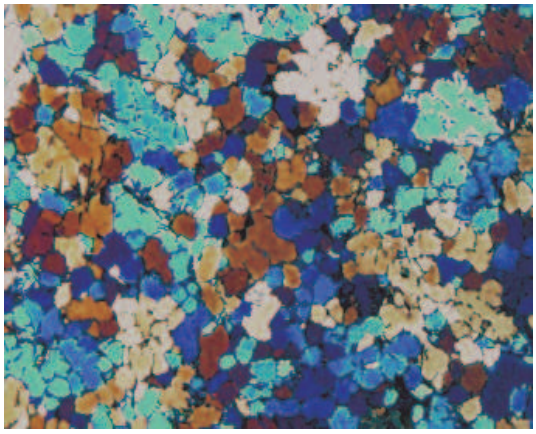

Grain Size (µm)	98
Circularity	0.77
Elongation	1.08

(b)

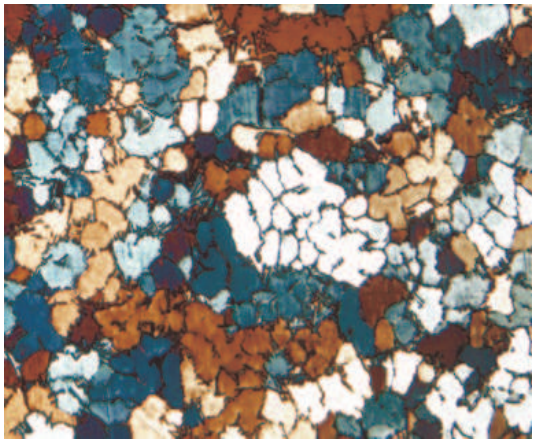

Grain Size (µm)	166
Circularity	0.58
Elongation	1.05

(c)

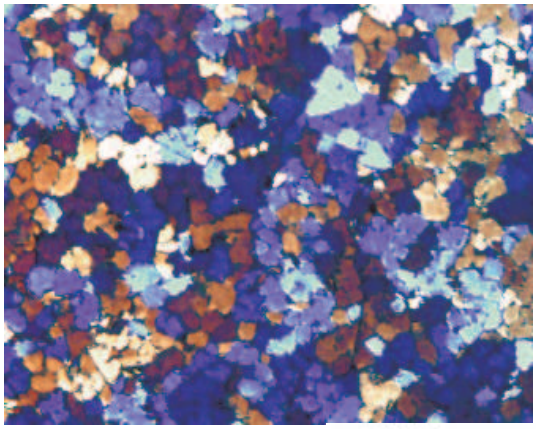

Grain Size (µm)	105
Circularity	0.71
Elongation	1.07

Fig. 5.13: The effect of low pouring temperature and low thermal gradient on microstructure as tabulated in Tables 4.3.1-4.3.6 and presented in section 4.3.2: (a) high shear force due to high inclination angle results in smaller grain size; (b) low shear force due to lower inclination angle results in larger grain size due to fewer fragments; and, (c) increase in contact time which results in more fragments and a smaller grain size.

(a)

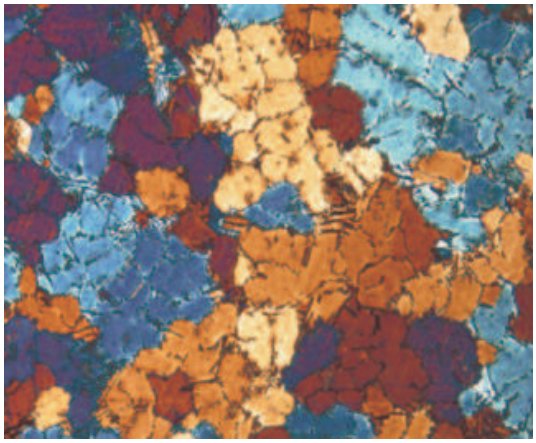

Grain Size (µm)	181
Circularity	0.67
Elongation	1.11

(b)

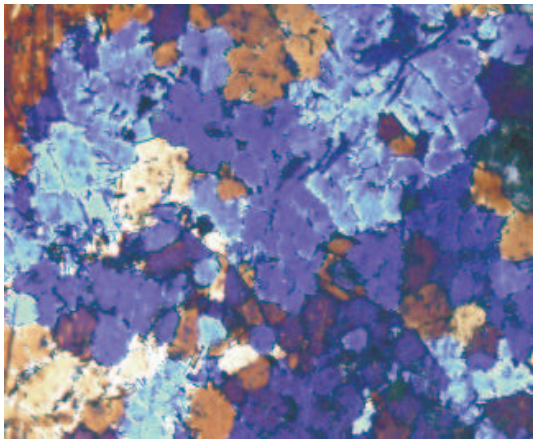

Grain Size (µm)	145
Circularity	0.61
Elongation	1.12

(c)

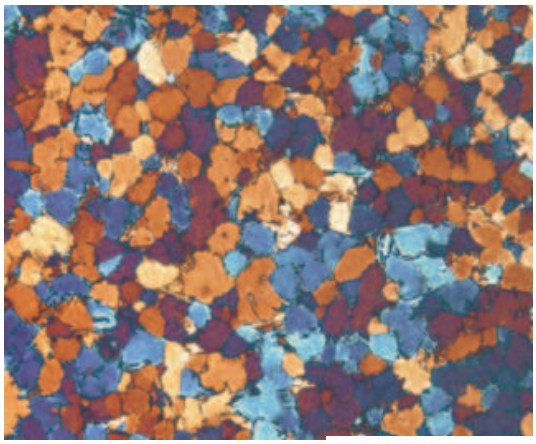

Grain Size (µm)	91
Circularity	0.86
Elongation	1.05

Fig. 5.14: The effect of high pouring temperature and thermal gradient on microstructure as tabulated in tables 4.3.1.-4.3.6 and presented in section 4.3.2: (a) large shear force but due to the formation of coarse thick dendrites, few fragment are created resulting in large grain size; (b) small shear force results in similar grain size to (a); and, (c) with increasing contact time a reduction in grain size was observed which could be possibly due to larger undercooling experienced.

(a)

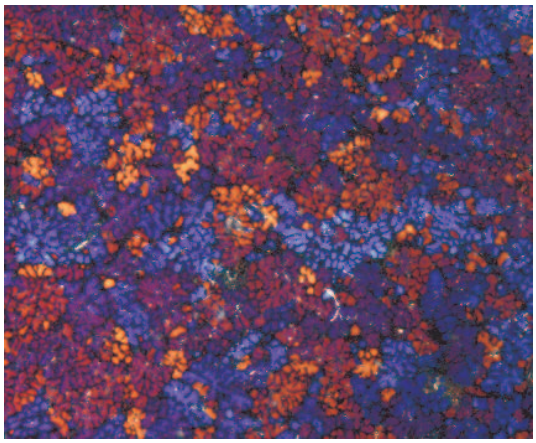

Grain Size (µm)	199
Circularity	0.46
Elongation	1.44

(b)

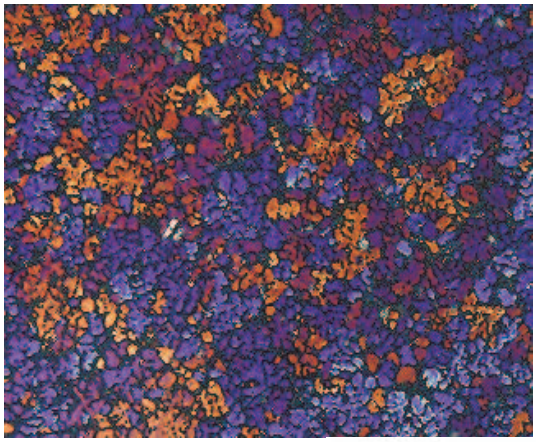

Grain Size (µm)	200
Circularity	0.48
Elongation	1.50

Fig. 5.15: The grain size of the commercial grain refined modified MHD A356 alloy remained unaffected for a lower pouring temperature with a change in shear force due to the CET induced by the grain refining particles. However, a slight increase in circularity and elongation was observed for lower inclination angle, showing the effect of imposed gradient on the growth.

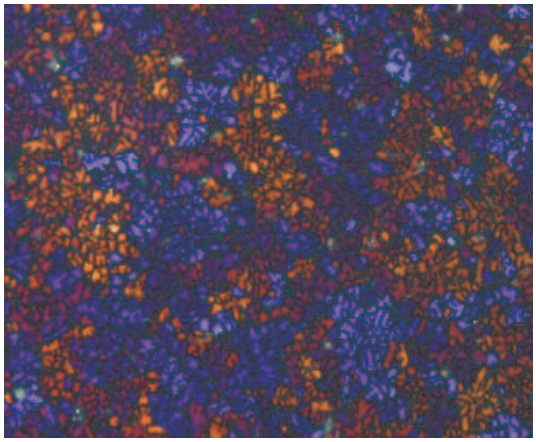

(a)

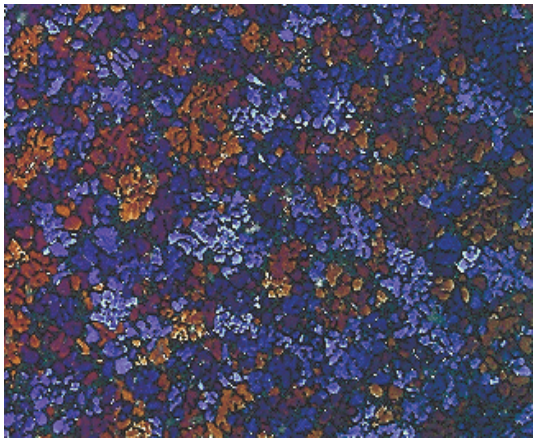

(c)

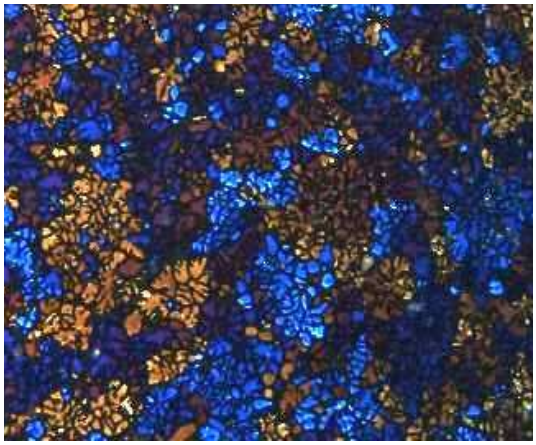

(b)

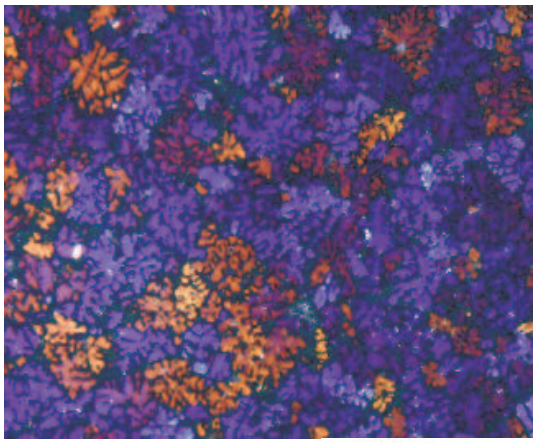

(d)

Coating	Graphite (a)	Boron Nitride (b)
Grain Size (µm)	179	158
Circularity	0.49	0.51
Elongation	1.45	1.48

Coating	Graphite (c)	Boron Nitride (d)
Grain Size (µm)	199	144
Circularity	0.46	0.54
Elongation	1.44	1.45

Fig. 5.16: The BN coating results in a finer grain size for the non-grain refined non-modified NGM AlSi7Mg alloy (b) than that for the graphite (a). A similar trend was also observed for the commercial grain refined and modified COM AlSi7Mg alloy ((c) and (d)) (see Section 4.6).

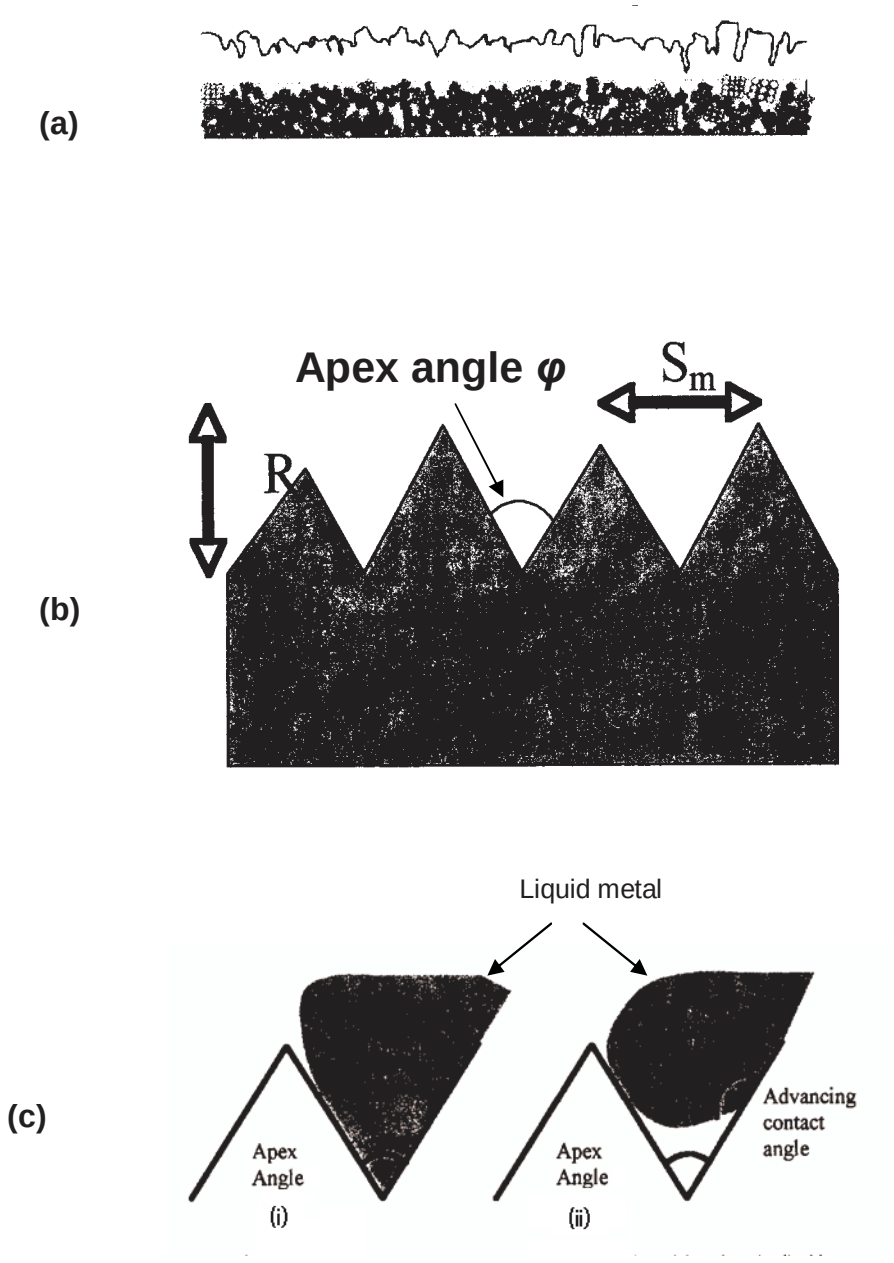

Fig. 5.17: Schematic representation of: (a) surface profile of the coating[257]; (b) surface roughness parameters R_z, S_m and apex angle φ[258]; and, (c) case (i); the contact angle of liquid metal is less than the apex angle and the metal filled the valley removing the air resulting in a higher thermal conductivity, case (ii); the contact angle of liquid metal was higher than apex angle of the coating resulting in partial filling of the cavity, and air entrapped will reduce the thermal conductivity [258].

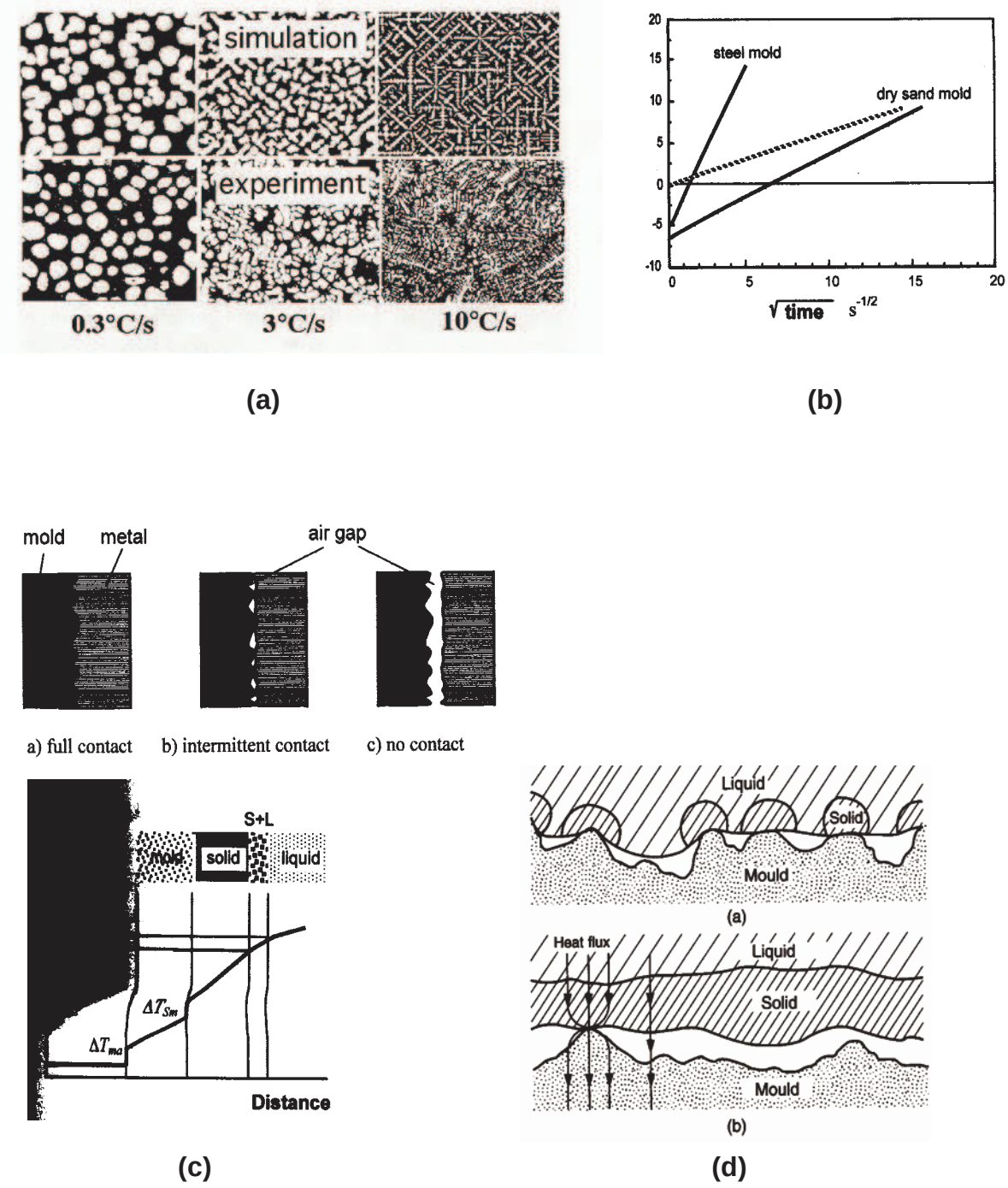

Fig. 5.18: Schematic representation of: (a) effect of cooling rate on microstructure[259]; (b) effect of mould material and the solidification time [15]; (c) solid layer formed during solidification and contact with mould surface and thermal gradient profile [15]; and (d) liquid metal and mould surface contact and heat flow behaviour[14].

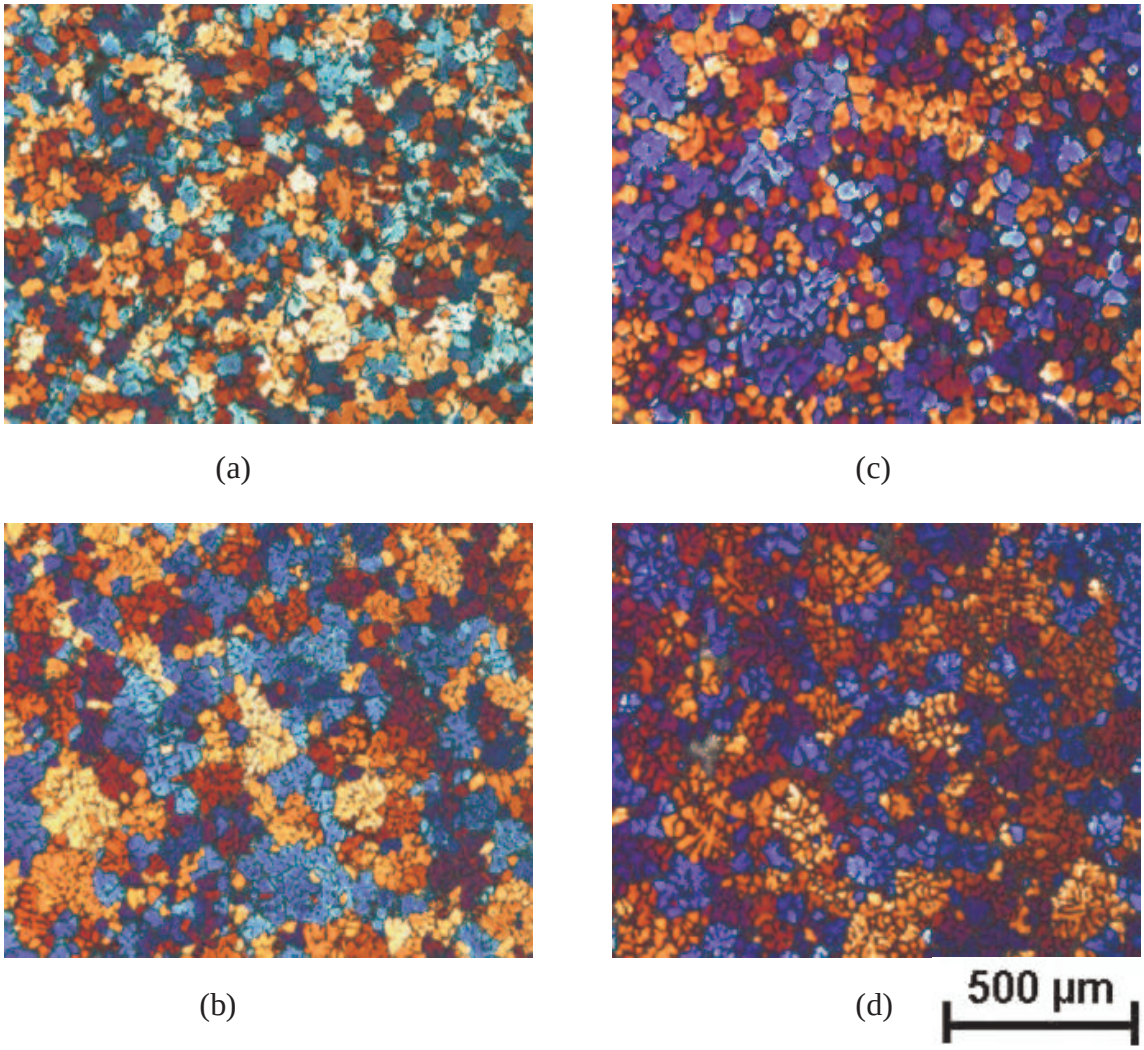

Mould	Sand (a)	Metallic (b)
Grain Size (µm)	95	124
Circularity	0.75	0.66
Elongation	1.11	1.41

Mould	Sand (a)	Metallic (b)
Grain Size (µm)	183	155
Circularity	0.50	0.50
Elongation	1.46	1.39

Fig. 5.19: A finer grain size for non-grain refined non-modified NGM AlSi7Mg alloy in sand mould as opposed to the metallic mould can be obtained depending on the processing conditions suitable for nucleation and growth (a and b) (see section 4.5). However for commercial COM AlSi7Mg alloy the grain size for the sand mould was coarser for the given experimental conditions ((c) and (d)).

Chapter 6

Conclusion

In this study a non-grain refined non-modified Al-7Si-Mg alloy, the NGM AlSi7Mg alloy, was analysed with respect to its solidification behaviour and resulting phase formations. Its suitability for semi-solid processing in terms of the change in fraction solid in its solidification temperature range and its fraction solid sensitivity were investigated. The alloy was processed using the cooling slope technique, which facilitated the formation of semi-solid characteristics. The effect of different processing parameters such as pouring temperature, contact time, and inclination angle, sample thickness, mould material (sand and metal), coating (graphite and/or boron nitride (BN)), and water and/or air cooling was studied.

A grain refined modified Al-7Si-Mg alloy (COM AlSi7Mg) and commercially produced semi-solid precursor material from a Al-7Si-Mg alloy (MHD A356) were also examined and compared with the NGM AlSi7Mg alloy with respect to the solidification range, solidification sequence and resulting phases, effect of mould material, coating material and cooling.

Considering the effect of variation in chemical composition in the alloys, the alloys were characterised and the following conclusions were made:

- A slight variation in chemical composition prominently affects the solidification characteristic temperatures, nature and amount of intermetallic phases and hence the solidification sequence.
- The change in solidification characteristic temperatures, particularly liquidus temperature, prominently affects the response of the melt to nucleation mechanisms and nucleation density when using the semi-solid processing cooling slope technique.

- The working range both the fraction solid and the temperature, each alloy does not correspond to the other similar alloys for the lowest processing temperature limit and the highest workable fraction solid, suitable for thixoforming. The fraction solid and corresponding temperature are drastically affected by a small change in fraction solid over the solidification range, which is affected by the change in chemical composition of the alloy.

A contact time in stead of contact length was used in this study and these conclusions are inferred from our findings:

- Contact time correlates well with the relative undercooling imposed by the cooling slope in the superheated melt for given inclination angle.
- Contact time generalizes the total amount of heat extracted from a melt poured on to the cooling slope technique at each inclination angle.
- Contact time also incorporates the effect of the melt flow velocity.

From the grain characterisation in the semi-solid processed microstructure, the following conclusions were made:

- To analyse grains with various grain morphologies i.e. from dendritic to rosette to globular, a 2D section can result in misleading grain morphologies.
- Optical microscopy of anodized samples using polarized light and Lambda (λ) filter is a useful technique to distinguish all the arms connected to one grain in 3D.
- The anodizing technique is a more effective technique than other grain characterizing techniques, as these are often prone to the degree of etching of the sample.

The nucleation mechanisms on the cooling slope inferred from the grain characteristic data obtained by changing different processing variables, resulted in the following conclusions:

- When pouring a low temperature melt on the cooling slope, the “Big Bang” mechanism was found to be dominant in the case of the non-grain refined non-modified AlSi7Mg alloy.

- When pouring a high temperature melt at the cooling slope, the “wall crystal” mechanism was found to be dominant in the case of non-grain refined non-modified AlSi7Mg alloy.
- When pouring a low temperature melt at a high inclination angle with higher contact time, the columnar to equiaxed transition (CET) mechanism promoted by the presence of heterogeneous grains grain a fine particles was dominant in the case of commercial AlSi7Mg alloy.

The growth mechanisms in the mould inferred from the grain characteristic data obtained by changing different processing variables, enabled the following conclusions to be drawn:

- In the sand mould a melt with low superheat results in a low and homogeneous temperature gradient which favoured the equiaxed growth of nuclei into a finer equiaxed grain size.
- In the sand mould a melt with high superheat results in remelting of existing free nuclei resulting in a coarser equiaxed grain.
- In the metallic mould, a melt with low superheat results in a finer structure display a less dendritic morphology due to the imposed thermal gradient.
- In the metallic mould, a melt with high superheat results in a relatively coarser structure with slightly higher degree of non-dendritic morphology due to the imposed thermal gradient.

Chapter 7

Future Work

In this study the ability of a non-grain refined non-modified AlSi7Mg alloy, processed using the cooling slope technique, to produce a non-dendritic equiaxed microstructure suitable for semi-solid processing was evaluated. In this regard the effect of processing parameters, such as pouring temperature, inclination angle, contact time, mould material, sample thickness and coating materials, on the microstructure obtained in a sand/metal mould at room temperature, has been studied. To evaluate fully the suitability of the non-grain refined non-modified AlSi7Mg alloy and the cooling slope technique for semi-solid processing (Rheocasting and Thixoforming) further work is required. This work includes:

1. As discussed in Section 11.2, the working temperature range and respective fraction solid was calculated for the non-grain refined non-modified AlSi7Mg alloy. The response of the material obtained using the cooling slope should be studied to evaluate the suitability of the alloy and the processing conditions for subsequent thixoforming by analysing effect of different heating rates, holding times in semi-solid range, semi-solid processing temperatures and feeding behaviour in the die.
2. To study the response towards rheocasting, the melt obtained from the cooling slope should be held or cooled in a controlled manner to different fraction solids and subsequent processing in the semi-solid state should be made to evaluate the suitability of the non-grain refined non-modified AlSi7Mg alloy slurry obtained from the cooling slope.
3. The nuclei formation and multiplication phenomena, as discussed in Section 5.3, and their relative contribution in the cooling slope technique is still not clear. To study the nucleation and growth mechanism, more rapidly quenched samples obtained by holding the melt from the cooling slope in the semi-solid range for different temperatures and times should be studied.

4. Investigation of the effect of a cooling slope on an AlCu4 alloy as a large thermal undercooling for this composition will result in a highly dendritic structure. The results with respect to the microstructure can thus be compared with the Al-Si alloys used in this study.
5. Modelling and simulation of the nucleation mechanism on the cooling slope should be conducted to correlate the grain morphologies.
6. The evaluation of the mechanical properties of the rheocast and thixoformed material and the material obtained with that of the non-grain refined non-modified AlSi7Mg alloy poured at room temperature using the cooling slope, thus enabling its evaluation for its suitability in commercial applications.

Bibliography

1. M.C. Flemings, Metall. Trans. 22A (1991) 957-981.
2. Z. Fan, Int. Mater. Rev. 47 (2002) 1-37.
3. H.V. Atkinson, Progress Mater. Sci. 50 (2005) 341-412.
4. D.B. Spencer, Ph.D. Thesis, Massachusetts Institute of Technology, USA, 1971.
5. A. Vogel, Ph.D. Thesis, University of Sussex, UK, 1979.
6. A. Vogel, R.D. Doherty, B. Cantor, Proc. Int. Conf. The Solidification and Casting of Metals, Uni. Sheffield, Metals Society (1979) 518-525.
7. A. Hellawell, Metall. Mater. Trans. 27A (1) (1996) 229-232.
8. A. Hellawell, Proc. 4th Int. Conf. Semi-solid Processing of Alloys and Composites, Sheffield, UK, 1996, 60-65.
9. D.R. Uhlmann, T.P. Seward III, B. Chalmers, Trans. Metall. Soc. AIME 236 (1966) 527-531.
10. K.A. Jackson, J.D. Hunt, D.R. Uhlmann, T.P. Seward III, Trans. Metall. Soc. AIME 236 (1966) 149-158.
11. B. Chalmers, J. Aust. Inst. Met. 8 (1963) 255-263.
12. H. Biloni, B. Chalmers, J. Mater. Sci. 3 (1968) 139-149.
13. A. Ohno, Solidification: The Separation Theory and its Practical Applications, Springer-Verlag, Berlin, Germany, 1987.
14. J. Campbell, Castings, Butterworth-Heinemann, Oxford, 2003.
15. D.M. Stefanescu, Science and Engineering of Casting Solidification, Kluwer Academic/ Plenum Publishers, NY, USA, 2002.
16. J.E. Zoqui, M.H. Robert, J. Mater. Proc. Technol. 109 (2001) 215-219.
17. H. Kaufmann, P.J. Uggowitzer, Adv. Eng. Mater. 3 (12) (2001) 963-967.
18. H. Kaufmann, P.J. Uggowitzer, Proc. 2001 TMS Annual Meeting, New Orleans, USA, 2001, 1063-1068.
19. J.A. Yurko, R.A. Matinez, M.C. Flemings, Metall. Sci. Technol. 21 (1) (2003) 10-15.
20. T. Haga, S. Suzuki, J. Mater. Proc. Technol. 118 (2001) 169-172.
21. R. Shibata, Proc. 5th Int. Conf. Semi-solid Processing of Alloys and Composites, Colorado, USA, 1998; li-lvi.
22. T. Haga, P. Kapranos, J. Mater. Proc. Technol. 130-131 (2002) 594-598.
23. D. Liu, H.V. Atkinson, H. Jones, Acta Mater. 53 (2005) 3807-3819.
24. E. Yano, N. Wada, N. Nishikawa, T. Motegi, J. Jpn. Inst. Met. 66 (11) (2002) 1131-1134.
25. A. Muumbo, M. Takita, H. Nomura, Mater. Trans. JIM 44 (5) (2003) 893-900.
26. A. Muumbo, H. Nomura, M. Takita, Int. J. Cast Met. Res. 16 (1-3) (2003) 359-364.
27. A. Muumbo, H. Nomura, M. Takita, Int. J. Cast Met. Res. 17 (1) (2004) 39-46.
28. N. Poolthong, H. Nomura, M. Takita, Proc. 65th World Foundry Congress, Gyeongju, Korea, (2002) 103-111.
29. N. Poolthong, H. Nomura, M. Takita, Int. J. Cast Met. Res. 16 (6) (2003) 573-578.
30. T. Haga, P. Kapranos, J. Mater. Proc. Technol. 130-131 (2002) 581-586.
31. W. Kurz, D.J. Fisher, Fudamentals of Solidification, Trans. Technol. Publications, Switzerland, 1998.
32. D.B.R. Spencer, R. Mehrabian, M.C. Flemings, Met. Trans. 3 (1972) 1925-1932.
33. R. Mehrabian, M.C. Flemings, AFS Trans. 80 (1972) 173-182.
34. M.C. Flemings, R. Mehrabian, AFS Trans. 81 (1973) 81-88.
35. K. Xia, G. Tausig, Mater. Sci. Eng. A246 (1998) 1-10.
36. N. Wang, H. Peng, K.K. Wang, Proc. 4th Int. Conf. Semi-solid Processing of Alloys and Composites, Sheffield, UK, 1996, 342-346.
37. W.L. Winterbottom, Metall. Sci. Technol. 18 (2) (2000) 5-10.
38. C.D. Yim, K.S. Shin, Mater. Sci. Eng. A395 (2005) 226-232.

39. M. Paes, E.G. Santos, E.J. Zoqui, J. Achiev. Mater. Manuf. Eng. 19 (2) (2006) 21-28.
40. X.F. Pan, H.F. Zhang, A.M. Wang, K.Q. Qiu, B.Z. Ding, Z.Q. Hu, Mater. Sci. Technol. 17 (2001) 1243-1248.
41. A.A. Tseng, J. Horský, M. Raudenský, P. Kotrbácek, Mater. Design, 22 (2001) 83-92.
42. K.P. Young, Proc. 4th Int. Conf. Semi-solid Processing of Alloys and Composites, Sheffield, UK, 1996, 229-233.
43. N.H. Nicholas, M.R. Trichka, K.P. Young, Proc. 5th Int. Conf. Semi-solid Processing of Alloys and Composites, Colorado, USA, 1998, 79-86.
44. M. Tsuchiya, H. Ueno, I. Takagi, JSAE Rev. 24 (2003) 205-214.
45. D.H. Kirkwood, Proc. 4th Int. Conf. Semi-solid Processing of Alloys and Composites, Sheffield, UK, 1996, 320-325.
46. M. Tsujikawa, K. Tanaka, C. Ushigome, S. Nishikawa, M. Kawamoto, Proc. 4th Int. Conf. Semi-solid Processing of Alloys and Composites, Sheffield, UK, 1996, 165-168.
47. P. Kapranos, P.J. Ward, H.V. Atkinson, D.H. Kirkwood, Mater. Design 21 (2000) 387-394.
48. W. Kahrmann, R. Schragner, K. Young, Proc. 4th Int. Conf. Semi-solid Processing of Alloys and Composites, Sheffield, UK, 1996, 154-158.
49. R. Mehrabian, M.C. Flemings, Casting in the liquid-solid Region, in: New Trends in Materials Processing, ASM, Metals Park, OH, USA, 1976 98-127.
50. M.C. Flemings, R.G. Riek, K.P. Young, Mater. Sci. Eng. 25 (1976) 108-117.
51. M. Mada, F. Ajersch, Mater. Sci. Eng. A212 (1) (1996) 157-170.
52. N. Wang, S. Guangji, Y. Hanguo, Yang, Mater. Trans. JIM 31 (8) (1990) 715-722.
53. H. Peng, K.K. Wang, Proc. 4th Int. Conf. Semi-solid Processing of Alloys and Composites, Sheffield, UK, 1996, 2-9.
54. M. Suéry, C.L. Martin, L. Salvo, Proc. 4th Int. Conf. Semi-solid Processing of Alloys and Composites, Sheffield, UK, 1996, 21-29.
55. C.J. Quaak, L. Katgerman, W.H. Kool, Proc. 4th Int. Conf. Semi-solid Processing of Alloys and Composites, Sheffield, UK, 1996, 35-39.
56. E. Tzimas, A. Zavaliangos, A. Lawley, C. Pumberger, Proc. 4th Int. Conf. Semi-solid Processing of Alloys and Composites, Sheffield, UK, 1996, 40-46.
57. E. Tzimas, A. Zavaliangos, A. Lawley, Proc. 5th Int. Conf. Semi-solid Processing of Alloys and Composites, Colorado, USA, 1998, 345-352.
58. E. Tzimas, A. Zavaliangos, Acta Mater. 47 (1999) 517-528.
59. C.D. Yim, K.S. Shin, Mater. Trans. JIM 44 (4) (2003) 558-561.
60. L. Salvo, M. Suéry, Y. De Charentenay, W. Loué, Proc. 4th Int. Conf. Semi-solid Processing of Alloys and Composites, Sheffield, UK, 1996, 10-15.
61. C.L. Martin, D. Favier, M. Suéry, Proc. 4th Int. Conf. Semi-solid Processing of Alloys and Composites, Sheffield, UK, 1996, 51-57.
62. H.L. Yang, Z.L. Zhang, I. Ohnaka, J. of Mater. Proc. Technol. 151 (2004) 155-164.
63. M.C. Flemings, Solidification Processing, McGraw Hill, NY, USA, 1974.
64. D.A. Porter, K.E. Easterling, Phase Transformations in Metals and Alloys, Nelson Thornes Ltd. UK, 1992.
65. ASM Handbook, Casting, Vol. 15, ASM International, Metals Park OH, USA, 1988.
66. J. Dong, J.Z. Cui, Q.C. Le, G.M. Lu, Mater. Sci. Eng. A345 (2003) 234-242.
67. S.E. Kisakurek, J. Mater. Sci. 19 (7) (1984) 2289-2305.
68. K. Ichikawa, S. Ishizuka, Mater. Trans. JIM 30 (11) (1989) 915-924.
69. R.D. Doherty, H.-I. Lee, E.A. Feest, Mater. Sci. Eng. 65 (1) (1984) 181-189.
70. R. Haghayeghi, E.J. Zoqui, A. Halvaee, M. Emamy, J. of Mater. Proc. Technol. 169 (2005) 382-387.
71. S. Wu, X. Wu, Z. Xiao, Acta Mater. 52 (2004) 3519-3524.
72. W. Mao, Y. Li, A. Zhao, X. Zhong, Sci. Technol. Adv. Mater. 2 (2001) 97-99.
73. M.A. Martorano, C. Beckermann, Ch. A. Gadin, Metall. Mater. Trans. A, 34 (2003) 1657-1674.

74. H. Esaka, T. Wakabayashi, K. Shinozuka, M. Tamura, ISIJ Int. 43 (9) (2003) 1415-1420.
75. F. Czerwinski, Acta Mater. 53 (2005) 1973-1984.
76. S. Ji, A. Das, Z. Fan, Scripta Mater. 46 (2002) 205-210.
77. A. Das, Z. Fan, Proc. 7th Inter. Conf. Semisolid Metal processing, Tsukuba, Japan, 2002, 449-454.
78. R.S. Qin, E.R. Wallach, Mater. Sci. Eng. A357 (2003) 45-54.
79. S. Nafisi, R. Ghomashchi, Mater. Sci. Eng. A437 (2006) 388-395.
80. W. Mao, H. Li, Y. Bai, S. Gao, J. University of Sci. Technol. Beijing, Min. Metall. Mater. 14 (1) 2007, 56-60.
81. G.J. Davies, Solidification and Casting, Applied Science Publishing Co., London, UK, 1973.
82. H. Wang, C.J. Davidson, D.H. StJohn, Mater. Sci. Eng. A368 (2004) 159-167.
83. M.A. Easton, H. Kaufmann, W. Fragner, J. Mater. Sci. Eng. A420 (2006) 135-143.
84. D.J. Browne, M.J. Hussey, A.J. Carr, D. Brabazon, Int. J. Cast Met. Res.16 (4) (2003) 418-426.
85. T. Li, W.D. Huang, X. Lin, The Chinese J. Nonferrous Met. 10 (5) (2000) 635-638.
86. S. Wu, X. Wu, Z. Xiao, Acta Mater. 52 (2004) 3519-3524.
87. F. Czerwinski, Magnesium Injection Moulding, Springer, NY, USA, 2008.
88. J.E.C. Hutt, D.H. StJohn, L. Hogan, A.K. Dhale, Mater. Sci. Technol. 15 (1999) 495-500.
89. H. Wang, Z.L. Ning, X.D. Yao, C.J. Davidson, D.H. StJohn, Mater. Forum 28 (2004) 1316-1321.
90. J.-X. Zhang, G.–J Liu, J.–Xu, L.K. Shi, Chinese J. Nonferrous Met. 10 (4) (2000) 511-515.
91. J.M.M. Molenaar, L.W. Katgerman, W.H. Kool, R.J. Smeulders, J. Mater. Sci. 21 (2) (1986) 389-394.
92. G. Bartos-Tausig, K. Xia, Proc. 4th Int. Conf. Semi-solid Processing of Alloys and Composites, Sheffield, UK, 1996, 290-295.
93. K. Miwa, T. Kakamu, T. Ohashi, Trans. Jpn. Inst. Met. 26 (8) (1985) 549-556.
94. Y.H. Ryoo, I.J. Kim, D.H., Kim, Proc. 4th Int. Conf. Semi-solid Processing of Alloys and Composites, Sheffield, UK, 1996, 66-70.
95. S. Nafisi, R. Ghomashchi, Materials Characterization 57 (2006) 371-385.
96. O. Lashkari, S. Nafisi, R. Ghomashchi, Mater. Sci. Eng. A441 (2006) 49-59.
97. W.W. Mullins, R.F. Sekerka, J. Appl. Phys. 34 (1963) 323–329.
98. J. Dong, J.Z. Cui, Q.C. Le, G.M. Lu, Mater. Sci. Eng. A345 (2003) 234-242.
99. F. Spaepen, J. Fransaer, Adv. Eng. Mater. 2 (9) (2000) 593-596.
100. W. Mao, Y. Bai, H. Lin, J. Uni. Sci. Technol. Beijing, Min. Metell. Mater. 13 (4) (2006) 324-328.
101. H. Wang, C.J. Davidson, J.A. Taylor, D.H. StJohn, Mater. Sci. Forum 396-402 (2002) 143-148
102. W. Mao, C. Cui, A. Zhao, J. Yang, X. Zhong, J. Mater. Sci. Technol. 17 (6) (2001) 615-619.
103. S. Midson, K. Young, 5th AFS Int. Conf. Molten Aluminum, 1998, 409–422.
104. W.W. Mullins, R.F. Sekerka, J. Appl. Phys. 35 (1964) 444-451.
105. P.J. Uggowitzer, H. Kaufmann, Steel Res. Int. 75 (8/9) (2004) 525-530.
106. M.F. Zhu, J.M. Kim, C.P. Hong, ISIJ Int. 41 (9) (2001) 992-998.
107. J.M. Kim, M.F. Zhu, C.P. Hong, Int. J. Cast Met. Res.15 (2002) 285-289.
108. Z. Fan, Mater. Sci. Eng. A413-414 (2005) 72-78.
109. S. Blais, W. Loué, C. Pluchon, Proc. 4th Int. Conf. Semi-solid Processing of Alloys and Composites, Sheffield, UK, 1996, 187-192.
110. H.D. Brody, M.C. Flemings, Trans. Metall. Soc. AIME 236 (1966) 615-624.
111. H. Kaufmann, M. Nakamura, H. Wabusseg, P.J. Uggowitzer, Diecasting World 16-17 (200) 14-17.
112. S. Nafisi, R. Ghomashchi, Mater. Sci. Eng. A415 (2006) 273-285.

113. T. Wang, B. Pustal, M. Abondano, T. Gimming, A. Bührig-Polaczeck, M. Wu, A. Ludwig, Trans. Nonferrous Met. Soc. China, 15 (2) (2005) 389-394.
114. .W.R. Kopp, T.M. Gisbert, http://hwww.rwth.aachen.de/sfb289/Ww/pdf/pub_ibf_metec99.pdf
115. T. Basner, SAE Technical Paper Series, Paper No. 2000-01-0059, 2000 World Congress (2000) 1-5.
116. E.F. Fascetta, R.G. Riek, R. Mehrabian, M.C. Flemings, AFS Trans. 82 (1974) 95-100.
117. J.G. Wang, P. Lu, H.Y. Wang, Q.C. Jiang, Mater. Letters 58 (30) (2004) 3852-3856.
118. J.G. Wang, P. Lu, H.Y. Wang, J.F. Liu, Q.C. Jiang, J. Alloys and Compounds 395 (2005)108-112.
119. C.J. Quaak, W.H. Kool, Mater. Sci. Eng. A188 (1994) 277-282.
120. J.-C. Lee, H.-I. Lee, D.-S. Shin, Proc. 5th Int. Conf. Semi-solid Processing of Alloys and Composites, Colorado, USA, 1998, 597-604.
121. F. Akhlaghi, A. Lajevardi, H.M. Maghanaki, J. Mater. Proc. Technol. 155-156 (2004) 1874-1881.
122. B.C. Pai, R.M. Pillai, K.G. Satyanarayana, Proc. 5th Int. Conf. Semi-solid Processing of Alloys and Composites, Colorado, USA, 1998, 423-430.
123. M.A. Taha, Adv. Eng. Mater. 5 (1) (2003) 805-812.
124. X.H. Qin, D.L. Jiang, S.M. Dong, Mater. Sci. Eng. A385 (2004) 31-37.
125. V. Agarwala, K.G. Satyanarayana, R.C. Agarwala, R. Garg, Mater. Sci. Eng. A327 (2002) 186-202.
126. D.M. Walukas, R.F. Decker, A.W. Totten, Magnesium Technology, TMS, Warrendale, PA, USA, 2001, 95-98.
127. S. LeBeau, R.F. Decker, Proc. 5th Int. Conf. Semi-solid Processing of Alloys and Composites, Colorado, USA, 1998, 387-395.
128. R.F. Decker, R.D. Carnahan, R. Vining, E. Eldener, Proc. 4th Int. Conf. Semi-solid Processing of Alloys and Composites, Sheffield, UK, 1996, 221-224.
129. N. Aoyagi, Y. Kojima, Proc. 5th Int. Conf. Semi-solid Processing of Alloys and Composites, Colorado, USA, 1998, 449-455.
130. Z. Fan, Proc. 7th Int. Conf. Semisolid Metal Processing, Tsukuba, Japan, 2002, 671-676.
131. S. Ji, Z. Fan, Proc. 6th Int. Conf. Semi-solid Processing of Alloys and Composites, Turin, Italy, 2000, 723-728.
132. S. Ji, Z. Fan, G. Liu, X. Fang, S. Song, Proc. 7th Int. Conf. Semisolid Metal Processing, Tsukuba, Japan, 2002, 683-688.
133. K. Young, P. Eisen, Metall. Sci. and Technol. 18 (2) (2000) 11-15.
134. N. Poolthong, P. Qui, H. Nomura, Sci. Technol. Adv. Mater. 4 (2003) 481-489.
135. N. Poolthong, H. Nomura, Int. J. Cast Met. Res. 15 (2003) 523-530.
136. G. Tausig, K. Xia Proc. 5th Int. Conf. Semi-solid Processing of Alloys and Composites, Colorado, USA, 1998, 473-480.
137. J. Aguilar, M. Fehlbier, A. Ludwig, A. Bührig-Polaczek, P.R. Sahm, Mater. Sci. Eng. A375-377 (2004) 651-655.
138. W. Lapkowski, J. Mater. Proc. Technol. 80-81(1998) 463-468.
139. M. Qian, Acta Mater. 54 (2006) 2241-2252.
140. S.C. Bergsma, M.C. Tolle, M.E. Kassner, X. Li, E. Evangelista, Proc. 5th Int. Conf. Semi-solid Processing of Alloys and Composites, Colorado, USA, 1998, 149-155.
141. M. Stucky, M. Richard, L. Salvo, M. Suéry, Proc. 5th Int. Conf. Semi-solid Processing of Alloys and Composites, Colorado, USA, 1998, 513-520.
142. K.-B. Kim, H.-I. Lee, H.-K. Moon, Proc. 5th Int. Conf. Semi-solid Processing of Alloys and Composites, Colorado, USA, 1998, 415-422.
143. C. Bertrand, P. Patrick, Proc. 4th Int. Conf. Semi-solid Processing of Alloys and Composites, Sheffield, UK, 1996, 169-173.
144. K.E. Blazek, J.E. Kelly, N.S. Pottore, ISIJ Int. 35 (1995) 813-818.
145. B, Wendinger, Proc. 4th Int. Conf. Semi-solid Processing of Alloys and Composites, Sheffield, UK, 1996, 239-241.

146. B.I. Jung, C.H. Jung, T.K. Han, Y.H. Kim, J. of Mater. Proc. Technol. 111 (2001) 69-73.
147. J.J. Valencia, T.G. Friedhoff; T.P. Creede, J.J. Cardarella, Proc. 5th Int. Conf. Semi-solid Processing of Alloys and Composites, Colorado, USA, 1998, 397-04.
148. J. Aguilar, M. Fehlbier, T. Grimmig, H. Bramann, C. Afrath, A. Bührig-Polaczek, Steel Res. Int. (75) (8/9) (2004) 492-505.
149. E. Yano, N. Wada, N. Nishikawa, T. Motegi, J. Jpn. Inst. Met. 66 (2002) 1131-1134.
150. D. Liu, H.V. Atkinson, P. Kapranos, W. Jirattiticharoean, H. Jones, Mater. Sci. Eng. A361 (2003), 213-224.
151. H. Watari, K. Davey, M.T. Rasgado, T. Haga, S. Izawa, J. Mater. Proc. Technol. 155-156 (2004) 1662-1667.
152. T. Haga, J. Mater. Proc. Technol. 130-131 (2002) 558-561.
153. T. Haga, K. Takahashi, M. Ikawa, H. Watari, J. Mater. Proc. Technol. 140 (2003) 610-615.
154. M. Kiuchi, S. Sugiyama, Proc. 4th Int. Conf. Semi-solid Processing of Alloys and Composites, Sheffield, UK, 1996, 197-201.
155. M. Kiuchi, S. Sugiyama, ISIJ Int. 35 (6) (1995) 790-797.
156. I. Seidel, R. Kopp, Steel Res. Int. 75 (8/9) (2004) 545-551.
157. T. Grimmig, C. Afrath, O. Klaassen, A. Bührig-Polaczek, P.R. Sahm, Proc. 7th Int. Conf. Semisolid Metal Processing, Tsukuba, Japan, 2000, 789-794.
158. T. Haga, J. Mater. Proc.Technol. 111 (2001) 64-68.
159. T. Haga, P. Kapranos, J. Mater. Proc. Technol. 157-258 (2004) 508-512.
160. E. Tzimas, A. Zavaliangos, Mater. Manuf. Proc. 14 (2) (1999) 217-231.
161. E. Tzimas, Ph.D. Thesis; Drexel University, USA, 1997.
162. H.B. Dong, M.R.M. Shin, E.C. Kurum, H. Cama, J.D. Hunt, Fluid Phase Equilibria, 212 (2003) 199-208.
163. R. Cremer, A. Winkelmann, G. Hirt, Proc. 4th Int. Conf. Semi-solid Processing of Alloys and Composites, Sheffield, UK, 1996, 159-164.
164. P.J. Uggowitzer, G.-C. Gullo, A. Wahlen, Proceedings of the first Ranshofener Leichtmetalltage (2000) 95-107.
165. H. Wabusseg, G.-C. Gullo, P.J. Uggowitzer, K. Steinhoff, H. Kaufmann, JOM 37 (2002) 1173-1178.
166. Y.Q. Liu, Z. Fan, Mater. Sci. Forum 396-402 (2002) 717-722.
167. Y.Q. Liu, Z. Fan, J. Patel, Proc. 7th Int. Conf. Semisolid Metal Processing, Tsukuba, Japan, 2002, 599-604.
168. Y.Q. Liu, Z. Fan, Proc. 7th Int. Conf. Semisolid Metal Processing, Tsukuba, Japan, 2002, 587-592.
169. Y.Q. Liu, A. Das, Z. Fan, Mater. Sci. and Technol. 20 (2004) 35-41.
170. E. Tzimas, A. Zavaliangos, Synthesis of Light Weight Metals III, TMS Society, 2000, 195-203.
171. S. Kleiner, E. Ogris, O. Beffort, P.J. Uggowitzer, Adv. Eng. Mater. 5 (9) (2003), 653–658.
172. X. Fang, Z. Fan, Mater. Sci. Technol. 21 (3) (2005) 366-372.
173. X. Fang, Z. Fan, Scripta Mater. 54 (2006) 789-793.
174. ASM Metals Handbook, Metallography and Microstructure, Vol. 9, ASM International, Metals Park, OH, USA. 1985.
175. E.J. Zoqui, J. Mater. Proc. Technol. 143-144 (2003) 195-201.
176. L. Salvo, W.R. Loué, M.Suéry, ISIJ, Int. 35 (6) (1995) 798-804.
177. E. de Freitas, M. Ferrante, V.F. da Silva, W.B. Filho, D. Spinelli, J. Mater. Proc. Technol. 155-156 (2004) 1629-1633.
178. W.R. Loué and M. Suéry, Mat. Sci. Eng. A203 (1995), 1-13.
179. D. Emadi, L.V. Whiting, S. Nafisi, R. Ghomashchi, J. Thermal Analysis and Calorimetry 81 (2005) 235-242.
180. I.G. Chen, D.M. Stefanescu, AFS Trans. 92 (1984) 947-964.
181. H. Cruz, C. Gonzalez, A. Juárez, H. Herrera, J. Juárez, J. Mater. Proc. Technol. 178 (2006) 128-134.

182. K.G. Upadhya, D.M. Stefanescu, K. Lieu, D.P. Yeager, AFS Trans. 97 (1989) 61-66.
183. J.C. Baez, C. González, M.R. Chavez, M. Castro, J. Juárez, J. Mater. Proc. Technol. 153-154 (2004) 531-536.
184. C. González-Rivera, B. Campillo, M. Castro, M. Herrera, J. Juárez-Islas, Mater. Sci. Eng. A279 (2000) 149-159.
185. D. Emadi, L.V. Whiting, AFS Trans. 110 (2002) 285-296.
186. L. Bäckerud, G. Chai, J. Tamminen, Characteristics of Alminium Alloys, Vol. 2: Foundary Alloys, AFS/Skanaluminium, USA, 1990.
187. D.P. Woodruff, The Solid-Liquid Interface, Cambridge University Press, Cambridge, UK, 1973.
188. G. Höhne, W. Hemminger, H.-J. Flammersheim, Differential Scanning Calorimetry: An Introduction to Practioners, Springer, 1996.
189. L.A. Chapman, J. Mater. Sci. 39 (2004) 7229-7236.
190. J.-P. Gabathuler, C. Ditzler, Proc. 4th Int. Conf. Semi-solid Processing of Alloys and Composites, Sheffield, UK, 1996, 331–335.
191. D.H. Kirkwood, Int. Mater. Rev. 39 (5) (1994) 173-189.
192. A.M. Camacho, H.V. Atkinson, P. Kapranos, B.B. Argent, Acta Mater. 51 (2003) 2319-2330.
193. E. Tzimas, A. Zavaliangos, J. Mater. Sci. 35 (2000) 5319-5329.
194. M. Braccini, C.L. Martin, A. Tourabi, Y. Bréchet, M. Suéry, Mater. Sci. Eng. A337 (2002) 1-11.
195. L. Arnberg, G. Chai, L. Bäckerud, Mater. Sci. Eng. A173 (1993) 101-103.
196. A.K. Dahle, L. Arnberg, Acta Mater. 45 (2) (1997) 547-559.
197. S.M. Nabulsi, T.A. Steinberg, C.J. Davidson, N.W. Page, Proc. 4th Int. Conf. Semi-solid Processing of Alloys and Composites, Sheffield, UK, 1996, 47-50.
198. A.K. Dahle, D.H. StJohn, Acta Mater. 47(1999) 31-41.
199. T. Sumitomo, D.H. StJohn, T. Steinberg, Mater. Sci. Eng. A289 (2000) 18-29.
200. R. Moschini, Proc. 4th Int. Conf. Semi-solid Processing of Alloys and Composites, Sheffield, UK, 1996, 248 -250.
201. D.H. Kirkwood, P.J. Ward, Steel Res. Int. 75 (8/9) (2004) 519-524.
202. W. Püttgen, W. Bleck, W. Seidle, R. Kopp, C. Bertrand, Adv. Eng. Mater. 7 (2) (2005) 726-735.
203. B. Hallstedt, E. Balitchev, H. Shimahara, D. Neuschütz, ISIJ Int. 46 (12) (2006) 1852-1857.
204. H. Bramann, C. Afrath, T. Grimmig, M. Fehlbier, A. Bührig-Polaczek, Steel Res. Int. 75 (8/9) (2004), 537-544.
205. B. Tambunan, Seminar National MIPA, 2005.
206. J.H. Chen, H.L. Tsai, AFS Trans. 133 (1990) 539-546.
207. N. Saunders, A.P. Miodowink, CALPHAD Calculation of Phase Diagrams – A Comprehensive Guide, Pergamon, 1998.
208. N. Saunders, A.P. Miodowink, J.-Ph. Schillé, Liquid Metal Processing, Nancy, France, 2003, 21-24.
209. T.F. Bower, H.D. Brody, M.C. Flemings, The M.C. Flemings Symposium on Solidification and Materials Processing, Cambridge, MA, USA, 2001, 23-33.
210. J.A. Sareal, G.J. Abbaschian, Metall. Trans.17A (1986) 2063-2073.
211. Thermo-Calc® Software, Foundation of Computational Thermodynamics, Stockholm, Sweden.
212. T.W. Clyne, W. Kurz, Metall. Trans. 12A (1981) 965-971.
213. C.D. Yim, Ph.D. Thesis, Seoul National University, South Korea.
214. L. Bäckerud, E. Król, J. Tamminen, Solidification Characteristics of Al alloys, vol. 1: Wrought Alloys, Skanaluminium, Oslo, Norway, 1986.
215. X.G. Chen, J. Langlais, Mater. Sci. Forum 331-333 (1-3) (2000) 215-221.
216. J.L. McNaughton, C.T. Mortimer, Differential Scanning Calrometry, Butterworths, London, 1975.
217. R. Shibata, T. Kaneuchi, T. Soda, Y. Iizuka, Proc. 4th Int. Conf. Semi-solid Processing of Alloys and Composites, Sheffield, UK, 1996, 296-300.

218. G. Chiarmetta, Proc. 5th Int. Conf. Semi-solid Processing of Alloys and Composites, Colorado, USA, 1998, 87-95.
219. P. Eisen, Proc. 5th Int. Conf. Semi-solid Processing of Alloys and Composites, Colorado, USA, 1998, ix-xvi
220. R. Shibata, T. Kaneuchi, T. Souda, H. Yamane, Proc. 5th Int. Conf. Semi-solid Processing of Alloys and Composites, Colorado, USA, 1998, 465-470.
221. J. Vinarcik, J.D. Taylor, K. Farris, Proc. 5th Int. Conf. Semi-solid Processing of Alloys and Composites, Colorado, USA, 1998,105-113.
222. S. LeBeau, J. Maffia, Eng. Casting Solutions (Fall) (2002) 33-35.
223. W.P. Graebel, Engineering Fluid Dynamics, Taylor and Francis Publishers, NY, USA, 2001.
224. W.H.M. Alsem, P.C. Van Wiggen, M. Vader, Light Metals, TMS Publications, Warrendale, PA, USA, 1992 821–829.
225. W.R. Loué and M. Suéry, Mat. Sci. Eng. A203 (1995) 1-13.
226. D. Brabazon, D.J. Browne, A.J. Carr, Mater. Sci. Eng. A326 (2002) 370-381.
227. Q.G. Wang, C.J. Davidson, J. Mater. Sci. 36 (2001) 739-750.
228. Smithells Metals Reference Book, E.A. Brandes, G.B. Brook (Ed.), 7th Ed., Butterworth-Heinmann, Oxford, UK, 1999.
229. F.C.R. Hernandez, M.B. Djurdjevic, W.T. Kierkus, J.H. Sokolowski, Mater. Sci. Eng. A396 (2005) 271-276.
230. G. Drossel, Giessereitechnik, 27 (1) (1981) 7-12.
231. D. Emadi, J.E. Gruzleski, J.M. Toguri, Metall. Trans. 24B (1993) 1055–1063.
232. P. Anson, J.E. Gruzleski, M. Stucky, AFS Trans. (2001) 1-9.
233. G. Chai, T. Rolland, L. Arnberg and L. Backerud, Proc. 2nd Int. Conf. Semi-Solid Processing of Alloys and Composites, Cambridge, MA, USA, TMS, Warrendale, PA (1992) 193–201.
234. Y.D. Kwon, Z.H. Lee, Mater. Sci. Eng. A360 (2003) 372-376.
235. A.K. Dahle, P.A. Tondel, C.J. Paradies, L. Arnberg, Metall. Trans. 27A (1996) 2305-2313.
236. D.A. Granger, R.R. Sawtell, M.M. Kesker, AFS Trans. 92 (1984)579-586.
237. L.F. Mondolfo, Alumnium Alloys: Structure and Properties, Butterworths, London, UK, 1976.
238. T. Joenoes, J.E. Gruzleski, Cast Met.4 (2) (1991) 62–71.
239. R. I. Mackay, J.E. Gruzleski, Int. J. Cast Met.Res.10 (5) (1998), 255-265.
240. B. Closset, J.E. Gruzleski, AFS Trans. 99 (1982) 453-464.
241. S. Argyropoulos, B. Closset, H. Oger, AFS Trans. 91 (1983) 351-363.
242. J.A. Taylor, D.H. StJohn, J. Barresi, M.J. Couper, Mater. Sci. Forum 331-337 (1) (1984) 277-282.
243. A.K. Dahle, K. Nogita, J.W. Zindel, S.D. McDonald, L.M. Hogan, Metall. Trans. 32A (2001) 949–960.
244. G.F. Van der Voort, Metallography Principles and Practice, ASM International, Materials Park Ohio, USA, 1999.
245. S. Nafisi, R. Ghomashchi, JOM 58 (2006) 24-30.
246. I.L. Ferreira, J.E. Spinelli, J.C. Pires, A. Garcia, Mater. Sci. Eng. A408 (2005) 317-325.
247. B. Niroumand, K. Xia, Proc. 5th Int. Conf. Semi-solid Processing of Alloys and Composites, Colorado, USA, 1998, 637-644.
248. E.J. Zoqui, M. Paes, E. Es-Sadiqi, J. Mater. Proc. Technol. 20 (2002) 365-373.
249. B. Niroumand, K. Xia, Mater. Sci. Eng. 283 (2000) 70-75.
250. S. Jabrane, B. Clement, F. Ajersch, Proc. Semi-solid Alloys and Composites, TMS, Warrendale, PA, USA, 1992, 223-236.
251. A. Assar, N. El-Mahallawy, M.A. Taha, Met. Technol. 9 (May) (1982) 165-170.
252. S. Sannes, L. Arnberg, M.C. Flemings, Light Metals, TMS, Warrendale, PA, USA, 1996, 795-798.
253. P. Falak, B. Niroumand, Scripta Mater. 53 (2005) 53-57.
254. P.A. Joly, R. Mehrabian, J. Mater. Sci. 11 (1976), 1393-1418.

255. R. J. Smeulders, F.H. Mischgofsky, H.J. Frankena, J. Crystal Growth, 76 (1986) 151-169.
256. A. M. Mullis, Acta Mater. 47 (1999) 1783-1789.
257. J.D. Hunt, Mater. Sci Eng. 65 (1984) 75-83.
258. A.L. Greer, P.S. Cooper, M.W. Meredith, W. Schneider, P. Schumacher, J.A. Spittle, A. Tronche, Adv. Eng. Mater. 5 (1-2) (2003) 81-91.
259. K. Kawai, W.D. Griffiths, FTJ (May) (2004) 169–172.
260. W.D. Griffiths, D.Whitworth, FTJ (March) (2006) 61–64.
261. J.M. Kim, M.F.Zhu, C.P. Hong, Int. J. Cast Met. Res. 15 (2002) 285-289.
262. H.-S. Kim, I.-S Cho, J.-S. Shin, S.-M. Lee, B.-M. Moon, ISIJ Int. 45 (2) (2005) 192-198.